Probing the structure and reactivity of zeolites in their interactions with water

Cameron Mark Rice

A thesis submitted for the degree of PhD
at the
University of St Andrews

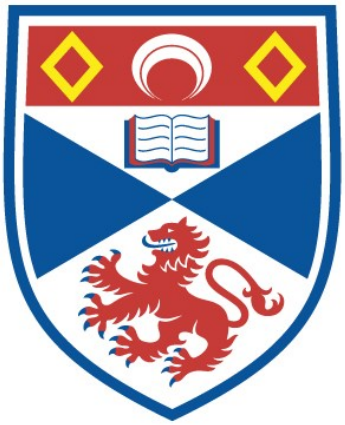

2022

Declaration

Candidate's declaration

I, Cameron Mark Rice, do hereby certify that this thesis, submitted for the degree of PhD, which is approximately 75,000 words in length, has been written by me, and that it is the record of work carried out by me, or principally by myself in collaboration with others as acknowledged, and that it has not been submitted in any previous application for any degree. I confirm that any appendices included in my thesis contain only material permitted by the 'Assessment of Postgraduate Research Students' policy.

I was admitted as a research student at the University of St Andrews in September 2017.

I received funding from an organisation or institution and have acknowledged the funder(s) in the full text of my thesis.

Date October 22, 2022 Signature of candidate

Supervisor's declaration

I hereby certify that the candidate has fulfilled the conditions of the Resolution and Regulations appropriate for the degree of PhD in the University of St Andrews and that the candidate is qualified to submit this thesis in application for that degree. I confirm that any appendices included in the thesis contain only material permitted by the 'Assessment of Postgraduate Research Students' policy.

Date October 22, 2022 Signature of supervisor

Date October 22, 2022 Signature of supervisor

Permission for publication

In submitting this thesis to the University of St Andrews we understand that we are giving permission for it to be made available for use in accordance with the regulations of the University Library for the time being in force, subject to any copyright vested in the work not being affected thereby. We also understand, unless exempt by an award of an embargo as requested below, that the title and the abstract will be published, and that a copy of the work may be made and supplied to any bona fide library or research worker, that this thesis will be electronically accessible for personal or research use and that the library has the right to migrate this thesis into new electronic forms as required to ensure continued access to the thesis.

I, Cameron Mark Rice, confirm that my thesis does not contain any third-party material that requires copyright clearance.

The following is an agreed request by candidate and supervisor regarding the publication of this thesis:

Printed copy

Embargo on all of print copy for a period of 2 years on the following ground(s):

- Publication would preclude future publication

Supporting statement for printed embargo request

Work contained in this thesis will form part of a manuscript being prepared for submission to a peer-reviewed journal.

Electronic copy

Embargo on all of electronic copy for a period of 2 years on the following ground(s):

- Publication would preclude future publication

Supporting statement for electronic embargo request

Work contained in this thesis will form part of a manuscript being prepared for submission to a peer-reviewed journal.

Title and Abstract

- I agree to the title and abstract being published.

Date October 22, 2022 Signature of candidate

Date October 22, 2022 Signature of supervisor

Date October 22, 2022 Signature of supervisor

Underpinning Research Data or Digital Outputs

Candidate's declaration

I, Cameron Mark Rice, understand that by declaring that I have original research data or digital outputs, I should make every effort in meeting the University's and research funders' requirements on the deposit and sharing of research data or research digital outputs.

Date October 22, 2022 Signature of candidate

Permission for publication of underpinning research data or digital outputs

We understand that for any original research data or digital outputs which are deposited, we are giving permission for them to be made available for use in accordance with the requirements of the University and research funders, for the time being in force.

We also understand that the title and the description will be published, and that the underpinning research data or digital outputs will be electronically accessible for use in accordance with the license specified at the point of deposit, unless exempt by award of an embargo as requested below.

The following is an agreed request by candidate and supervisor regarding the publication of underpinning research data or digital outputs:

Embargo on all of electronic files for a period of 2 years on the following ground(s):

- Publication would preclude future publication

Supporting statement for embargo request

Work contained in this thesis will form part of a manuscript being prepared for submission to a peer-reviewed journal.

Date October 22, 2022 Signature of candidate

Date October 22, 2022 Signature of candidate

Date October 22, 2022 Signature of candidate

Acknowledgements

Firstly, I would like to thank my supervisors, Russell and Sharon, for giving me the opportunity to pursue a PhD in their groups and for the guidance and input over the past four years. I am also particularly grateful for the opportunities to attend scientific conferences (often in wonderful places) and encouragement to present my work. As well as increasing my scientific understanding, these conferences have contributed some great moments throughout my PhD.

I would also like to express my thanks to the facility managers, who have enabled me to obtain the results presented in this thesis. A particular thanks goes to Dr Daniel Dawson for maintaining Scotland's 'biggest and best' solid-state NMR facility and for always saying it like it is. Thanks also go to Dr Yuri Andreev, for maintaining the in-house PXRD facility, and to those at the UK High Field Solid-state NMR facility, for all things associated with running experiments, often virtually, of small things in big magnets.

Thank you to the members of both the Morris and Ashbrook groups, both past and present, for providing a great working atmosphere, battling through fires, lockdowns and the rest of it. Thank you too to the members of coffee and wine clubs for ensuring I was caffeinated at or inebriated at (mostly) the appropriate times. Thank you to Dr Giulia Bignami for your training in both solid-state NMR and zeolite and MOF synthesis, to Dr Daniel Rainer for valuable discussions on zeolites and to Dr Suzi Pugh for discussions on NMR of zeolites and always laughing at my awful jokes.

To those on the University Postgraduate Society committee, I hope you enjoyed our time working together as much as I. Thank you also to the Students' Association for allowing as much of our budget to go on wine and cheese as it did. Cheers also to Chemsoc and thanks to the RSC Tayside committee for letting me get involved and hopefully making a difference.

Thank you to Simon for being a great flatmate and an even better friend. You truly are one of a kind. Your refreshing point of view, generosity with home-cooking and always making sure our glasses were filled made our time living together a blast. Thank you to my family for your unwavering support throughout my studies, especially when we found ourselves back under one roof in early 2020, working through uncertain times. Finally, a special thank you to Carrie, for bringing out the best in me over what has been a funny few years and for often being the only one there. Thank you for providing perspective, helping me to take a step back and for putting me in my place on the squash court.

For my family.

Abstract

The work presented in this thesis has been performed to increase the understanding of the interactions of zeolites with water, under a range of reaction conditions. The systems studied have been selected on the basis of their known hydrolytic instability or as model systems for which new avenues for hydrolytic instability can more easily be followed.

The focus of research detailed in this thesis is split into three main sections. The mechanism of the ADOR (Assembly, Disassembly, Organisation, Reassembly) process for the synthesis of new zeolites from germanosilicate **UTL** is probed to deepen the understanding of the intermediate species formed and how the local structure and long-range order of the products are affected by reaction variables. Subsequently, the **CHA** framework has been selected as a model system for the study of a newly-identified bond lability exhibited by some non-'ADORable' aluminosilicate zeolite materials. To further aid characterisation and understanding of this lability, a series of inter-zeolite transformations from the **FAU** to **CHA** framework have been adapted to allow ^{17}O enrichment and ^{17}O NMR spectroscopic investigation, to characterise and identify key intermediate and framework species.

The complexity and high structural disorder of the materials studied in this work mean that a multivariate approach to characterisation and analysis is required. Primarily, solid-state NMR spectroscopy and powder X-ray diffraction have been used to characterise the materials, elucidating differences between their local structure and long-range order. In addition, energy-dispersive X-ray spectroscopy, scanning electron microscopy, thermogravimetric analysis and density functional theory calculations have also been used to further aid characterisation and understanding of these complex systems.

Results presented demonstrate that both zeolites and water interact strongly with one another when combined. Zeolites and water are found to be reactive even under mild conditions, *e.g.* room temperatures, where ^{17}O NMR spectroscopy has shown the rapid exchange of $H_2{}^{17}O$ oxygen into the frameworks of **UTL**, **CHA** and **FAU** zeolites, by

resolving signals attributed to framework zeolite linkages. Whilst favourable under ambient conditions, these bond lability processes are also found to be selective, with observed enrichment found to differ between frameworks with different topologies, compositions and extraframework cations. In some cases, observed exchange of framework oxygen species has been attributed in part to the defective nature of zeolite frameworks. A further mechanistic explanation for the enrichment of zeolites for which the structure is not thought to be defective has also been predicted by collaborators using molecular dynamics. Whilst this mechanism may explain the facile bond lability seen for **CHA** frameworks, its widespread applicability to other zeolite frameworks that show rapid exchange of framework oxygen with that in water is not known. Water is also found to interact strongly with zeolite frameworks undergoing structural transformations, such as during the ADOR process or during post-synthetic transformations. Here, under the elevated temperatures of reaction conditions, ^{17}O supplied from $H_2{}^{17}O$ reagent has been shown to be incorporated into the structure of zeolite frameworks, especially in regions considered non-reactive within the reaction.

These results demonstrate that both zeolites and water interact and react when combined and provide further evidence to the contrary that zeolites are perceived as static, inert scaffolds. The findings have potential implications for the commercial uses of zeolites, where a balance between framework stability and flexibility is important.

Publications

Publications arising from this work:

Chapter 4 is based on work published in:

Kinetics and Mechanism of the Hydrolysis and Rearrangement Processes within the Assembly-Disassembly-Organization-Reassembly Synthesis of Zeolites.
Susan E. Henkelis, Michal Mazur, Cameron M. Rice, Paul S. Wheatley, Sharon E. Ashbrook and Russell E. Morris, *J. Am. Chem. Soc.*, 2019, **141**, 4453-4459.

A procedure for identifying possible products in the assembly-disassembly-organization-reassembly (ADOR) synthesis of zeolites.
Susan E. Henkelis, Michal Mazur, Cameron M. Rice, Giulia P. M. Bignami, Paul S. Wheatley, Sharon E. Ashbrook, Jiří Čejka and Russell E. Morris, *Nat. Protoc.*, 2019, **14**, 781-794.

Mechanochemically assisted hydrolysis in the ADOR process.
Daniel N. Rainer, Cameron M. Rice, Stewart J. Warrender, Sharon E. Ashbrook and Russell E. Morris, *Chem. Sci.*, 2020, **11**, 7060-7069.

Understanding the Synthesis and Reactivity of ADORable Zeolites using NMR Spectroscopy.
Sharon E. Ashbrook, Russell E. Morris and Cameron M Rice, *Curr. Opin. Colloid. In.*, 2022, **61**, 101634.

Chapter 5 is based on work published in:

Fast room temperature lability of aluminosilicate zeolites.
Christopher J. Heard, Lukáš Grajciar, Cameron M. Rice, Suzi M. Pugh, Petr Nachtigall, Sharon E. Ashbrook and Russell E. Morris, *Nat. Commun.*, 2019, **10**, 4060-4067.

Publications related to this work:

^{17}O NMR spectroscopy of crystalline microporous materials.
Sharon E. Ashbrook, Zachary H. Davis, Russell E. Morris and Cameron M. Rice, *Chem. Sci.*, 2021, **12**, 5016-5036.

Publications outside the scope of this work:

Following the unusual breathing behaviour of ^{17}O-enriched mixed-metal (Al,Ga)-MIL-53 using NMR crystallography.
Cameron M. Rice, Zachary H. Davis, David McKay, Giulia P. M. Bignami, Ruxandra G. Chitac, Daniel M. Dawson, Russell E. Morris and Sharon E. Ashbrook, *Phys. Chem. Chem. Phys.*, 2020, **22**, 14514-14526.

Controlled Synthesis of Large Single Crystals of Metal-Organic Framework CPO-27-Ni Prepared by a Modulation Approach: In situ Single-Crystal X-ray Diffraction Studies.
Simon M. Vornholt, Caroline G. Elliott, Cameron M. Rice, Samantha E. Russell, Peter J. Kerr, Daniel N. Rainer, Michal Mazur, Mark R. Warren, Paul S. Wheatley, and Russell E. Morris, *Chem. Eur. J.*, 2021, **27**, 18537-8546.

Contents

Chapter 1

Materials and Concepts Introduction

This chapter serves as a general introduction to the background of zeolites and to the specific materials and reaction methodology employed in the research presented in this thesis.

1.1 Zeolites

1.1.1 Background

Zeolites are a class of inorganic aluminosilicate material first reported in the 1700s by Swedish mineralogist Baron Axel F. Crønstedt.[1–3] The name zeolite is derived from the Greek "ζεο", (zeo, to boil) and "λιτηος", (lithos, stone) as Crønstedt observed the evolution of steam from the surface of the zeolite, stilbite, as it was heated in a blow-pipe.[1] Zeolites are characterised by their unique topology, where silicate (SiO_4^{4-}) and aluminate (AlO_4^{5-}) TO_4 tetrahedra are connected through bridging oxygen linkages to form fully-connected, three-dimensional, periodic, crystalline frameworks. To date, there are 253 unique framework topologies recognised by the International Zeolite Association (IZA). Each of these is identifiable by a three-letter code, which generally serves as a signature of the laboratory credited with their discovery. In this thesis, framework codes in the text will be denoted in boldface *e.g.* **LTA**, corresponding to **L**inde **T**ype **A**.[4,5]

Zeolites are perhaps the most applicable and valuable class of porous solid to commercial application, due to their widely-perceived stability and tolerance to a range of physical conditions and to the molecular geometry of their pores and cavities.[6] Some zeolites, such as Crønstedt's stilbite, are found in large naturally-occurring deposits across the globe. These materials were likely useful for application even before their formal identification in the 1700s, and are now still excavated on a multi-million tonne scale every

year for a wide range of applications; from agriculture and water treatment to building materials.[6–10] The advent of synthetic zeolites in the 1940s marked the start of a new era for the field, increasing the range of zeolites available and an enabling tuneability of their properties.[11] These new synthetic materials now dominate the focus of modern zeolite research and have led to a blossoming of application into fields such as industrial catalysis, gas storage and capture and molecular sieving.[6,8,9,11–18] Synthetic zeolites now comprise approximately 80% of the verified frameworks to date,[4,19] with recent studies estimating that this makes up just over half the global market value of $ 30 bn. (USD) for zeolites.[20,21]

1.1.2 Structure and Composition

The arrangement of TO_4 tetrahedra within a zeolite framework is most easily described by breaking the structure down to either composite or secondary building units (CBUs or SBUs). SBUs are achiral units comprising up to 16 T atoms and 16 have been identified to date. SBUs are denoted by indicating the number of atoms that make up that ring. In instances where several rings make up an SBU, the numbers of atoms in each ring are separated by a hyphen (Figure 1.1). A zeolite framework is said to be derivable from a certain SBU if an integer number of a single SBUs can be used to produce the full unit cell of a framework. Relatedly, CBUs are fragments of zeolite frameworks, however they can be chiral. Further, the combination of multiple different CBUs may be required to describe the structure of a single framework although their combination may not necessarily derive its overall composition. They are most useful, however in the comparison of different frameworks who share certain structural motifs. At last report there were in the region of 60 CBUs common to more than one topology. CBUs are denoted using a three-character italicised identifier (Figure 1.1).[4,5,22–24]

Considering a purely siliceous framework, the empirical formula of all zeolites can be simplified to SiO_2 with the resultant materials representing crystalline polymorphs of silica. However, the substitution of trivalent aluminium for tetravalent silicon at T-sites within the periodic lattice imparts a negative charge on the framework. Substitution of silicon for aluminium into zeolite materials is permitted so long as Löewenstein's rule for aluminium avoidance is held. This dictates that no two aluminium will be found adjacent to each other in the framework, in effect prohibiting Al-O-Al linkages and the formation of zeolite material with $Si/Al < 1$.[25] As substitution with aluminium results in a negative framework, a source of positive charge is required in order to restore charge neutrality. This is achieved by extra-framework cations, e.g. H^+, Na^+, K^+, Cs^+, Cu^{2+}, Zn^{2+}, NH_4^+, which locate in the pores and cavities of the zeolite. Naturally occurring zeolites are often

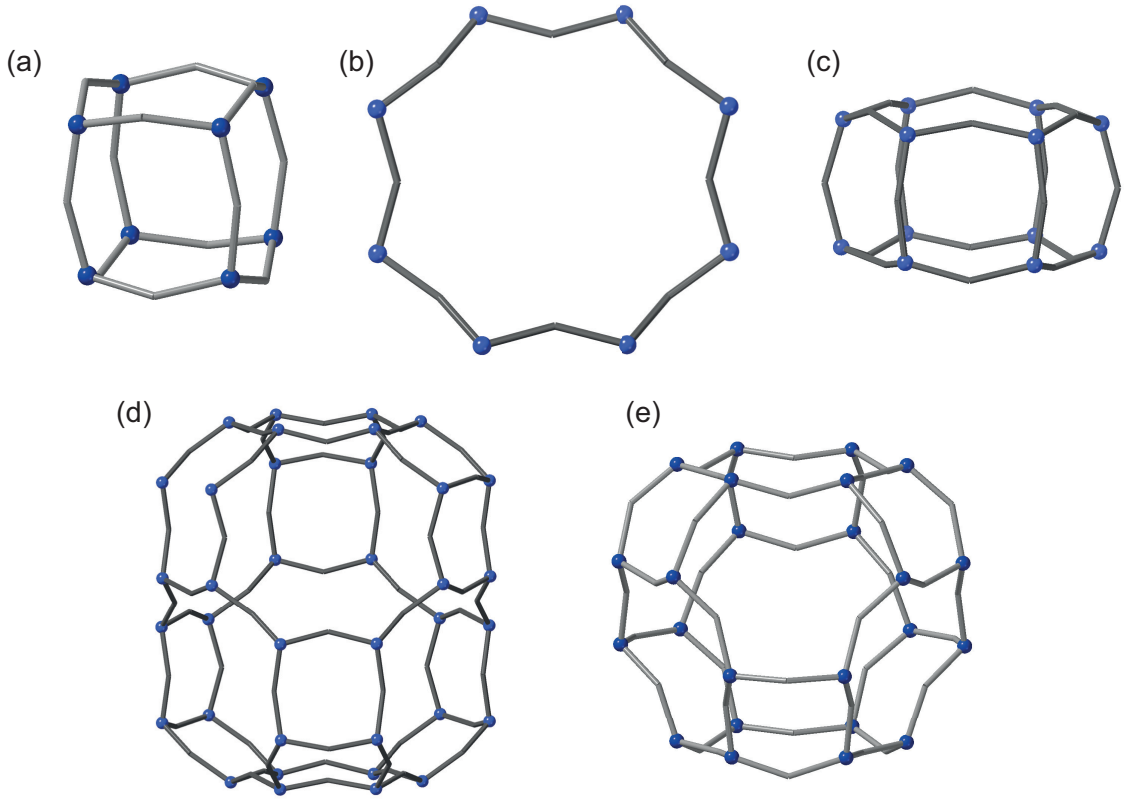

Figure 1.1: Structures of some common zeolite building units with shorthand names indicated. (a) double four ring (*d4r*) BU (4-4), (b) eight ring (8) SBU, (c) double six ring (*d6r*) BU (6-6), (d) chabazite cage (*cha*) CBU and (e) sodalite cage (*sod*) CBU. Note some building units can be represented within zeolite structures as both SBUs and CBUs. T atoms represented by blue dots, O atoms located at non-marked vertices.

found with multiple charge-balancing cations present, whereas synthetic zeolites typically only have one - determined initially by the cations present in the synthesis gel (often Na^+, K^+). Charge-balancing cations present in a framework can be exchanged by mild aqueous ion exchange procedures and many different cations and combinations of cations can be used to charge-balance a zeolite material, with the cation(s) of choice often having an effect on the properties and catalytic application of the zeolite, particularly in cases where active catalytic sites play a role in material function.[6,26,27] For example, the **CHA** material with high Si/Al ratio, SSZ-13, has proven applications as a MTO (methanol to olefin), gas separation and NH_3-SCR (selective catalytic reduction) catalyst, when exchanged to the proton (H^+), ammonium (NH_4^+) or copper (Cu^{2+}) forms, respectively.[28–32] Zeolites have a high affinity to water as a consequence of their synthesis, the molecular geometry of their pores and any species within them. Consequently, zeolites are often found in a hydrated state with approximately 10-20 % of their mass coming from surface coordinated water. With respect to this and the above discussed characteristics, zeolites can be expressed by the empirical formula:

$$M_{x/n}{}^{n+}[Si_{1-x}Al_xO_2]\cdot yH_2O, \tag{1.1}$$

where M is an extra-framework cation of valence n, x is < 0.5 and y may take any value. Additional to the necessity for extra-framework cations, the inclusion of aluminium within the structure of a zeolite has effect on the overall chemical properties of the material. Naturally occurring zeolites are typically found to have moderate to high aluminium content (Si/Al < 5), as did a number of the first synthetic zeolites (*e.g.* A, X, Y, mordenite), all of which were formed from Al-rich, dilute, organic structure-directing agent (SDA)-free gels. The aluminium content of synthetic zeolites is dependent on a number of conditions, but the composition of the synthesis gel is the most important, with higher aluminium and water contents, presence of sodium cations and absence of organic SDAs favouring materials with low Si/Al.[6,33–36] A pure SiO_2 framework is highly hydrophobic and all crystallographically same T-sites within it are degenerate. The incorporation of aluminium during synthesis removes the degeneracy of crystallographically same T-sites within the structure and contributes to an overall increase in material hydrophilicity as the framework becomes charged and its bonds experience an average increase in polarity. Aluminium is often considered to locate randomly within the structure of zeolites, although some studies have shown it to locate with some preference at different sites and types of ring in zeolites within certain topologies and likely through kinetically controlled processes.[37–45] Due to the importance of aluminium in zeolites for control of properties such as Brønsted acidity, catalytic properties and hydrophobicity, the study of its siting and distribution are a topic of major focus in zeolite research.[46–49] The ability to predict and control aluminium siting and distribution during zeolite formation or transformation would prove revolutionary in sectors such as industrial catalysis. Both steps have associated difficulties, however; prediction is hampered by the isoelectronic nature of Si^{4+} and Al^{3+}, making diffraction studies on known systems difficult, and control is hampered by the many factors associated with hydrothermal synthesis. Although some studies have showed promise so far, the field of aluminium location predictability and subsequent siting control is still very much a developing area.[6,46,50–54]

1.1.3 Heteroatomic 'Zeolites'

By definition, zeolites are confined to materials of aluminosilicate composition, however the desire for implementation of these materials into commercial application has necessitated the extension of scope of their structural-chemical properties. This has resulted in a growing class of materials whose structures class as identical to zeolites but whose properties are enhanced by the replacement of aluminium for a different dopant element.[55–58]

Many so-called 'heteroatomic zeolites' or 'zeolite materials' have been prepared with a wide range of heteroatoms including *e.g.* main group: Ga^{3+}, Ge^{4+}; non-metal: B^{3+} and transition metal: Ti^{4+}, Zn^{3+} elements. Heteroatomic zeolites have expanded the scope of zeolite science by producing materials with enhanced properties, such as titanosilicate TS-1 (**MFI**), which serves as a superior selective oxidation catalyst with H_2O_2; stannosilicate Sn-**BEA**, an excellent catalyst for a range of reactions, particularly biomass conversion, and borosilicate materials, whose weaker Lewis acidity can be more suitable for some catalytic reactions than those of aluminosilicates.[59–63] Heteroatomic substituted zeolites have also produced materials with novel topologies. One class of these materials which have attracted particular attention is the germanosilicates. The larger size of the Ge atom and its more diffuse bonding facilitates both larger rings in so-called 'extra-large pore' materials as well as locating preferentially within smaller rings, such as *d4r*. The germanium atoms also introduce a point of hydrolytic instability into the material, which in the case of germanosilicate IM-12 **UTL**, can be exploited for selective disassembly.[64–66]

1.2 NMR Spectroscopy of Zeolites

Zeolites are suited to characterisation by NMR spectroscopy as the spectra of many NMR-active nuclei found within their frameworks can be acquired with relative ease and can provide information on their local structure, coordination and reactivity.[67–76] Together with complementary techniques, such as X-ray diffraction and electron microscopy, an increased bank of knowledge about a particular zeolite can be obtained. A selection of the NMR-active nuclei most-relevant to this project are introduced below.

1.2.1 ^{29}Si NMR

^{29}Si is the NMR-active isotope of silicon with a natural abundance of 4.7% and a nuclear spin (I) of $\frac{1}{2}$. In NMR spectra of zeolites, the observed chemical shift (δ) for a silicon atom is principally determined by the crystallographic location of its T site within the framework and its local connectivity through its oxygen linkages to its **N**ext **N**earest **N**eighbours (NNN, X) $Si(O-X)_4$ (X = Si, Al or H). Fully coordinated silicon bound tetrahedrally within the lattice (X = Si, Al) is referred to as Q^4 silicon, which can be distinguished from those silicon atoms for which the lattice is broken and nH atoms (forming silanols) coordinate to the framework through oxygen, producing Q^{4-n} silicon sites. With respect to the above, ^{29}Si NMR is one of the most common techniques employed for the characterisation of zeolites using NMR spectroscopy.[77–82]

For a defect-free pure silica zeolite, all silicon atoms have the same NNN ($Si(O-Si)_4$) and the observed distribution of chemical shifts in a ^{29}Si NMR spectrum is dependent on the crystallographic locations of the different T sites and their relative populations, symmetries and geometries.[83] Incorporation of aluminium into the zeolite results in a change to the atomic ordering (and therefore NNN) of the material, which is reflected in the ^{29}Si NMR spectra. There are now five possibilities for NNN; $Si(O-Si)_{4-x}(O-Al)_x$, (x = 0-4), each of which causes a shift of approximately $+x\cdot 5$ ppm from the original x = 0 peak, resulting in a spectrum split into up to five distinctive peaks (see Figure 1.2).[84,85]

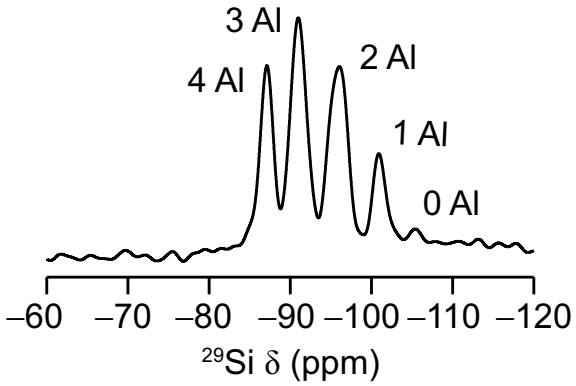

Figure 1.2: ^{29}Si NMR spectrum of zeolite Y (**FAU**) (K^+ form), with a calculated Si/Al ratio of 1.8. The peaks present correspond to tetrahedrally coordinated silicon atoms of which the label indicates the number of aluminium atoms at the nodes of the tetrahedron.

This splitting of silicon environments by proximity to NNN aluminium in ^{29}Si NMR spectra allows the silicon to aluminium ratio (Si/Al) of a zeolite to be calculated from its relative integrals (I) using:

$$(\mathrm{Si/Al_{NMR}}) = \sum_{n=0}^{4} I_{\mathrm{Si}(n\mathrm{Al})} \Big/ \sum_{n=0}^{4} 0.25\, n I_{\mathrm{Si}(n\mathrm{Al})}, \tag{1.2}$$

provided the spectrum used is sufficiently quantitative and the material is assumed to be free of defects and Al-O-Al.[77,86,87] Quantitative NMR measurements are achieved by having sufficient gaps between successive pulse and acquisition cycles to allow the spins in the nucleus of interest to relax and realign with the external magnetic field. The spin-lattice relaxation times for silicon are comparatively long and as such, experimental relaxation times required for zeolites are often in the region of 120 s. This provides a limiting factor for the speed of acquisition of ^{29}Si NMR of zeolites.[77,78] Consequently, $^{1}H^{29}Si$ cross-polarisation experiments are often used where magnetisation is transferred from excited protons to silicon atoms in the local vicinity.[88] This reduces the required recycle delay significantly, however it comes at the expense of quantitative interpretation

as those silicon atoms in the framework closer to excited protons are enhanced disproportionately (covered in more detail in Section 2.1.4.4).[70]

1.2.2 ^{27}Al NMR

^{27}Al is the 100% abundant, NMR-active isotope of aluminium, which possesses I = $\frac{5}{2}$. As a quadrupole, the non-spherical charge distribution surrounding ^{27}Al nuclei result in a net tensor; the Quadrupolar Moment (Q) of 14.66 fm^2 and a moderate ratio of magnetic moment to angular momentum (gyromagnetic ratio, γ) of 6.976 x 10^{-7} rad s^{-1} T^{-1}.

Similar to the ^{29}Si nuclide, the isotropic chemical shift, δ_{iso}, of ^{27}Al is dependent on the crystallographic location of the aluminium within the zeolite framework. Although the expected coordination number (CN) of aluminium in zeolites is four (Al_{IV}), both five (Al_V) and six (Al_{VI}) can also exist, often as a result of processes such as hydration, hydrolysis or dealumination (see Figure 1.3). The valency of ^{27}Al in zeolites has the greatest effect on the observed chemical shift and Al_{IV}, Al_V and Al_{VI} have typical chemical shift ranges of 50-70 ppm, 25-40 ppm and 0-20 ppm, respectively. Further, as a result of second-order quadrupolar broadening effects present in NMR spectra of ^{27}Al zeolites recorded with sample rotation, the peaks observed are broadened such that little to no structural or siting information other than CN can be obtained easily. Consequently, NMR methodologies that supress second-order broadening effects, such as the use of high magnetic fields or multiple-quantum (MQ)-MAS, are often used to extract further information in ^{27}Al NMR studies (see section 2.1.4.5).[47,67,70,77,89,90]

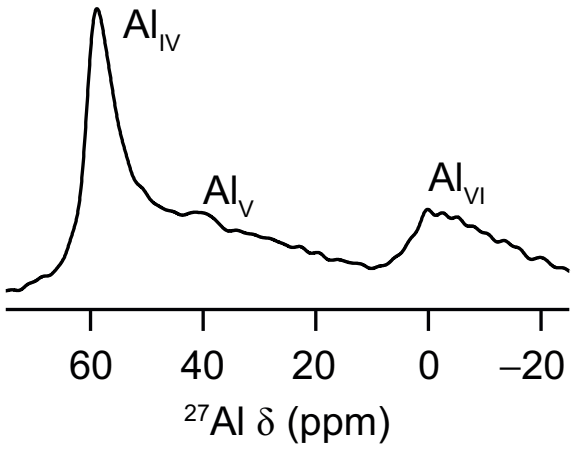

Figure 1.3: ^{27}Al NMR spectrum of SSZ-13(H$^+$) (**CHA**), with a range of aluminium species of differing CN. Species with CN Al_{IV}, Al_V and Al_{VI} are indicated.

1.2.3 ^{17}O NMR

Oxygen is the most abundant element in zeolite frameworks and the only one for which it is possible to connect to silicon and aluminium and to interact with any extra-framework cations. This unique coordination environment for oxygen presents the opportunity for extraction of large amounts of structural and chemical reactivity information by oxygen NMR studies. This, however is made challenging by the characteristics of the only NMR-active isotope of oxygen, ^{17}O. The ^{17}O nucleus is quadrupolar with I = $\frac{5}{2}$, Q = -2.558 fm^2 and a γ of -3.626 x 10^{-7} rad s^{-1} T^{-1}. These characteristics make deconvolution of NMR spectra especially difficult as when spectra are obtained, the lineshape components appear broad and often overlapped due to second-order quadrupolar broadening. Further, the extremely low natural abundance of 0.037% of the isotope necessitates the need for isotopic enrichment in materials of study in order to provide ^{17}O NMR spectra on a reasonable timescale.[68,73] This, however is compounded by the high-cost of isotopically-enriched oxygen-containing reagents, such as $H_2{}^{17}O$ $\approx$ 90% enriched €1000-1500 / mL and $^{17}O_{2(g)}$ $\approx$ €2000-3000 / L. The results of isotopic enrichment can be affected by the method of ^{17}O incorporation (gas-enrichment, mechanochemical treatment, hydrothermal steaming, room-temperature slurrying, *etc.*) and so care must be taken to achieve suitable enrichment, however a degree of control and selectivity can be achieved by choosing the correct method.[73]

There are a greater number of crystallographically-distinct oxygen atoms in zeolites than T-sites, as such ^{17}O NMR is often unable to distinguish between these and spectral-assignments are regularly between different framework Si-O-X (X = Si, Al, B, Ga, Ge, Ti, Zn) bonds or groups thereof, silanols (Si-OH) and if possible, Brønsted acid Si-O(H)-Al sites.[73] The chemical shift ranges of δ_{iso} for zeolites are small $\approx$ 60 ppm, so the broadened resonances for like and non-like linkages often overlap (see Figure 1.4). However, as these resonances regularly have differing quadrupolar coupling constants (C_Q) (*e.g.* Si-^{17}O-Si 4.6 – 5.2 MHz, Si-^{17}O-Al 3.1 – 3.2 MHz), they can be separated and high-resolution spectra achieved through multiple-quantum MAS techniques and/or by increasing magnetic field strength.[73,91]

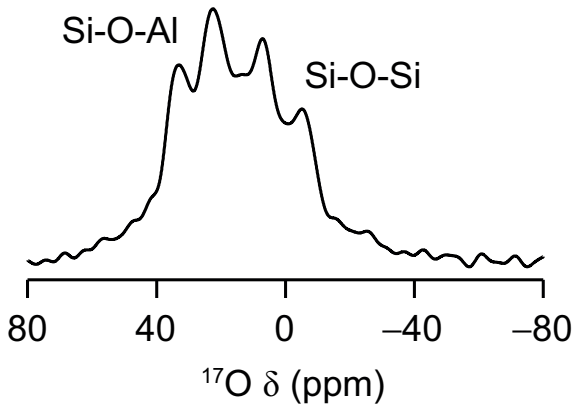

Figure 1.4: ^{17}O NMR spectrum of ^{17}O-enriched SSZ-13(H^+) (**CHA**), with overlapped regions for Si-O-Si and Si-O-Al resonances indicated.

Oxygen NMR studies in zeolites have proven to hold a wide variety of information on the structure and characterisation of zeolite frameworks.[73] Some examples include the use of ^{17}O solid-state NMR to fully characterise aluminosilicate **LTA**, **FAU** and siliceous **FAU**, or to probe the effect of extra-framework cation on δ_{iso}.[73,92–95] Similar studies have also made use of a range of experimental techniques that can probe chemical reactivities of zeolites for *e.g.* absorption, catalysis, Brønsted acidity or can probe directly the chemical reactions of zeolites *e.g.* hydrolysis, lability, *etc.* using *in-situ* NMR measurements.[73,96–104]

1.2.4 ^{1}H NMR

Protons are regularly found bound to zeolite frameworks; through bonds to oxygen to silicon as silanols (Si-OH) in defects or in layered structures; through oxygen to aluminium (Al-OH) in extra-framework aluminium species or through oxygen bound to both silicon and aluminium as in Brønsted acid sites (Si-O(H)-Al). Further, the affinity of water to zeolite frameworks means that water molecules (and protons) are almost always absorbed to the surface of the zeolite interacting with surface silicon and aluminium atoms.

The NMR-favourable properties (99.99%, (I) = $\frac{1}{2}$) of the proton and the diversity of its species found in zeolite samples make ^{1}H NMR spectroscopy a potentially useful tool to aid material characterisation. However, ^{1}H NMR is not regularly used alone in NMR spectroscopy of zeolites, owing to large dipolar couplings found between ^{1}H nuclei, which result in broadened spectra in the solid state, requiring high sample rotation frequencies or homonuclear decoupling techniques to remove. This tends to limit the use of ^{1}H NMR spectroscopy alone unless specific information held by protons only is needed; ^{1}H – ^{1}H double- and triple-quantum experiments have been used to discern the proximity of and relationship between SDA location and silanol density in several zeolites.[105] Protons are often employed in routine zeolite characterisation however, as a magnetisation-transfer medium as their spins readily couple to other nuclei in the material.[106] Exploiting this using the cross-polarisation experiment[88] (see section 2.1.4.4) can yield information on spatial proximities of framework atoms and material defect levels.

1.2.5 Other Nuclei of Relevance

Other nuclei present in some zeolites, such as ^{11}B, ^{19}F and ^{23}Na can provide useful information through NMR spectroscopy. Just as the behaviour of boron and aluminium in zeolites are similar, so too is the information contained in their respective NMR spectra.

^{11}B has a very coordination-sensitive δ_{iso} and can readily distinguish between different trigonal, tetrahedral and other extra framework environments often found in borosilicate zeolites.[107–111] Fluorine and sodium are often found as extra-framework species in zeolites and so ^{19}F and ^{23}Na NMR spectra can provide structural information in systems of interest. ^{19}F NMR can indicate different structural motifs found within materials synthesised in the presence of fluoride as well as being used to monitor other processes such as dealumination by tracking the formation of alumino-fluoro species.[112,113] ^{23}Na NMR spectra can be used to indicate the location and siting preference for extra-framework

cations in materials, where sodium, argably the most common extra-framework cation in zeolites is present. In the case of the **CHA** framework, ^{23}Na NMR has aided identification of the four main cation siting environments in the framework and given an indication of how alkali metals site in mixed-metal cases.[114,115]

1.3 Traditional Approaches to Synthetic Zeolites

Although established, the field of zeolite synthesis is continually expanding, with new methodologies being developed to produce new materials and improve existing synthetic routes. The majority of zeolite and zeolite material syntheses follow the same general protocol and are typically carried out under hydrothermal conditions. Zeolites are synthesised by the combination of silicas and aluminas in basic media to form amorphous gels, which may also incorporate metal salts, organic templating agents and mineralising species. These reagents reversibly self-organise to form metastable, inorganic species which precipitate out of aqueous solution as crystalline tectosilicate networks.[6,35,36] This section serves to set out the main principles of traditional zeolite synthesis and introduce some of the synthetic concepts used in this work.

1.3.1 Hydrothermal Autoclave Synthesis

Hydrothermal synthesis *via* the autoclave route is the most popular method of making zeolites. Reagents are combined and placed in Teflon liners, which are placed in steel autoclaves that in turn are sealed and heated to temperatures $\approx$ 120-180 °C (see Figure 1.5). Typically, a reaction gel is formed by the dissolution of silicon and aluminium (or a heteroatomic species) in water. The high polarity, permittivity, specific heat capacity and wide liquid-phase temperature range of water make it a suitable solvent for dissolution of zeolite reagents, facilitating the transport of ions and charged species during the zeolite synthesis process. Dissolution of reagents is often aided by the introduction of basic media, such as alkali metal hydroxides, which increase the pH to form the correct species in solution for coordination ($Si(OH)_4{}^{4-}$, $AlOH_4{}^{3-}$) under hydrothermal conditions. The form in which silicon and aluminium is added to the water can have consequences on the synthesis; silicon can be added as fine solid silica (SiO_2) powders, dispersed in colloidal silica solutions, such as Ludox, or in the form of a coordinated organic, such as the alkoxide tetraethylorthosilicate (TEOS), which is first hydrolysed in solution to the reactive form.

Figure 1.5: Components of an autoclave used in hydrothermal zeolite synthesis. Left to right, steel body, Teflon liner and lid, steel blast ring, steel plate and lid.

At elevated temperatures and consequential autogenous pressures, the reactive species form critical solutions, which possess a thermodynamic driving force for crystallisation. However, due to the kinetic effects also present at elevated temperatures, reactive zeolite gels possess a high degree of reversibility and many transient oligomeric species form, before a thermodynamic sink leads to nucleation and agglomeration.[116] Nuclei continue to agglomerate and if they reach a minimum critical size, crystallisation occurs.[116,117] Indeed, several agglomerated zeolite phases may form during synthesis with the final product achieved dependent on the selected reaction conditions.[118,119] The difficulties associated with predicting the crystallisation of metastable reactive phases under these conditions and the influence of many different factors, *e.g.*, mixing times, reaction times, temperature, makes predictability and control in zeolite synthesis challenging.[6]

1.3.2 Reaction Variables and Mechanism

In addition to reaction conditions, reaction components can also influence the observed products. A typical aluminosilicate reaction gel will satisfy the expression:

$$1\mathrm{SiO_2} : 0-0.5\mathrm{Al_2O_3} : 0-0.5\mathit{SDA}-\mathit{OH} : 0-0.5\mathrm{M_2O} : 5-100\mathrm{H_2O} : 0-0.1\mathrm{HF}, \quad (1.3)$$

where SDA-OH is the hydroxide form of the SDA and M has a valency of one. All components added to the autoclave are accounted for within the reaction gel and the ratio of silicon to aluminium generally reflects the expected silicon and aluminium content of the material produced.[6] Greater concentrations of basic media generally support the crystallisation of lower Si/Al materials, however if the same absolute volume of hydroxide is present in more dilute solution this may hamper the crystallisation of a phase

as the agglomerates prefer to stay dissolved in the alkaline mother liquor. This trade-off has to be weighed up against the factors for desired crystallite size and economics; concentrated solutions and shorter reactions yield smaller crystallite sizes but longer reactions of dilute mixtures may offer large 'single' crystals. Further, smaller crystallite sizes approaching the nanoscale can hamper reaction processing but long reaction times and large volumes of solvent are economically unfeasible.[116,117,120]

The choice of source of hydroxide also influences the reaction products; the high concentration of hydroxide required in low-silica gels is achieved using alkali bases as the abundance of the accompanying metal cation aids charge matching, reducing the positive charge deficit introduced by Al^{3+}. The positive alkali metal cations in the base can also act loosely as a 'template' around which the aluminosilicate species grows.[116,117,120] In syntheses of higher Si/Al zeolites, the templating role of the inorganic base is fulfilled by an organic structure directing agent (SDA) (see Figure 1.6).

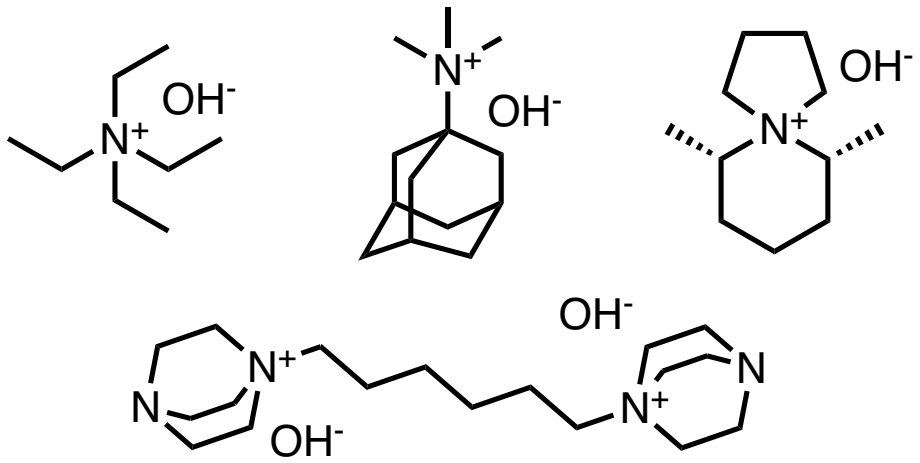

Figure 1.6: Some examples of SDAs used in zeolite syntheses and their common abbreviations. (a) tetraethylammonium hydroxide (TEA-OH), (b) N,N,N-trimethyladamantammonium hydroxide (TmAda-OH), (c) (*6R, 10S*) 6, 10-dimethylazoniaspiro[4.5.]decane hydroxide, (DMAD-OH) and (d) 1,1'-(hexane-1,6-diyl)bis(1,4-diazabicyclo[2.2.2.]octan-1-ium) hydroxide (diDABCO-C6)

Zeolite SDAs take the form of salts of alkylated quaternary amines, in either their as-synthesised halide form or more commonly, as the analogous hydroxide salt obtained through ion-exchange. In solution, SDAs disassociate to leave the positively charged quaternary amine that acts to solve the charge imbalance brought about by aluminium in the reaction medium. The larger size of organic amines over metal cations means that the charge is distributed uniformly throughout the reaction gel, and clustering of aluminium in the final product is limited. The organic SDA also serves to 'direct' the dissolved

aluminosilicate species within the reaction medium, interacting with water and silica in solution to form clathrates, resulting in the formation of a framework representative of the SDA used. This 'templating' effect of the SDA was first proven using the silicalite-1 (**MFI**) - TPA (tetrapropylammonium) system by Chang and Bell in 1991 and later backed up by Burkett and Davis in further studies on the same system utilising solid-state NMR.[121–124] The synthetic tunability of alkylammonium salts presents an almost infinite field for the synthesis of novel SDAs, where variations in chain lengths, bulk, charge density, *etc.* can effect to produce zeolite frameworks with novel topologies.[6,9,125,126]

As mentioned above, the primary role of hydroxide within zeolite syntheses is to convert the silicas and aluminas to their reactive species through increasing reaction pH. For low and medium Si/Al ratio zeolites, the hydroxide contributed from alkali bases or SDA solutions is often sufficient. However, in instances where high Si/Al (> 20) or pure-silica frameworks are desired, additional mineralising agents and alteration of the reaction system may be needed. The most popular choice for this is the use of fluoride, and in particular HF, which promotes synthesis of high- and pure-silica materials in low water, acidic conditions. The presence of fluoride in syntheses promotes large crystal growth and mineralises reaction mixtures by countering the effect of positively charged SDA molecules; in high-silica syntheses the latter is also achieved by the trivalent metal source (Al^{3+}, B^{3+}, *etc.*). Like the SDA, fluoride anions in the material are removed following calcination, so high silica zeolites synthesised *via* the fluoride route typically have a high level of defects once calcined. For siliceous zeolites however, fluoride forms negatively charged pentacoordinate $(Si-O-)_4SiF$ centres that, once calcined produce a neutral, defect-free tetracoordinate framework. The most common source of F^- as a mineralising agent in zeolite synthesis is HF; its use aiding the crystallisation of several all-silica zeolite analogues.[9,125,127–129]

1.3.3 Issues with Hydrothermal Synthesis

The wealth of techniques developed to produce zeolites have yielded success, however the number of structures actually produced makes up only a very small proportion of those possible. *in-silico* studies predict that <0.1% of all feasible zeolites have been produced in the laboratory, meaning a great void exists between the success of our established synthetic techniques and what is, in theory, possible.[130–132]

This so-called 'zeolite conundrum' primarily exists as a result of a disparity between thermodynamic accessibility and kinetic feasibility. Many predicted zeolite structures lie within 30 $kJmol^{-1}$ of quartz and yet never materialise in real life as they remain

kinetically inaccessible under traditional hydrothermal conditions. The plot in Figure 1.7 shows how synthesised structures lie at the lower density edge of the predicted region for zeolitic materials and how many more materials exist with higher framework energies, densities or both.

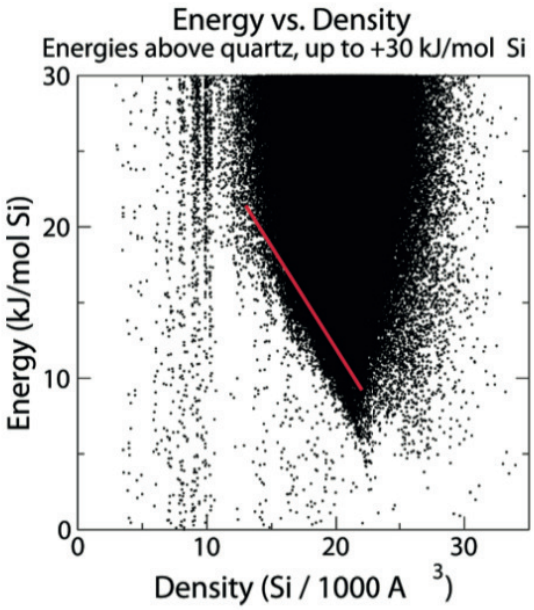

Figure 1.7: A plot showing the relationship between framework energy and framework density for computationally predicted (black dots) and synthetically produced (red line) zeolites. Figure adapted from Deem *et al.*.[130]

1.4 Alternative Routes to Zeolites

Alternative strategies have been developed to increase the numbers of zeolite frameworks to optimise the routes to known structures. These methods, utilising non-conventional synthetic techniques, such as ionothermal or solvent-free conditions, ball-milling or microwave treatment have yielded new materials from amorphous gel systems with some success. A recent review by Deneyer *et al.*[132] attributes the success of these methods to the increased degrees of freedom within syntheses, be it in the chemistry of the system (composition, *etc.*) or in the environment itself (external system treatment, *etc.*). The former strategy, where the chemistry and interactions of components within the system is altered, has proven to be the most successful in forming new structures and synthetic routes. Affecting the component interactions alters the kinetic profile of the reaction resulting in new potential opportunities to access novel materials.

A number of key methodologies for successful synthesis of new, or facile synthesis of useful zeolites involve pre-formed zeolites as starting materials; the so-called 'top-down' approach.[133,134] Transformations of existing zeolites open up new kinetic routes at higher energies than those of amorphous gel syntheses ('bottom-up') as zeolites, utilising the greater framework energy of the zeolite as a starting platform. Some significant top-down approaches used in this work are introduced in Section 1.4.2.

1.4.1 Low-solvent Routes to Zeolites

An issue associated with hydrothermal synthesis of zeolites is the amount of water and organic structure directing agent present in the reaction medium. Both variables are associated with increased manufacturing cost and have negative implications for waste disposal. In order to reduce reaction costs and utilise 'greener' syntheses, low-solvent or solvent-free reactions are sought.[135–138] The high atom economy of these synthetic strategies pose a particular advantage to this project, where *in-situ* ^{17}O-isotopic enrichment of materials is desired.

1.4.1.1 Vapour-phase Transport and Dry-gel Conversion

Vapour-phase transport processes proceed by permitting the movement of certain reactants in the gas phase. The process still requires small amounts of water, occasionally having the OSDA (organic SDA) dissolved within. The dry-gel components; silicas, aluminas and/or any heteroatom source; may be reacted before to kick-start the reaction and are placed within the autoclave, separate from the liquid phase. Upon heating, the vapour-phase transport network is initiated and crystalline zeolite materials can be made. This technique for the synthesis of zeolites was first employed in the preparation of ZSM-5 (**MFI**) by Xu, *et al.* in 1990.[135]

In this work, the low solvent volume and high atom economy of the dry-gel conversion process has been used to synthesise and modify the structure of zeolite materials and combine them with $H_2{}^{17}O$ vapour, resulting in new ^{17}O-isotopically enriched materials.

1.4.1.2 Mechanochemistry

Mechanochemical treatments can also be used in the preparation of zeolites to supply energy to reagents and ensure their intimate mixing prior to heated reaction, or to assist in place of heat and liquid in the form of post-synthetic reactivity of zeolites.[138]

Mechanochemical approaches to zeolite formation have gathered a great deal of attention within the scientific literature and within industrial applications, owing to their low solvent requirements, the ability to scale syntheses with ease and the reduction in the required heating time. The cleaner, greener syntheses associated with mechanochemical treatments reduces processing time and energy dependence, making them particularly attractive for industrial applications. However, the knowledge of key parameters for the mechanochemical preparation of zeolites is still developing with the preparation of only some frameworks successful using this approach.[138]

In this work, mechanochemical treatments have been used in the preparation of several zeolites to ensure mixing of reagents prior to reaction and to assist in selective disassembly and ^{17}O-isotopic enrichment reactions of an ADOR-able zeolite (see Section 1.4.2.2).

1.4.2 Post-synthetic Reactivity of Zeolites

Zeolites are often perceived as stable, inert solids due to their use as catalysts, support media, *etc.* under a range of harsh operating conditions. They can also be very reactive, with positive and negative consequences. Reactivity can of course be a hindrance, resulting in material deactivation and degradation. However under certain conditions, weaknesses can be exploited to form zeolites with novel topologies, convert between known topologies and to alter material characteristics, such as framework composition.[46,132,139,140] A selection of post-synthetic reactions on zeolites important to this work are introduced in this section.

1.4.2.1 Zeolite Instability

Aluminosilicate zeolite structures are susceptible to framework degradation through a host of processes. Most often, excessive heat treatments or hydrolytic action are responsible for reactions with zeolites, resulting in loss of function through catalytic deactivation, dealumination and silanol nest formation.[6,139,140]

Aluminosilicates with higher aluminium contents have a lower hydrothermal stability due to the increased prevalence of weaker Si-O-Al linkages and the greater hydrophilicity of the material. When heated, aluminosilicate linkages are most readily cleaved, leading to zeolite dealumination and possibly structural degradation. Dealumination results in the formation of penta- and hexa-coordinate aluminium within the material or on its surface, altering its catalytic properties. Dealuminiation processes can be assisted by the

presence of water and under some circumstances can provide routes to the formation of new materials with enhanced properties. Heat-treatment and lanthanide-exchange of Y zeolite (**FAU**) in the presence of steam, for example, results in dealuminated US-Y (ultra-stable Y), which shows enhanced hydrothermal stability and exceptional FCC (fluid catalytic cracking) turnover rates.[6,141–143] Recent studies of water's role in dealumination mechanisms have suggested that although rate-determining steps differ across frameworks, the process was always initiated by attack of a water molecule anti- to the position of the proton on the Brønsted acid site, forming distorted tetra-/penta-hedral aluminium structures.[140,144,145]

The threat posed to zeolites by water is not limited to dealumination conditions. The size of the water molecule means that it can readily navigate zeolite architectures and its nucleophilicity and polarity enable it to interact with itself and the structure of the zeolite. The framework interaction often highlights zeolite instability through hydrolysis of framework bonds, such as Si – O – Si, Si – O – Al, Si – O – B and Si – O – Ge. The result can be detrimental to zeolites in commerce; deactivating catalysts and support materials. In some instances however, instability can be advantageous. As the action of water on a zeolite is heavily dependent on the material topology and composition and the nature of the water present, several steps, such as choice of dopant atom, temperature and pH can be taken to engineer material (in)stability in application.[139,140,146]

1.4.2.2 The ADOR Process

The ADOR (*Assembly*, *Disassembly*, *Organisation*, *Reassembly*) process is a methodology for synthesising new, high-silica zeolite structures through selective deconstruction and reconstruction of a parent zeolite material (see Figure 1.8). The process exploits the hydrolytic instability present in the structure of a parent germanosilicate zeolite, most often IM-12 (**UTL**). Incorporation of germanium (Ge^{4+}) into zeolites produces heteroatomic, charge neutral materials with large pore and channel dimensions and readily hydrolysable Ge – O bonds.[66,146–150]

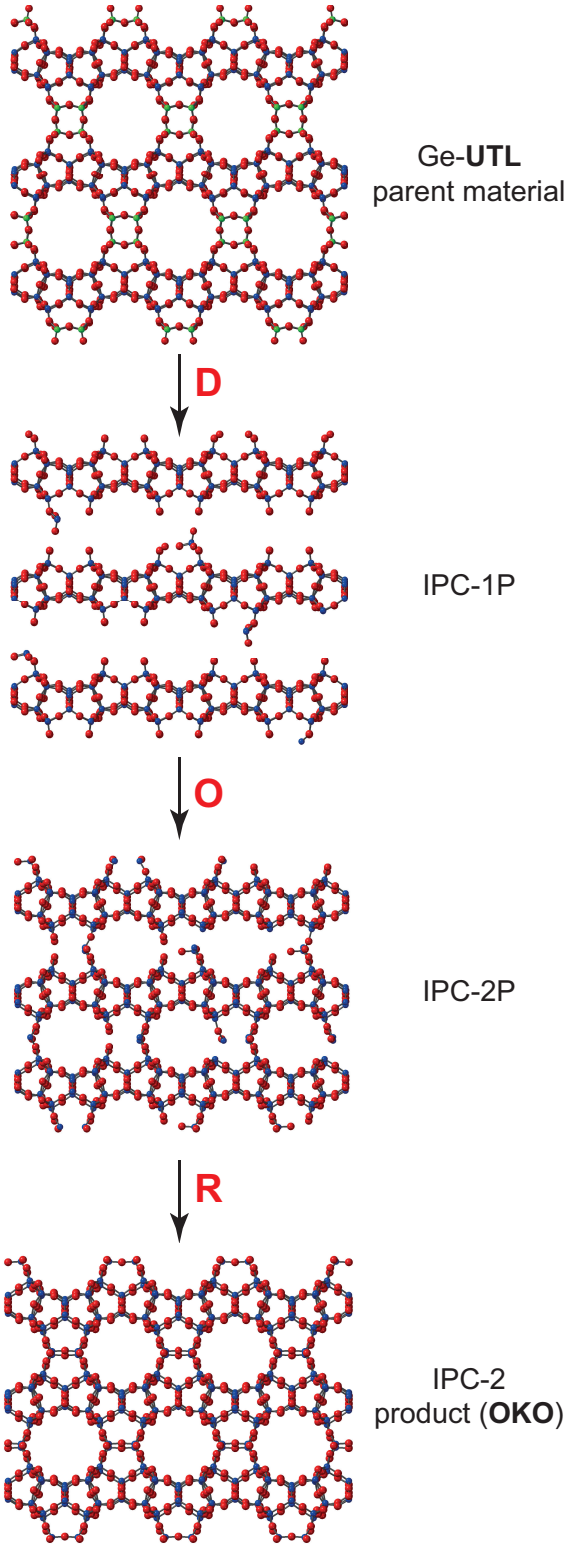

Figure 1.8: A schematic of a typical ADOR reaction for Ge-**UTL**. Disassembly (D), Organisation (O) and Reassembly (R) stages and key reaction intermediates are shown.

Within the structure of **UTL**, germanium locates preferentially in double four ring (*d4r*) units found between two-dimensional layers, resulting in a structure of silicate-rich layers separated by germanium-containing *d4r*s and a perpendicular large-pore *12r* and *14r* channel system.[64,65,151,152] In the most simple ADOR transformation of **UTL**, the Ge – O bonds in the *d4r* are hydrolysed, dismantling the unit and producing two-dimensional sheets, following treatment with water;. Removal of the majority of the germanium from the structure causes a contraction of the silicate sheets in the inter-layer spaces and forms a disorganised, crystalline intermediate, IPC-2P*. The transient formation of IPC-2P* and its structural disorder mean that its exact long-range order and structure is not fully known. Further reaction in the inter-layer space results in the breakage of of some Si – O linkages and deintercalation of Si from the *d4r*s. This results in further contraction of the two-dimensional layers, producing a very disorganised intermediate with no interlayer species, referred to as IPC-1P. Further reaction in water allows reintercalation of some silicon from solution and a gradual increase in inter-layer space. When intercalation results in the equivalent reinsertion of a single four ring (*s4r*) into the structure, the material can be isolated as IPC-2P, which is found to have the same inter-layer spacing as IPC-2P*. Capturing the intermediate mid-way between the IPC-1P to IPC-2P transformation isolates the IPC-6P intermediate. Upon isolation, the intermediate species can be topotactically condensed by calcination processes to form high-silica zeolites with novel topologies; IPC-1P to IPC-4 (**PCR**), IPC-2P to IPC-2 (**OKO**) and IPC-6P to IPC-6.[66,103,153] The progress of the ADOR process can be tracked using powder X-ray diffraction by studying the change in d_{200} reflection, corresponding to the distance between silicate layers within the structure of **UTL** (see Figure 1.9).

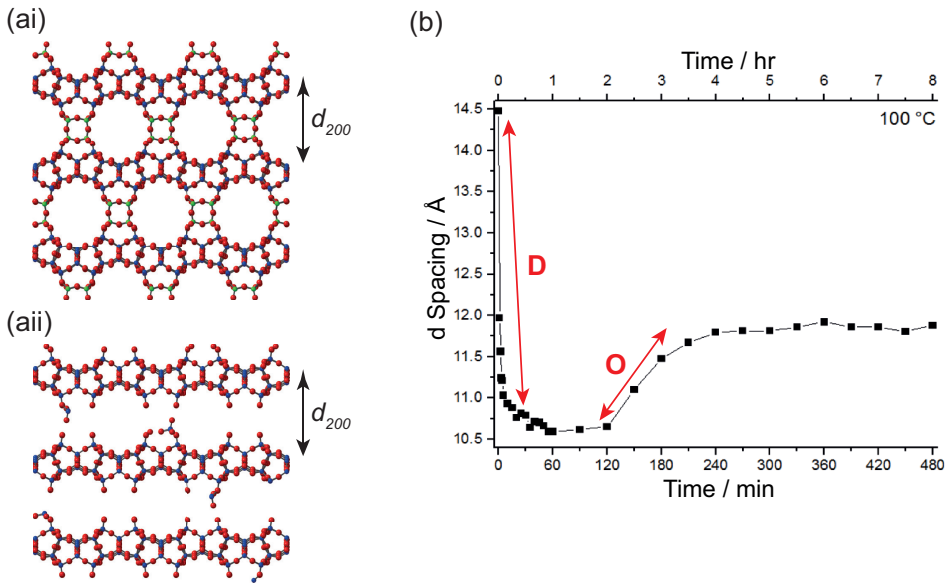

Figure 1.9: Structures of (ai) Ge-**UTL** and (aii) IPC-1P, indicating the interlayer spacings equivalent to d_{200} reflection in ADOR intermediates and (b) a plot of d_{200} reflection value versus time for Ge-**UTL** hydrolysis in water at 100 °C. Disassembly (D) and organisation (O) steps are indicated.

The ADOR transformation process is found to be very dependent on a range of conditions, such as hydrolysis time and temperature, pH of hydrolysing media, presence of extra organic species, pressure and heteroatom content. To date, 12 new zeolites of novel topologies have been made as a result of ADOR transformation processes, many of which are silica-rich and possess a greater framework energy than the starting zeolite, driving into the region to the right of the traditional synthesis vector in Figure 1.7.[66,154]

1.4.2.3 Post-synthetic Transformations

An alternative approach for obtaining a desired zeolite framework is through post-synthetic transformation (PST) (or inter-zeolite conversion) of a formed zeolite material (see Figure 1.10). This approach can be used to form zeolites with novel topologies, convert between known topologies and to alter material characteristics, such as framework composition. Similar to Section 1.4.2.2, post-synthetic transformations of zeolites proceed by targeting instability in the parent zeolite and pushing the framework to form new materials dependent on the reaction conditions and presence of extra reaction species, such as structure-directing agents, and occasionally extra silicon/aluminium sources. The instability in the parent material is usually introduced by carrying out the reactions in basic media, which is strong enough to cause bond cleavage of certain bonds in the structure under reaction conditions, but not so strong that the overall structure is digested.[155,156] Again, the starting materials possess a greater energy than typical zeolite reagents so less

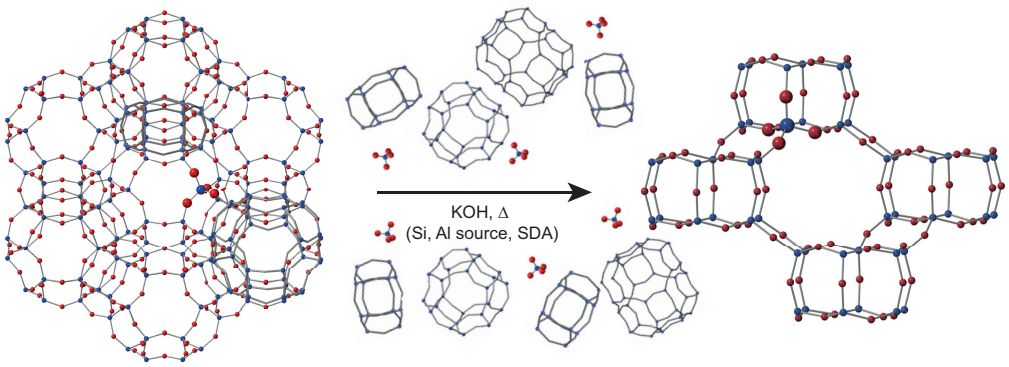

Figure 1.10: Schematic of a post-synthetic transformation of **FAU** to **CHA** inter-zeolite conversion reaction.

energy is required to convert zeolitic starting materials to the high-energy products of different topology, reducing costs and reaction times. These modifications have fewer degrees of freedom also, so procedures are more likely to result in zeolitic materials. To a degree, products can be predicted as there are known conversion routes between some main groups of zeolites, such as **FAU**, **CHA**, **MFI**, **STF** and **MTW**.[155] Alteration of framework composition and characteristics is achievable through post-synthetic topology conversion, however this is not required and mild compositional alteration procedures that do not compromise the integrity of the initial framework, such as demetallation and ion-exchange are routinely used to modify zeolites without the need to synthesise bottom-up.[46]

The increased probability of reaction success and the savings in time, energy and reagent costs that inter-zeolite conversions offer compared to hydrothermal syntheses makes them sought after for application. However, the extent to which PSTs can be applied to transform zeolites between one another is not fully understood. Aside from trial and error, few methods have successfully predicted large groups of possible transformations which are backed up by experiment. Some factors are predicted to have an effect, such as whether the transformation involves an increase in framework density, whether the frameworks can exist as competing phases, or are diffusionally or intergrowth linked, or share topological and graph similarities.[155–157]

1.4.2.4 Metallation and Demetallation

Framework composition alteration of zeolites is a useful post-synthetic strategy for targeting specific zeolite catalysts. The strategy circumvents the necessity to synthesise a framework in its desired composition, which can be challenging. Aluminium content is

often altered in zeolites either to access more useful, higher Si/Al materials, exchanged with other metals *e.g.* Ge or reinserted after dealumination processes.[46]

Demetallation processes, such as the removal of aluminium can be achieved through steaming (as in dealumination), however this often leads to silanol nest formation, so processes where reagents, such as $SiCl_4$ and SF_6 can be employed to remove aluminium and repair defects. Similar processes resulting in the formation of high- and pure-silica zeolites can be applied to 'metalloid' boro- and germano-silicate zeolites. High-silica materials can be made from borosilicates by hydrothermal reaction in acetic acid and as discussed in Section 1.4.2.2, germanium can be removed from materials by hydrolysis reaction.[46,63,66]

The reintroduction of aluminium into zeolites can also be performed using mild treatments, typically involving solutions of sodium aluminate or aluminium chloride, with aluminium directing into vacancies in the framework. The reinsertion process has recently been achieved as a reversible post-synthetic process for germanosilicate **UTL**. This enables a high level of control over the desired level of heteroatoms within the structure.[158,159]

1.4.2.5 Ion-exchange

The least-intrusive way to tune the properties of a zeolite is through ion-exchange of the extra-framework charge-balancing cations. As mentioned in Section 1.1.2, zeolites are most commonly synthesised in their sodium or potassium forms, but are readily converted to other cation forms, through successive mild aqueous thermal treatments in the presence of the desired exchange cation. Typically, simple ionic salt solutions like chlorides and sulfates of $\approx$ 1-3 M are used for ion-exchange. In order to access the catalytically-useful Brønsted acidic form of materials, one must first exchange to the ammonium form; often using ammonium chloride solution; before calcination in air, liberating ammonia gas and the H^+ form of the material.

Cation-exchange is dependent on the kinetics of the exchange, affected by the nature of the cation itself, the zeolite and the temperature of the exchange system. Extra-framework cations have a preference to site close to the net-negatively charged heteroatom (Al^{3+}, B^{3+}, *etc.*), interacting with the adjacent framework oxygen atoms. However, X-ray diffraction studies reveal that within the zeolite framework, cations are found to site at specific locations, dependent on their relative energies of association. Within these

location sites, the energies and molecular geometry of zeolite architectures can preclude the passage of cations, which are accompanied by large hydration spheres, so different exchange profiles and properties are seen for different cations. In some instances, this preclusion has a temperature gating effect and additional heating of ion-exchange solutions can produce different exchange profiles.[26,27] The gravity of this effect has been demonstrated for the **CHA** where a selection of alkali metal cations; Li, Na and K produced different cation siting profiles, which were found to be dependent on the energy of association and size of the metal ion in solution.[114,115] The location of cations within the material may also be associated with their stability; divalent ions, such as Cu^{2+}, Zn^{2+} and Ca^{2+} in the chabazite framework are more likely to be found associated with the *d6r* unit as they can be stabilised by the presence of two framework aluminium in close proximity, if the Si/Al permits.[160–164] The location and siting of the cations within the framework can have important concenquences for the reactivity of the material.

The absolute hydration state of the zeolite also effects the siting environment of cations in the structure. The large hydration spheres surrounding extra-framework cations in hydrated zeolites mean that metals or Brønsted acidic protons are found further from the zeolite framework oxygens. However, the loss of hydration sphere upon dehydration means they move much closer to the framework and in the case of Brønsted acidic site, bind directly to the oxygens adjacent to the heteroatom. These changes in association can be picked up by localised coordination-sensitive analysis techniques like solid-state NMR.[73,98]

1.5 ^{17}O Isotopic Enrichment of Zeolites

The variety of reactivity discussed in Sections 1.3 and 1.4.2 demonstrate the flexibility within and tunability of synthesis and modifications of zeolite frameworks. In all reactions discussed, chemical bonds within the structure of the zeolite will be made and or broken. As all bonds in a zeolite framework involve oxygen, this widespread bond lability presents an enormous opportunity for framework ^{17}O exchange to study framework reactivity under different conditions.[73]

Incorporation of ^{17}O into a zeolite can be achieved in several ways, employing both during and post-synthesis strategies. The approach used and the form of the ^{17}O isotope may be determined by the type of reaction or enrichment process studied. In this section, ^{17}O enrichment techniques relevant to this project are introduced.

1.5.1 Reaction Incorporation

The simplest way to incorporate ^{17}O into materials to study their reactivity is to do so during a reaction. This *in-situ* incorporation almost always uses $H_2{}^{17}O$ as the ^{17}O source for facile incorporation into the reaction system (see Figure 1.11). When incorporating $H_2{}^{17}O$ into a reaction, the uniformity of material enrichment and overall concentration of ^{17}O in solution is an important consideration of the final enrichment level of the material. The high costs associated with $H_2{}^{17}O$ mean that reaction system optimisation is an important consideration.

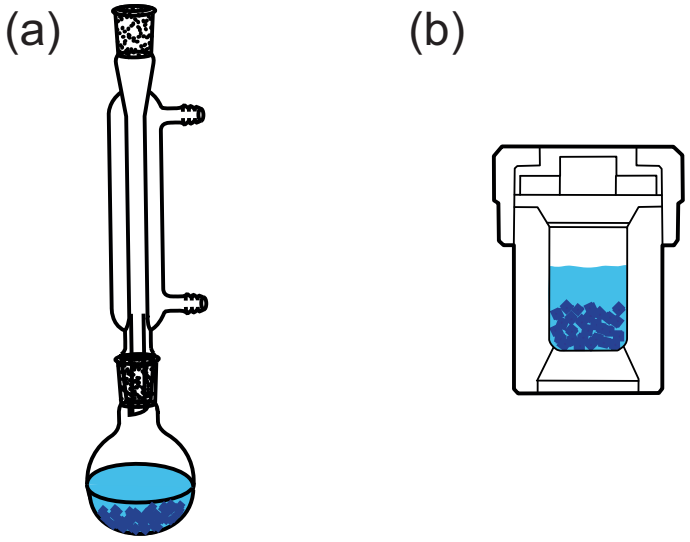

Figure 1.11: Examples of methods for ^{17}O isotopic enrichment of zeolites *via* reaction incorporation: (a) reflux and (b) hydrothermal autoclave treatment.

Literature reports several examples of introduction of $H_2{}^{17}O$ into a reaction system to study zeolites. First examples of ^{17}O-enrichment of zeolites involved post-synthetic hydrothermal exchange of ^{17}O into the framework by heating the material in $H_2{}^{17}O$ in a sealed autoclave. This approach requires acceptable amounts of $H_2{}^{17}O$ 50-100% of the mass of zeolite to be enriched.[91,165–169] More recently, **UTL** zeolite has been enriched during its disassembly in $H_2{}^{17}O$ to form ^{17}O-enriched layered ADORable intermediates.[103] Similar strategies for ^{17}O-enrichment have been attempted on zeolites and related materials *via* mechanochemical means. All of these strategies run the risk of non-uniform enrichment as those bonds which are perturbed during the reaction are at a greater possibility of enrichment than those that aren't.[73]

A reliable way to ensure uniform enrichment of a zeolite is to perform direct enrichment of zeolites during synthesis. However, the large amounts of water (and therefore $H_2{}^{17}O$) required in this case makes the reactions quite uneconomical and so this method is scarcely employed unless low-water reaction conditions have been optimised.[73]

1.5.2 $^{17}O_{2(g)}$ Post-synthetic Gas Exchange

The most widely accepted method to achieve uniform ^{17}O-enrichment of a zeolite is through post-synthetic $^{17}O_2$ gas-exchange. By heating the chosen zeolite to temperatures $\approx$ 500-700 °C under an atmosphere of $^{17}O_2$ gas, framework bonds are broken reversibly, exchanging ^{17}O for ^{16}O in the framework. (see Figure 1.12) This method has been reported for the isotopic enrichment of a number of zeolites. The stability of the parent material is an important consideration for this method with thermal degradation and dealumination processes possible at elevated temperatures.[73]

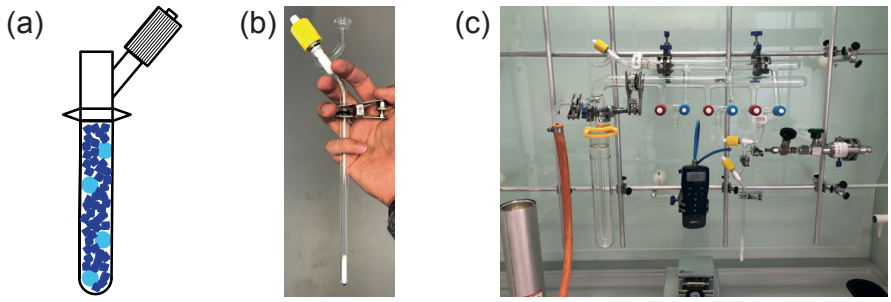

Figure 1.12: Method for $^{17}O_{2(g)}$ gas-exchange of zeolites. (a) Schematic of quartz tube and sample experimental set-up, (b) zeolite sample in a quartz tube for enrichment and (c) Schlenk apparatus used for enrichment.

1.5.3 Slurrying

Recent interest in the characterisation of microporous materials and their interaction with water under ambient conditions has led to the development of new enrichment techniques, which can be studied *in-situ*. The method of 'slurrying' is one such technique, whereby small amounts of $H_2{}^{17}O$ and material of study are combined, typically in a 1 : 1 or 2 : 1 ratio at room temperature in a sealed system and subsequent analyses are taken (see Figure 1.13).[73,104]

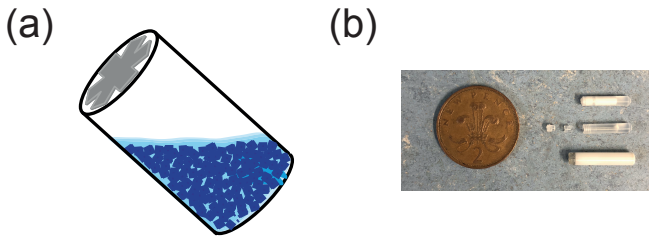

Figure 1.13: Method for $H_2{}^{17}O$ slurrying enrichment of zeolites. (a) schematic of prepared slurrying insert within NMR rotor and (b) experimental set-up of loaded and unloaded slurrying inserts and NMR rotor.

This method has been adapted for solid-state NMR studies of zeolites by sealing the material and enriched water in 4 mm HRMAS rotor inserts, which in turn are sealed in 4 mm rotors for NMR acquisition. Although facile, economical and proving to show interesting results about the room-temperature reactivity of some zeolites, this method occasionally produces results where non-uniform, no or very little ^{17}O-enrichment is observed.[73,104]

1.6 Selected Frameworks Introduction

A general introduction to the zeolite frameworks for which the majority of this project is focused, **CHA**, **FAU** and **UTL**, is provided.

1.6.1 Chabazite (CHA)

CHA framework materials receive a large amount of research interest with proven applications. Chabazite is a small-pore zeolite and its framework materials are applied to gas separation, MTO and NH_3-SCR catalysis.[28–32]

Structurally the **CHA** framework is simple, with one crystallographically-distinct T site and four crystallographically-distinct T site oxygen sites. The constituent atoms combine to form a periodic structure of *d6r* and *cha* cages with an atomic unit cell of $T_{36}O_{72}$.[170] Each of the four crystallographically-distinct oxygen sites ($O_1 - O_4$) sit in a unique combination of rings; two 4-rings and a 6-ring (O_1), a 4-ring and two 8-rings (O_2), a 4-ring a 6-ring and an 8-ring (O_3), and two 4-rings and an 8-ring (O_4). Note that different nomenclature is used in this report to that of original and other published assignments.[170–172] Designations for O_1 and O_4 have been swapped, making for easier comparison to the verified crystal structure used in calculations and resulting discussions.[4]

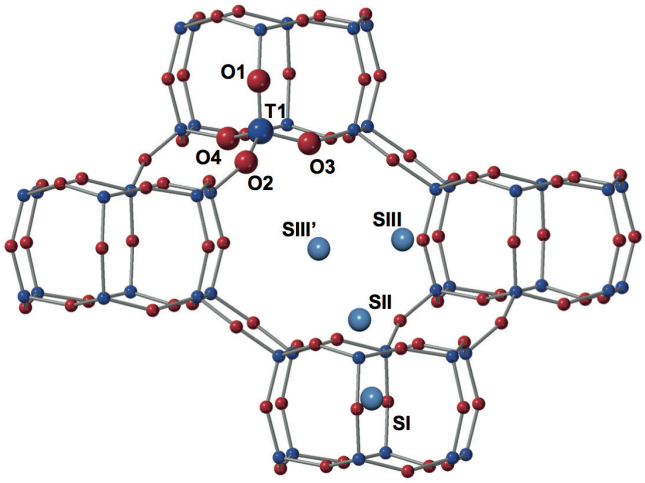

Figure 1.14: Structure of **CHA** framework showing crystallographically distinct framework atoms and the locations of extra-framework cations with crystallographic designations.

When tri-/di-valent heteroatoms are present within the **CHA** structure, extra-framework cations are found in up to four main locations (see Figure 1.14). The sites, denoted herein as SI – SIII and SIII′, are located within the *d6r* ring (SI), in the *cha* cage, just above plane of the *6r* ring of the *d6r* (SII) and in the *cha* cage at the *8r* window, either close to the corner of the *4r* of the hexagonal prism or almost at the centre of the *8r* (SIII and SIII′), respectively. The site of choice for extra-framework cations depends on the size and charge of the cation and on the presence of other cations already in the framework. Generally, however, divalent cations sit on SI and SII, with monovalent alkali metals preferring SII, SIII and SIII′. In the acidic form of SSZ-13 **CHA**, where protons sit on the framework, the Brønsted protons are found to bond to O_1 and O_3, pointing into the *d6r* and *8r* window of the *cha* cage, respectively.[172]

1.6.2 Faujasite (FAU)

Like chabazite, faujasite is another example of a naturally-occurring zeolite, for which materials of the same **FAU** topology can be prepared synthetically. Aluminosilicate **FAU** materials, such as the Linde X and Linde Y, with Si/Al of 1-3 and < 3, respectively were some of the first materials to be prepared synthetically on an industrial scale. Both X and Y have applications as fluid catalytic cracking (FCC) catalysts, with the latter showing superior qualities.

The **FAU** topology is crystallographically similar to that of **CHA**, with one and four crystallographically-distinct T and oxygen sites, respectively. The constituent atoms combine to form a periodic structure of *d6r* and *sod* cages with an atomic unit cell

of $T_{192}O_{384}$. The arrangement of the *d6r* and *sod* cages are such that the unit cell contains eight distorted hexagonal prism supercages with *12r* windows. Each of the four crystallographically-distinct oxygen sites (O_1 – O_4) are sited in two 4-rings and a supercage 12-ring (O_1), a 4-ring and two 6-rings (O_2), two 4-rings and a 6-ring (O_3), and a 4-ring, a 6-ring and a supercage 12-ring (O_4).[173]

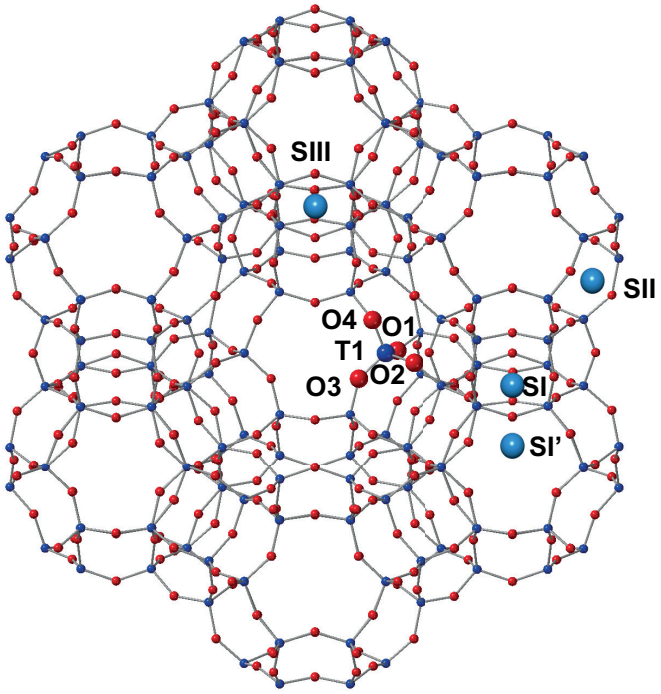

Figure 1.15: Structure of **FAU** framework showing crystallographically distinct framework atoms and the locations of extra-framework cations with crystallographic designations.

Extra-framework cations occupy four main sites within the structure of **FAU**; SI, SI′, SII and SIII. With the exception of SIII, these are located along the threefold symmetry axis (see Figure 1.15). They are found: at the centre of the *d6r* that connect *sod* cages (SI), facing SI within the *sod* cage at the *6r* window (SI′), within the supercage at the *6r* window to the *sod* cages (SII) and in the supercage at the *4r* windows to the *d6r* units and *sod* cages. Occasionally cations can be found at a site referred to as SIII′ at *12r* windows of adjacent supercages, these are scarcely populated however, due to their higher energies. Sodium and potassium cations, of interest to this project, are found to site preferentially at SI. SI, SI′ and SII are the only sites populated when the Si/Al of the zeolite < 2.[173–175]

1.6.3 IM-12 (UTL)

The **UTL** framework topology contains two-dimensional sheets that lie parallel to one-another, separated by *d4r* units (see Figure 1.16). Perpendicular *12r* and *14r* channels run between the two-dimensional sheets. The framework, which has a unit cell of $T_{76}O_{152}$, comprising 12 and 23 crystallographically-distinct T and oxygen sites was the first to be dubbed an 'ultra-large pore' zeolite due to the existence of its 12- and 14-membered cavities, which are permitted by the inclusion of germanium in the synthesis.[64,151]

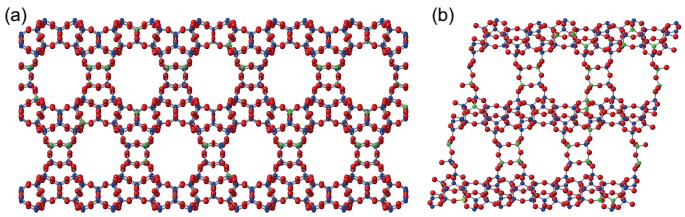

Figure 1.16: Structure of Ge-**UTL** framework with preferential distribution of germanium throughout the framework indicated. Viewed down (a) z and (b) y axes.

The greater diffusivity of the germanium coordination sphere supports the larger cavities and leads to a preferential incorporation within the strained *d4r* of material. Studies have shown that germanium populates the *d4r* exclusively up to the point where approximately $\frac{3}{8}$ of the positions are filled. At this level of germanium incorporation, there is a tendency to avoid Ge – O – Ge linkages and they are located as far away from each other in the *d4r* as possible. At increased germanium loading, the dopant element can also be found at a random distribution throughout the two-dimensional sheets, whilst increasing its occupancy and forming Ge – O – Ge in the *d4r*. Si/Ge levels of the zeolite often approach 3-4.5. Si/Ge of 11 and 3.5 are obtained by assuming sole occupancy of Ge in the *d4r* at $\frac{3}{8}$ and $\frac{8}{8}$ population, respectively.[152]

1.7 References

[1] A. F. Cronstedt, *Kongl. Vetenskaps Acad. Handl. Stockholm*, 1756, **17**, 120 – 123.

[2] A. F. Cronstedt, *Försök til mineralogie : eller mineral-rikets*, Wildiska, Stockholm, 1758.

[3] C. Colella and A. F. Gualtieri, *Microporous Mesoporous Mater.*, 2007, **105**, 213–221.

[4] C. Baerlocher and L. B. McCusker, *Database of Zeolite Structures*, http://www.iza-structure.org/databases/.

[5] C. Baerlocher, L. B. Mccusker and D. H. Olson, *Atlas of Zeolite Framework Types*, Elsevier, Amsterdam, 6th edn., 2007.

[6] P. A. Wright, *Microporous Framework Solids*, Royal Society of Chemistry, Cambridge, 1st edn., 2008.

[7] B. Jha and D. N. Singh, *Fly Ash Zeolites*, Springer Singapore, Singapore, 2016, vol. 78.

[8] J. Čejka, H. V. Bekkum, A. Corma and F. Schüth, *Introduction to Zeolite Science and Practice*, Elsevier, Amsterdam, 3rd edn., 2007, vol. 168.

[9] J. Čejka, R. E. Morris and P. Nachtigall, *Zeolites in Catalysis*, Royal Society of Chemistry, Cambridge, 1st edn., 2017.

[10] K. Stocker, M. Ellersdorfer, M. Lehner and J. G. Raith, *BHM Berg- und Hüttenmännische Monatshefte*, 2017, **162**, 142–147.

[11] M. E. Davis, *Nature*, 2002, **417**, 813–821.

[12] A. Corma, *Chem. Rev.*, 1997, **97**, 2373–2420.

[13] C. J. Rhodes, *Annu. Reports Sect. C. Physical Chem.*, 2007, **103**, 287.

[14] C. J. Rhodes, *Sci. Prog.*, 2010, **93**, 223–284.

[15] R. M. Milton, *Molecular Sieves*, Soc. Chem. Ind., London, 1968, pp. 199–203.

[16] R. M. Milton, *Molecular Sieve Science and Technology*, ACS, Washington DC, 1st edn., 1989, pp. 1–10.

[17] E. M. Flanigen, in *Zeolites Sci. Technol.*, Springer Netherlands, Dordrecht, 1984, vol. 53, pp. 3–34.

[18] J. D. Sherman, *Proc. Natl. Acad. Sci.*, 1999, **96**, 3471–3478.

[19] C. Colella and W. S. Wise, *Microporous Mesoporous Mater.*, 2014, **189**, 4–10.

[20] *Synthetic Zeolites Market by Type (Zeolite A, Zeolite Y, Zeolite X, Zeolite Zsm-5), Application (Detergents, Catalysts, Adsorbents), and Region - Global Forecast to 2022'*, Marketsandmarkets technical report, 2017.

[21] *Global Zeolite Market Size & Analysis Industry Report 2012-2022*, Grand view research technical report, 2018.

[22] J. V. Smith, *Tetrahedral Frameworks of Zeolites, Clathrates*, Springer-Verlag, Berlin/Heidelberg, 2000.

[23] H. van Koningsveld, *Compendium of Zeolite Framework Types*, Elsevier, Amsterdam, 1st edn., 2007.

[24] H. van Koningsveld, *Stud. Surf. Sci. Catal.*, 2007, **170**, 698–704.

[25] W. Loewenstein, *Acta Miner.*, 1950, **39**, 92–96.

[26] R. Townsend, *Stud. Surf. Sci. Catal.*, 1986, **28**, 273–282.

[27] R. P. Townsend and E. N. Coker, in *Stud. Surf. Sci. Catal.*, 2001, vol. 137, pp. 467–524.

[28] S. I. Zones, *U.S. Patent 4544538*, 1985.

[29] L.-T. Yuen, S. Zones, T. Harris, E. Gallegos and A. Auroux, *Microporous Mater.*, 1994, **2**, 105–117.

[30] F. Bleken, M. Bjørgen, L. Palumbo, S. Bordiga, S. Svelle, K.-P. Lillerud and U. Olsbye, *Top. Catal.*, 2009, **52**, 218–228.

[31] J. Tang, Y. Zhou, W. Su, X. Liu and Y. Sun, *Adsorpt. Sci. Technol.*, 2013, **31**, 549–558.

[32] I. Bull, R. S. Boorse, W. M. Jaglowski, G. S. Koermer, A. Moini, J. A. Patchett, W.-M. Xue, P. Burk, J. C. Dettling and M. T. Caudle, *U.S. Patent US2008/0226545A1*, 2008.

[33] E. M. Flanigen, in *Adsorbents: Fundamentals and Applications*, John Wiley & Sons, Inc., Hoboken, NJ, USA, 1991, vol. 1862, pp. 13–34.

[34] M. E. Davis and R. F. Lobo, *Chem. Mater.*, 1992, **4**, 756–768.

[35] C. S. Cundy and P. A. Cox, *Chem. Rev.*, 2003, **103**, 663–702.

[36] C. S. Cundy and P. A. Cox, *Microporous Mesoporous Mater.*, 2005, **82**, 1–78.

[37] M. T. Melchior, D. E. Vaughan and C. F. Pictroski, *J. Phys. Chem.*, 1995, **99**, 6128–6144.

[38] A. J. Vega, *J. Phys. Chem.*, 1996, **100**, 833–836.

[39] J. Holzinger, P. Beato, L. F. Lundegaard and J. Skibsted, *J. Phys. Chem. C*, 2018, **122**, 15595–15613.

[40] J. Dědeček, E. Tabor and S. Sklenak, *ChemSusChem*, 2019, **12**, 556–576.

[41] K. Mlekodaj, J. Dedecek, V. Pashkova, E. Tabor, P. Klein, M. Urbanova, R. Karcz, P. Sazama, S. R. Whittleton, H. M. Thomas, A. V. Fishchuk and S. Sklenak, *J. Phys. Chem. C*, 2019, **123**, 7968–7987.

[42] A. E. Alvarado-Swaisgood, M. K. Barr, P. J. Hay and A. Redondo, *J. Phys. Chem.*, 1991, **95**, 10031–10036.

[43] D. H. Olson, N. Khosrovani, A. W. Peters and B. H. Toby, *J. Phys. Chem. B*, 2000, **104**, 4844–4848.

[44] S. Sklenak, J. Dědeček, C. Li, B. Wichterlová, V. Gábová, M. Sierka and J. Sauer, *Angew. Chemie Int. Ed.*, 2007, **46**, 7286–7289.

[45] S. Sklenak, J. Dědeček, C. Li, B. Wichterlová, V. Gábová, M. Sierka and J. Sauer, *Phys. Chem. Chem. Phys.*, 2009, **11**, 1237–1247.

[46] J. Čejka, A. Corma and S. Zones, *Zeolites and Catalysis*, Wiley-Blackwell, Weinheim, 1st edn., 2010.

[47] J. Dědeček, Z. Sobalík and B. Wichterlová, *Catalysis Reviews*, 2012, **54**, 135–223.

[48] J. A. van Bokhoven and C. Lamberti, *Coord. Chem. Rev.*, 2014, **277-278**, 275–290.

[49] M. Ravi, V. L. Sushkevich and J. A. van Bokhoven, *Nat. Mater.*, 2020, **19**, 1047–1056.

[50] K. Muraoka, W. Chaikittisilp, Y. Yanaba, T. Yoshikawa and T. Okubo, *Angew. Chem. Int. Ed.*, 2018, **57**, 3742–3746.

[51] J. R. Di Iorio and R. Gounder, *Chem. Mater.*, 2016, **28**, 2236–2247.

[52] B. C. Knott, C. T. Nimlos, D. J. Robichaud, M. R. Nimlos, S. Kim and R. Gounder, *ACS Catal.*, 2018, **8**, 770–784.

[53] S. Li, R. Gounder, A. Debellis, I. B. Müller, S. Prasad, A. Moini and W. F. Schneider, *J. Phys. Chem. C*, 2019, **123**, 17454–17458.

[54] J. R. Di Iorio, S. Li, C. B. Jones, C. T. Nimlos, Y. Wang, E. Kunkes, V. Vattipalli, S. Prasad, A. Moini, W. F. Schneider and R. Gounder, *J. Am. Chem. Soc.*, 2020, **142**, 4807–4819.

[55] J. To, A. A. Sokol, S. A. French, C. R. A. Catlow, P. Sherwood and H. J. Van Dam, *Angew. Chemie - Int. Ed.*, 2006, **45**, 1633–1638.

[56] J. Li, A. Corma and J. Yu, *Chem. Soc. Rev.*, 2015, **44**, 7112–7127.

[57] X. Ouyang, S. J. Hwang, D. Xie, T. Rea, S. I. Zones and A. Katz, *ACS Catal.*, 2015, **5**, 3108–3119.

[58] T. Pang, X. Yang, C. Yuan, A. A. Elzatahry, A. Alghamdi, X. He, X. Cheng and Y. Deng, *Chin. Chem. Lett.*, 2021, **32**, 328–338.

[59] M. Taramasso, S. Milanese, G. Perego, Milan and B. Notari, *U.S. Patent 4410501*, 1983.

[60] B. Notari, *Adv. Catal.*, 1996, **41**, 253–334.

[61] G. Qi, Q. Wang, J. Xu, Q. Wu, C. Wang, X. Zhao, X. Meng, F. Xiao and F. Deng, *Commun. Chem.*, 2018, **1**, 1–22.

[62] R. Millini, G. Perego and G. Bellussi, *Top. Catal.*, 1999, **9**, 13–34.

[63] H. Koller, C.-Y. Chen and S. I. Zones, *Top. Catal.*, 2015, **58**, 451–479.

[64] J.-l. Paillaud, B. Harbuzaru, J. Patarin and N. Bats, *Science*, 2004, **304**, 990–993.

[65] N. Kasian, A. Tuel, E. Verheyen, C. E. A. Kirschhock, F. Taulelle and J. A. Martens, *Chem. Mater.*, 2014, **26**, 5556–5565.

[66] P. Eliášová, M. Opanasenko, P. S. Wheatley, M. Shamzhy, M. Mazur, P. Nachtigall, W. J. Roth, R. E. Morris and J. Čejka, *Chem. Soc. Rev.*, 2015, **44**, 7177–7206.

[67] K. J. D. Mackenzie and M. E. Smith, *Multinuclear Solid-State Nuclear Magnetic Resonance of Inorganic Materials*, Pergamon, Oxford, 1st edn., 2002.

[68] S. E. Ashbrook and M. E. Smith, *Chem. Soc. Rev.*, 2006, **35**, 718–735.

[69] S. E. Ashbrook, D. M. Dawson and V. R. Seymour, *Phys. Chem. Chem. Phys.*, 2014, **16**, 8223–8242.

[70] S. E. Ashbrook, D. M. Dawson and J. M. Griffin, in *Local Struct. Characterisation*, ed. D. O'Hare and R. I. Walton, John Wiley & Sons, Ltd, 1st edn., 2014, pp. 1–88.

[71] S. E. Ashbrook and D. McKay, *Chem. Commun.*, 2016, **52**, 7186–7204.

[72] S. E. Ashbrook, J. M. Griffin and K. E. Johnston, *Annu. Rev. Anal. Chem.*, 2018, **11**, 485–508.

[73] S. E. Ashbrook, Z. H. Davis, R. E. Morris and C. M. Rice, *Chem. Sci.*, 2021, **12**, 5016–5036.

[74] D. M. Dawson, R. F. Moran and S. E. Ashbrook, *J. Phys. Chem. C*, 2017, **121**, 15198–15210.

[75] R. F. Moran, D. M. Dawson and S. E. Ashbrook, *Int. Rev. Phys. Chem.*, 2017, **36**, 39–115.

[76] B. Reif, S. E. Ashbrook, L. Emsley and M. Hong, *Nat. Rev. Methods Prim.*, 2021, **1**, 1–23.

[77] J. Klinowski, *Prog. Nucl. Magn. Reson. Spectrosc.*, 1984, **16**, 237–309.

[78] J. Klinowski, *Annu. Rev. Mater. Sci.*, 1988, **18**, 189–218.

[79] J. Klinowski, *Colloids and Surfaces*, 1989, **36**, 133–154.

[80] D. H. Brouwer, R. J. Darton, R. E. Morris and M. H. Levitt, *J. Am. Chem. Soc.*, 2005, **127**, 10365–10370.

[81] D. H. Brouwer and J. Van Huizen, *Magn. Reson. Chem.*, 2019, **57**, 167–175.

[82] D. H. Brouwer, C. C. Brouwer, S. Mesa, C. A. Semelhago, E. E. Steckley, M. P. Sun, J. G. Mikolajewski and C. Baerlocher, *Microporous Mesoporous Mater.*, 2020, **297**, 110000.

[83] M. C. Venetos, S. Dwaraknath and K. A. Persson, *J. Phys. Chem. C*, 2021, acs.jpcc.1c04829.

[84] E. Lippmaa, M. Maegi, A. Samoson, G. Engelhardt and A. R. Grimmer, *J. Am. Chem. Soc.*, 1980, **102**, 4889–4893.

[85] E. Lippmaa, M. Maegi, A. Samoson, M. Tarmak and G. Engelhardt, *J. Am. Chem. Soc.*, 1981, **103**, 4992–4996.

[86] S. Ramdas, J. M. Thomas, J. Klinowski, C. A. Fyfe and J. S. Hartmann, *Nature*, 1981, **292**, 228–230.

[87] J. Klinowski, S. Ramdas, J. M. Thomas, C. A. Fyfe and J. S. Hartman, *J. Chem. Soc. Faraday Trans. 2*, 1982, **78**, 1025.

[88] A. Pines, M. G. Gibby and J. S. Waugh, *J. Chem. Phys.*, 1972, **56**, 1776–1777.

[89] L. Frydman and J. S. Harwood, *J. Am. Chem. Soc.*, 1995, **117**, 5367–5368.

[90] J.-P. Amoureux, C. Fernandez and S. Steuernagel, *J. Magn. Reson. Ser. A*, 1996, **118**, 116–118.

[91] H. K. C. Timken, G. L. Turner, E. Oldfield, J. P. Gilson and L. B. Welsh, *J. Am. Chem. Soc.*, 1986, **108**, 7231–7235.

[92] J. E. Readman, C. P. Grey, M. Ziliox, L. M. Bull and A. Samoson, *Solid State Nucl. Magn. Reson.*, 2004, **26**, 153–159.

[93] L. Peng, H. Huo, Z. Gan and C. P. Grey, *Microporous Mesoporous Mater.*, 2008, **109**, 156–162.

[94] J. E. Readman, N. Kim, M. Ziliox and C. P. Grey, *Chem. Commun.*, 2002, **2**, 2808–2809.

[95] L. M. Bull, A. K. Cheetham, T. Anupold, A. Reinhold, A. Samoson, J. Sauer, B. Bussemer, Y. Lee, S. Gann, J. Shore, A. Pines and R. Dupree, *J. Am. Chem. Soc.*, 1998, **120**, 3510–3511.

[96] D. Schneider, H. Toufar, A. Samoson and D. Freude, *Solid State Nucl. Magn. Reson.*, 2009, **35**, 87–92.

[97] I. Maupin, J. Mijoin, T. Belin, C. Morais, V. Montouillout, D. Duprez and N. Bion, *J. Catal.*, 2013, **300**, 136–140.

[98] L. Peng, Y. Liu, N. Kim, J. E. Readman and C. P. Grey, *Nat. Mater.*, 2005, **4**, 216–219.

[99] L. Peng, H. Huo, Y. Liu and C. P. Grey, *J. Am. Chem. Soc.*, 2007, **129**, 335–346.

[100] H. Huo, L. Peng and C. P. Grey, *Stud. Surf. Sci. Catal.*, 2007, **170**, 783–789.

[101] H. Huo, L. Peng and C. P. Grey, *J. Phys. Chem. C*, 2011, **115**, 2030–2037.

[102] H. Huo, L. Peng, Z. Gan and C. P. Grey, *J. Am. Chem. Soc.*, 2012, **134**, 9708–9720.

[103] G. P. M. Bignami, D. M. Dawson, V. R. Seymour, P. S. Wheatley, R. E. Morris and S. E. Ashbrook, *J. Am. Chem. Soc.*, 2017, **139**, 5140–5148.

[104] S. M. Pugh, P. A. Wright, D. J. Law, N. Thompson and S. E. Ashbrook, *J. Am. Chem. Soc.*, 2020, **142**, 900–906.

[105] G. Brunklaus, H. Koller and S. I. Zones, *Angew. Chemie - Int. Ed.*, 2016, **55**, 14459–14463.

[106] S. Li, O. Lafon, W. Wang, Q. Wang, X. Wang, Y. Li, J. Xu and F. Deng, *Adv. Mater.*, 2020, **32**, 2002879.

[107] G. Coudurier, A. Auroux, J. C. Vedrine, R. D. Farlee, L. Abrams and R. D. Shannon, *J. Catal.*, 1987, **108**, 1–14.

[108] R. de Ruiter, A. Kentgens, J. Grootendorst, J. Jansen and H. van Bekkum, *Zeolites*, 1993, **13**, 128–138.

[109] C. Fild, D. F. Shantz, R. F. Lobo and H. Koller, *Phys. Chem. Chem. Phys.*, 2000, **2**, 3091–3098.

[110] M. R. Hansen, T. Vosegaard, H. J. Jakobsen and J. Skibsted, *J. Phys. Chem. A*, 2004, **108**, 586–594.

[111] S. J. Hwang, C. Y. Chen and S. I. Zones, *J. Phys. Chem. B*, 2004, **108**, 18535–18546.

[112] H.-m. Kao and Y.-c. Chen, *J. Phys. Chem. B*, 2003, **107**, 3367–3375.

[113] R. M. Shayib, N. C. George, R. Seshadri, A. W. Burton, S. I. Zones and B. F. Chmelka, *J. Am. Chem. Soc.*, 2011, **133**, 18728–18741.

[114] L. J. Smith, H. Eckert and A. K. Cheetham, *J. Am. Chem. Soc.*, 2000, **122**, 1700–1708.

[115] L. J. Smith, H. Eckert and A. K. Cheetham, *Chem. Mater.*, 2001, **13**, 385–391.

[116] A. V. McCormick and A. T. Bell, *Catal. Rev.*, 1989, **31**, 97–127.

[117] D. W. Breck, *J. Chem. Educ.*, 1964, **41**, 678–689.

[118] S. I. Zones and R. A. V. Nordstrand, 1988, 409–415.

[119] S. I. Zones and R. A. V. Nordstrand, *Zeolites*, 1988, **8**, 166–174.

[120] R. M. Barrer, *Zeolites*, 1981, **1**, 130–140.

[121] C. D. Chang and A. T. Bell, *Catal. Letters*, 1991, **8**, 305–316.

[122] S. L. Burkett and M. E. Davis, *J. Phys. Chem.*, 1994, **98**, 4647–4653.

[123] S. L. Burkett and M. E. Davis, *Chem. Mater.*, 1995, **7**, 920–928.

[124] S. L. Burkett and M. E. Davis, *Chem. Mater.*, 1995, **7**, 1453–1463.

[125] A. Burton, *Catal. Rev.*, 2018, **60**, 132–175.

[126] M. Dusselier and M. E. Davis, *Chem. Rev.*, 2018, **118**, 5265–5329.

[127] E. M. Flanigen and R. L. Patton, *U.S. Patent 4073865*, 1978.

[128] E. M. Flanigen, J. M. Bennett, R. W. Grose, J. P. Cohen, R. L. Patton, R. M. Kirchner and J. V. Smith, *Nature*, 1978, **271**, 512–516.

[129] S. I. Zones, S.-J. Hwang, S. Elomari, I. Ogino, M. E. Davis and A. W. Burton, *Comptes Rendus Chim.*, 2005, **8**, 267–282.

[130] M. W. Deem, R. Pophale, P. A. Cheeseman and D. J. Earl, *J. Phys. Chem. C*, 2009, **113**, 21353–21360.

[131] R. Pophale, P. A. Cheeseman and M. W. Deem, *Phys. Chem. Chem. Phys.*, 2011, **13**, 12407.

[132] A. Deneyer, Q. Ke, J. Devos and M. Dusselier, *Chem. Mater.*, 2020, **32**, 4884–4919.

[133] J. Přech, P. Pizarro, D. P. Serrano and J. Čejka, *Chem. Soc. Rev.*, 2018, **47**, 8263–8306.

[134] X. Jia, W. Khan, Z. Wu, J. Choi and A. C. Yip, *Adv. Powder Technol.*, 2019, **30**, 467–484.

[135] W. Xu, J. Dong, J. Li, J. Li and F. Wu, *J. Chem. Soc. Chem. Commun.*, 1990, 755–756.

[136] L. Ren, Q. Wu, C. Yang, L. Zhu, C. Li, P. Zhang, H. Zhang, X. Meng and F.-s. Xiao, *J. Am. Chem. Soc.*, 2012, **134**, 15173–15176.

[137] J. Mei, A. Duan and X. Wang, *Materials (Basel).*, 2021, **14**, 788–801.

[138] D. N. Rainer and R. E. Morris, *Dalt. Trans.*, 2021, **50**, 8995–9009.

[139] C. J. Heard, L. Grajciar, F. Uhlík, M. Shamzhy, M. Opanasenko, J. Čejka and P. Nachtigall, *Adv. Mater.*, 2020, **32**, 2003264.

[140] D. E. Resasco, S. P. Crossley, B. Wang and J. L. White, *Catal. Rev.*, 2021, **63**, 302–362.

[141] G. T. Kerr, *J. Phys. Chem.*, 1967, **71**, 4155–4156.

[142] J. Klinowski, J. M. Thomas, C. A. Fyfe, G. C. Gobbi and J. S. Hartman, *Inorg. Chem.*, 1983, **22**, 63–66.

[143] D. Verboekend, N. Nuttens, R. Locus, J. Van Aelst, P. Verolme, J. C. Groen, J. Pérez-Ramírez and B. F. Sels, *Chem. Soc. Rev.*, 2016, **45**, 3331–3352.

[144] M. C. Silaghi, C. Chizallet, J. Sauer and P. Raybaud, *J. Catal.*, 2016, **339**, 242–255.

[145] K. Chen, S. Horstmeier, V. T. Nguyen, B. Wang, S. P. Crossley, T. Pham, Z. Gan, I. Hung and J. L. White, *J. Am. Chem. Soc.*, 2020, **142**, 7514–7523.

[146] R. E. Morris and J. Čejka, *Nat. Chem.*, 2015, **7**, 381–388.

[147] W. J. Roth, O. V. Shvets, M. Shamzhy, P. Chlubná, M. Kubů, P. Nachtigall and J. Čejka, *J. Am. Chem. Soc.*, 2011, **133**, 6130–6133.

[148] W. J. Roth, P. Nachtigall, R. E. Morris, P. S. Wheatley, V. R. Seymour, S. E. Ashbrook, P. Chlubná, L. Grajciar, M. Položij, A. Zukal, O. Shvets and J. Čejka, *Nat. Chem.*, 2013, **5**, 628–633.

[149] W. J. Roth, P. Nachtigall, R. E. Morris and J. Čejka, *Chem. Rev.*, 2014, **114**, 4807–4837.

[150] M. Mazur, P. S. Wheatley, M. Navarro, W. J. Roth, M. Položij, A. Mayoral, P. Eliášová, P. Nachtigall, J. Čejka and R. E. Morris, *Nat. Chem.*, 2016, **8**, 58–62.

[151] A. Corma, M. J. Díaz-Cabañas, F. Rey, S. Nicolopoulus and K. Boulahya, *Chem. Commun.*, 2004, 1356–1357.

[152] S. O. Odoh, M. W. Deem and L. Gagliardi, *J. Phys. Chem. C*, 2014, **118**, 26939–26946.

[153] S. A. Morris, G. P. M. Bignami, Y. Tian, M. Navarro, D. S. Firth, J. Čejka, P. S. Wheatley, D. M. Dawson, W. A. Slawinski, D. S. Wragg, R. E. Morris and S. E. Ashbrook, *Nat. Chem.*, 2017, **9**, 1012–1018.

[154] M. V. Shamzhy, O. V. Shvets, M. V. Opanasenko, P. S. Yaremov, L. G. Sarkisyan, P. Chlubná, A. Zukal, V. R. Marthala, M. Hartmann and J. Čejka, *J. Mater. Chem.*, 2012, **22**, 15793.

[155] S. Goel, S. I. Zones and E. Iglesia, *Chem. Mater.*, 2015, **27**, 2056–2066.

[156] C. Li, M. Moliner and A. Corma, *Angew. Chemie Int. Ed.*, 2018, **57**, 15330–15353.

[157] D. Schwalbe-Koda, Z. Jensen, E. Olivetti and R. Gómez-Bombarelli, *Nat. Mater.*, 2019, **18**, 1177–1181.

[158] B. Sulikowski, J. Rakoczy, H. Hamdan and J. Klinowski, *J. Chem. Soc. Chem. Commun.*, 1987, 1542.

[159] J. Zhang, O. Veselý, Z. Tošner, M. Mazur, M. Opanasenko, J. Čejka and M. Shamzhy, *Chem. Mater.*, 2021, **33**, 1228–1237.

[160] R. Barrer, J. Davies and L. Rees, *J. Inorg. Nucl. Chem.*, 1969, **31**, 219–232.

[161] T. Grey, J. Gale, D. Nicholson and B. Peterson, *Microporous Mesoporous Mater.*, 1999, **31**, 45–59.

[162] L. A. M. M. Barbosa, R. A. van Santen and J. Hafner, *J. Am. Chem. Soc.*, 2001, **123**, 4530–4540.

[163] D. W. Fickel and R. F. Lobo, *J. Phys. Chem. C*, 2010, **114**, 1633–1640.

[164] Q. Guo, F. Fan, D. A. J. M. Ligthart, G. Li, Z. Feng, E. J. M. Hensen and C. Li, *ChemCatChem*, 2014, **6**, 634–639.

[165] Z. Xu and J. F. Stebbins, *Solid State Nucl. Magn. Reson.*, 1998, **11**, 243–251.

[166] D. Freude, T. Loeser, D. Michel, U. Pingel and D. Prochnow, *Solid State Nucl. Magn. Reson.*, 2001, **20**, 46–60.

[167] P. Zhao, P. S. Neuhoff and J. F. Stebbins, *Chem. Phys. Lett.*, 2001, **344**, 325–332.

[168] P. S. Neuhoff, P. Zhao and J. F. Stebbins, *Microporous Mesoporous Mater.*, 2002, **55**, 239–251.

[169] D. Freude and T. Loeser, *Lect. Notes Phys.*, 2004, **634**, 163–183.

[170] L. S. Dent and J. V. Smith, *Nature*, 1958, **181**, 1794–1796.

[171] M. Calligaris, G. Nardin and L. Randaccio, *Zeolites*, 1983, **3**, 205–208.

[172] B. Civalleri, A. M. Ferrari, M. Llunell, R. Orlando, M. Mérawa and P. Ugliengo, *Chem. Mater.*, 2003, **15**, 3996–4004.

[173] G. R. Eulenberger, D. P. Shoemaker and J. G. Keil, *J. Phys. Chem.*, 1967, **71**, 1812–1819.

[174] J. A. Kaduk and J. Faber, *Rigaku J.*, 1995, **12**, 14–34.

[175] C. Beauvais, X. Guerrault, F. X. Coudert, A. Boutin and A. H. Fuchs, *J. Phys. Chem. B*, 2004, **108**, 399–404.

Chapter 2

Characterisation Techniques

In this section a brief overview of the characterisation techniques used in this thesis and the theory that underpins them will be provided. Instrument-specific details and practical methodology are outlined in the following chapter.

2.1 Nuclear Magnetic Resonance Spectroscopy

Nuclear magnetic resonance (NMR) spectroscopy is a widely used spectroscopic technique for the characterisation of molecules and materials. The technique provides element-specific information about the local environment of a nucleus, including the local electronic structure and bonding arrangement. Not limited to routine structural characterisation, the application of NMR spectroscopy to chemical systems can provide information on chemical reactivity, reaction mechanism and short-lived intermediates.

The use of NMR spectroscopy in scientific research is divided broadly into liquid-state and solid-state approaches. The former is most widely used, with spectra characterised by sharp, well-resolved lineshapes, providing detailed information primarily on organic or biological molecules. Solid-state NMR spectroscopy on the other hand is less widely used, with the extraction of structural information often hampered by the anisotropic nature of the interactions present, contributing to a broadening of lineshapes, which is removed in solution by rapid molecular tumbling. It would appear then that solid-state NMR spectroscopy has to overcome more challenges to extract structural information. However, the anisotropic interactions can provide a wealth of information about chemical environments, which is simply averaged away in solution-state NMR spectroscopy. Solid-state NMR spectroscopy therefore is widely applied to the field of materials chemistry where it excels in the characterisation of the structure and processes occurring in inorganic and hybrid organic-inorganic materials.[1,2]

One advantage of NMR spectroscopy over other characterisation techniques is its sensitivity to the local coordination environment of nuclei, meaning reactivity-based changes are easy to investigate. Other characterisation techniques may only see these through secondary changes, *e.g.*, crystalline structure or structural stability and as such their detection of system reactivity is indirect. Consequently, there is a huge potential for the use of NMR spectroscopy to characterise reactions in real time for both solution- and solid-state, utilising *in-situ* techniques,[3–10] which is a particular focus in this project.

2.1.1 Nuclear Magnetic Resonance

NMR spectroscopy is based on the study of nuclei with a net magnetic moment *i.e.*, a non-zero nuclear spin. When placed in an external magnetic field ($\boldsymbol{B}_0$) and applied with soft radio-frequency (RF) pulses, signature resonances of the nucleus of study are detected, providing much information on local atomic structure and coordination environments.[11]

2.1.1.1 Fundamentals

A description of the fundamental underlying principles of magnetic resonance is given below.[2,11–15]

Nuclei that possess a non-zero spin quantum number, I (*e.g.* $\frac{1}{2}$, 1, $\frac{3}{2}$, 2, $\frac{5}{2}$, ...), will possess a spin angular momentum, $\boldsymbol{I}$. The magnitude of $\boldsymbol{I}$ is quantised in units of $\hbar$ and is given as,

$$|\boldsymbol{I}| = [I(I+1)]^{\frac{1}{2}}\hbar. \tag{2.1}$$

As it has both direction and magnitude, spin angular momentum is a vector quantity. In addition to the quantisation of the magnitude of $\boldsymbol{I}$, the orientation is also quantized by convention along the z-axis, giving the z-component of the spin vector as,

$$I_z = m_I\hbar, \tag{2.2}$$

were, m_I is the magnetic quantum number, which can take $2I+1$ values between $+I$ and $-I$.

The overall magnetic moment, $\boldsymbol{\mu}$ of a precessing nucleus, is related to $\boldsymbol{I}$ through the gyromagnetic ratio of the nucleus, γ, which has the units of $\text{rad}^{-1}\text{T}^{-1}$. Importantly, the

magnetic moment of a nucleus is not simply the sum of the magnetic moments of its constituent nucleons. Instead, the magnitude of γ, which is inherent for each isotope, is related to the $\boldsymbol{\mu}$ and $\boldsymbol{I}$ by:

$$\boldsymbol{\mu} = \gamma \boldsymbol{I}, \tag{2.3}$$

providing an indication of the sensitivity of the nucleus to NMR. Combining Equations 2.2 and 2.3, it follows that the z-axis of the magnetic moment for a nucleus is:

$$\mu_z = \gamma m_I \hbar. \tag{2.4}$$

In the absence of a magnetic field, the $2I + 1$ possible orientations of the spin vector (and corresponding magnetic moment) are degenerate. Upon application of an external magnetic field, $\boldsymbol{B}_0$, the degeneracy of nuclei is lifted (known as the Zeeman interaction) and the energy (E) becomes:

$$E_{m_I} = -\mu_z B_0, \tag{2.5}$$

as shown schematically in Figure 2.1.

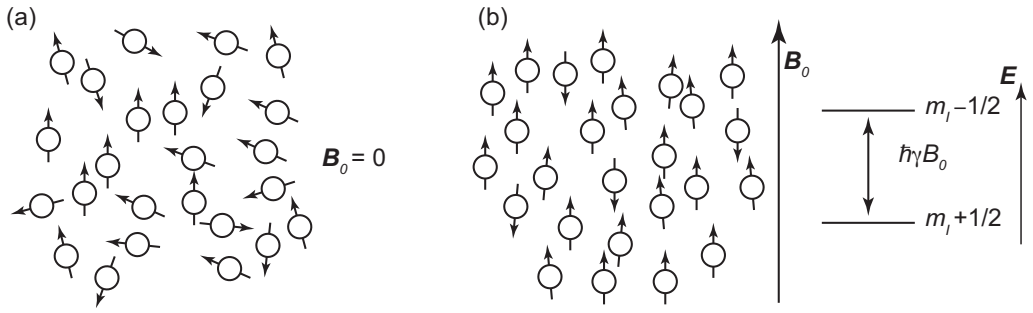

Figure 2.1: Schematic representation of an ensemble of $I = \frac{1}{2}$ nuclei and associated magnetic moments in the (a) absence and (b) presence of an applied external magnetic field, $\boldsymbol{B}_0$. The relative energies of the spin states (assuming γ is negative) and transition frequencies are indicated.

Combining Equations 2.4 and 2.5, where the magnetic quantum number, m_I can take $2I + 1$ values, gives $2I + 1$ energy states, termed the Zeeman states, having energies of:

$$E_{m_I} = -\gamma m_I \hbar B_0. \tag{2.6}$$

In the case of a spin-$\frac{1}{2}$ nucleus, the two possible orientations, 'spin-up' or 'spin-down' are often referred to as α and β, respectively.

The population of the $I = \frac{1}{2}$ Zeeman energy levels at thermal equilibrium is given by the Boltzmann distribution,

$$\frac{N_\beta}{N_\alpha} = e^{\frac{-\gamma\hbar \boldsymbol{B}_0}{k_B T}}, \tag{2.7}$$

where N is the population of the $m_I{}^{th}$ state, k_B is the Boltzmann constant and T is the absolute temperature. The quantum selection rule for a spectroscopic transition is,

$$\Delta m_I = \pm 1, \tag{2.8}$$

giving for $I = \frac{1}{2}$ nuclei one transition with,

$$\Delta E = h\nu_0 = \gamma\hbar B_0. \tag{2.9}$$

Typically, the difference in populations of the ground and excited state is very small as almost 50% of nuclei sit in the ground state. For example, for protons in a 9.4 T field at 300 K gives an energy gap of 2.65 $\times$ 10 $^{-25}$ J, providing a population difference of $\approx$ one spin in every 16,000. This makes NMR spectroscopy an inherently insensitive spectroscopic technique, leading to a drive for higher magnetic field strengths to increase this population difference. Equation 2.9 can be rearranged to give the transition frequency,

$$\nu_0 = \frac{\gamma \boldsymbol{B}_0}{2\pi}, \tag{2.10}$$

termed Larmor frequency, ν_0 (in Hz). At the magnetic field strengths (1-28 T) commonly used in NMR spectroscopy, Larmor frequencies typically fall within the radiofrequency region of the electromagnetic spectrum, *e.g.*, 10 to 1200 MHz. The Larmor frequency can also be expressed as an angular frequency (ω_0), in rad s^{-1}:

$$\omega_0 = -\gamma B_0. \tag{2.11}$$

2.1.1.2 The NMR Experiment

In order to effect transitions between Zeeman states, energy must be supplied to the sample in the form of a radiofrequency pulse, with a frequency,

$$\omega_{rf} \approx \omega_0. \tag{2.12}$$

For an ensemble of n, $I = \frac{1}{2}$ spins, the difference in population between the two Zeeman states gives rise to a net bulk magnetisation vector ($\boldsymbol{M}$) along the z-axis, given by the sum of the components of magnetic moments for the n^{th} nucleus as,

$$M_z = \sum_n \mu_{zn}. \tag{2.13}$$

If $\boldsymbol{M}$ is perturbed from its thermal equilibrium position along the z-axis it will precess around this axis at the Larmor frequency, ω_0.

In the simplest NMR experiment, a single, short radiofrequency (RF) pulse is applied at a frequency $\approx \omega_{\mathrm{rf}}$, which will interact with the spins and affect the bulk magnetization vector, $\boldsymbol{M}$. A pulse can be considered as two counter rotating magnetic fields (with frequencies $\pm\ \omega_{\mathrm{rf}}$). The interaction is difficult to visualise in the static laboratory frame and is best viewed in the rotating frame, a frame of reference that is itself rotating about the z-axis at a frequency ω_{rf}. In the rotating frame one component of the pulse can be viewed as a static magnetic field that can interact with the spins, while the second (with $-\omega_{\mathrm{rf}}$) now rotates at $-2\ \omega_{\mathrm{rf}}$ and can be neglected. It follows therefore that precession of the M in the rotating frame occurs at an offset frequency, Ω,

$$\Omega = \omega_0 - \omega_{rf}. \tag{2.14}$$

around an effective magnetic field of,

$$B_{eff} = \frac{\Omega}{\gamma}. \tag{2.15}$$

Depending on the frequency of the applied ω_{rf}, Ω may be positive, negative or zero. For example, from Equation 2.14, if ω_{rf} is greater than ω_0, Ω will be negative and $\boldsymbol{M}$ will appear to precess backwards in the rotating frame. If ω_{rf} is exactly equal to ω_0 (termed "on resonance"), $\boldsymbol{M}$ will be completely static, while if ω_{rf} is smaller, then Ω is positive and $\boldsymbol{M}$ will precess forwards in the rotating frame.

The application of the RF pulse can be more easily visualized using the vector model of Bloch,[16,17] within the rotating frame, as shown in Figure 2.2. The application of the pulse, a static field, B_1, applied along an axis in the xy-plane, results in nutation of $\boldsymbol{M}$ around this axis at a rate or frequency given by,

$$\omega_1 = -\gamma B_1. \tag{2.16}$$

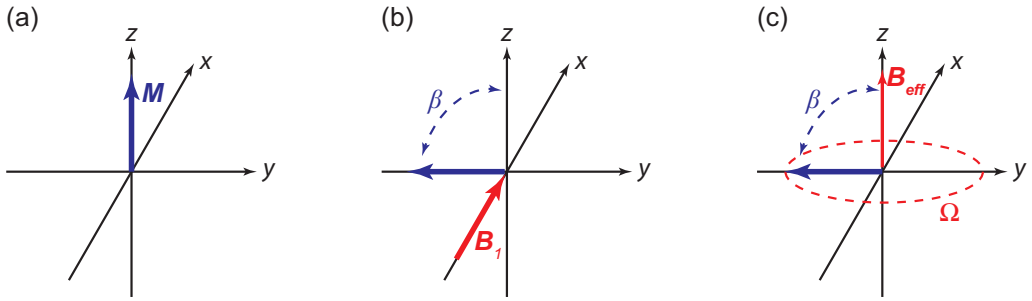

Figure 2.2: Vector model representing the effect of a pulse on the bulk magnetisation vector, $\boldsymbol{M}$, within the rotating frame. (a) initially aligned along the z-axis at thermal equilibrium, (b) nutated into the xy-plane at an angle, β due to application of an RF pulse B_1 along the x-axis and (c) subsequent free precession of the magnetisation in the xy-plane at a rate of Ω after application of the pulse.

The extent to which the pulse causes nutation of **M** into the xy-plane is referred to as the 'flip angle', β, given by,

$$\beta = \omega_1 \tau_p, \tag{2.17}$$

where τ_p is the pulse duration. When β = 90°, as in Figure 2.2b, $\boldsymbol{M}$ would lie in the xy-plane itself, while β = 180°would place $\boldsymbol{M}$ along the z-axis. After the pulse has been applied precession of $\boldsymbol{M}$ about B_{eff} at a frequency Ω will occur. This precession is damped by relaxation processes that aim to return the system to thermal equilibrium. The gradual return of M to the z-axis is the longitudinal relaxation, often termed T_1 relaxation. The time taken for this process to occur can be determined using:

$$M_z(t) - M_0 = [M_z(0) - M_0]e^{\frac{-t}{T_1}}, \tag{2.18}$$

where $M_z(0)$ is the magnetisation on the z-axis after the pulse is applied and M_0 is the equilibrium magnetisation. For solids, the value of T_1 can be low (*i.e.* relaxation can be rapid) for certain lattices but it is more common for this relaxation to take minutes or even hours in the solid state. The loss of coherent magnetisation in the xy-plane is the spin-spin, or T_2 relaxation, which is related to the duration for which a signal can be recorded.

It is during the relaxation period of the sample that spectral acquisition takes place, with data recorded used to produce NMR spectra. The damped procession of nuclear spins about $\boldsymbol{M}$ at a frequency Ω is recorded by detectors in the xy-plane and is known as the free-induction decay (FID), containing a signal S(t), with both real and imaginary parts,

$$S(t) = e^{i\Omega t} e^{\frac{-t}{T_2}}. \tag{2.19}$$

To produce a frequency-dependent spectrum, a Fourier transform is needed,[18] giving:

$$S(\omega) = \int_0^\infty e^{i\omega t}\, dt. \tag{2.20}$$

2.1.2 Interactions in NMR Spectroscopy

A description of the atomic-level interactions that affect the nuclei present in a sample and their effect on NMR spectra is provided.[2,11–15]

From the discussion above, all nuclides of one isotope (*e.g.*, with the same γ) would behave identically in response to the RF pulse. This would result in the production of a single precession frequency and, hence, a single lineshape in the NMR spectrum. However, the reason NMR spectroscopy has proven such a useful analytical tool in the chemical sciences is that the nuclear spins are also affected by a variety of different interactions, some between the spins and some between the spins and their environment. This leads to different precession frequencies and signals in the spectrum that reflect the difference in the local chemical environment of the spins.

2.1.2.1 Chemical Shift

The great attraction of NMR spectroscopy is that information on the local structural environment of a nucleus of study is contained in its NMR spectra. When a nucleus is placed in an external magnetic field, this causes a precession of the electrons creating a local magnetic field (***B'***) which can oppose or add to the external $\boldsymbol{B}_0$ field. The currents created will depend on the nature of the electron distribution (and therefore on the local bonding or closely coordinated atoms). The field experienced by the nucleus, $\boldsymbol{B}$, is given by,

$$\boldsymbol{B} = \boldsymbol{B}_0 - \boldsymbol{B'} = \boldsymbol{B}_0(1-\sigma), \tag{2.21}$$

where σ is a field independent shielding parameter. This results in a pertubation of the Larmor frequency for the nucleus to,

$$\omega_{obs} = \gamma \boldsymbol{B} = \gamma \boldsymbol{B}_0(1-\sigma). \tag{2.22}$$

The above equation shows that nuclei that experience different effective magnetic fields will have inherently different Larmor frequencies. Distinguishing these frequencies from one-another in a practical way is made challenging by σ, the absolute shielding, which is both small in magnitude and difficult to determine. Practically therefore, different

resonance frequencies are defined as a chemical shift (δ) (a deshielding parameter, usually quoted in ppm), relative to a reference compound (with shielding σ_{ref}) as:

$$\delta = 10^6 \frac{\sigma - \sigma_{ref}}{1 - \sigma_{ref}} \approx 10^6 (1 - \sigma_{ref}). \tag{2.23}$$

The chemical shift can be related to the corresponding frequencies by:

$$\delta = 10^6 \frac{\omega_{obs} - \omega_{ref}}{\omega_{ref}}. \tag{2.24}$$

2.1.2.2 Chemical Shift Anisotropy

The aforementioned equations would hold for cases where the electron distribution around a nucleus was spherical. This, however, is not usually the case (owing to the directional nature of many bonding interactions) as the shielding is anisotropic, or orientationally dependent. This is best described as a second-rank tensor, σ, with a corresponding shift tensor, δ. In their principal axis systems (PAS) these two tensors are diagonal (*i.e.*, with three principal components). For example, δ_{PAS} is given by,

$$\delta^{\text{PAS}} = \begin{pmatrix} \delta_{11} & 0 & 0 \\ 0 & \delta_{22} & 0 \\ 0 & 0 & \delta_{33} \end{pmatrix}, \tag{2.25}$$

The observed chemical shift of a resonance is given by,

$$\delta = \delta_{11} \sin^2\theta \cos^2\phi + \delta_{22} \sin^2\theta \sin^2\phi + \delta_{33} \cos^2\theta, \tag{2.26}$$

where θ and ϕ describe the orientation of the PAS of the tensor, relative to B_0. A schematic of a chemical shift tensor ellipsoid, with labelled angles and components is displayed in Figure 2.3.

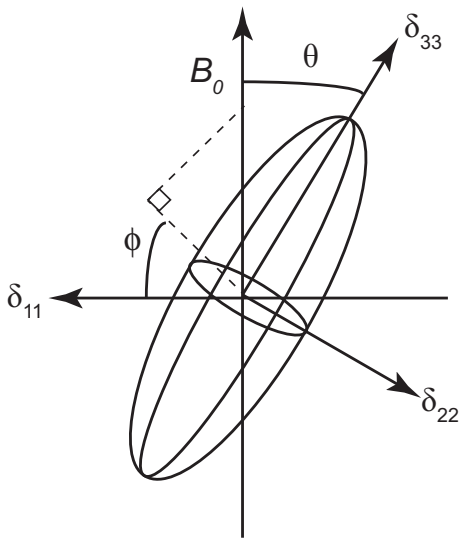

Figure 2.3: Schematic of an ellipsoid representing a chemical shift tensor, labelled with angles that indicate ellipsoid orientation relative to the external magnetic field.

Each component contained within Equation 2.26 is clearly anisotropic, and δ itself is clearly also orientationally-dependent. It is possible however, to rewrite Equation 2.26 in terms of three different parameters, showing that the chemical shift interaction is composed of an isotropic term and an anisotropic component. In the standard convention tensor components, $\delta_{11} \geq \delta_{22} \geq \delta_{33}$, however the Haeberlen convention[19] used in this thesis follows $|\delta_{33} - \delta_{\mathrm{iso}}| \geq |\delta_{11} - \delta_{\mathrm{iso}}| \geq |\delta_{22} - \delta_{\mathrm{iso}}|$. The isotropic chemical shift is given by,

$$\delta_{iso} = \frac{\delta_{11} + \delta_{22} + \delta_{33}}{3}. \tag{2.27}$$

The anisotropy is defined by an asymmetry, for which $0 \leq \eta \leq 1$,

$$\eta = \frac{\delta_{22} - \delta_{11}}{\delta_{33} - \delta_{iso}}, \tag{2.28}$$

and a magnitude,

$$\Delta = \delta_{33} - \delta_{iso}. \tag{2.29}$$

This gives the observed shift as,

$$\delta = \delta_{iso} + \frac{\Delta}{2}[(3\cos^2\theta - 1) + \eta(\sin^2\theta\cos 2\phi)]. \tag{2.30}$$

While an orientation dependent shift will be seen for a single crystal, the effect of the anisotropic nature of the chemical-shift anisotropy (CSA) for a powdered sample (where many millions of crystallites with different orientations are present simultaneously) will

be to broaden the spectral lines. For example, the effect of varying η on the observed powder pattern lineshape is shown in Figure 2.4. In solution, the anisotropy is averaged to zero by the rapid tumbling of molecules, but the isotropic shift is retained, reducing Equation 2.30 to $\delta = \delta_{\mathrm{iso}}$.

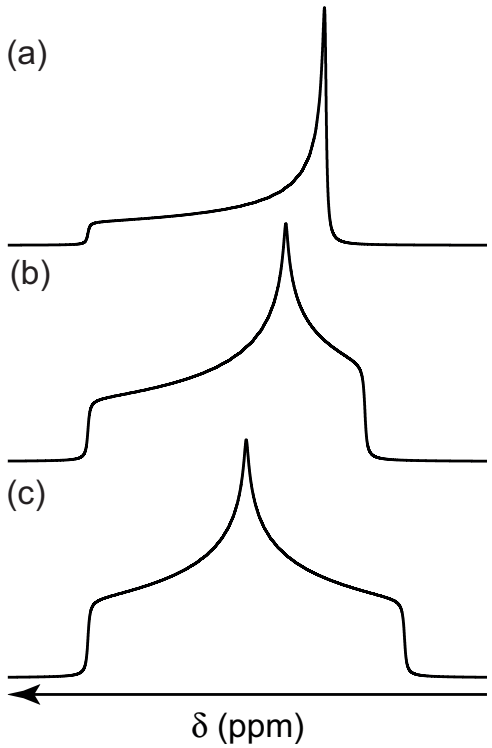

Figure 2.4: Effect of varying η on a simulated lineshape for an isolated spin $I = \frac{1}{2}$ nucleus. The lineshape asymmetry takes values of η at (a) 0, (b) 0.5 and (c) 1.

2.1.2.3 Dipolar Coupling

The CSA is not the only anisotropic interaction that broadens lines in solid-state NMR spectra. Another major contributing component is the dipolar coupling. The dipolar coupling is a through-space magnetic interaction between two spins, occurring as a result of the effect of the magnetic field generated by one spin at the second. The magnitude of the dipolar coupling for two isolated spins (I and S) at a distance r apart and at an angle of θ to the external magnetic field (see Figure 2.5) is given by:

$$\omega = -\omega_D^{PAS}\frac{1}{2}(3\cos^2\theta - 1), \tag{2.31}$$

where $\omega_{\mathrm{D}}{}^{\mathrm{PAS}}$ is the dipolar coupling constant (and PAS denotes the principal axis system of the dipolar tensor) and is given by,

$$\omega_D^{PAS} = \frac{\mu_0}{4\pi}\frac{\gamma_I\gamma_S\hbar}{r_{IS}^3}, \tag{2.32}$$

where r_{IS} is the internuclear distance between the two spins.

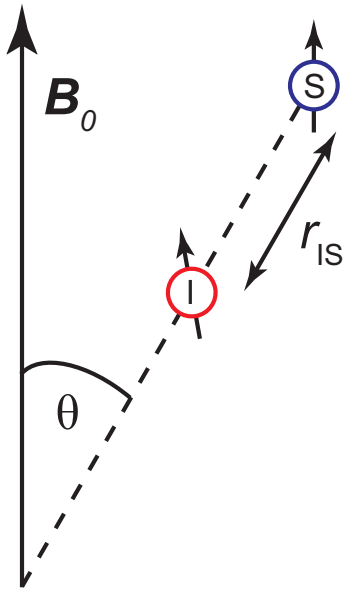

Figure 2.5: Schematic showing the key parameters of the dipolar coupling between a two-spin (I, S), $I = \frac{1}{2}$ system.

For a powdered sample for two $I = \frac{1}{2}$ nuclei as an isolated spin pair, this results in a Pake-doublet powder-pattern lineshape, with a maximum width of $2\,\omega_{\mathrm{D}}{}^{\mathrm{PAS}}$. However, in a real NMR sample there are likely to be many different dipolar couplings to different spins at different internuclear distances, this usually results in a Gaussian broadening of the lineshape, significantly hampering the spectral analysis. For a homonuclear dipolar coupling the spectrum is similar but splittings of $2\,\omega_{\mathrm{D}}$ for a single crystal and a maximum width of $3\,\omega_{\mathrm{D}}{}^{\mathrm{PAS}}$ for a Pake powder pattern would be observed (Figure 2.6).

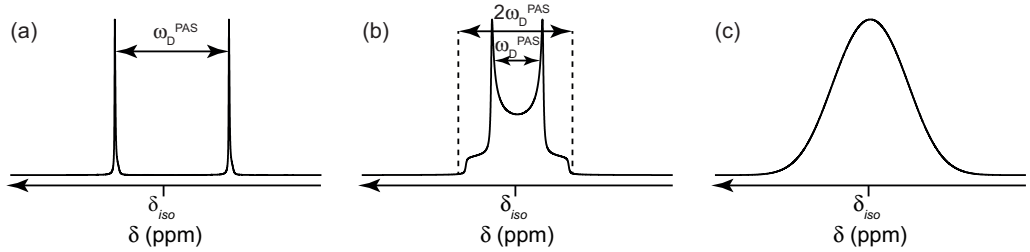

Figure 2.6: Schematic showing the effect of a heteronuclear dipolar coupling between two spin $I = \frac{1}{2}$ for (a) a single crystallite, (b) a powdered sample. (c) shows the typical Gaussian-broadening of an NMR spectrum that is seen when multiple such couplings are present.

2.1.2.4 *J* coupling

A second type of spin-spin interaction present in NMR spectroscopy is the *J* coupling, which is a through-bond interaction between the spins, mediated by the bonding electrons.[20,21] The *J* coupling has anisotropic and isotropic components and is described by a tensor, $\mathbf{J}^{\mathrm{PAS}}$. However, it is often much smaller in magnitude (usually less than 1000 Hz and often just 1-10 Hz) than the dipolar coupling (or CSA) and the multiplet lineshapes that are produced by the couplings are often not resolved in the solid state. The interaction has a much greater impact on NMR spectra in solution, where dipolar and CSA interactions are averaged to zero, but the isotropic component of the coupling, J_{iso}, is retained.

2.1.2.5 Quadrupolar Interaction

There is an additional interaction that affects almost three quarters of nuclides in the Periodic table, that can have severe consequences on the appearance of solid-state NMR spectra. Nuclei with $I > \frac{1}{2}$ are termed quadrupolar nuclei and possess a permanent non-spherical nuclear charge distribution, or nuclear quadrupolar moment (Q) which is specific to each nuclide. This interacts with the electric field gradient (EFG) present at the nucleus and can lead to broadening of the lineshapes on the order of MHz.

The EFG is described by a tensor, $\mathbf{V}$. which in its PAS ($\mathbf{V}^{\mathrm{PAS}}$) is given by:

$$\mathbf{V}^{\mathrm{PAS}} = \begin{pmatrix} \mathrm{V_{xx}} & 0 & 0 \\ 0 & \mathrm{V_{yy}} & 0 \\ 0 & 0 & \mathrm{V_{zz}} \end{pmatrix}, \tag{2.33}$$

where, $|\mathrm{V_{zz}}| > |\mathrm{V_{yy}}| > |\mathrm{V_{xx}}|$. The quadrupolar interaction is described by both its magnitude, or the quadrupolar coupling constant (in Hz); value of Q can be described by both its magnitude (C_Q);

$$C_Q = \frac{eQV_{zz}}{h}, \tag{2.34}$$

and asymmetry (η_{Q});

$$\eta_Q = \frac{V_{xx} - V_{yy}}{V_{zz}}, \tag{2.35}$$

such that $0 \leq \eta_{\mathrm{Q}} \leq 1$.

From both C_Q and η_Q, the overall quadrupolar product, P_Q (in Hz) can be calculated:

$$P_Q = C_Q \sqrt{1 + \frac{\eta_Q^2}{3}}. \tag{2.36}$$

The quadrupolar interaction, although large, can usually be treated as a perturbation of the Zeeman energy levels. As previously outlined Section 2.1.1.1, there are $2I + 1$ spin states, meaning there are up to $2I$ possible degenerate transitions, each at the Larmor frequency (ω_0), as shown in Figure 2.7.

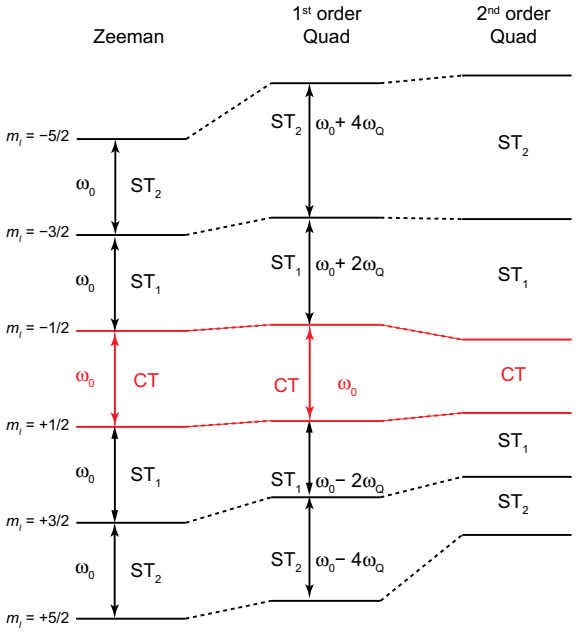

Figure 2.7: Schematic showing the effect of the first- and second-order quadrupolar perturbation of the Zeeman energy levels for a spin $I = 5/2$ nucleus. The first-order interaction affects satellite transitions only, whist the second-order interaction perturbs all transitions.

For the case of an I = 5/2 nucleus (and all half-integer spin quadrupolar nuclei) as in Figure 2.7, there are five possible transitions between energy levels. The effect of the quadrupolar interaction to a first-order approximation is to perturb all energy levels, lifting the degeneracy of the transitions. However, the central transition (CT) between levels with $m_I = \pm \frac{1}{2}$ is unaffected, remaining at the Larmor frequency. The remaining transitions, referred to as satellite transitions (ST) are perturbed by the quadrupolar interaction, and their frequency now depends on ω_Q, the quadrupolar splitting parameter, giving rise to five lines within the NMR spectrum.

Integer-spin quadrupolar nuclei have no CT and all single-quantum transitions are anisotropically broadened in the presence of even a small EFG. However, symmetrical

MQ transitions are not affected by the first-order perturbation. As for half-integer-spin nuclei, the symmetrical MQ transitions become anisotropically broadened by the second-order perturbation.

The quadrupolar splitting is orientationally dependent and is given by,

$$\omega_Q = \frac{\omega_Q^{PAS}}{2}[(3\cos^2\beta - 1) + \eta_Q(\sin^2\beta)\cos 2\gamma], \tag{2.37}$$

where, β and γ relate the PAS of the EFG to the laboratory frame and The value of $\omega_{\mathrm{Q}}{}^{\mathrm{PAS}}$ is given by,

$$\omega_Q^{PAS} = 3\pi\frac{C_Q}{2I(I+1)}, \tag{2.38}$$

in rads^{-1}. However, it is not always sufficient to describe the quadrupolar interaction by a first-order perturbation and if the interaction is significant second-order effects must be included. The second-order contribution to the transition frequency is given by,

$$\omega = \frac{(\omega_Q^{PAS})^2}{2\omega_0}[A^0_{I,m_I}B^0(\eta_Q) + A^2_{I,m_I}B^2(\eta_Q\alpha,\beta,\gamma) + A^4_{I,m_I}B^4(\eta_Q\alpha,\beta,\gamma)]. \tag{2.39}$$

This interaction is anisotropic *i.e.* orientationally dependent and affects all transitions, including the CT. Here, A^n and B^n are spin- and transition-dependent coefficients, and the Euler angles α, β, γ describe the orientation of the EFG PAS with respect to the laboratory frame. Equation 2.39 also contains an isotropic term (resulting in a shift of the signal away from the isotropic chemical shift, δ_{iso}), and two anisotropic terms, a second-rank and fourth-rank term, which have different orientational dependences. As the second-order broadening is proportional to $(\omega_{\mathrm{Q}}{}^{\mathrm{PAS}})^2/\omega_{\mathrm{Q}}$ its magnitude is usually a lot smaller than the first-order term but can still have important consequences for the width of the CT lineshape. The larger magnitude of the first-order broadening (proportional to $\omega_{\mathrm{Q}}{}^{\mathrm{PAS}}$), means that in many practically relevant cases the ST are too broad to be observed and only CT lineshapes are acquired.

Further, the local coordination environment around the nucleus has a large effect on the magnitude of the EFG and the width of the quadrupolar broadened lineshape, with higher-symmetry coordination environments, such as octahedral and tetrahedral coordination often having lower C_Q than those with more distorted environments or five-coordinate or trigonal sites.[22–24] Examples of how lineshapes for spin I = 5/2 nucleus vary with C_Q and η_{Q} are shown in Figure 2.8.

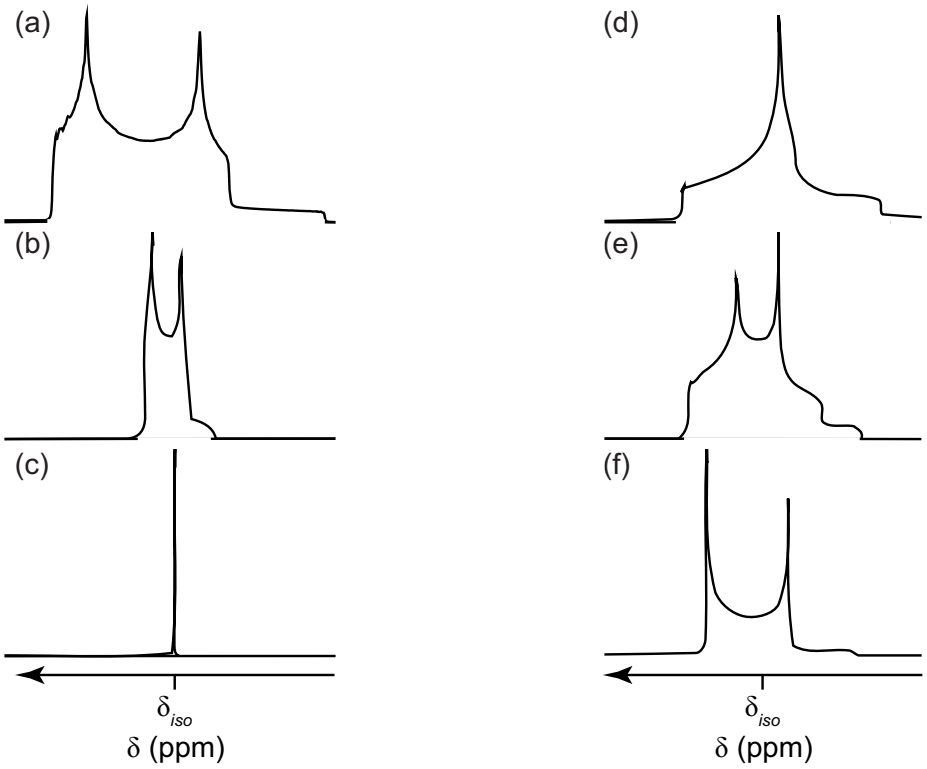

Figure 2.8: Schematic showing the effect of varying ((a)-(c)) C_Q and ((d)-(f)) η_Q on a simulated quadrupolar lineshape for a spin $I = 5/2$ nucleus. (a)-(c), fixed $\eta_Q = 0.2$ and C_Q (a) = 0 MHz, (b) = 2 MHz, (c) = 4 MHz. (d)-(f), fixed $C_Q = 3$ MHz and η_Q (a) = 0, (b) = 0.5, (c) = 1.

2.1.3 Solid-state NMR Spectroscopy

The application of magnetic resonance to this project is primarily focused on extracting information from materials in the solid state. In light of this, an overview of some of the key experimental techniques and principles used in this project are given here.

2.1.3.1 Magic-Angle Spinning

As outlined throughout Section 2.1.2, a number of interactions exist between nuclei that can lead to the broadening of spectral lines in NMR spectra of solids. In solution these anisotropic interactions do not cause as many problems as the continual rapid tumbling of molecules averages the anisotropic contributions to the CSA, dipolar coupling, J-coupling and quadrupolar interaction to zero, enabling site specific information to be extracted more easily.

In order to overcome the limited resolution in NMR spectra of solids, inspiration from solution is taken, mimicking the tumbling of molecules through physical motion of the sample. This is achieved by rapid rotation about an axis inclined at an angle (termed, the magic angle, θ_M) to the external magnetic field.[25–27] When θ_M is 54.736°, $3\cos^2\theta - 1 = 0$, the interactions that have this orientational dependence (*i.e.* the CSA (Equation 2.30), dipolar coupling (Equation 2.31), J-coupling and first-order quadrupolar coupling (Equation 2.37)) are removed, providing sample rotation is sufficiently rapid. This process is referred to magic-angle spinning (MAS), a schematic of which is shown in Figure 2.9.

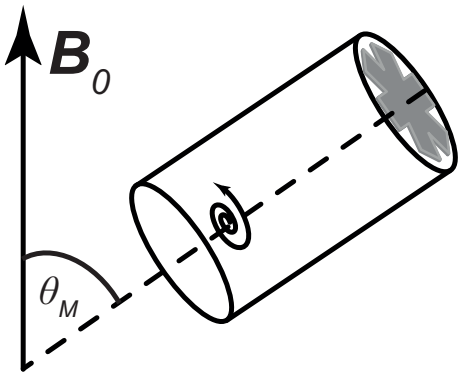

Figure 2.9: Schematic depicting magic-angle spinning. Typical MAS rates are on the order of 10 -100 kHz. The angle θ_M is equal to 54.736°.

By rotating the sample rapidly about the magic angle, the average orientation of all the crystallites within the rotor is aligned with θ_M. This has the effect of cancelling the (second-rank) anisotropic contributions of the interactions, producing sharper lineshapes but retaining any isotropic terms. In order to completely remove the anisotropic contributions, the MAS rate has to be sufficiently rapid relative to the magnitude of the interaction considered. To achieve this, solid-state NMR samples are packed into small, cylindrical ZrO_2 rotors sealed with a finned cap which results in sample rotation upon the application of a stream of compressed air. MAS rates for solid-state NMR experimentation are typically between 5 and 120 kHz, and although the notion to eliminate all anisotropic effects may lead one to the assumption that the highest MAS rates should always be used, application of these is not always practical. The greater the MAS rate employed, the smaller the rotor volume that can withstand the associated forces. Hence, fast MAS comes with the sacrifice of sample volume, causing a decrease in sensitivity, an increase in experiment time or possible prohibition of time-limited experiments or those that require specific reaction volume, such as sealed slurry systems. An example of the effect of sufficiently rapid MAS is shown in Figure 2.10, where anisotropic contributions to the ^{13}C NMR spectrum of Al-MIL-53 metal-organic framework (MOF) are removed by the rotation.

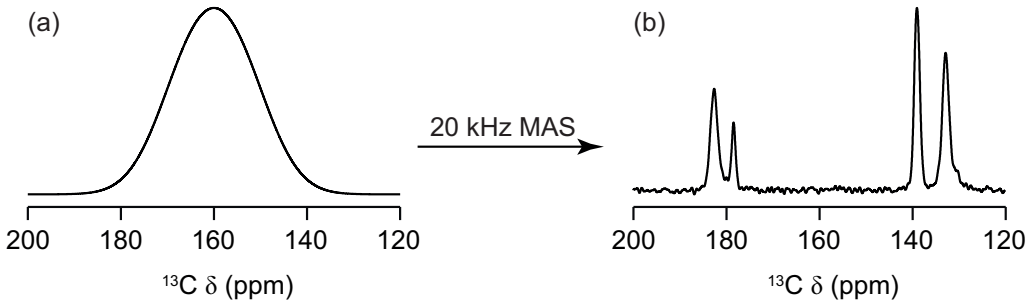

Figure 2.10: Example of the effect of MAS on the ^{13}C (14.1 T) cross-polarised NMR spectrum of an Al-MIL-53 metal-organic framework. (a) spectrum recorded under static conditions, (b) identical experiment recorded under 20 kHz MAS.

In the cases where MAS is insufficient to completely remove the broadening, additional signals termed spinning sidebands (SSBs) are seen, separated from the central isotropic peak by intervals of the MAS frequency. Whilst the presence of additional signals could be a potential complication in spectral analysis at the MAS rates available and for the magnitude of the interactions present in the samples studies in this work, this is not detrimental to the spectrum overall. However, if integrating spectra to obtain concentration/ratio-dependent information, the SSB contributions must also be considered.

For quadrupolar nuclei however, MAS is not always able to remove the anisotropic broadening. Although MAS can successfully remove first-order quadrupolar anisotropic contributions to the lineshape, these are often many MHz in size, and sufficiently rapid MAS rates are not possible. Even under MAS then, the focus is often purely on the CT. However, MAS is unable to remove the associated second-order contributions. The second-rank term would be removed by MAS (as it is proportional to $3\cos^2\theta - 1$), but the fourth-rank anisotropic term would not (owing to its more complex angular dependence). The forth-rank term remains under MAS and although the lineshape is narrowed a true isotropic spectrum cannot be obtained, no matter how rapidly the sample is rotated. Under MAS the second-order contribution to the quadrupolar interaction is modified from Equation 2.39.

$$\omega_Q = \frac{\omega_Q^{PAS}}{\omega_0}[A^0_{I,m_I}B^0(\eta_Q) + A^2_{I,m_I}B^2(\eta_{Q,\beta',\gamma'}) + A^4_{I,m_I}B^4(\eta_{Q,\beta',\gamma'})]. \qquad (2.40)$$

It is still possible to extract the NMR parameters from quadrupolar broadened linehsapes C_Q, η_{Q} and δ_{iso} from quadrupolar broadened lineshapes using analytical fitting. However, this can become complicated if more than one spectral component is overlapped.

2.1.3.2 Practical Considerations

When acquiring a solid-state NMR spectrum there are a number of practical considerations that need to be taken into account in order to produce the optimum spectrum from a given experiment. In this section, several considerations that apply to the majority of cases will be outlined.

The signal produced for a particular NMR experiment is dependent on the gyromagnetic ratio and the natural abundance of the isotope under study. However, as described in Section 2.1.1.1 the low Boltzmann population differences result in inherently low sensitivity for NMR. In order to increase the sensitivity of a spectrum N repeated experiments (or transients) are acquired and combined to produce the overall FID which can then be Fourier transformed. When this is the case the signal recorded in the experiments increases by a factor of N, however the more random noise increases by only $\sqrt{N}$, giving an effective $\sqrt{N}$ increase in signal-to-noise per transient.

Combining successive transients is an effective way to increase the signal-to-noise in NMR spectra, however it comes with implications for the overall experiment time. Between successive transients, the sample needs to be allowed to fully relax for $\boldsymbol{M}$ to re-align along B_0. If this does not happen, not only will the sensitivity gain be compromised, but the unequal averaging of signals in more sophisticated experiments (see Section 2.1.4) may lead to distorted spectra. It is good practice, therefore, to wait ≈ 5 T_1 increments before recycling the pulse program to ensure the spins are fully relaxed. Long recycle intervals, of several minutes, or hours may be needed between scans due to the lack of significant motion in the solid state. This can cause long experiment times when many scans are needed to achieve suitable $\sqrt{N}$ increase in signal-to-noise. The strength of the magnetic field can help to reduce T_1, with samples in greater magnetic fields returning to alignment of $\boldsymbol{M}$ along B_0 more quickly. Several experimental techniques, discussed in more detail in Section 2.1.4, can also help tackle this, although this may limit the extraction of quantitative information from the spectrum.

Another effective way to decrease the time required to produce a reasonable NMR spectrum is simply to increase the number of NMR-active spins in the sample. As the signal to noise increases with a factor of $\sqrt{N}$, the addition of more nuclide effectively increases the rate of acquisition by the square of the nuclide concentration. However, when the sample size is increased (and larger rotors are used) the maximum available MAS rate decreases. This risks the incomplete removal of some anisotropic components, as dis-

cussed in Section 2.1.3, producing broadened spectra, (which has concomitant effects on sensitivity). Another approach to reduce the time for spectral acquisition is through the use of isotopic enrichment (for nuclides where the natural abundance is <100%). By isotopically enriching the sample, the same square effect in the decrease of reaction time is observed. The challenge arising from this technique is the development of cost-effective and atom-efficient synthetic routes that are not detrimental to the material that is desired.[1]

2.1.4 Experimental Techniques

The key NMR experiments used in this thesis are outlined in this section.

2.1.4.1 Single-pulse

As shown in Figure 2.11 the simplest NMR experiment consists of a single pulse of RF radiation applied to the sample placed within an external magnetic field, before acquisition of the FID The radiofrequency pulse is applied to nutate the bulk magnetisation vector into the *xy*-plane (*i.e.*, a flip angle of 90° is used for maximum sensitivity).

Although in principle acquisition of the FID should start immediately after the pulse, practically there is a short time (or dead time, τ_D) where the signal cannot be recorded (shown schematically in Figure 2.11), owing to the effects of the pulse itself (termed ringing). Following acquisition, a recycle interval ideally equal to 5 T_1 is left before the subsequent pulse, as outlined in Section 2.1.3.2.

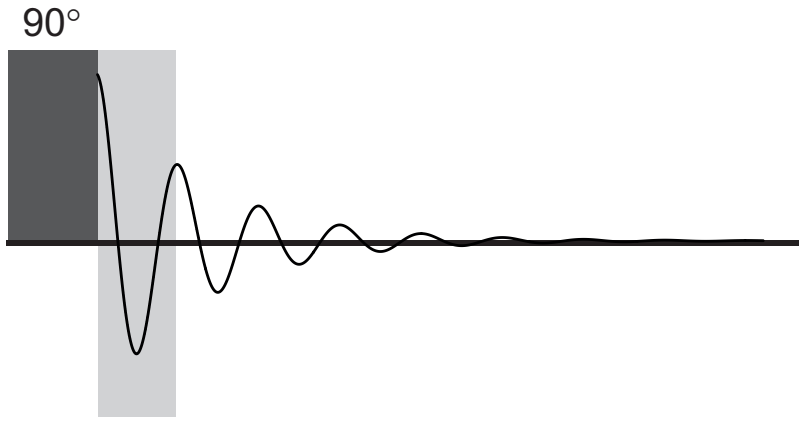

Figure 2.11: Schematic pulse sequence and subsequent FID for a conventional single-pulse NMR experiment. The 90°pulse (dark grey) nutates magnetisation fully into the *xy*-plane. The dead time τ_D is indicated by the light grey box.

In some instances, particularly where there are several components that nutate at different rates in an NMR sample (which can be the case for quadrupolar nuclei as the nutation rate

observed depends on the magnitude of the quadrupolar coupling), it may be beneficial to apply pulses with different flip angles, either to optimize the signal for particular components of the system, or to use much shorter flip angles where more quantitative results can be obtained. This latter approach also has the benefit of enabling more rapid spectral acquisition (as the system returns to thermal equilibrium more quickly), but does result in lower sensitivity per transient. In this work, 'short-flip' angle experiments have been used extensively when studying $H_2{}^{17}O$ slurry-zeolite mixtures using ^{17}O NMR experiments. Here the free water in the slurry often produces a more significant signal in the ^{17}O NMR spectrum than the zeolite, but it nutates at a slower rate than the signals from different chemical species in the zeolite framework. By shortening the flip angle, the unwanted signal from water in the spectrum is reduced whilst the signals from the ^{17}O-enriched zeolite framework can be more easily seen (and any nutation differences between these are minimised).

2.1.4.2 Spin-echo

The need for the dead time (τ_D) as described above not only reduces the sensitivity (as some signal is not recorded), it can lead to distorted spectra. One approach to counteract this is the spin-echo experiment (Figure 2.12). This involves the application of a second pulse (with a flip angle of 180°) following the initial 90°pulse after a short time period, τ.[28] This has the result that the start of the FID is delayed by a similar time, τ, enabling a complete FID to be acquired (assuming $\tau > \tau_D$), and resulting in undistorted lineshapes and minimizing the loss of information.

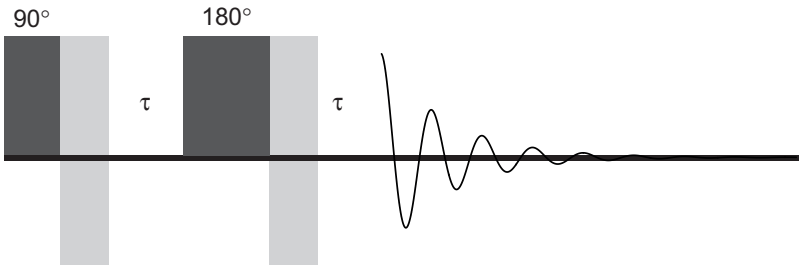

Figure 2.12: Schematic depicting the pulse sequence and subsequent FID for a conventional spin-echo NMR experiment. τ indicates the delay period that enables refocusing of the magnetisation.

2.1.4.3 Decoupling

Whilst MAS is usually effective at reducing the dipolar couplings between neighbouring spins, in some cases (*i.e.*, where these are very large) it is not capable of fully removing them, leading to residual broadening and poorer spectral resolution. For dipolar couplings that remain under insufficiently rapid MAS (and for the isotropic J coupling that is retained under sample rotation), decoupling can be used to further suppress the effect of couplings between spins.

Heteronuclear decoupling works by effectively removing the interaction of spin S during acquisition of the FID for spin I (Figure 2.13). This is achieved through the application of a pulse, or series of pulses, on spin S that cause continual reorientation of the S spin magnetisation, such that this coupling no longer broadens the spectral lines. Unsurprisingly, there are many effective heteronuclear decoupling techniques that employ trains of different pulses to remove the larger dipolar interaction. The most basic of these is continuous wave (CW) decoupling (as shown in in Figure 2.13) where there is a constant irradiation of spin S with a high-power RF pulse during the acquisition of the FID.

Some more sophisticated multi-pulse decoupling techniques used in this work include the TPPM and SPINAL-64 sequences.[29–32] TPPM (two phase pulse modulation) decoupling involves application of a train of pulses of alternating phases of $+\phi$ and $-\phi$ to spin S, typically referred to as TPPM-ϕ.[29] When needed, a greater suppression of the dipolar coupling was achieved by using the SPINAL-64 sequence, which involves similar trains of alternating phase pulses but also varies ϕ part way through the cycle. Cycles are stitched together to produce a total 64-pulse train.[30]

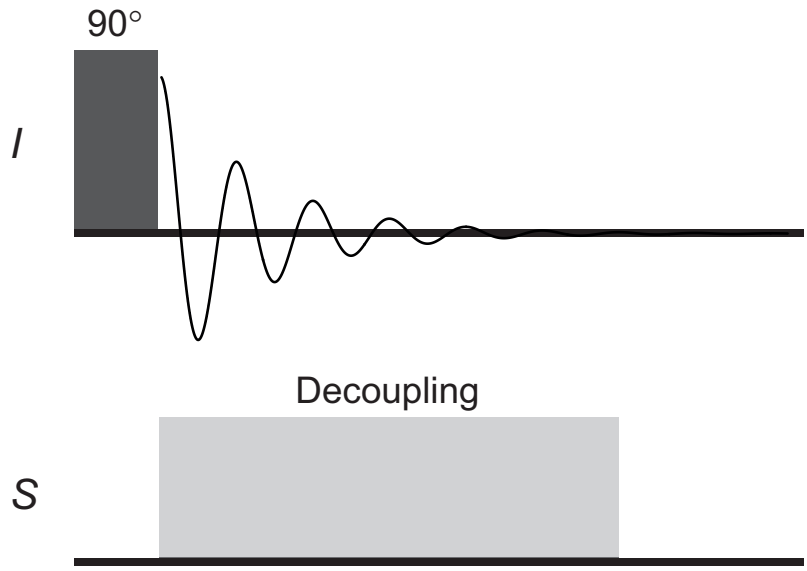

Figure 2.13: Schematic pulse sequence and subsequent FID for a conventional single-pulse NMR experiment for spin *I*, whilst applying decoupling on spin *S*.

The concept of heteronuclear decoupling as described here is fairly easily implemented owing to the appreciable differences in resonant frequency of neighbouring spins *e.g.* ^{1}H – ^{17}O or ^{1}H – ^{27}Al. This however, does mean the residual dipolar couplings from same-spin nuclei will still exist, potentially broadening spectral lines. Efforts to remove these through homonuclear decoupling techniques are significantly more complex and experimentally challenging, however as they are not a specific concern to the work in this thesis they will not be considered here.[2]

2.1.4.4 Cross-polarisation

Whilst improving the resolution of NMR experiments is important, the low natural abundance or low inherent insensitivity of some nuclei makes acquisition of useful NMR spectra in a reasonable time difficult. The problem of a low abundance isotope can in principle, be addressed through isotopic enrichment, as described above. However, this can be costly and involves additional lengthy synthetic procedures.[1] The problem of inherent insensitivity, however, is more difficult to solve. Those nuclei with low gyromagnetic ratio are less sensitive in NMR experiments (see Equations 2.3 and 2.4),[13] which can make spectral acquisition lengthy, particularly in the solid state where T_1 relaxation times can be long.

In order to overcome this, the cross-polarisation (CP) experiment was developed by Pines, Gibby and Waugh,[33] which exploits the ability to transfer magnetisation between dipolar coupled spins, I and S. This transfer is only facilitated if the eponymously named Hartmann-Hahn match,

$$\gamma_I B_{1I} = \gamma_S B_{1S}, \tag{2.41}$$

is fulfilled.[34] Provided this holds *i.e.*, the nutation rates are matched, then magnetisation can be transferred between dipolar-coupled spins. When experiments are performed under MAS, the conditions for the Hartmann-Hahn match are altered such that they become dependent on the MAS rate (in rads^{-1}) with,

$$\gamma_I B_{1I} = \gamma_S B_{1S} \pm \omega_R, \tag{2.42}$$

where $n = 1$ or 2. By fulfilling this match for a low-γ dilute spin of interest, S with a highly abundant, high-γ spin, I, the magnetization from I can be transferred to S to provide an intense FID with good signal. This is the basis for the cross-polarisation experiment (Figure 2.14). Practically, a selective 90°pulse is applied to highly abundant, high-γ spin I, after which magnetisation transfer occurs (assuming the Hartmann-Hahn condition is met) during a spin lock, where long continuous pulses are applied to both spins, keeping the magnetization 'locked' along a particular axis, exciting spin S. The S spin FID is then acquired, with S spin decoupling if desired.

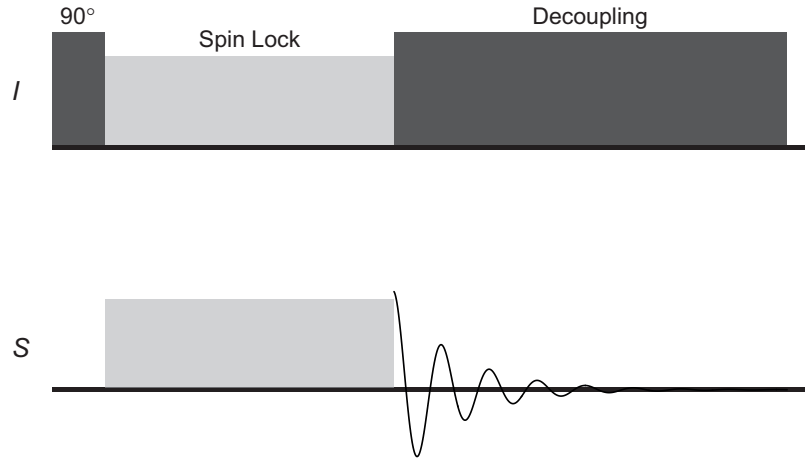

Figure 2.14: Schematic pulse sequence and subsequent FID for a cross-polarisation (CP) NMR experiment. The magnetisation from an initial pulse on an abundant spin, I is transferred during the spin-lock (sometimes referred to as contact pulse) to a lower-abundant, low-γ, spin S. The I spin FID is then acquired for S, whilst decoupling is applied for spin I.

CP experiments are a great resource for obtaining enhanced information about dilute spins in reduced experimental times. The information within them however, must be

analysed with caution. As the magnetisation transfer from I to S occurs through the dipolar coupling, the signal obtained is strongly dependent on their respective spatial proximities. Consequently, CP spectra are non-quantitative as not all of the dilute spins in the molecule will be enhanced equally. This can in some instances have advantages as by comparing spectra of the same material recorded with different spin-lock 'contact times' can provide qualitative information on the local distances between non-equivalent spins. Further, as the sequence starts with an I spin pulse the recycle intervals required depend on the relaxation time of the more abundant, higher-γ I spin, increasing the rate of acquisition and increasing the sensitivity per unit time.

Selection of the most appropriate I, S spin pairs is also an important consideration for CP experiments, as the maximum sensitivity gain relative to that of a single-pulse experiment (*i.e.*, $M_S{}^{SP}/M_S{}^{CP}$) is given by γ_I/γ_S, but also depends on a factor, ε which reflects the number of spins in each nucleus,[33,35]

$$\frac{M_S^{CP}}{M_S^{SP}} = \frac{\gamma_I}{\gamma_S}\frac{1}{(1+\varepsilon)}. \tag{2.43}$$

Typical sensitivity gains associated with using CP experiments can be on the order of 10.[33] Here, epsilon is equal to the ratio of the population of spins (N_I and N_S) for I and S, respectively with,

$$\varepsilon = \frac{S(S+1)N_S}{I(I+1)N_I}. \tag{2.44}$$

For these reasons it is advantageous to choose a spin with a high natural abundance and high-γ that is prevalent within the sample as spin I. This is almost always ^{1}H, but the properties of ^{19}F and its role in the synthesis of zeolites also make it a popular choice for work related to this project.[36–38] CP has been used extensively in this project for acquisition of ^{29}Si NMR spectra, as ^{29}Si has a reasonably low γ, a natural abundance of only 4.7% and typically long T_1 relaxation times. ^{1}H^{29}Si CP has a particular advantage here as it also enhances the visibility of silanol defect sites in the material, which are often present only in low concentrations but have important consequences on the stability of zeolites.[39–42]

The above discussion has described the CP experiment and considerations between two $I = \frac{1}{2}$ nuclei as this encompasses the level up to which the technique has been utilised in this work. It is possible to cross-polarise quadrupolar nuclei for experimental sensitivity gains, however it is experimentally much more challenging, with more complex spin dynamics, which will not be discussed in detail here.[11]

2.1.4.5 Multiple-quantum MAS

As discussed in Section 2.1.2.5, the quadrupolar interaction can broaden lineshapes observed in NMR spectra, precluding the extraction of useful information. Although MAS techniques (Section 2.1.3.1) are capable of removing first- and second-order contributions to the quadrupolar broadening, it is unable to suppress the anisotropic, fourth order terms in the second-order quadrupolar interaction, which have a more complex angular dependence. In an attempt to improve the resolution of the lineshapes of half-integer quadrupolar nuclei (and completely remove the second-order broadening), techniques such as dynamic angle spinning (DAS) and double rotation (DOR) have been developed, which utilise spinning about two axes; sequentially for DAS and simultaneously for DOR.[43,44] Together, these rotations can completely remove the second- and fourth-rank anisotropic terms of the second-order quadrupolar broadening. Whilst effective, these techniques require the use of sophisticated, specialised hardware and lengthy experimental set-up, introducing cost and skill barriers to their successful implementation, and so are not widely used.

In 1995, however, the MQMAS experiment was introduced by Frydman and Hardwood.[45,46] The experiment (for which a simple pulse sequence is shown in Figure 2.15), can be performed under MAS conditions on standard laboratory hardware, and involves a two-dimensional correlation of the central-transition (CT), collected in a time period t_2 with that of a multiple-quantum transition of the same half-integer quadrupolar nucleus, collected indirectly in t_2.[47] The most commonly used experiments correlate the CT with the triple-quantum (3Q) transition (referred to as 3QMAS), owing to their better sensitivity, but 5Q, 7Q and 9Q examples are also possible, which can have advantages in terms of resolution but at the (often significant) cost of sensitivity.[48] As multiple-quantum transitions are formally forbidden by the quantum-selection rules, MQMAS experiments are associated with low sensitivity (with losses of a factor $\approx$10 over conventional single pulse spectra) and are inherently non quantitative as the excitation and conversion efficiency depends on the quadrupolar coupling. Importantly however, maximum efficiency is obtained using the same pulse durations irrespective of the quadrupolar coupling, enabling these to be optimized easily within the experiment or on a related model system (if sensitivity is limiting). Efficiency is improved (for all but the smallest C_Q) as ω_1 increases, so high power pulses are usually used for the excitation and conversion steps. MQMAS efficiency does decrease with MAS rate, however, and these conditions result in optimum pulse durations that are typically shorter.[49,50]

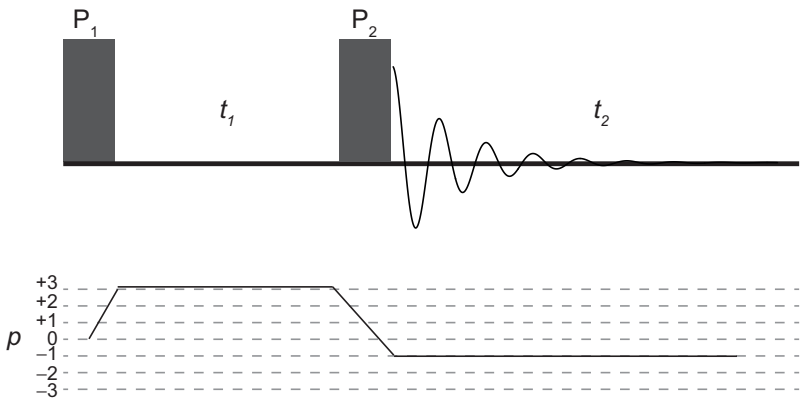

Figure 2.15: Schematic pulse sequence, coherence pathway transfer diagram and subsequent FID for a triple-quantum MAS experiment. Two (typically high-power) pulses are applied, exciting triple-quantum state magnetisation (P_1), before converting this to an observable single-quantum state (P_2).

The initial pulse sequence introduced by Frydman and Harwood involves a series of pulses for multiple-quantum excitation (reflecting approaches used in solution NMR), but it has since been found that a longer high-power pulse (P_1), typically a factor of 2.5 – 3 longer than P_2 gives greater multiple-quantum excitation.

The two-pulse MQMAS experiment introduced initially produces spectra which contain both absorptive and dispersive components, which can cause spectral overlap, the distortion of lineshapes and limit resolution. To address this, amplitude modulated z-filtered pulse sequences have been developed.[49,50] These select a symmetrical multiple-quantum coherence pathway upon excitation ($0 \rightarrow \pm\,\mathrm{p} \rightarrow 0 \rightarrow -1$) which, if combined equally using a conversion pulse result in a purely absorptive two-dimensional lineshape. The addition of a third pulse (P_3) is required to excite observable single-quantum CT signal. As shown in Figure 2.16, in contrast to the high-power, or 'hard', pulses P_1 and P_2, P_3 is 'soft' and of low power in order to selectively excite only the CT. A short delay, τ is included (where desired magnetization is stored along the z axis – hence z-filter) before P_3 to ensure the decay of any unwanted transverse magnetisation that may interfere with the spectrum.

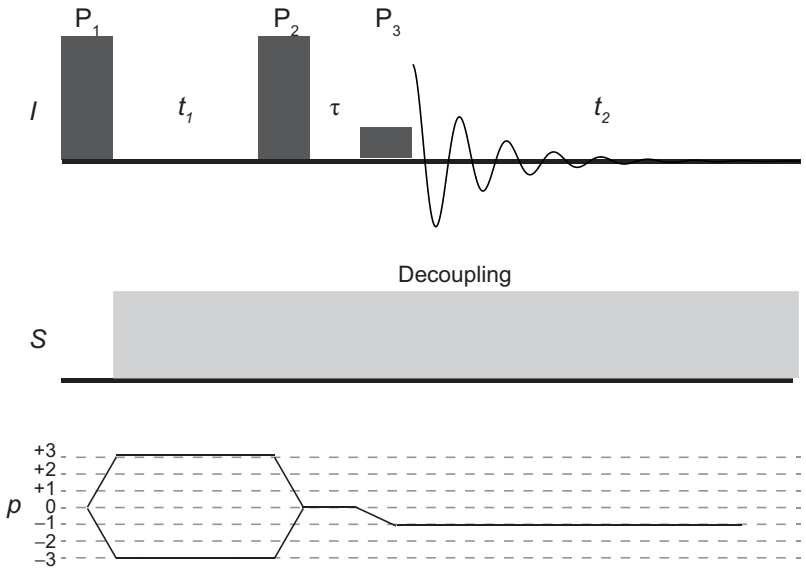

Figure 2.16: Schematic pulse sequence, coherence transfer pathway diagram and subsequent FID for a three-pulse triple-quantum *z*-filtered MQMAS NMR experiment for spin *I*. Three pulses are applied to the nucleus of interest; the first exciting triple-quantum coherences (P_1), before a second (P_2) converts this to longitudinal magnetisation. A third, soft, pulse (P_3) is then applied, selectively exciting the single-quantum CT. CW decoupling for spin *S* is applied if needed.

As discussed in Section 2.1.4.3, decoupling can often be employed to improve the quality of NMR spectra by removing the effects of dipolar coupling between neighbouring nuclei. In this thesis, heteronuclear CW decoupling of ^{1}H has been used extensively to obtain good ^{17}O 3QMAS NMR spectra. The pulse sequence for this applied to a *z*-filter experiment is indicated in Figure 2.16.

Acquisition of an MQMAS experiment records successive CT FIDs in t_2 at increments of the t_2 evolution. This builds up a series of FIDs correlating the CT in t_2 with the indirectly collected multiple-quantum transitions in t_1, with a double Fourier transform producing the two-dimensional spectrum. In such a spectrum signals appear as a set of 'ridges' that lie along an axis with gradient, R, termed the MQMAS ratio. This is determined by the ratio of the relative magnitude of the fourth-rank broadening of the two transitions, (*i.e.*, the A^4 terms which depend on *I* and the coherence order, *p*) *i.e.*,

$$R = A^4_{m_i} / A^4_{m_{\frac{1}{2}}}. \tag{2.45}$$

An isotropic spectrum, free from broadening can be obtained from a projection orthogonal to this axis, as shown schematically in Figure 2.17. In order to extract this spectrum more easily it is usual to apply a 'shearing' transformation which yields ridges parallel to δ_2, enabling the isotropic spectrum to be obtained from a projection onto δ_1. Cross-

sections along each taken parallel to δ_2 along each ridge yield MAS lineshapes for each individual species, from which δ_{iso}, η_Q and C_Q can be determined using analytical fitting. In this thesis the isotropic dimension of MQMAS spectra are referenced according to the convention outlined in reference 48. Further information can be obtained from the position of the centre-of-gravity of each lineshape, which gives δ_{iso} and P_Q. This can be particularly useful for more disordered materials where simple MAS cross sections cannot be easily extracted and fitted, but information on the average values of δ_{iso} and P_Q can still be obtained.[48,51–53]

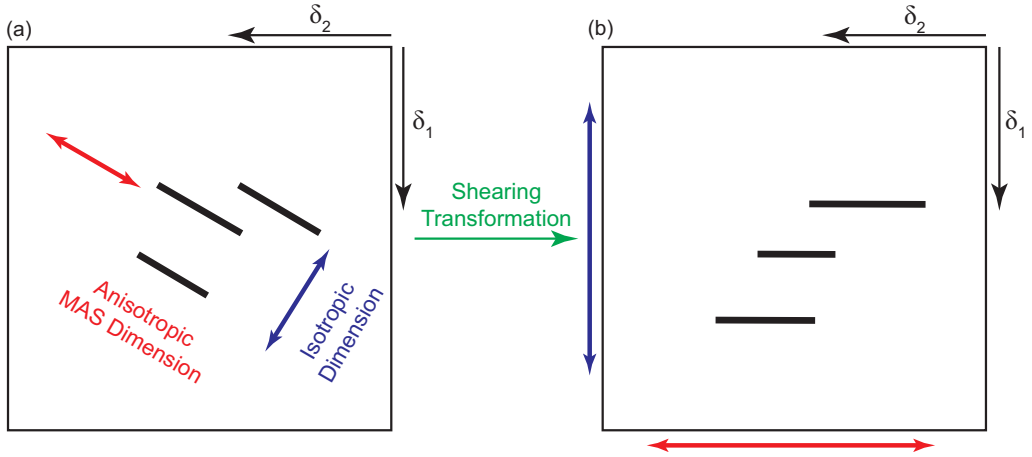

Figure 2.17: Schematic showing the effect of a shearing transformation for the triple-quantum MAS NMR spectrum of a spin 3/2 nucleus.

The MQMAS ratios, R are given in Table 2.1.

Nuclear Spin (I)	3Q	5Q	7Q	9Q
3/2	– 7/9	n/a	n/a	n/a
5/2	19/12	– 25/12	n/a	n/a
7/2	101/45	11/9	– 161/45	n/a
9/2	91/36	95/36	7/18	– 31/6

Table 2.1: MQMAS ratios, R, for half-integer spin nuclei.

2.2 X-ray Diffraction

PXRD is the ideal technique for rapid, routine analysis of crystalline material structure, providing an overview of the long-range structural order of the material. In this thesis, XRD has been used only for rapid, routine analysis, and while more extensive structural studies are possible (*i.e.* Rietveld), only this aspect will be concentrated on here. When combined with solid-state NMR spectroscopy which probes the local structural environment (as described in Section 2.1), a deeper understanding of the effects that various

hydrolytic treatments have on zeolite materials can be obtained. Due to the sample volumes used, the general crystallite size and the level of information needed, powder X-ray diffraction techniques were used exclusively in this thesis. Within this section the background and application of the diffraction-based techniques used are outlined.

2.2.1 Crystallography

Crystalline solids are comprised of a regular, periodic array of atoms. Crystallography is the practice used to determine the arrangement of these atoms, providing information in the form of a crystal structure. Within a crystalline material, the smallest volume repeating unit is referred to as the primitive unit cell. A unit cell is described by a three-dimensional parallelepiped, as shown in Figure 2.18, with sides of length a, b and c and angles α, β and γ. As the repeating unit of the material, the unit cell can be used to build up a picture of the overall long-range structure of the crystalline material.

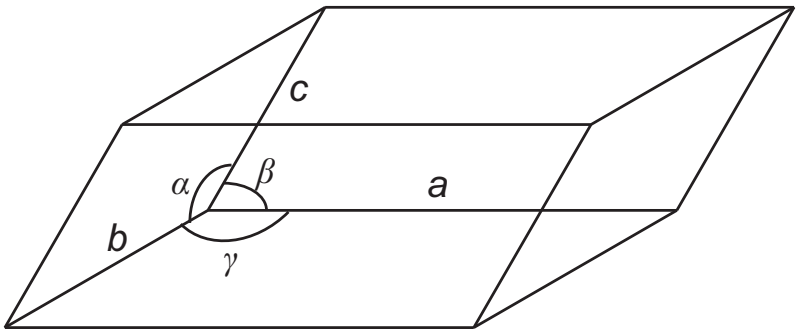

Figure 2.18: Schematic representation of an arbitrary unit cell with cell lengths a, b and c and angles α, β and γ.

To make up the structure atoms are then placed within the unit cell (with positions usually described using fractional coordinates and the relevant symmetry operations that are required to produce all symmetry related positions). Any crystal structure can be described as belonging to one of seven crystal systems and one of 230 symmetry-related space groups, which can be used to make symmetry-related distinctions between crystalline solids. The seven crystal systems and 230 space groups are often referred to using a short-hand Hermann Mauguin notation that describes some of their structural features. The most basic unit cell classification of crystal system, which details the unit cell parameters of the cell is shown in Table 2.2.

Crystal System	Shorthand	lengths	angles
Cubic	c	$a = b = c$	$\alpha = \beta = \gamma = 90°$
Rhombohedral	h	$a = b = c$	$\alpha = \beta = \gamma$
Hexagonal	h	$a = b \neq c$	$\alpha = \beta = 90°, \gamma = 120°$
Tetragonal	t	$a = b \neq c$	$\alpha = \beta = \gamma = 90°$
Orthorhombic	o	$a \neq b \neq c$	$\alpha = \beta = \gamma = 90°$
Monoclinic	m	$a \neq b \neq c$	$\alpha = \gamma = 90°, \beta =$ any
Triclinic	a	$a \neq b \neq c$	any

Table 2.2: Unit cell parameters of the seven different crystal systems.

Planes within a crystalline structure can be described using Miller Indices (*hkl*). The point at which a Miller plane *hkl* bisects the *abc* axes of the unit cell is given by *a*/*h*, *b*/*k* and *c*/*l*. A visual representation of selected miller planes for a cubic unit cell is given in Figure 2.19. As reflections related to Miller planes can be present in PXRD patterns, it can be useful to use Miller planes to describe structural features in materials of study.

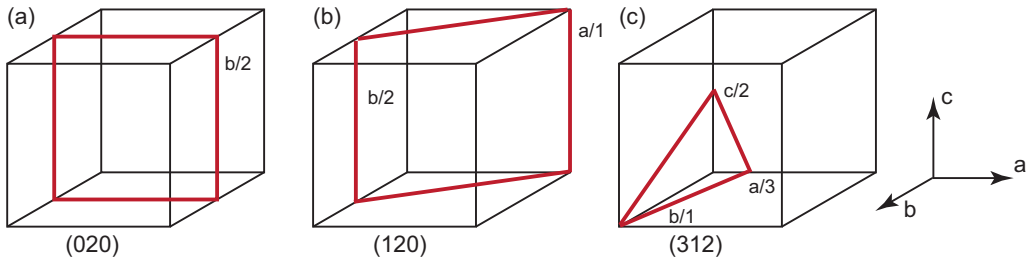

Figure 2.19: Schematic showing the (a) (020), (b) (120) and (c) (312) Miller planes within a cubic unit cell.

2.2.2 Bragg's Law

When a wave encounters an obstacle, it can be diffracted, This phenomenon forms basis of the diffraction experiment that was discovered in 1914 by Max von Laue, who observed the deflection of monochromatic waves of electromagnetic radiation when incident upon a material. When waves are diffracted, several diffraction pathways can be formed which may result in constructive or destructive interference. The conditions required for these constructive, superimposed wavefronts is encompassed by Bragg's law, which states that there is a relation between the wavelength of incident monochromatic radiation, λ and the scattering angle, θ, such that,

$$n\lambda = 2d\sin\theta. \tag{2.46}$$

Constructive interference is only observed for angles of incident radiation at specific distances, d between parallel lattice planes. A visual representation of the conditions required to satisfy Bragg's law is shown in Figure 2.20.

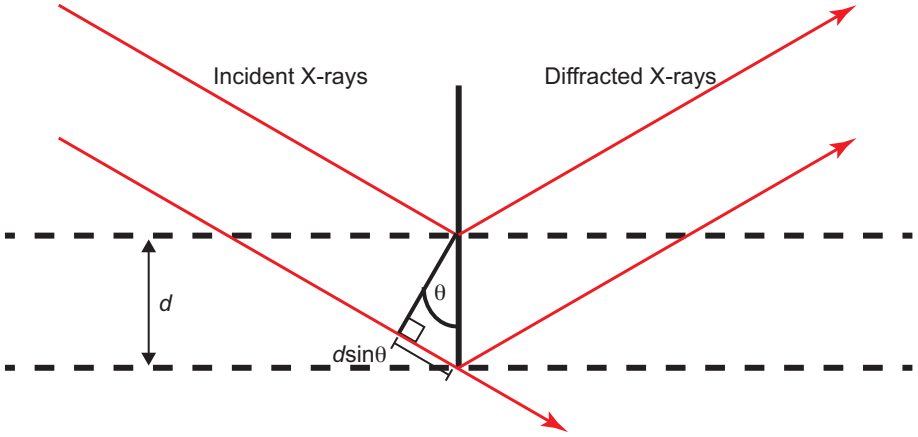

Figure 2.20: Schematic representation of the derivation of Bragg's law for the diffraction of X-rays by two parallel planes within a crystal lattice.

As a reflection present in a diffraction pattern will have been caused by diffraction of the incident X-ray beam, if the angle of diffraction is known, one should be able to assign the reflection to a Miller plane within the material. As an example, by obtaining d from Equation 2.46 for a cubic crystal system (all lengths = a), possible values of a, h, k and l can be derived:

$$\frac{1}{d^2} = \frac{h^2 + k^2 + l^2}{a^2}. \tag{2.47}$$

2.2.3 The Diffraction Experiment

As described above, the diffraction experiment relies on the production of coherent reflections of monochromatic radiation, through diffraction from a crystalline sample. The ideal case of this occurs when X-rays are diffracted from a single crystallite; a method referred to as single-crystal X-ray diffraction (see Figure 2.21).

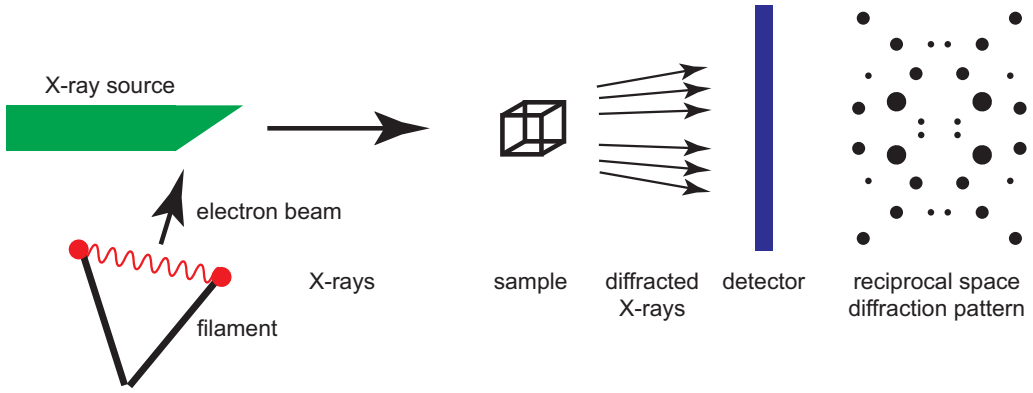

Figure 2.21: Schematic representation of the X-ray diffraction experiment for a single crystal.

Here, X-rays are generated by excitation of an X-ray source by bombardment with electrons by acceleration across a potential. Ejection of a core-shell electron in the X-ray source, causes de-excitation of an outer-shell electron and emission of a characteristic X-ray. Typical X-ray sources include copper and molybdenum, both of which often utilise the Kα_1 emission, which specifically relates to emission from the highest energy occupied L shell p-orbital n = 2 to fill a vacancy in the core K shell s-orbital n = 1. The X-ray passes through gratings to ensure it is monochromatic before striking the sample. Diffracted X-rays strike a detector at a diffraction angle, providing a reciprocal-space picture of the crystal structure (or lattice) of study. Single-crystal X-ray diffraction can provide full structural characterisation from the reciprocal lattice, including information such as the internuclear distances between atoms within the crystalline material. The method is however associated with some difficulties, such as the challenge of preparing crystals of an appropriate size, the mounting of the crystals in the diffractometer and the structure solution methods.

2.2.4 Powder X-ray Diffraction

A far more routine method of structural characterisation is powder X-ray diffraction. The experimental set-up is similar to that of single-crystal X-ray diffraction, although this time the sample is a poly-crystalline powder packed into a capillary tube or sample holder or equivalent (see Figure 2.22). Incident X-rays are then diffracted by interaction with the sample as before. However, as now there are multiple crystallites with varied orientations relative to the incident X-ray beam, the diffraction spots of the reciprocal lattice form a series of concentric circles, referred to as Debye-Scherrer cones owing to the orientational distribution of the diffracted signal over multiple crystallites. In order to capture this, a large flat-plate detector that captures all of the cone-shaped diffracted X-rays would be required. Practically however, the detection of X-rays is routinely achieved by moving

a smaller detector about an angle relative to the sample, which captures the X-rays to provide diffraction-angle specific information.

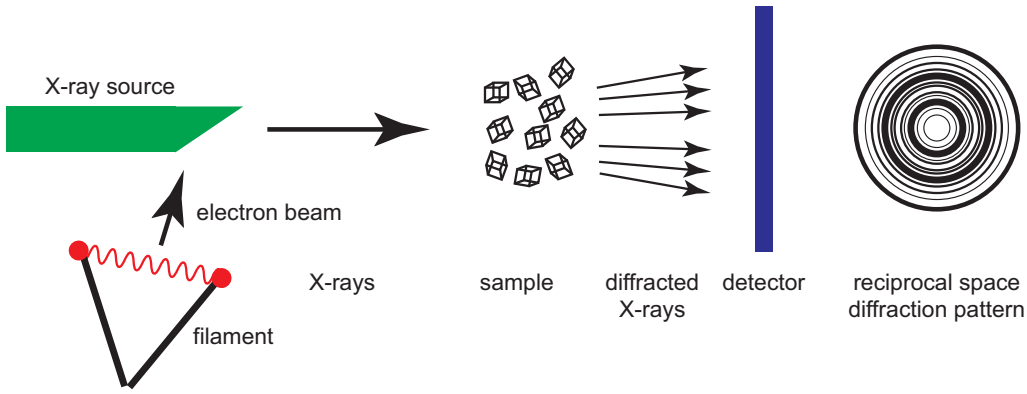

Figure 2.22: Schematic representation of the powder X-ray diffraction experiment.

The powder X-ray diffraction experiment produces an output of diffracted reflection intensity versus the diffraction angle, 2θ. As the diffraction pattern observed should be similar for like materials, the method is used for routine structure characterisation. Owing to the orientational averaging caused by the large number of crystallites in a powder sample, some information is lost compared to that of the single crystal case and it is difficult to determine exact atomic positions directly in a full structure solution. In some cases, structures can be solved from high quality powder diffraction patterns. This is commonly achieved using the Rietveld method which can determine atom positions using a structural model and a least squares approach that considers the peak positions, widths and intensities in the powder pattern.[54] Most often though, data may not be of acceptable quality or no related structural model is available and the unit cell parameters can only be obtained by examining the positions of *hkl* peaks across a whole diffraction pattern through Pawley or Le Bail methods.[55–57]

2.2.5 Le Bail Refinement

The Le Bail refinement method has been used in this thesis to examine a series of post-synthetically transformed zeolite materials where a zeolite with one topology is converted to one with another. In this transformation there is an obvious change in crystalline topology, and occasions where mixtures of two known crystalline materials are present. Disregarding peak intensities and using a structureless model as in a Le Bail fit, is well suited to confirming the identities of phases present in these post-synthetically transformed materials.

The Le Bail method can be used to check and refine the unit cell parameters of the different phases by applying a least-squares fitting approach of the powder pattern against a structureless model. The method essentially fits the best unit cell (*i.e.* peak positions), peak shape and other instrument factors, (such as the zero point error) but without taking into account the atomic positions, letting the peak intensities vary randomly. Therefore, this fitting method serves as a very convenient way of checking whether the right material has been formed.

2.3 Scanning Electron Microscopy

Optical microscopy produces an image for the viewer by focusing on the visible light refection off of a subject. In an analogous manner, electron microscopy produces an image by capturing the refection of electrons incident on a subject. Electron microscopy is used routinely in the characterisation of solid materials to provide information on particle size and morphology.

Practically, the sample under study is placed on a carbon black-coated specimen holder and set within an evacuated chamber. For most materials, the sample is 'sputtered' with a thin gold coating prior to sample acquisition, in order to reduce sample charging when in the incident electron beam. However, electron microscopy of zeolites is one of the few examples where this sputtering is not always needed as the materials are non-conductive and scarcely build up any charge.[58] Once the sample is mounted, a focused beam of electrons is generated by heating a thermionic filament, typically a W or a LaB_6 source. The formed electron beam is funnelled and accelerated by application of a voltage (typically 5 kV) through the chamber to the sample, where it is rastered over the surface. Upon interaction with the material, the incident electrons behave mainly in two different ways; becoming either backscattered or exchanging places with an electron in the material and knocking it out, referred to as secondary scattering. The scattered electrons then strike a detector, contributing to the image brightness, from which topographical information can be drawn.[58,59]

Backscattered electrons are produced by direct collision with atoms in the solid sample and are reflected back at an angle of the incident electron beam with minimal (<1 keV) energy loss. In this instance, electrons can collide with atoms up to several micrometres below the surface of the material. As such, back-scattered images produced in a modulated manner can be used to give depth-related information about the composition of certain materials.

Of most relevance to this project however, is the study of secondary scattered electrons. The liberation of secondary scattered electrons from a material is also an inelastic process. Secondary scattered electrons are typically of much lower energy, compared to backscattered electrons, ≈50 eV. Furthermore, as the probability of an electron escaping from a material is proportional to the depth at which it sits within it, secondary scattered electrons typically originate from the first few surface layers (< 1 μm sample depth) of a material only. Hence, proper detection gives an excellent indication of the external surface of sample crystallites. Furthermore, as the specific orientation of crystallites and fragments on crystallites will scatter secondary electrons at different angles, detection can provide a degree of contrast to the images, resulting in a textured appearance and depth gauge in images.[58,59]

To produce a focused, well-resolved and properly contrasted scanning electron microscopy (SEM) image, practical acquisition parameters, such as the acceleration voltage, working distance and spot size must be considered. Acceleration voltages between 5-10 kV are appropriate for routine imaging – at energies below this, the incident electron beam is typically incapable of liberating secondary-scattered electrons for imaging. The working distance of the measurements *i.e.*, the distance between the sample and the beam-focusing condenser lens, must be controlled to ensure the effective electron current at the sample does not result in a loss of focus of the sample or sample degradation. Typically, a working distance of 10 mm is used for routine imaging applications. The spot size is the effective size of the electron beam incident upon the sample. Control of the spot size is important as it is proportional to the current delivered to the sample, with larger spot sizes producing larger currents, resulting in more secondary electrons and bright, poorly contrasted images. The spot size is affected by the working distance and acceleration voltage but can also be controlled by variation of lens apertures. Variation of lens apertures affects the angle of incidence of the electron beam, affecting the area covered by the incident electron beam. Typical spot sizes used for imaging are 15-20 nm.[58–61] A schematic of a scanning electron microscope is shown in Figure 2.23.

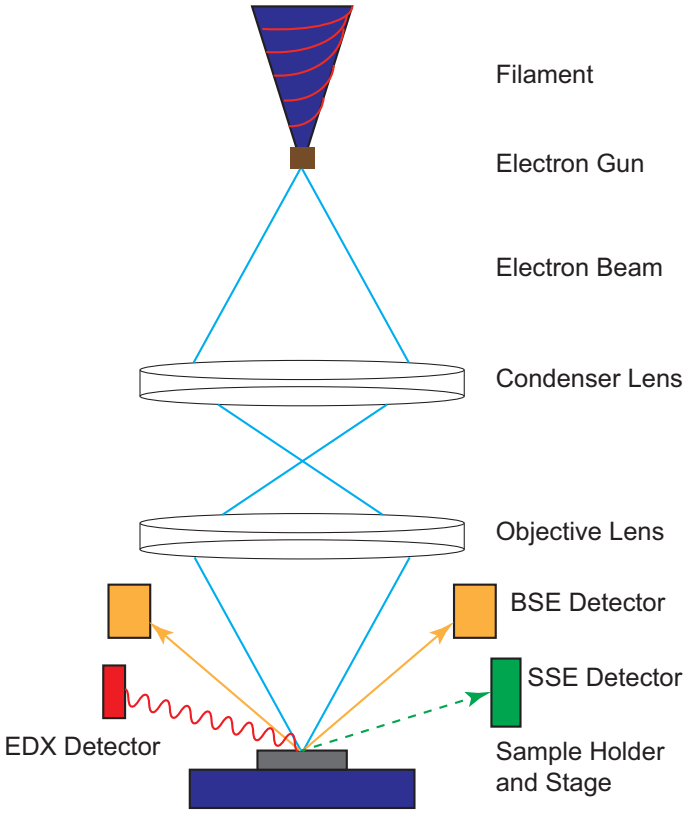

Figure 2.23: Schematic of a conventional SEM-EDX instrument. Abbreviations: BSE (Backscattered Electron), SSE (Secondary Scattered Electron).

2.4 Energy Dispersive X-ray Spectroscopy

Energy Dispersive X-ray Spectroscopy (EDX) is a technique related to SEM, that detects the emitted X-rays from a sample following the application of an incident electron beam. The nature of the X-rays emitted from an irradiated sample depends on its elemental composition. EDX spectroscopy is often carried out in tandem with SEM imaging, through the use of coupled EDX detectors fitted to the microscope.

Within EDX spectroscopy, the goal is to sufficiently bombard the sample with electrons such that core-shell electrons originating from atoms within the sample are emitted. When this happens, outer-shell electrons from the same atom de-excite in order to fill the vacancy, restore the core shell electronic configuration. Upon de-excitation of the outer-shell electrons, characteristic X-rays are emitted that depend on the element and transition, enabling the identification of elements within the sample. The majority of the time, the wavelengths of X-rays detected in EDX experiments correspond to the $K\alpha_1$ transition, similar to those in X-ray diffraction (see Section 2.2).

Ejection of a core-shell electron requires significantly enhanced penetration into the sample, compared to SEM imaging. Consequently, far higher acceleration voltages are used, typically 30-40 kV. Further alterations to the acquisition parameters, namely an increased working distance to ≈20 mm and an increased spot size help to maximize current transfer to the sample and increase X-ray evolution.

Although accurate at determining specific wavelengths of X-rays emitted from the sample and providing a good idea of the elemental composition of crystallites, the accuracy of EDX results can be hampered by the nature and the design of the experiments. Firstly, the depth of penetration of electrons into the sample has a strong influence on the X-rays released and so only those atoms on the surface ($< 3\ \mu$m sample depth) of materials typically emit electrons, providing a surface-coverage-skewed picture of the elemental composition of different crystallites. Further, the number of crystallite points selected for EDX analysis can also skew results and multiple points (typically > 30) should be selected to get a reliable elemental composition of the material.[61]

2.5 Thermogravimetric Analysis

Thermogravimetric analysis (TGA) is a characterisation technique, used to provide information about the thermal stability of materials. Practically, a small amount of sample (3-5 mg) is placed in an inert crucible, typically aluminium oxide, and set on a microbalance within a sealed chamber. A carrier gas, often compressed air or nitrogen, flows through the chamberas the chamber is gradually heated. During heating, the microbalance records the mass of the sample, which can be used indirectly to provide information on processes, such as decomposition or the loss of physisorbed / chemisorbed species.

In zeolites, the main element of mass loss observed in TGA traces arises from the loss of the SDA or physisorbed water from framework pores, channels and from the solvation spheres of extra-framework cations. The loss of organic material and water typically happens up to temperatures of 300 °C, although the latter is a reversible process as frameworks rehydrate upon exposure to atmospheric moisture.[62] In this thesis, where the effect of reagent water is important, it is useful to know the typical hydration state (or % hydration level) of zeolites and the structural stability of materials so that dehydrated frameworks can be obtained.

In cases where structural decomposition does occur for thermal treatment of zeolites, it is not often accompanied by mass loss in TGA traces. This is attributed to the non-volatile nature of silicon and aluminium and their respective solid oxides, which are formed at high temperatures. This is in contrast to other materials, *e.g.*, MOFs, whose organic linkers from framework decomposition are volatile and oxidise to $CO_{x_{(g)}}$ species. Hence, decomposition processes in zeolites are mainly characterised by exothermic / endothermic processes with no significant mass change. These heat flows can be characterised by some TGA apparatus, which have integrated differential thermal analysis (DTA) units.

2.6 Density Functional Theory

The assignment of solid-state NMR spectra, and therefore the extraction of detailed structural information, can pose a significant challenge. In recent years there has been growing use of computational approaches alongside NMR experiments, to help interpret and assign NMR spectra. Many of these calculations are carried out using Density functional theory (DFT) to determine the electronic ground state of molecules and systems, by approximating the respective time-independent, non-relativistic Schrödinger equation. As the equation can only be fully solved for single-electron systems, which are of scarce interest, methodology has been developed to simplify approximations without any considerable loss of accuracy.[63–65]

2.6.1 Quantum Mechanical Background

The time-independent, non-relativistic Schrödinger equation is,

$$\hat{H}\Psi = E\Psi, \tag{2.48}$$

where $\hat{H}$ is the Hamiltonian operator, E is the energy of the system and Ψ is the ground state wavefunction. The Hamiltonian operator for the system consists of terms related to kinetic (T) and potential (electrostatic interaction) (V) energy, for both nuclei (n) and electrons (e);

$$\hat{\mathrm{H}} = \hat{T}_{\mathrm{ee}} + \hat{T}_{\mathrm{nn}} + \hat{V}_{\mathrm{ee}} + \hat{V}_{\mathrm{nn}} + \hat{V}_{\mathrm{ne}}. \tag{2.49}$$

The Hamiltonian can be simplified using the Born-Oppenheimer approximation, which allows the separation of the nuclear and electronic terms (with nuclei effectively assumed to be static on the electronic timescale).[66] However, the above equation assumes electrons behave as classical point charges, which is not the case and electronic exchange (E_X), and electronic correlation (C_X) interaction energies must be considered. E_X arises from

the Pauli exclusion principle, where no two electrons can occupy the same quantum state, altering electronic energy of the system.

C_X describes the distribution of all electrons in a system simultaneously, which are found to be partially localised. For simplicity, these two terms are often combined and referred to as the exchange-correlation (E_{XC}). This results in the electronic Hamiltonian, $\hat{H}_{\text{elec}}$ given by:

$$\hat{H}_{\text{elec}} = \hat{T}_{\text{ee}} + \hat{V}_{\text{ee}} + E_{XC}. \tag{2.50}$$

This simplifies the dependence of the Schrödinger equation to be approximated to electrons only as,

$$\hat{H}_{\text{elec}}\Psi_{\text{elec}} = E_{\text{elec}}\Psi_{\text{elec}}. \tag{2.51}$$

2.6.2 Density Functional Theory Approximations

The approach of DFT to solving the Schrödinger equation for systems follows calculation of the electronic densities of individual constituent components. Whilst most components of the equation can be calculated accurately, it is difficult to determine exactly the interaction between electrons, referred to as the 'exchange correlation'. In DFT this is overcome by the introduction of assumptions. A commonly used assumption is the Local Density Assumption (LDA), which assumes that for a small unit of space, the electron density is constant and equal to that of a uniform gas. In practice, this works well for solid lattice systems, however in some instances more complex approximations, such as GGA (generalised gradient approximation), which associates a gradient with the electronic densities can be employed at an additional computational cost.[13]

2.6.3 Application to Study of Periodic Lattice Materials

Computational modelling using DFT is of great use to the materials chemist, particularly when periodic systems, such as zeolites are of interest. The nature of the DFT approach to calculation of energies using electronic density configurations mean that large savings in experimental time can be achieved by simplifying the periodic system to a repeating unit, representative of the structure as a whole. This follows Bloch's Theorem that the potential, V at position $\mathbf{r}$ is the same as it is at position $\mathbf{r}$, displaced by lattice vector, $\mathbf{L}$,[16]

$$V(\mathbf{r}) = V(\mathbf{r}+\mathbf{L}). \tag{2.52}$$

The unit typically used for zeolite materials is based on the crystallographic unit cell for that topology. This information is conveniently readily available as symmetry relations and atomic positions in a crystallographic information file (CIF) obtained from diffraction-based characterisation experiments. The IZA database hosts an extensive repository of these files for zeolite topologies and any compositional variants.[67]

Since electron density is periodic in most solids, so too is the magnitude of the wavefunction being described. Consequently, sampling points along the wavefunction are needed for accurate characterisation. This is achieved by translation of the wavefunction to a reciprocal lattice and a value for spacing between sampling points, referred to as *k*-points, selected. Selection of sufficient *k*-points is critical for an accurate description of the wavefunction, with too few likely to result in inaccurate results and too many an unnecessary computational expense.[65] The periodic nature of the electron density often results in the use of plane waves as a basis set for the expansion of the wavefunction, with the computational accuracy then controlled by the number of planewaves (*i.e.*, the energy cut off) used.
Of interest to this project is the application of DFT calculations to model zeolite materials to from idealised framework structures and from this, calculate their idealised NMR parameters. Employing computation in this project is of particular value as the systems dealt with often possess a degree of disorder and/or contain complex local structures with many features that result in complex and/or overlapped NMR spectra. Hence, using computation to predict the expected structural features and their associated NMR parameters for systems of interest can greatly help with understanding the experimentally obtained spectra. This, in turn, increases our understanding of the processes taking place on an atomic level. To predict NMR parameters for some zeolites in this thesis, the Cambridge Serial Total Energy Package (CASTEP) DFT code was used.[68–72]

2.6.3.1 Geometry Optimisation

Optimisation of the starting structure is an important step for the accurate determination of NMR parameters. To perform this optimisation, an initial model often, but not always, obtained from diffraction of a similar or related material is modified. For this work, this may involve the substitution of some silicon atoms in a siliceous unit cell for a heteroatom (Al, Ge, B, *etc.*). In instances where the substitution is not charge neutral, a charge-balancing cation, such as a Brønsted proton or other metal cation also needs to be included in the unit cell and its position in the framework optimized. Other molecules, like water can also be added. This initial model is then modified by reducing the DFT calculated

energy of the system by minimising the forces on the atoms. However, the DFT geometry optimisation takes place under vacuum at absolute zero, comparisons to fully hydrated systems or deductions about the effect of water inclusion must be made carefully.

2.6.3.2 Calculation of NMR Parameters

Following geometry optimisation, the NMR parameters for the specific atomic configuration can be calculated. For chemical shifts, the calculated shieldings must be referenced to compare with experimental measurements. This is usually achieved using a reference shielding, σ_{ref}, that produces a computed chemical shift, $\sigma_{\text{iso}}^{\text{calc}}$ by,

$$\sigma_{\text{ref}} = \sigma_{\text{iso}}^{\text{calc}} + \delta_{\text{iso}}^{\text{exp}}. \tag{2.53}$$

The reference shielding is obtained by matching the experimental and calculated data from one or more known reference compounds.

2.7 Molecular Dynamics

Molecular dynamics (MD) is a method for simulating the displacement and interaction of atomic and molecular bodies within a system, according to Newtonian laws of motion. Specifically, the forces acting on individual system components are calculated at time intervals and then allowed to evolve for a time, Δt, before the same force calculations are performed at the next interval. From this, MD aims to provide a snapshot of the movement of atoms and molecules within a system on short timescales, typically on the order of picoseconds (10^{-12} s), giving an idea of the theoretical dynamic evolution of the system over time.

The information provided by MD helps to give a greater understanding of active chemical systems and can show how processes, such as molecule motion, formation of transition state intermediates and bond cleavage take place.

In this thesis MD has been used (in collaboration) specifically to explore the cleavage of silicate and aluminosilicate bonds in zeolite frameworks, including the formation of the active transition state. To do this, a sub-set of molecular dynamics, *ab-initio* molecular dynamics (AIMD) has been employed. Classical MD techniques consider only a single potential energy surface, typically the system ground state, to calculate the potential at each interval. Selection of the ground state follows the implementation of the Born- Op-

penheimer approximation. In some instances where excited states are of interest, as is the case here, consideration of the ground state only is insufficient and incorporation of electronic effects is required to obtain a more complete picture of system behaviour. AIMD incorporates the system electronic behaviour through DFT calculation of the varying electronic degrees of freedom. Unsurprisingly, this consideration requires considerably more computation power meaning AIMD studies must be well-designed and tend to be on the shorter side (5-15 ps). The application to AIMD in this specific project has significant advantages over the classical empirical MD methodology as DFT characterises well the energies associated with the changes to electronic state that occur when covalent bonds are broken.[73]

2.8 References

[1] S. E. Ashbrook, Z. H. Davis, R. E. Morris and C. M. Rice, *Chem. Sci.*, 2021, **12**, 5016–5036.

[2] B. Reif, S. E. Ashbrook, L. Emsley and M. Hong, *Nat. Rev. Methods Prim.*, 2021, **1**, 2.

[3] M. Xu, K. D. M. Harris, J. M. Thomas and D. E. W. Vaughan, *ChemPhysChem*, 2007, **8**, 1311–1313.

[4] M. Hunger, *Prog. Nucl. Magn. Reson. Spectrosc.*, 2008, **53**, 105–127.

[5] T. Blasco, *Chem. Soc. Rev.*, 2010, **39**, 4685–4702.

[6] O. Pecher, A. Vyalikh and C. P. Grey, *AIP Conf. Proc.*, 2016, **1765**, 020011.

[7] K. D. M. Harris, C. E. Hughes and P. A. Williams, *Solid State Nucl. Magn. Reson.*, 2015, **65**, 107–113.

[8] K. D. M. Harris, *Appl. Petrochemical Res.*, 2016, **6**, 295–306.

[9] K. D. M. Harris, C. E. Hughes, P. A. Williams and G. R. Edwards-Gau, *Acta Crystallogr. Sect. C Struct. Chem.*, 2017, **73**, 137–148.

[10] M. Haouas, *Materials (Basel).*, 2018, **11**, 1–19.

[11] M. J. Duer, *Solid-state NMR Spectroscopy*, Blackwell Publishing, Oxford, 1st edn., 2004.

[12] D. C. Apperley, R. K. Harris and P. Hodgkinson, *Solid-State NMR: Basic Principles and Practice*, Momentum Press, New York, 2012.

[13] S. E. Ashbrook, D. M. Dawson and J. M. Griffin, in *Local Struct. Characterisation*, ed. D. O'Hare and R. I. Walton, John Wiley & Sons, Ltd, 1st edn., 2014, pp. 1–88.

[14] P. Hore, *Nuclear magnetic Resonance*, Oxford University Press, Oxford, 1995.

[15] R. F. Moran, D. M. Dawson and S. E. Ashbrook, *Int. Rev. Phys. Chem.*, 2017, **36**, 39–115.

[16] F. Bloch, *Ph.D. thesis*, Universität Leipzig, 1927.

[17] F. Bloch, *Phys. Rev.*, 1946, **70**, 460–474.

[18] J.-B.-J. Fourier, *Theorie Analytique De La Chaleur*, Didot, 1822.

[19] U. Haeberlen, *Advances in Magnetic Resonance*, Academic Press, New York, 1976.

[20] O. L. Malkina and V. G. Malkin, *Angew. Chem. Int. Ed.*, 2003, **42**, 4335–4338.

[21] J. R. Yates, *Magon. Reson. Chem.*, 2010, **48**, S23–S31.

[22] D. Freude, in *Encycl. Anal. Chem.*, ed. R. A. Meyers, Wiley, Chichester, 2000, pp. 12188–12224.

[23] E. Lippmaa, A. Samoson and M. Magi, *J. Am. Chem. Soc.*, 1986, **108**, 1730–1735.

[24] B. V. Padlyak, N. A. Sergeev, M. Olszewski and P. Stępień, *Nukleonika*, 2015, **60**, 417–421.

[25] E. R. Andrew, A. Bradbury and R. G. Eades, *Nature*, 1958, **183**, 1659.

[26] E. R. Andrew, A. Bradbury and R. G. Eades, *Nature*, 1959, **183**, 1802–1803.

[27] I. J. Lowe, *Phys. Rev. Lett.*, 1959, **2**, 285–287.

[28] E. L. Hahn, *Phys. Rev.*, 1950, **80**, 580–594.

[29] A. E. Bennett, C. M. Rienstra, M. Auger, K. V. Lakshmi and R. G. Griffin, *J. Chem. Phys.*, 1995, **103**, 6951–6958.

[30] B. M. Fung, A. K. Khitrin and K. Ermolaev, *J. Magn. Reson.*, 2000, **142**, 97–101.

[31] *Topics in Current Chemistry: Solid State NMR*, ed. C. C. J. Chan, Springer Berlin Heidelberg, Berlin, Heidelberg, 2008, vol. 273.

[32] I. Scholz, P. Hodgkinson, B. H. Meier and M. Ernst, *J. Chem. Phys.*, 2009, **130**, year.

[33] A. Pines, M. G. Gibby and J. S. Waugh, *J. Chem. Phys.*, 1972, **56**, 1776–1777.

[34] S. R. Hartmann and E. L. Hahn, *Phys. Rev.*, 1962, **128**, 2042–2053.

[35] F. M. Lurie and C. P. Slichter, *Phys. Rev. Lett.*, 1963, **10**, 403–405.

[36] X. Liu, U. Ravon and A. Tuel, *Chem. Mater.*, 2011, **23**, 5052–5057.

[37] X. Liu, U. Ravon and A. Tuel, *Angew. Chemie - Int. Ed.*, 2011, **50**, 5900–5903.

[38] X. Liu, U. Ravon, F. Bosselet, G. Bergeret and A. Tuel, *Chem. Mater.*, 2012, **24**, 3016–3022.

[39] H. Koller, R. F. Lobo, S. L. Burkett and M. E. Davis, *J. Phys. Chem.*, 1995, **99**, 12588–12596.

[40] H. Koller and M. Weiß, in *Solid State NMR Porous Mater.*, Springer, 2012, vol. 306, pp. 189–228.

[41] G. Brunklaus, H. Koller and S. I. Zones, *Angew. Chemie Int. Ed.*, 2016, **55**, 14459–14463.

[42] C. J. Heard, L. Grajciar, F. Uhlík, M. Shamzhy, M. Opanasenko, J. Čejka and P. Nachtigall, *Adv. Mater.*, 2020, **32**, 2003264.

[43] A. Samoson and A. Pines, *Rev. Sci. Instrum.*, 1989, **60**, 3239–3241.

[44] B. F. Chmelka, K. T. Mueller, A. Pines, J. Stebbins, Y. Wu and J. W. Zwanziger, *Nature*, 1989, **339**, 42–43.

[45] L. Frydman and J. S. Harwood, *J. Am. Chem. Soc.*, 1995, **117**, 5367–5368.

[46] A. Medek, J. S. Harwood and L. Frydman, *J. Am. Chem. Soc.*, 1995, **117**, 12779–12787.

[47] S. P. Brown and S. Wimperis, *J. Magn. Reson.*, 1997, **61**, 42–61.

[48] K. J. Pike, R. P. Malde, S. E. Ashbrook, J. McManus and S. Wimperis, *Solid State Nucl. Magn. Reson.*, 2000, **16**, 203–215.

[49] J.-p. Amoureux, C. Fernandez and L. Frydman, *Chem. Phys. Lett.*, 1996, **4**, 347–355.

[50] J.-p. Amoureux, C. Fernandez and S. Steuernagel, *J. Magn. Reson. Ser. A*, 1996, **118**, 116–118.

[51] S. Wang, Z. Xu, J. Baltisberger, L. Bull, J. Stebbins and A. Pines, *Solid State Nucl. Magn. Reson.*, 1997, **8**, 1–16.

[52] S. E. Ashbrook and S. Wimperis, *Prog. Nucl. Magn. Reson. Spectrosc.*, 2004, **45**, 53–108.

[53] S. E. Ashbrook, A. J. Berry, D. J. Frost, A. Gregorovic, C. J. Pickard, J. E. Readman and S. Wimperis, *J. Am. Chem. Soc.*, 2007, **129**, 13213–13224.

[54] H. M. Rietveld, *J. Appl. Cryst.*, 1969, **2**, 65–71.

[55] G. S. Pawley, *J. Appl. Cryst*, 1981, **14**, 357–361.

[56] A. Le Bail, H. Duroy and J. Fourquet, *Mat. Res. Bull.*, 1988, **23**, 447–452.

[57] A. Le Bail, *Powder Diffr.*, 2005, **20**, 316–326.

[58] *Zeolite Chemistry and Catalysis*, ed. A. W. Chester and E. Derouane, Springer Netherlands, Dordrecht, 1st edn., 2009.

[59] J. Čejka, R. E. Morris and P. Nachtigall, *Zeolites in Catalysis*, Royal Society of Chemistry, Cambridge, 1st edn., 2017.

[60] L. Reimer, *Scanning Electron Microscopy*, Springer Berlin Heidelberg, Berlin, Heidelberg, 2nd edn., 1998, vol. 45.

[61] J. I. Goldstein, D. E. Newbury, J. R. Michael, N. W. M. Ritchie, J. H. J. Scott and D. C. Joy, in *Scanning Electron Microsc. X-Ray Microanal.*, Springer New York, New York, NY, 4th edn., 2018.

[62] P. A. Wright, *Microporous Framework Solids*, Royal Society of Chemistry, Cambridge, 1st edn., 2008.

[63] W. Koch and M. C. Holthausen, *A Chemist's Guide to Density Functional Theory*, Wiley-VCH, Weinheim, 4th edn., 2007.

[64] C. Bonhomme, C. Gervais, F. Babonneau, C. Coelho, F. Pourpoint, T. Azaïs, S. E. Ashbrook, J. M. Griffin, J. R. Yates, F. Mauri and C. J. Pickard, *Chem. Rev.*, 2012, **112**, 5733–5779.

[65] S. E. Ashbrook and D. McKay, *Chem. Commun.*, 2016, **52**, 7186–7204.

[66] M. Born and R. Oppenheimer, *Ann. Phys.*, 1927, **389**, 457–484.

[67] C. Baerlocher and L. B. McCusker, *Database of Zeolite Structures*, http://www.iza-structure.org/databases/.

[68] C. J. Pickard and F. Mauri, *Phys. Rev. B - Condens. Matter Mater. Phys.*, 2001, **63**, 2451011–2451013.

[69] M. D. Segall, P. J. D. Lindan, M. J. Probert, C. J. Pickard, P. J. Hasnip, S. J. Clark and M. C. Payne, *J. Phys. Condens. Matter*, 2002, **14**, 2717–2744.

[70] M. Profeta, F. Mauri and C. J. Pickard, *J. Am. Chem. Soc.*, 2003, **125**, 541–548.

[71] S. J. Clark, M. D. Segall, C. J. Pickard, P. J. Hasnip, M. I. Probert, K. Refson and M. C. Payne, *Zeitschrift fur Krist.*, 2005, **220**, 567–570.

[72] J. R. Yates, C. J. Pickard and F. Mauri, *Phys. Rev. B*, 2007, **76**, 024401.

[73] D. C. Rapaport, *The Art of Molecular Dynamics Simulation*, Cambridge University Press, 2nd edn., 2004.

Chapter 3

Materials & Methods

This chapter details the synthetic protocols followed and details of analytical methodology used in this thesis. A break-down of the information detailed in this chapter and its relation to any specific work is given at the start of each section.

A breakdown of the structural / chemical properties of ^{17}O isotopically enriched samples discussed in this thesis is given in the Appendix B.

3.1 Acknowledgements

The work performed in this chapter would not have been possible without the provision of funding or the collaborative assistance of colleagues.

Dr Daniel Dawson is thanked for his maintenance of the University of St Andrews solid-state NMR spectroscopy facility and assistance with NMR measurements at all fields detailed in this thesis. Dr Trent Franks and Dr Dinu Iuga are thanked for maintenance of the UK High-Field Solid-state NMR facility at the University of Warwick as well as for the running of samples during remote acquisition time. Dr Yuri Andreev is thanked for the provision and maintenance of the powder X-ray diffractometers at the University of St Andrews. Dr Tomas Lebl and Dr Siobhan Smith are thanked for the provision of the University of St Andrews liquid-state NMR service. Ms Sylvia Williamson and Dr Gavin Peters are acknowledged for the maintenance of the University of St Andrews TGA apparatus and Dr Simon Vornholt is thanked for his assistance in performing the TGA measurements. Dr Aaron Naden, Dr David Miller and Mr Ross Blackley are thanked for their maintenance of the university of St Andrews Electron Microscopy facility. Ms Ruxandra Chitac, Dr Magdelena Lozinska and Professor Paul Wright of the University of St Andrews are thanked for the use of and assistance with operation of their rotary oven.

Funding for the provision of the UK High-Field Solid-state NMR facility at the University of Warwick from EPSRC, BBSRC, Advantage West Midlands and the European Regional Development Fund is acknowledged. Funding for the provision of the Scottish High-Field Solid-state NMR facility at the University of Edinburgh from EPSRC is acknowledged.

3.2 SDA Syntheses

Synthetic details and liquid-state NMR spectra (^{1}H and ^{13}C) are provided.

3.2.1 (6R,10S)-6,10-dimethyl-5-azoniaspiro[4.5]decane hydroxide (DMAD-OH)

Synthesis of DMAD-OH (Figure 3.1) was adapted from procedures in Wheatley *et al.* and Marino *et al.*.[1,2]

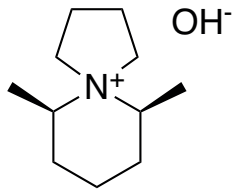

Figure 3.1: Structure of (6R,10S)-6,10-dimethyl-5-azoniaspiro[4.5]decane hydroxide.

The corresponding bromide salt, (6R,10S)-6,10-dimethyl-5-azoniaspiro[4.5]decane bromide was prepared by adding 1,4-dibromobutane (125.95 g, 0.5 mol) dropwise to a mixture of potassium carbonate (82.93 g, 0.6 mol) and 2,6-dimethylpiperidine (56.06 g, 0.5 mol) in acetonitrile (500 cm^3) at room temperature. Following addition, the mixture was heated to 95 °C and stirred vigorously for 20 hours. The solution was cooled to room temperature. The majority of the acetonitrile was removed under reduced pressure leaving a mixture of product, product solution and potassium carbonate. The mixture was dispersed in ethanol (100 cm^3) and the potassium carbonate removed by filtration. The solution was condensed and the minimum volume of diethyl-ether added to precipitate the bromide salt.

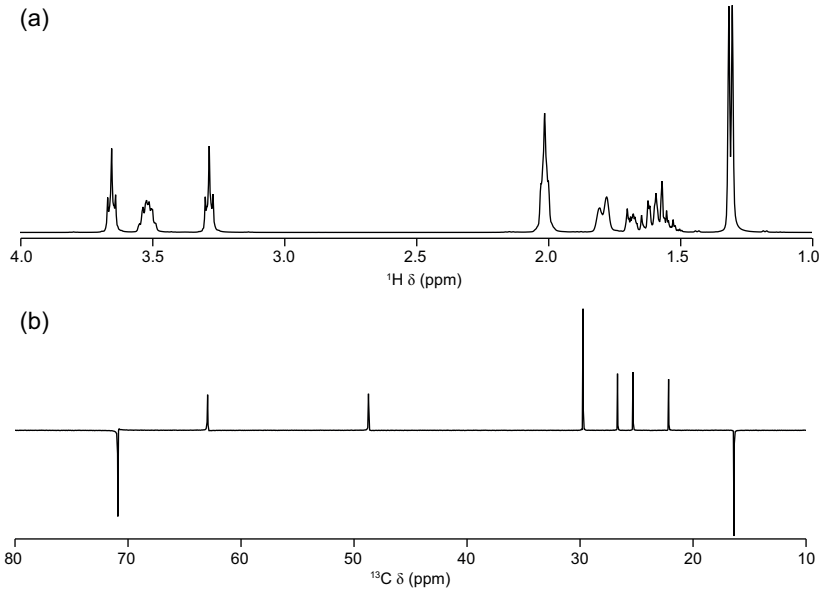

Figure 3.2: 9.4 T solution-state NMR spectra of (6R,10S)-6,10-dimethyl-5-azoniaspiro[4.5]decane hydroxide synthesised in this work. (a) ^{1}H and (b) ^{13}C NMR spectrum.

The presence of the bromide salt was confirmed by ^{1}H and ^{13}C solution-sate NMR spectroscopy (Figure 3.2)

^{1}H NMR (300 MHz, D_2O): δ (ppm) = 3.65 (t, 2 H), 3.52 (td, 4 H), 3.26 (t, 4 H), 2.08 (t, 2 H), 1.78 (d, 2 H), 1.65 (m, 1 H), 1.56 (m, 1 H), 1.34 (d, 6 H).
^{1}H NMR (300 MHz, D_2O): δ (ppm) = 70.3, 63.5, 49.1, 30.4, 27.0, 25.8, 22.0, 17.5.

The bromide salt (74.4 g, 300 mmol) was exchanged to the hydroxide form by stirring in distilled water (300 cm^3) and Ambserb 900-OH ion-exchange resin (60 g) for 24 hours. The solution was filtered and the process repeated once, forming a halide-free solution (see Section 3.2.3).

3.2.2 N,N,N-Trimethyl-1-adamantylammonium hydroxide (TMAA-OH)

Synthesis of TMAA-OH (Figure 3.3) was adapted from procedures in Zones, Hu *et al.* and Kioke *et al.*.[3–5]

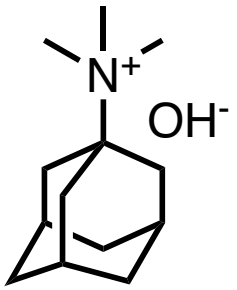

Figure 3.3: Structure of N,N,N-Trimethyl-1-adamantylammonium hydroxide.

The corresponding iodide salt, N,N,N-Trimethyl-1-adamantylammonium iodide was prepared by dissolving 1-adamantylamine (20.0 g, 132 mmol) in chloroform (120 mL) at room temperature. Tributylamine (58 g, 312 mmol, 74.4 cm^3) was added and the solution stirred for 15 minutes and cooled over ice. The solution is wrapped in tin foil before methyl iodide (58.4 g, 400 mmol, 25 cm^3) was added dropwise to the ice-cooled solution. The solution was kept wrapped in tin foil to exclude light and stirred at 35 °C for 7 days. The mixture was cooled and filtered before stirring with diethyl-ether (100 cm^3) for 30 minutes. The precipitated solid was filtered and washed with diethyl ether.

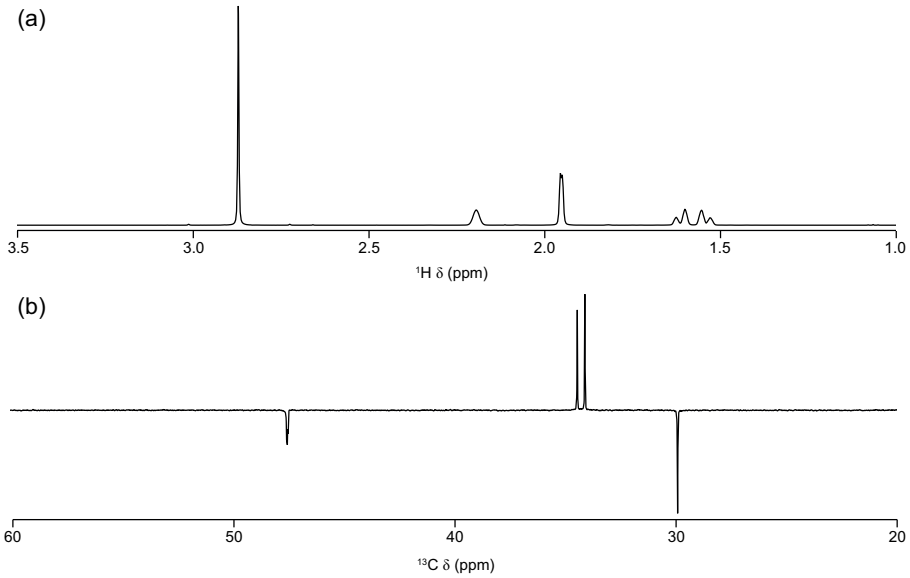

Figure 3.4: 11.8 T solution-state NMR spectra of N,N,N-Trimethyl-1-adamantylammonium hydroxide synthesised in this work. (a) ^1H and (b) ^{13}C NMR spectrum.

The presence of the iodide salt was confirmed by ^1H and ^{13}C solution-state NMR spectroscopy (Figure 3.4)

^{1}H NMR (300 MHz, D_2O): δ (ppm) = 2.85 (s, 9 H), 2.20 (s, 6 H), 1.96 (d, 3 H), 1.58 (dd, 6 H).
^{1}H NMR (300 MHz, D_2O): δ (ppm) = 57.4, 57.3, 34.6, 33.9, 29.9.

The iodide salt (25 g, 70 mmol) was exchanged to the hydroxide form by stirring in distilled water (100 cm^3) and Ambserb 900-OH ion-exchange resin (25 g) for 24 hours. The solution was filtered and the process repeated twice, forming a halide-free solution (see Section 3.2.3).

3.2.3 SDA Quality Control

Completeness of SDA ion-exchange from the halide salt to the desired hydroxide form was confirmed through silver nitrate test. SDA solution (0.25 cm^3) was acidified in HCl solution (1.0 M, 2 cm^3), before a few drops of silver nitrate solution (0.05 M) were added. If no 'silver mirror' precipitate was observed, the solution was free of halide and the exchange was complete.
[6]

The concentration of SDA hydroxide salt within aqueous solution was determined through titration of the solution against HCl (0.01 M).

3.3 Zeolite Syntheses

3.3.1 High-Ge Ge-UTL

High germanium content Ge-**UTL** was prepared using methods adapted from the literature.[6–9]

GeO_2 (19.60 g, 188 mmol) was added to a solution of DMAD-OH (0.625 M, 240 cm^3, 150 mmol) and mechanically stirred for 15 minutes, before SiO_2 (Cab-O-Sil M5) (17.98 g, 300 mmol) was added portionwise under stirring. The mixture was stirred under high shear for 30 minutes, forming a reaction gel of composition:

$$0.5Ge : 0.4DMAD-OH : 0.8SiO_2 : 35H_2O. \tag{3.1}$$

The gel was sealed in Teflon-lined steel autoclaves and heated to 180 °C for 7 days, before quenching, cooling and filtering the product. The product was washed with distilled water and acetone and dried at 80 °C. Calcination (Section 3.5.1) was performed at 575 °C for 6 hours. Product Si/Ge = 3 (EDX).

3.3.2 Low-Ge Ge-UTL

Low germanium content Ge-**UTL** was prepared using methods adapted from the literature.[6–9]

GeO_2 (15.68 g, 150 mmol) was added to a solution of DMAD-OH (0.625 M, 240 cm^3, 150 mmol) and mechanically stirred for 15 minutes, before SiO_2 (Cab-O-Sil M5) (17.98 g, 300 mmol) was added portionwise under stirring. The mixture was stirred under high shear for 30 minutes, forming a reaction gel of composition:

$$0.4Ge : 0.4DMAD - OH : 0.8SiO_2 : 35H_2O. \tag{3.2}$$

The gel was sealed in Teflon-lined steel autoclaves and heated to 180 °C for 7 days, before quenching, cooling and filtering the product. The product was washed with distilled water and acetone and dried at 80 °C. Calcination (Section 3.5.1) was performed at 575 °C for 6 hours. Product Si/Ge = 4.5 (EDX).

3.3.3 Si-UTL

Siliceous Si-**UTL** was prepared using a method adapted from Xu *et al.*.[10]

Uncalcined high-Ge Ge-**UTL** (3.3.1, 300 mg) was stirred in HNO_3 (1 M, 15 cm^3) for 30 minutes. The mixture was sealed in an autoclave at 180 °C for 24 hours before quenching, cooling and filtering. The material was then calcined to 550 °C for 6 hours.

The acidic heating process was repeated using the calcined material (now 250 mg). Calcination (Section 3.5.1) was performed on the end product at 550 °C for 6 hours. Product Si/Ge = 120 (EDX).

3.3.4 Al,Ge-UTL

Alumino-germanosilicate Al,Ge-**UTL** was prepared using methods adapted from the literature.[11,12]

GeO_2 (10.46 g, 100 mmol) was added to a solution of DMAD-OH (0.625 M, 160 cm^3, 100 mmol) and Al_2O_3 (0.15 g, 3 mmol) and mechanically stirred for 30 minutes, before SiO_2 (Cab-O-Sil M5) (11.86 g, 197 mmol) was added portionwise under stirring. The mixture was stirred under high shear for 30 minutes, forming a reaction gel of composition:

$$0.788SiO_2 : 0.4Ge : 0.012Al_2O_3 : 0.4DMAD-OH : 30H_2O. \tag{3.3}$$

Further DMAD-OH was added to adjust the pH to 12, before the gel was sealed in Teflon-lined steel autoclaves and heated to 175 °C for 20 days, before quenching, cooling and filtering the product. The product was washed with distilled water and acetone and dried at 80 °C. Calcination (Section 3.5.1) was performed at 550 °C for 6 hours. Product Si/Ge/Al = 17:5:1 (EDX).

3.3.5 Al-CHA(Na) (SSZ-13(Na))

SSZ-13-type aluminosilicate Al-**CHA**(Na) was prepared using methods adapted from the literature.[3,13,14]

A solution of NaOH (1 M, 2.00 cm^3, 2 mmol), TMAA-OH (0.72 M, 2.78 cm^3, 2 mmol) and H_2O (3.22 cm^3, 17.8 mmol) was prepared before $Al(OH)_3$ (0.05 g, 0.65 mmol) was added and stirred until the mixture was clear. SiO_2 (Cab-O-Sil M5) (0.6 g, 10 mmol) was added portionwise and the mixture was stirred under high shear for 15 minutes, forming a reaction gel of composition:

$$10Na_2O : 2.5Al_2O_3 : 100SiO_2 : 20TMAA-OH : 4400H_2O. \tag{3.4}$$

The gel was sealed in Teflon-lined steel autoclaves and heated to 160 °C for 4 days, before quenching, cooling and filtering the product. The product was washed with distilled water and acetone until the pH reaced 12.5 and was then dried at 80 °C. Calcination (Section 3.5.1) was performed at 575 °C for 6 hours. Product Si/Al = 12 (EDX).

3.3.6 Al-CHA(K)

Al-rich Al-**CHA**(K) was prepared using methods detailed in Akiporiaye *et al.*.[15]

$Al(OH)_3$ (2.05 g, 10 mmol) was added to a solution of KOH (3.25 g, 25 mmol) in H_2O (99.75 cm^3, 5.55 mol) and stirred until dissolved. SiO_2 (Ludox AS-30 Colloidal Silica) (30%, 10.0 g, 50 mmol) was added portionwise and the mixture was stirred under high shear for 15 minutes, forming a thick reaction gel of composition:

$$2.5K_2O : 1Al_2O_3 : 5SiO_2 : 600H_2O. \tag{3.5}$$

The gel was sealed in Teflon-lined steel autoclaves and heated to 150 °C for 5 days, before quenching, cooling and filtering the product. The product was washed with distilled water and dried at 80 °C. Product Si/Al = 5 (EDX).

3.3.7 Al-CHA(H)

Aluminosilicate Al-**CHA**(H) was prepared directly in the H-form using methods adapted from the literature.[16,17]

A solution of $Al(OH)_3$ (0.051 g, 0.50 mmol), TMAA-OH (1.14 M, 1.05 cm^3, 5 mmol) and H_2O (3.68 cm^3, 20.4 mmol) was prepared. SiO_2 (Ludox AS-40 Colloidal Silica) (40%, 1.5 g, 10 mmol) was added portionwise and the mixture stirred on high shear for 2 hours, forming a reaction gel of composition:

$$0.1Al_2O_3 : 1SiO_2 : 0.5TMAA-OH : 44H_2O. \tag{3.6}$$

2 wt % SSZ-13(H) **CHA** seeds were then added and the gel stirred for 2 minutes. The gel was sealed in Teflon-lined steel autoclaves and heated to 150 °C for 24 hours, before quenching, cooling and filtering the product. The product was washed with distilled water and acetone and then dried at 80 °C. Calcination (Section 3.5.1) was performed at 575 °C for 6 hours. Product Si/Al = 23 (EDX).

3.3.8 Si-CHA

Siliceous Si-**CHA** was prepared directly using methods adapted from the literature.[18,19]

Tetraethylorthosilicate (TEOS) (10.4 g, 50 mmol SiO_2) was added dropwise to an aqueous solution containing TMAA-OH (1.10 M, 22.72 cm^3, 25 mmol). The solution was mechanically stirred and left to react for three days until the ethanol and water had evaporated, leaving the desired SiO_2 : H_2O ratio. Following this, HF (46.9%, 1.07 g, 25 mmol) was added until the gel of molar composition,

$$1SiO_2 : 0.5TMAA-OH : 0.5HF : 3H_2O, \tag{3.7}$$

was reached and the mixture homogenised thoroughly by hand for 20 minutes. The gel was sealed in Teflon-lined steel autoclaves and heated to 150 °C under rotation (300 rpm) for 3 days, before quenching, cooling and filtering the product. The product was washed with distilled water and acetone until the filtrate had neutral pH and then dried at 80 °C. Calcination (Section 3.5.1) was performed at 600 °C for 6 hours. Product 100% Si (EDX).

3.3.9 B-CHA(H)

Borosilicate B-**CHA**(H) was prepared using methods detailed in the literature.[17,20]

H_3BO_3 (0.124 g, 2 mmol) was added to an aqueous solution containing TMAA-OH (0.72 M, 5.56 cm^3, 4 mmol), which was topped up with H_2O (2.36 cm^3, 130 mmol) and stirred mechanically for 15 minutes. To this SiO_2 (Cab-O-Sil M5) (0.6 g, 10 mmol) was added portionwise and the mixture stirred on high shear for two hours until the desired water content had been reached to satisfy the gel composition:

$$1SiO_2 : 0.4TMAA-OH : 0.1B_2O_3 : 44H_2O. \tag{3.8}$$

At this point, 2 wt% Si-**CHA** (Section 3.3.8) seeds were added and the gel was sealed in Teflon-lined steel autoclaves and heated to 150 °C for 24 hours, before quenching, cooling and filtering the product. The product was washed with distilled water and acetone until the filtrate had neutral pH and then dried at 80 °C. Calcination (Section 3.5.1) was performed at 550 °C for 5 hours. Product Si/B = 8 (EDX).

3.3.10 Ti-CHA(H)

Titanosilicate Ti-**CHA**(H) was prepared directly in the H-form using methods adapted from the literature.[17]

$Ti(OBu)_4$ (0.17 g, 0.5 mmol) was added to an aqueous solution containing TMAA-OH (0.82 M, 17.1 cm^3, 14 mmol) and stirred mechanically for 15 minutes. To this SiO_2 (Ludox AS-40 Colloidal Silica) (1.5 g, 10 mmol) was added portionwise and the mixture stirred on high shear overnight until the desired water content had been reached to satisfy the gel composition:

$$1SiO_2 : 1.4TMAA-OH : 0.05TiO_2 : 1.4HF : 6H_2O. \tag{3.9}$$

At this point, HF (46.9%, 0.597 g, 14 mmol) was added and the mixture homogenised by hand. 2 wt% Si-**CHA** (Section 3.3.8) seeds were then added and the mixture further combined by hand for 2 minutes.The gel was sealed in Teflon-lined steel autoclaves and heated to 150 °C for 30 hours, before quenching, cooling and filtering the product. The product was washed with distilled water and acetone until the filtrate had neutral pH and then dried at 80 °C. Calcination (Section 3.5.1) was performed at 600 °C for 5 hours. Product Si/Ti = 22 (EDX).

3.3.11 Zn-CHA(H)

Zincosilicate Zn-**CHA**(H) was prepared directly in the H-form using methods adapted from the literature.[5]

A solution of LiOH (0.034 g, 0.8 mmol) and H_2O (2.4 cm^3, 130 mmol) was prepared before SiO_2 (Cab-O-Sil M5) (0.6 g, 10 mmol) was added and the mixture stirred mechanically for two hours to obtain a clear suspension. A second aqueous solution of TMAA-OH (1.14 M, 3.68 cm^3, 42 mmol) and $Zn(OAc)_2$ (0.066 g, 0.3 mmol) was prepared and stirred for five minutes, before addition to the silicate solution to form the gel of composition:

$$1SiO_2 : 0.42TMAA-OH : 0.03ZnO : 0.08LiOH : 30H_2O. \tag{3.10}$$

2 wt% Si-**CHA** (Section 3.3.8) seeds were added directly after the zinc solution and the mixture stirred for 20 minutes. The gel was sealed in Teflon-lined steel autoclaves and heated to 150 °C for 7 days, before quenching, cooling and filtering the product. The product was washed with distilled water and acetone until the filtrate had neutral pH and

then dried at 80 °C. Calcination (Section 3.5.1) was performed at 600 °C for 5 hours. Product Si/Zn = 18 (EDX).

3.3.12 Al-FAU(Na) (Linde Type-Y)

Linde Y-type aluminosilicate Al-**FAU**(Na) was prepared using methods adapted from the literature.[14,21]

H_2O (9.98 cm^3, 554 mmol), NaOH (2.04 g, 51 mmol) and $NaAlO_2$ (1.05 g, 12.8 mmol) was stirred mechanically until dissolved. Following this, Na_2SiO_3 (30% SiO_2) (11.36 g, 56.8 mmol SiO_2) was added and stirred under high shear as a thick gel forms to give a seed gel of composition:

$$10.67Na_2O : 1Al_2O_3 : 10SiO_2 : 180H_2O. \tag{3.11}$$

The gel was placed in a sealed container and left to incubate at room temperature for 24 hours. A batch gel was then prepared from H_2O (65.49 cm^3, 3.64 mol), NaOH (0.07 g, 1.75 mmol) and $NaAlO_2$ (13.09 g, 160 mmol) was stirred mechanically until dissolved. Following this, Na_2SiO_3 (30% SiO_2) (71.22 g, 831 mmol SiO_2) was added and stirred under high shear until smooth (20 minutes). The batch gel takes the composition given by:

$$4.3Na_2O : 1Al_2O_3 : 10SiO_2 : 180H_2O. \tag{3.12}$$

An overall reaction gel was then prepared by taking seed gel (8.25 g) and adding slowly to the seed gel. Thorough mechanical mixing on high shear for 20 minutes was needed to homogenise the gel. Following this, the reaction gel of composition:

$$4.62Na_2O : 1Al_2O_3 : 10SiO_2 : 180H_2O, \tag{3.13}$$

was left to incubate at room temperature for 24 hours in a sealed poly bottle, before heating to 100 °C for 6 hours. By this point the product had precipitated out of solution, leaving a clear supernatant. The product was recovered by centrifugation, washing with distilled water until the filtrate had pH 9 and was then dried at 80 °C. Product Si/Al = 1.7 (EDX).

3.3.13 Al-FAU(Na) (Linde Type-X)

Linde X-type aluminosilicate Al-**FAU**(Na) was prepared using methods adapted from the literature.[14,22]

H_2O (30 cm^3, 1.67 mol) and $NaAlO_2$ (22.37 g, 273 mmol) was stirred mechanically until dissolved, whilst separately, H_2O (70 cm^3, 3.89 mol), KOH (21.53 g, 384 mmol) and NaOH (31.09 g, 775 mmol) are combined and stirred until dissolved. The aluminate solution is added quickly to the basic solution under mechanical stirring before H_2O (71.8 cm^3, 3.98 mol) and Na_2SiO_3 (30% SiO_2) (46 g, 230 mmol SiO_2) was added and stirred under high shear for 20 minutes. Stirring forms a gel of composition:

$$5.5Na_2O : 1.655.5K_2O : 1Al_2O_3 : 2.2SiO_2 : 122H_2O. \tag{3.14}$$

The gel was placed in a poly bottle and heated to 70 °C for 3 hours to incubate before heating to 100 °C for 2 hours. By this point the product had precipitated out of solution, leaving a clear supernatant. The product was filtered, washing with distilled water and 0.01 M NaOH and was then dried at 80 °C. Product Si/Al = 1 (EDX).

3.3.14 Al-LTA(Na) (Linde Type-A)

Linde A-type aluminosilicate Al-**LTA**(Na) was prepared using methods adapted from the literature.[14,23]

H_2O (80 cm^3, 4.44 mol) and NaOH (0.723 g, 18 mmol) was stirred mechanically until dissolved, and divided into two portions. To the first solution, $NaAlO_2$ (8.26 g, 102 mmol) was added and the mixture shaken in a capped poly bottle until the solution was clear (5 minutes). To the second solution, Na_2SiO_3 (30% SiO_2) (15.48 g, 77.4 mmol SiO_2) was added and the mixture shaken in a capped poly bottle for 10 minutes. The silicate solution was then added to the aluminate solution, rapidly forming a gel of composition:

$$3.165Na_2O : 1Al_2O_3 : 1.926SiO_2 : 128H_2O. \tag{3.15}$$

The gel was homogenised by vigorous shaking in a capped poly bottle for 20 minutes. The gel was then heated to 100 °C for 4 hours.The product was cooled to 5 °C in an ice water bath and then filtered. The product was washed with distilled water until the pH was less than 9 and was then dried at 80 °C. Product Si/Al = 1 (EDX).

3.4 Synthesis by Post-synthetic Transformation

3.4.1 FAU to CHA

Post-synthetic transformation of **FAU** to **CHA** was adapted from methods detailed in the literature,[13,14,24–32] particularly Muraoka *et al.*.[33]

Starting material **FAU**(Na) (Si/Al = 1.7, 5 g) was ion-exchanged to K^+ form by 3 x exchange in KCl (0.66 M, 250 cm^3) at 60 °C. Formed **FAU**(K) (Si/Al = 1.6, 0.5 g), KOH (0.13 g, 2.32 mmol) and H_2O (5.15 cm^3, 286 mmol), was stirred together to form the mixture of composition:

$$1.1K_2O : 0.5Al_2O_3 : 2.7SiO_2 : 150H_2O. \tag{3.16}$$

Certain components of the gel are provided by the **FAU**(K) zeolite. The gel was sealed in Teflon-lined steel autoclaves and heated to 150 °C for 4.5 days, before quenching, cooling and filtering the product. The product was washed with distilled water and acetone and then dried at 80 °C. Product Si/Al = 1.6 (EDX).

3.4.2 LTA to CHA

Post-synthetic transformation of **LTA** to **CHA** was attempted using methods detailed in the literature.[34]

H_2O (35.7 cm^3, 1.99 mol), NaOH (1.82 g, 46 mmol) and TMAA-OH (0.588 g, 2.8 mmol)was stirred mechanically for 10 minutes, before dehydrated **LTA**(Na) zeolite (Si/Al = 1, 1 g) was added and the mixture stirred for a further 20 minutes. To this SiO_2 (Ludox AS-40 Colloidal Silica) (14 g, 70 mmol) was added and the mixture stirred on high shear for 2 hours, forming a solution of composition:

$$0.38Na_2O : 0.05Al_2O_3 : 1SiO_2 : 0.04TMAA - OH : 36H_2O. \tag{3.17}$$

Certain components of the gel are provided by the **LTA**(Na) zeolite. The gel was sealed in Teflon-lined steel autoclaves and heated to 150 °C for 24 hours, before quenching, cooling and filtering the product. The product was washed with distilled water and acetone until the filtrate had neutral pH and then dried at 80 °C.

3.5 General Experimental Protocols

3.5.1 Calcination

Calcination is performed by placing zeolite material into an inert crucible and placing in the calcination tube furnace, which is open to the atmosphere. The tube furnace is set to ramp at a rate of 1 °C/min up to the target temperature, before holding for the specified period of time and then ramping back down to room temperature at a rate of 2 °C/min.

3.5.2 Ion-exchange

Ion-exchange is performed by placing zeolite material in a 1-3 M solution of the chloride or nitrate salt of the desired exchange cation, with a typical solid : solute ratio of 1 : 60. The mixture is stirred and heated to 80 °C for 18 hours, before the mixture is cooled, filtered and the solid is re-suspended in a fresh solution of the desired ion-exchange cation. The heating exchange procedure is repeated 2-4 times.

In the case of exchange to proton (H^+) form, the zeolite material is first exchanged to the ammonium ($NH_4{}^+$) form using NH_4Cl in the manner described above. Calcination to the proton form, liberating ammonia gas is achieved by heating in a Carbolite tube furnace to 700 °C for two hours in the manner described in Section 3.5.1.

3.5.3 Dehydration

Dehydration is performed by placing zeolite material into an open-ended glass vial within a Schlenk tube, which is connected to a Schlenk line. The Schlenk tube is evacuated down to a pressure of $\approx 10^{-2}$ Torr. The Schlenk tube is placed in a Buchi tube oven and heated at a rate of 1 °C/min up to the target temperature and held at that temperature for 18 hours. Following dehydration, the pressure registers $\approx 10^{-4}$ Torr and the Schlenk tube is cooled to room temperature. The Schlenk tube is flushed with argon and opened to the atmosphere under flowing argon. The glass vials are then flame-sealed using a Bunsen burner.

3.5.4 Slurry Preparation

Slurries are prepared by combining 25 mg of zeolite material with 25 μL of water; either $H_2^{16}O$ or $H_2{}^{17}O$ in a Bruker 4mm HRMAS PTFE rotor insert, which is sealed with plug and screw-cap. The sealed inserts are stored in sample vials on the experimental bench.

3.5.5 $^{17}O_2$ gas-enrichment

$^{17}O_2$ gas-enrichment was performed on a custom-built Schlenk apparatus. Zeolite material is placed in a quartz tube fitted with a Youngs tap and attached to the apparatus. The apparatus is evacuated, before introducing vacuum to the sample and leaving to equilibrate at 0-10 mbar under dynamic vacuum for $\approx$ 10 minutes. The sample tube is then submerged in liquid nitrogen under dynamic vacuum at 0-1 mbar and left to equilibrate for $\approx$ 10 minutes. The system is then switched to static vacuum before $^{17}O_2$ is introduced to the sample until a residual static pressure of $\approx$ 200 mbar gas is left in the system. The quartz tube is then sealed, removed from the Schlenk apparatus and liquid nitrogen and left to return to room temperature. The sample is then heated in a Carbolite tube furnace at a rate of 5 °C/min up to 300-800 °C, where it is held for 12-96 hours before cooling to room temperature at a rate of 5 °C/min.

3.6 Analytical and Characterisation Equipment

Details of analytical and characterisation equipment are provided here. Any specific software, hardware or experimental settings used are also included.

3.6.1 Solid-state NMR Spectrometers

Solid-state NMR spectra were acquired at five field strengths: 9.4 T (400 MHz), 14.1 T (600 MHz), 18.8 (800 MHz), 20.0 (850 MHz) and 23.5 T (1 GHz) on the following, respective Bruker spectrometers; four-channel Avance III, three-channel Avance III, four-channel Avance Neo, four-channel Avance Neo and four-channel Avance Neo. All spectrometers were equipped with wide bore magnets, with the exception of 18.8 T (narrow bore). 4.0 mm low-γ HX probes have been used for ^{1}H, ^{17}O and ^{29}Si, acquisition, 4.0 mm HX probes have been used for ^{1}H, ^{13}C, ^{23}Na and ^{27}Al acqusition, 4.0 mm HFX probes have been used for ^{1}H, ^{11}B and ^{19}F and 3.2 mm HX probes have been used for ^{1}H and ^{17}O acquisition.

Chemical shift reference samples used were $C_3H_7NO_2$ (alanine) for ^{1}H, BPO_4 (boron phosphate) for ^{11}B, $^{13}C_3H_7NO_2$ (^{13}C-enriched alanine) for ^{13}C, H_2O (water) for ^{17}O, $(C_2F_4)_n$ (polytetrafluoroethylene (PTFE)) for ^{19}F, NaCl (sodium chloride) for ^{23}Na, $Al(C_5H_7O_2)_3$ (aluminium acetylacetonate) for ^{27}Al and $C_{24}H_{72}O_{20}Si_{16}$ (octakis(trimethylsiloxy)silsesquioxane (Q8M8)) for ^{29}Si.

3.6.2 Liquid-state NMR Spectrometers

Liquid-state NMR spectroscopy was acquired at 9.4 (400 MHz) and 11.8 T (500 MHz) Bruker Avance III spectrometers using BBFO (Broad Band Fluorine Observation) probes.

3.6.3 X-ray Diffractometers

X-ray diffraction data have been acquired using capillary format. Data have been acquired on STOE STADIP capillary diffractometers using CuKα radiation and MoKα radiation at room temperature. Diffractometers were operated in Debye-Scherrer mode. Data have been collected in the ranges of 3-50 θ (Cu) and 3-30 θ (Mo). Data in this thesis is presented in CuKα format. This has been achieved by translation of MoKα data using a script written by Ms Caroline Elliott.

3.6.4 Thermal gravimetric Analyser

Thermal gravimetric analysis was performed with TGA/DTA measurement on a Stanton Redcroft STA-780 was used.

3.6.5 Scanning Electron Microscope

SEM images were collected on a Jeol JSM-5600 (tungsten filament) with a resolution of 3.5 nm using an acceleration voltage of 5 kV and a working distance of 10 mm. Further SEM images were collected on a Jeol JSM-IT200 (tungsten filament) with a resolution of 1.5 nm using an acceleration voltage of 5 kV and a working distance of 10 mm.

3.6.6 Energy Dispersive X-ray Analyser

EDX data was collected using the electron gun integrated within a Jeol JSM-5600 electron microscope with a resolution of 3.5 nm. An acceleration voltage of 20 kV and a working distance of 20 mm was used. Additional EDX data was collected on an integrated Jeol JSM-6700F scanning electron microscope.

3.7 Computational Studies

3.7.1 Density Functional Theory Calculations

Geometry optimisations and NMR parameter calculations were performed using the CASTEP (CAmbridge Serial Total Energy Package) 19.11 code.[35–39] PBE/TS and ZORA were used with an energy cut-off of 60 Ry and a k-point spacing of $0.04\,2\,\pi\text{Å}^{-1}$. Structure files were taken from the IZA Database.[40]

3.7.2 Molecular Dynamics Simulations

Ab initio molecular dynamics simulations were performed at 300 K for 15 picoseconds with an increment of 5 femtoseconds. MD simulations were employed DFT using the VASP 5.4. code, dispersion correction at the PBE functional level.[41] Further details can be found in the methods section of the publication by Heard *et al.* in reference 41

3.8 References

[1] P. S. Wheatley, P. Chlubná-Eliášová, H. Greer, W. Zhou, V. R. Seymour, D. M. Dawson, S. E. Ashbrook, A. B. Pinar, L. B. McCusker, M. Opanasenko, J. Čejka and R. E. Morris, *Angew. Chem. Int. Ed.*, 2014, **53**, 13210–13214.

[2] M. G. Marino and K. D. Kreuer, *ChemSusChem*, 2015, **8**, 513–523.

[3] S. I. Zones, *US Patent 4544538*, 1985.

[4] J. Hu, F. W. Yang and M. G. Huang, *Adv. Mater. Res.*, 2011, **391-392**, 1159–1163.

[5] N. Koike, K. Iyoki, S. H. Keoh, W. Chaikittisilp and T. Okubo, *Chem. Eur. J.*, 2018, **24**, 808–812.

[6] P. S. Wheatley, J. Čejka and R. E. Morris, *J. Vis. Exp.*, 2016, **2016**, 9–14.

[7] J.-l. Paillaud, B. Harbuzaru, J. Patarin and N. Bats, *Science*, 2004, **304**, 990–993.

[8] A. Corma, M. J. Díaz-Cabañas, F. Rey, S. Nicolopoulus and K. Boulahya, *Chem. Commun.*, 2004, 1356–1357.

[9] G. P. M. Bignami, D. M. Dawson, V. R. Seymour, P. S. Wheatley, R. E. Morris and S. E. Ashbrook, *J. Am. Chem. Soc.*, 2017, **139**, 5140–5148.

[10] H. Xu, J.-g. Jiang, B. Yang, L. Zhang, M. He and P. Wu, *Angew. Chem. Int. Ed.*, 2014, **53**, 1355–1359.

[11] M. V. Shamzhy, O. V. Shvets, M. V. Opanasenko, P. S. Yaremov, L. G. Sarkisyan, P. Chlubná, A. Zukal, V. R. Marthala, M. Hartmann and J. Čejka, *J. Mater. Chem.*, 2012, **22**, 15793.

[12] O. V. Shvets, N. Kasian, A. Zukal, J. Pinkas and J. Čejka, *Chem. Mater.*, 2010, **22**, 3482–3495.

[13] S. I. Zones and R. A. V. Nordstrand, *Zeolites*, 1988, **8**, 166–174.

[14] *Verified Syntheses of Zeolitic Materials*, ed. S. Mintova, Elsevier, 3rd edn., 2016.

[15] D. E. Akporiaye, I. M. Dahl, H. B. Mostad and R. Wendelbo, *J. Phys. Chem.*, 1996, **100**, 4148–4153.

[16] J. R. Di Iorio and R. Gounder, *Chem. Mater.*, 2016, **28**, 2236–2247.

[17] Q. Yue, J. Zhang, M. Shamzhy and M. Opanasenko, *Microporous Mesoporous Mater.*, 2019, **280**, 331–336.

[18] M.-J. Díaz-Cabañas, P. A. Barrett and M. A. Camblor, *Chem. Commun.*, 1998, 1881–1882.

[19] L. A. Villaescusa, I. Bull, P. S. Wheatley, P. Lightfoot and R. E. Morris, *J. Mater. Chem.*, 2003, **13**, 1978–1982.

[20] J. Liang, J. Su, Y. Wang, Z. Lin, W. Mu, H. Zheng, R. Zou, F. Liao and J. Lin, *Microporous Mesoporous Mater.*, 2014, **194**, 97–105.

[21] D. M. Ginter, A. T. Bell and C. J. Radke, *Synthesis of Microporous Materials*, Van Nostrand Reinhold, New York, 1992, p. 1600.

[22] G. H. Kühl, *Zeolites*, 1987, **7**, 451–457.

[23] G. Engelhardt, B. Fahlke, M. Mägi and E. Lippmaa, *Zeolites*, 1985, **5**, 49–52.

[24] S. Miyagawa, K. Miyake, Y. Hirota, N. Nishiyama, M. Miyamoto, Y. Oumi and S. Tanaka, *Microporous Mesoporous Mater.*, 2019, **278**, 219–224.

[25] W. Qin, R. Jain, F. C. Robles Hernández and J. D. Rimer, *Chem. Eur. J.*, 2019, **25**, 5893–5898.

[26] T. Tanigawa, N. Tsunoji, M. Sadakane and T. Sano, *Dalton Trans.*, 2020, **49**, 9972–9982.

[27] L. Van Dang, T. T. M. Nguyen, D. Van Do, S. T. Le, T. D. Pham and A. T. M. Le, *J. Anal. Methods Chem.*, 2021, **2021**, year.

[28] X. Xiong, D. Yuan, Q. Wu, F. Chen, X. Meng, R. Lv, D. Dai, S. Maurer, R. McGuire, M. Feyen, U. Müller, W. Zhang, T. Yokoi, X. Bao, H. Gies, B. Marler, D. E. De Vos, U. Kolb, A. Moini and F.-S. Xiao, *J. Mater. Chem. A*, 2017, **5**, 9076–9080.

[29] H. Xu, J. Zhu, J. Qiao, X. Yu, N. B. Sun, C. Bian, J. Li and L. Zhu, *Microporous Mesoporous Mater.*, 2021, **312**, 110736.

[30] M. Bourgogne, J.-L. Guth and R. Wey, *US Patent 4503024*, 1985.

[31] S. I. Zones, *J. Chem. Soc., Faraday trans.*, 1991, **87**, 3709–3716.

[32] S. Goel, S. I. Zones and E. Iglesia, *Chem. Mater.*, 2015, **27**, 2056–2066.

[33] K. Muraoka, Y. Sada, A. Shimojima, W. Chaikittisilp and T. Okubo, *Chem. Sci.*, 2019, **10**, 8533–8540.

[34] H. Geng, G. Li, D. Liu and C. Liu, *J. Solid State Chem.*, 2018, **265**, 193–199.

[35] C. J. Pickard and F. Mauri, *Phys. Rev. B - Condens. Matter Mater. Phys.*, 2001, **63**, 2451011–2451013.

[36] M. D. Segall, P. J. D. Lindan, M. J. Probert, C. J. Pickard, P. J. Hasnip, S. J. Clark and M. C. Payne, *J. Phys. Condens. Matter*, 2002, **14**, 2717–2744.

[37] M. Profeta, F. Mauri and C. J. Pickard, *J. Am. Chem. Soc.*, 2003, **125**, 541–548.

[38] S. J. Clark, M. D. Segall, C. J. Pickard, P. J. Hasnip, M. I. Probert, K. Refson and M. C. Payne, *Zeitschrift fur Krist.*, 2005, **220**, 567–570.

[39] J. R. Yates, C. J. Pickard and F. Mauri, *Phys. Rev. B*, 2007, **76**, 024401.

[40] C. Baerlocher and L. B. McCusker, *Database of Zeolite Structures*, http://www.iza-structure.org/databases/.

[41] C. J. Heard, L. Grajciar, C. M. Rice, S. M. Pugh, P. Nachtigall, S. E. Ashbrook and R. E. Morris, *Nat. Commun.*, 2019, **10**, 4690–4967.

Chapter 4

Mechanistic Investigations of the ADOR Process

4.1 Declaration

Some of the work detailed in this chapter has been carried out in collaboration with researchers at the University of St Andrews. Some *ex-situ* diffraction samples were prepared and their powder patterns recorded by project student Olivia Dovernor. Development of the hydrolysis protocol for *ex-situ* ^{29}Si NMR spectroscopic investigation was, in part, carried out in collaboration with Dr Susan Henkelis. The ball-milling protocol for ADOR hydrolysis and preparation of subsequent ^{17}O-enriched sample was prepared in collaboration with Dr Daniel Rainer. DFT calculations were performed and referenced by Professor Sharon Ashbrook. Selected ^{17}O NMR spectra were carried out at the UK High-Field Solid-state NMR Spectroscopy Facility, based at the University of Warwick. High-field experiments were enabled by collaborative assistance from Dr Daniel Dawson, Dr Dinu Iuga and Dr Trent Franks.

4.2 Introduction

The ADOR process is a recently established method for synthesising new, high-silica zeolite materials from pre-existing zeolites by exploiting inherent weaknesses within their parent structures. In order to work, the reaction system requires a starting zeolite material possessing a structural weakness which can be exploited under mild reaction conditions, without detriment to or compromise of the bulk of the zeolite layers. Germanosilicate zeolites provide an ideal system for application of the ADOR protocol owing to the more hydrolytically unstable Ge – O bonds woven into a stable silicious material. The ADOR reactivity of germanosilicate zeolites has proven very versatile under variation of a range

of conditions; starting material, temperature, pH, solvent system, pressure, reaction volume, reaction time, reaction set up and atmosphere.[1–22] These investigations have produced a range of materials with a varied composition, pore structure and catalytic activity.[23–28]

To date, six different germanosilicate zeolites have been found to be 'ADORable', producing 13 new zeolites with novel topologies (see Table 4.1) The most successful zeolite for producing new materials has been **UTL**.[29,30] Consequently, the focus of the work detailed in this chapter is the ADOR reactivity of **UTL** in water. Chemistry falling within this reaction space has received much attention since the inception of the methodology, producing seven new materials to date. Despite this, the exact process by which the parent **UTL** zeolite disassembles and rearranges to form isolatable crystalline intermediates and zeolite precursors is still unclear.

New Zeolite	Parent Material	Pore System	Reference
IPC-2 (**OKO**)	**UTL**	$12x10$	ref. 2
IPC-4 (**PCR**)	**UTL**	$10x8$	ref. 2
IPC-6 (***PCR**)	**UTL**	$10x8 + 12x10$	ref. 14
IPC-7	**UTL**	$12x10 + 14x12$	ref. 14
IPC-8	**UTL**	$10x8 + 14x12$	ref. 8 (synthesis not disclosed)
IPC-9	**UTL**	$10x7$	ref. 7
IPC-10	**UTL**	$12x9$	ref. 7
IPC-12	**UOV**	12-8 (1D)	ref. 31
IPC-13	CIT-13 (***CTH**)	$12x8$	ref. 8 (synthesis not disclosed)
IPC-15	SAZ-1 (***CTH**)	10	ref. 32
IPC-16	SAZ-1 (***CTH**)	$12x8$	ref. 32
IPC-17	**IWR**	$12x8$	ref's 4,8 (synthesis not disclosed)
IPC-18	**IWW**	$12\text{-}8x8$	ref. 17

Table 4.1: Table detailing zeolites made by the ADOR protocol. Note only some new ADORable zeolites have to date been verified and assigned framework codes by the IZA.

Contributing factors to the gap in understanding include; the unknown chemical composition of some early intermediates of the ADOR process, the speed with which the ADORable species react and rearrange in hot water during hydrolysis, the disparity between the similar long-range order and different local structure of some isolatable intermediates and the significance of the post-disassembly, pre-assembly induction period seen in some reactions. Through high-throughput powder X-ray diffraction analysis, local structural disorder analysis and the development of novel ^{17}O-enrichment protocols for *in-* and ex-situ reaction monitoring using solid-state NMR spectroscopy, specific reaction intermediates along the ADOR process have been isolated and char-

acterised, providing novel insights to the disassembly and rearrangement of **UTL** in water.

Solid-state NMR spectroscopy and X-ray diffraction techniques are ideally suited to monitor the changes occurring in the ADOR process, which involve both local structural changes and long-range order rearrangements. In this chapter, these techniques have successfully been employed to increase mechanistic understanding of ADOR zeolite disassembly, organisation and reassembly.

4.3 Starting Materials Synthesis and Characterisation

The characterisation of parent **UTL** materials are discussed here. Synthesis details are disclosed in Section 3.3.

4.3.1 Ge-UTL 'High-Ge'

High-germanium content **UTL** was synthesised according to the procedure in Section 3.3.1, producing a highly crystalline material, stable to calcination at 550 °C (see Figure 4.1). SEM and EDX analyses show a single phase of large platelet type crystals, typical for **UTL** materials, with a Si/Ge ratio of ≈ 3.[29]

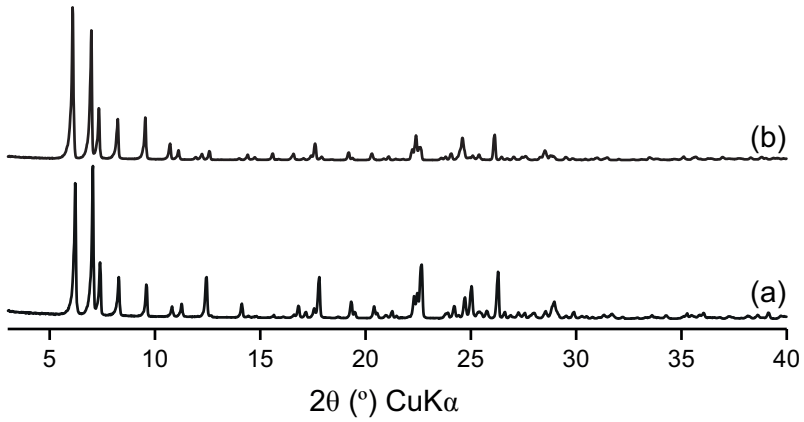

Figure 4.1: Powder X-ray diffraction patterns for (a) reference **UTL** material[29] and (b) synthesised high-Ge Ge-**UTL**.

Solid-state NMR spectroscopic characterisation of the calcined framework show a broad lineshape centred at 4 ppm for ^{1}H, typical of the water present in hydrated zeolite frameworks. The ^{29}Si MAS and CP MAS NMR spectra reveal an expected overlapped lineshape owing to the presence of a number of crystallographically inequivalent Q^4 framework silicon sites and a very low level of Q^3 defects. (see Figure 4.2) This confirms the material has been successfully reproduced as a low-defect, periodic tectosilicate zeolite framework.

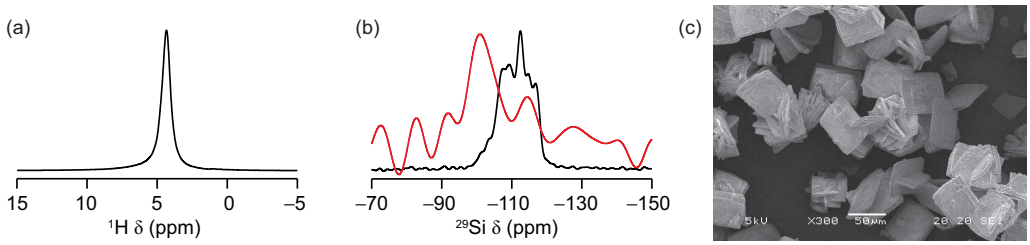

Figure 4.2: (a) ^{1}H and (b) ^{29}Si (14 kHz MAS, 9.4 T) NMR spectra and (c) SEM image of synthesised high-Ge Ge**UTL** used in this project. Red overlay in (b) corresponds to ^{1}H^{29}Si CP spectrum (5000 μs contact time).

4.3.2 Ge-UTL 'Low-Ge'

Low-germanium content **UTL** was synthesised according to the procedure in Section 3.3.2, producing a highly crystalline material, stable to calcination at 550 °C (see Figure 4.3). SEM and EDX analyses show a single phase of large platelet type crystals, typical for **UTL** materials, with a Si/Ge ratio of ≈ 4.5.[29]

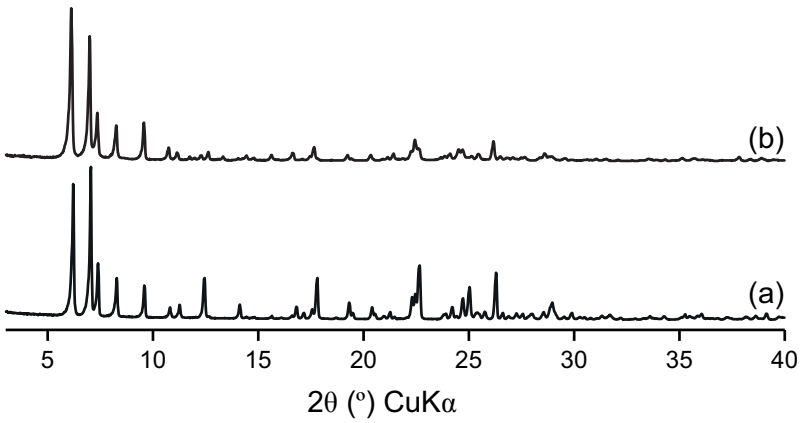

Figure 4.3: Powder X-ray diffraction patterns for (a) reference **UTL** material[29] and (b) synthesised low-Ge Ge-**UTL**.

Solid-state NMR characterisation of the calcined framework show a broad lineshape centred at 4 ppm for ^{1}H, typical of water in hydrated zeolite frameworks, with a small shoulder at 7 ppm indicative of silanol species. The ^{29}Si MAS and CP MAS NMR spectra reveal an overlapped lineshape owing to the range of crystallographically inequivalent Q^4 framework silicon sites and a very low-level of Q^3 defects (see Figure 4.4). Although some evidence of silanols in the ^{1}H spectrum, overall this confirms the material has been successfully synthesised as a low-defect, periodic tectosilicate zeolite framework.

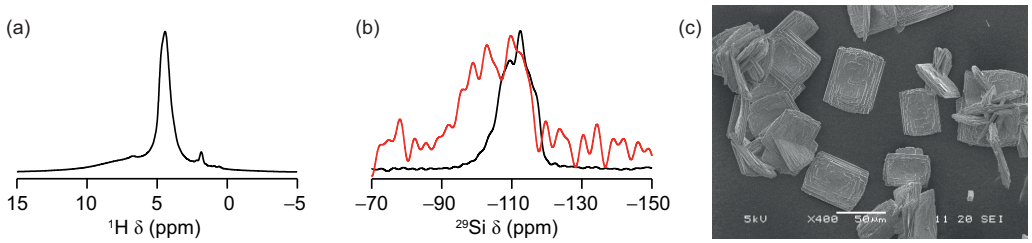

Figure 4.4: (a) ^{1}H and (b) ^{29}Si (14 kHz MAS, 9.4 T) NMR spectra and (c) SEM image of synthesised low-Ge Ge**UTL** used in this project. Red overlay in (b) corresponds to ^{1}H^{29}Si CP spectrum (5000 μs contact time).

4.3.3 Si-UTL

Siliceous **UTL** was synthesised according to the procedure in Section 3.3.3, producing a crystalline material, stable to calcination at 550 °C. SEM and EDX analyses show a single phase of distorted platelet type crystals, with a Si/Ge ratio of $\approx$ 180 (see Figure 4.5). The change in morphology and visible degradation of the crystals indicate the integrity of the material is slightly compromised by the degermanation process.[33,34]

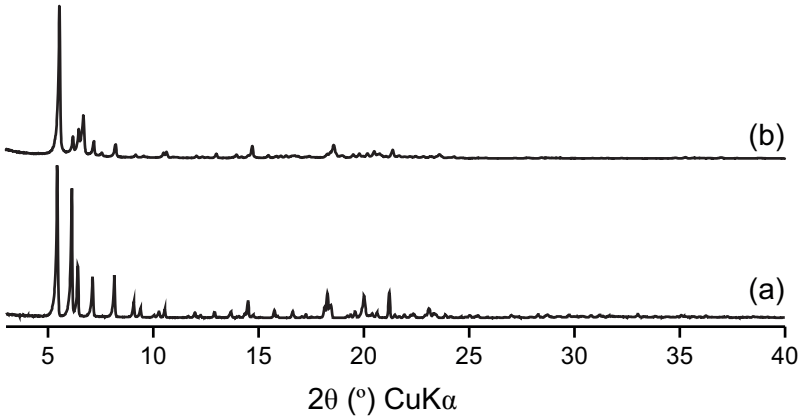

Figure 4.5: Powder X-ray diffraction patterns for (a) reference **UTL** material[29] and (b) synthesised Si-**UTL**.

Solid-state NMR spectroscopic characterisation of the calcined framework show a broad lineshape centred at 0 ppm for ^{1}H, typical of water in hydrated zeolite frameworks, with a shoulder at 7 ppm indicative of silanol defect species. The ^{29}Si MAS and CP MAS NMR spectra reveal an overlapped lineshape owing to the range of crystallographically inequivalent Q^4 framework silicon sites, but with a more significant level of Q^3 and a small amount of Q^2 defects (see Figure 4.6). This analysis confirms the material has been successfully synthesised but with an amount of silanol defects. This is likely caused by the lack of an additional silicon source in the acidic degermanation-stabilisation process.

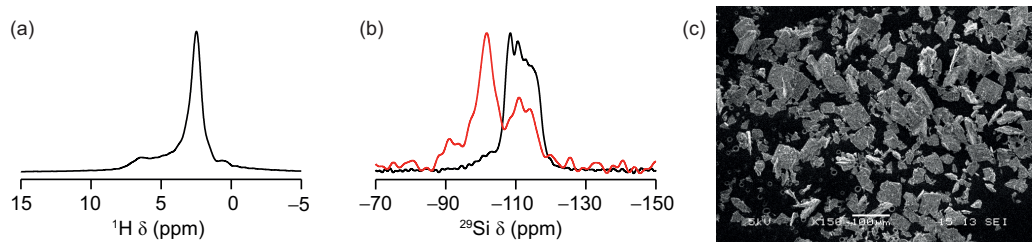

Figure 4.6: (a) ^{1}H and (b) ^{29}Si (14 kHz MAS, 9.4 T) NMR spectra and (c) SEM image of synthesised Si-**UTL** used in this project. Red overlay in (b) corresponds to ^{1}H^{29}Si CP spectrum (5000 μs contact time).

4.3.4 Al-UTL

Aluminated **UTL** was synthesised according to the procedure in Section 3.3.4, producing a crystalline material, stable to calcination at 550 °C (see Figure 4.7). SEM and EDX analyses show a single phase of large platelet type crystals, typical for **UTL** materials, with a Si/Al ratio of ≈ 18 and a residual germanium content by atom of 1% (Si/Al/Ge = 90/5/1).[23]

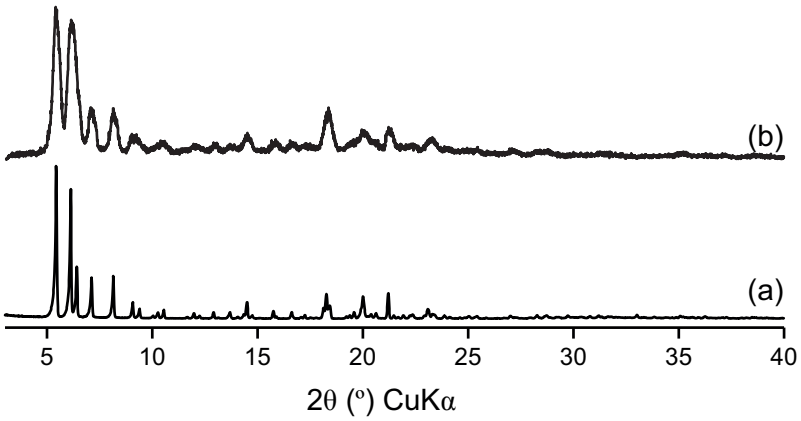

Figure 4.7: Powder X-ray diffraction patterns for (a) reference **UTL** material[29] and (b) synthesised Al-**UTL**.

Solid-state NMR spectroscopic characterisation of the calcined framework show a broad lineshape centred at 3 ppm for ^{1}H, typical of water in hydrated zeolite frameworks. The small amount of Brønsted acid sites stabilising the negatively charged aluminosilicate framework are likely to overlap with this peak. The ^{29}Si MAS and CP MAS NMR spectra reveal an overlapped lineshape owing to the range of crystallographically inequivalent Q^4 framework silicon sites and a significant level of Q^3 and small amount of Q^2 defects. The ^{27}Al MAS NMR confirms tetrahedral aluminium the material, however the significant peak at 0 ppm also confirms a significant amount of 6-coordinate aluminium is also present (see Figure 4.8). The very sharp lineshape may suggest that this species is extra framework Al that is hydrated within the pore. The above confirms the material has been successfully synthesised, although the framework is likely to contain a large amount of defects where aluminium has been incorporated in place of germanium.

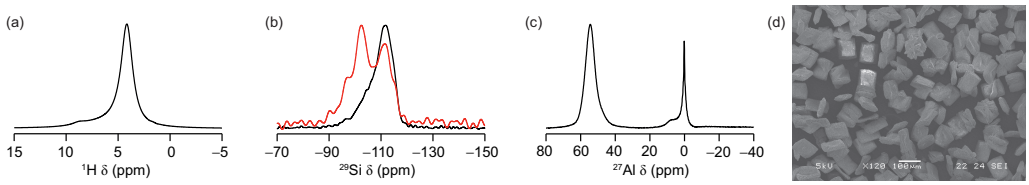

Figure 4.8: (a) ^{1}H, (b) ^{29}Si and (c) ^{27}Al (14 kHz MAS, 9.4 T) NMR spectra and (d) SEM image of synthesised Al-**UTL** used in this project. Red overlay in (b) corresponds to ^{1}H^{29}Si CP spectrum (5000 μs contact time).

4.4 Following the ADOR Process using *ex-situ* X-ray Diffraction

As outlined in Section 1.4.2.2, owing to the differences in the interplanar spacing of disassembled intermediates of the ADOR process, the (200) reflection; present in all diffraction patterns concerning the ADOR transformations of **UTL**; can be used to follow disassembly and organisation steps of an ADOR transformation by isolating reactive intermediates. The development of a standard protocol by Henkelis *et al.*,[12,13] provided a starting point for optimisation of the reaction conditions applicable to X-ray diffraction analysis that enabled the ADOR transformation in water, to be followed.

In this section, optimisation of initial reaction conditions for ADOR hydrolyses to be studied using solid-state NMR spectroscopy were developed, using the work in references 12 and 13 as a starting point. PXRD was used as the primary characterisation method for optimisation reactions.

4.4.1 Optimisation of Reaction Conditions

Henkelis *et al.* developed a reaction protocol for tracking the ADOR process where small samples were taken throughout a reaction to track the disassembly and rearrangement in water at a range of temperatures. Owing to the small sample volume required for PXRD analysis, sampling could take place frequently even at high temperatures; every minute for the first five minutes and thereafter every five minutes up to and including 60 minutes, after which samples were taken every 30 minutes. This method proved effective at enabling the reaction transformation to be followed, using PXRD analysis. Employing this method at 100 °C, the disassembly step is completed after approximately five minutes, with reassembly starting after a 60 minute induction period and completing within four hours of the reaction starting. Thus, a complete ADOR rearrangement can be comfortably captured at 100 °C in eight hours.[12,13]

In this work, larger sample sizes applicable for solid-state NMR analysis (using 4 mm rotors for ^{29}Si NMR experiments were required at specified intervals. It was seen by Henkelis *et al.* that it was not possible to achieve these larger sample sizes at higher temperatures as the time taken to remove sufficient product from the reaction flask was greater than the generation and evolution of intermediates, particularly within the first 60 minutes of reaction.[12,13] Consequently, the reaction temperature in this study was reduced to 92 °C as this slowed the rate of disassembly sufficiently without compromising the reaction mechanism.

4.4.2 Development of Standard Protocols for High-throughput ADOR Hydrolysis

To ensure consistency in analysis of the ADOR hydrolysis reaction in water for Ge-**UTL** in this thesis, a set of standard hydrolysis protocols were devised (see Section 4.4.5). To aid this, a full time profile for this reaction system was required and as such, a complete set of PXRD measurements for the 92 °C hydrolysis was obtained, using the high-throughput technique as documented in reference 13 at 92 °C, with a standard solid : water ratio of 1:200 and a starting **UTL** material of Si/Ge = 4.5 (see Figure 4.9). Specific reaction details are found in Section 4.4.5.1.

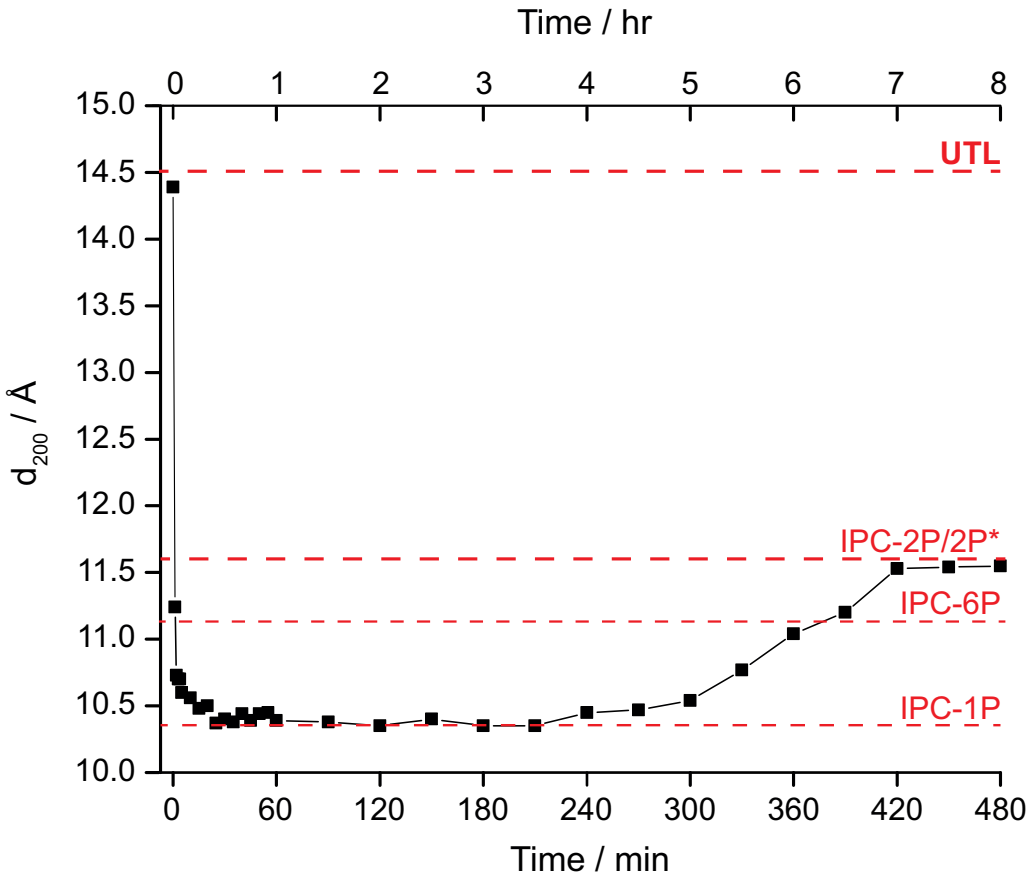

Figure 4.9: Plot showing the variation in *d*-spacing for the d_{200} reflection in *ex-situ* PXRD patterns of samples taken throughout the disassembly, organisation and reassembly of 'low-Ge' Ge-**UTL** in water at 92 °C. Typical d-spacing for (200) reflection of key intermediate materials indicated on plot.

The results, shown in Figure 4.9 suggest the ADOR reaction follows the desired pathway at 92 °C in water for Ge-**UTL** hydrolysis, although it was found to be slightly slower than that reported by Henkelis.[12,13] Initially the material rapidly hydrolyses through IPC-2P* (one minute) to IPC-1P ($\approx$ 20 minutes), before a three-hour induction period is found, after which rearrangement occurs and the material passes through IPC-6P (six hours), before forming the end product IPC-2P (seven hours). The expected and achieved (200) reflection positions for key intermediates are listed in Table 4.2.

Intermediate	Expected d_{200} / Å	Experimental d_{200} / Å	Experimental Cu K$_\alpha$ 2θ (°)	Formed After
UTL	14.53	14.39	6.14	n/a
IPC-2P*	11.62	11.21	7.81	1 min
IPC-1P	10.40	10.42	8.48	30 min
IPC-6P	11.15	11.20	7.87	360 min
IPC-2P	11.62	11.73	7.58	420 min

Table 4.2: Key intermediates in the ADOR hydrolysis transformation for Ge-**UTL** in water and their d_{200} and Cu K$_\alpha$ 2θ reflection positions.

4.4.3 Intermediate Identification

The versatility of the ADOR process means the method of producing materials by various hydrolysis routes has a negligible effect on the quality of the final product and as such, appropriate hydrolyses can be employed to target desired structures under specific conditions. Furthermore, structurally similar isolated materials prepared by different routes are comparable using powder X-ray diffraction.

The powder diffraction patterns of intermediates of interest to this project, formed through the hydrolysis of Ge-**UTL** (Si/Ge = 4.5) in water at 92 °C under standard conditions (see Section 4.4.5.2) are displayed in Figure 4.10. IPC-X materials (X = 1P, 2P, 2P*, 6P) are highly disordered and as such their PXRD patterns exhibit broad and sometimes featureless lineshapes (see Figure 4.10). The intermediates are characterised typically by the position of their (200) reflection only.[18,35–37] EDX analyses of disassembled precursor materials show all germanium has been removed from disassembled precursor materials and these are completely siliceous, with the exception of IPC-2P*, which has Si/Ge $\approx$ 12.

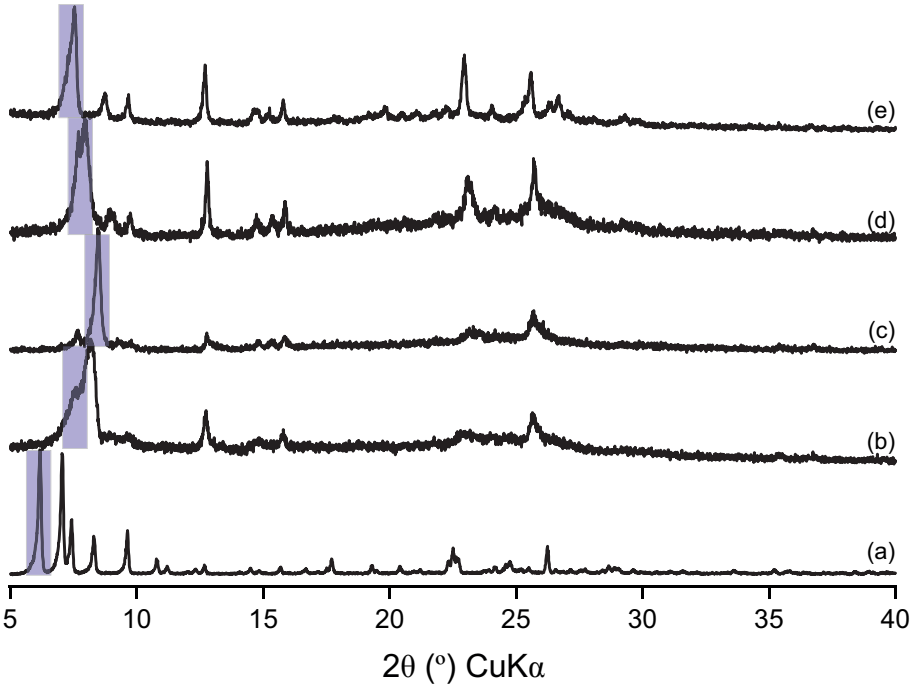

Figure 4.10: Plot showing the PXRD patterns of isolated intermediates in the disassembly, organisation and reassembly of 'low-Ge' Ge-**UTL** in water at 92 °C. (a) Parent Ge-**UTL** Si/Ge = 4.5, (b) IPC-2P*, isolated after 1 minute, (c) IPC-1P, isolated after 1 hour, (d) IPC-6P, isolated after 6 hours and (e) IPC-2P, isolated after 8 hours. (200) reflection highlighted in blue for each plotted material.

4.4.4 Further Considerations for ADOR Hydrolyses

To build a more detailed picture of the versatility of the ADOR hydrolysis reaction at 92 °C in water and to explore the possibility for further adaptions *e.g.*, for ^{17}O-enrichment during the hydrolyses, the conditions for the standard ADOR hydrolysis reaction detailed above was further optimised.

An important consideration for the hydrolysis reaction developed here is the effect of sampling (*i.e.* removing solid and reaction solution from the reaction) and the implications this has on the propagation of the reaction, particularly if large sample volumes are required. Although zeolites remain insoluble in water at all temperatures, highly soluble species are generated during the ADOR hydrolysis of **UTL**. For example, germanium oxides and aqueous silicate species, which may play important roles in reintercalation and the kinetics of rearrangement and formation of IPC-1P, IPC-6P and IPC-2P intermediates are generated.[36,37] Depending on the point in the reaction at which the sampling occurrs (*e.g.*, disassembly, organisation, reassembly) and the amount of sample/solution removed, the concentrations of aqueous species will be affected, possibly then affecting the overall progress of the reaction.

Using a standard solid : water ratio of 1:200 reaction of Ge-**UTL** in water at 92 and 100 °C, reactions, the methods in Section 4.4.5.3 and 4.4.5.4 were performed and the products compared. Sampling ≈ 100 mg of material required the removal of 10-20 mL solvent, which appeared to have an effect on the rate of the hydrolytic disassembly and rearrangement (see Figure 4.11). The reduced rate of reaction when filtrate is returned to the flask is ascribed to the decreased concentration of hydrolysed solid in the reaction mixture, which results in a reduced proabability of collision with important dissolved species for reintercalation processes. Further, the strong temperature dependence of organisation and reassembly steps mean that returning cold filtrate to the reaction flask will negatively affect the reaction rate.

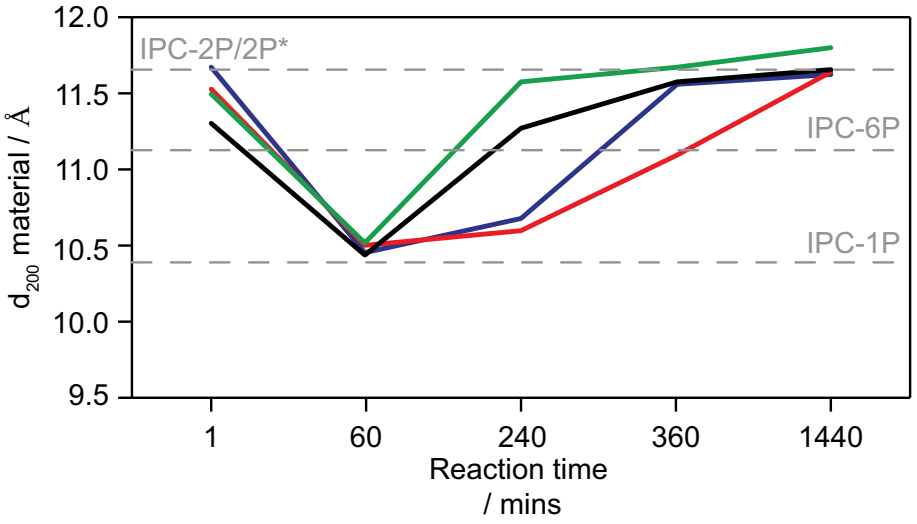

Figure 4.11: Plot of d_{200} reflection position as a function of reaction time of the disassembly and organisation steps in continual Ge-**UTL** hydrolyses under a range of conditions. 92 °C filtrate discard = red, 100 °C filtrate discard = blue, 92 °C filtrate replace = black, 100 °C filtrate replace = green. Expected d_{200} reflection position for key ADOR intermediates indicated on plot in grey.

The absolute ratio of solid : water is known to affect the expected products; Bignami *et al.* showed how the mechanism of the ADOR rearrangement is completely changed under low solid : water ratios, where the IPC-1P intermediate never fully forms and instead a gradual degermanation and reintercalation process of silicate species takes place, producing IPC-2P-like materials with increased disorder.[19]

To assess the effect of solid : water on the formation of intermediates in the ADOR hydrolysis of Ge-**UTL** in water at 92 °C, a series of reactions were carried out by varying this ratio and their products compared. Hydrolysing Ge-**UTL** for two hours should, under

standard conditions (solid : water 1:200) form IPC-1P. In some cases, however, lower solid : water hydrolyses may be desired; for example when ^{17}O-enriched materials are targeted (see Section 4.6.3).[19] Table 4.3 below shows that a ratio of 1:80 is sufficient at preserving the 'standard' 'high-volume' ADOR pathway at 92 °C and 100 °C, as evidenced by the formation of IPC-1P after 2 hours of reaction. This finding will be exploited to achieve ^{17}O-enriched materials that have been fully and extensively hydrolysed.

solid : water	Filtrate Discarded		Filtrate Replaced	
	IPC-1P formed? (92 °C)	IPC-1P formed? (100 °C)	IPC-1P formed? (92 °C)	IPC-1P formed? (100 °C)
1:200	✓	✓	✓	✓
1:80	✓	✓	✓	✓
1:60	✗	✗	✗	✓
1:40	✗	✗	✗	✗
1:8	✗	✗	✗	✗

Table 4.3: Formation of IPC-1P ADOR intermediate for the hydrolysis of Ge-**UTL** in water under varying solid : water and temperature conditions after two hours of reaction.

Considering the results of the reactions carried out in this section, some general considerations to be taken in to account for following ADOR reactions of Ge-**UTL** when aiming to follow the hydrolysis mechanism for 'high-volume' hydrolyses are as follows: all reactions where an external heat source is applied will be carried out at 92 °C, solid : water ratios of 1:80 or 1:200 will be used, and when taking multiple samples at specified time points during a continuing hydrolysis reaction, a similar proportion of the reaction solution will be removed from the flask as that of the proportion of solid removed from the overall reaction mixture and any reaction solution removed during sampling will not be returned to the reaction flask.

4.4.5 Optimised Reaction Protocols

4.4.5.1 Standard High-throughput Reaction

Zeolite **UTL** Si/Ge = 4.5 (600 mg) was hydrolysed in distilled water (120 cm^3) (solid : water 1:200) at 92 °C under rotation at 400 rpm for 8 hours. Samples were taken from the reaction at specified time intervals (for 1-5 minutes; every minute, for 5-60 minutes; every 5 minutes and for 60-480 minutes; every 30 minutes) in the minimum amount of hydrolysing solution. Isolated intermediates were filtered, washed with distilled water and dried at 80 °C for 10 minutes, before PXRD analysis.

4.4.5.2 Standard Hydrolyses

Zeolite **UTL** Si/Ge = 4.5 (200 mg) was hydrolysed in distilled water (40 cm^3) (solid : water 1:200) at 92 °C under rotation at 400 rpm for 1-24 hours. Samples were filtered, washed with distilled water and dried at 80 °C for 60 minutes.

4.4.5.3 Filtrate Replacement Hydrolyses

Zeolite **UTL** Si/Ge = 4.5 (600 mg) was hydrolysed in distilled water (120 cm^3) (solid : solute 1:200) at 92 °C under rotation at 400 rpm for 24 hours. Samples $\approx$ 100 mg in $\approx$ 15-20 cm^3 solute were taken from the reaction at specified time intervals (1, 60, 120, 300 and 1440 minutes) and were filtered and dried at 80 °C for 60 minutes. The isolated filtrate was returned to the reaction flask.

4.4.5.4 Filtrate Discard Hydrolyses

Zeolite **UTL** Si/Ge = 4.5 (600 mg) was hydrolysed in distilled water (120 cm^3) (solid : water 1:200) at 92 °C under rotation at 400 rpm for 24 hours. Samples $\approx$ 100 mg in $\approx$ 15-20 cm^3 water were taken from the reaction at specified time intervals (1, 60, 120, 300 and 1440 minutes) and were filtered and dried at 80 °C for 60 minutes.

4.4.5.5 Varied solid : water Hydrolyses

Zeolite **UTL** Si/Ge = 4.5 (200 mg) was hydrolysed in different volumes of distilled water (1.6, 8, 16, 40 cm^3) (solid : water 1:8, 1:40, 1:80, 1:200) at 92 °C under rotation at 400 rpm for 1-24 hours. Samples were filtered, washed with distilled water and dried at 80 °C for 60 minutes.

4.5 Following the ADOR Process using *ex-situ* ^{29}Si NMR Spectroscopy

The previous section addressed optimisation of ADOR hydrolyses to assess the mechanism of disassembly and reassembly of Ge-**UTL** in water. Although PXRD is effective at capturing the formation and lifetimes of different hydrolytic intermediates generated during hydrolysis, it provides an average picture of the long-range order of the system

and is unable to offer significant insight into the changes to local structure and the atomic-scale mechanism of disassembly or organisation taking place. However, the sensitivity to local structural disorder of solid-state NMR spectroscopy and the ability to probe certain species present in ADOR intermediates; such as Si – OH, using $^{1}H^{29}Si$ CP experiments; make it well-suited to study materials, processes and intermediates generated through the ADOR process.

Solid-state NMR spectroscopy has been used extensively in study of the ADOR process, shedding light on several important structural and mechanistic aspects unattainable through diffraction-based approaches. ^{29}Si NMR spectroscopy has been used to characterise the chemical environments of new zeolites and intermediates formed through the ADOR process, providing information on defect level and disparities between expected silanol concentrations from diffraction models and actual level of disassembly using Q^3:Q^4 ratios.[2,13,14,17–19,21,22,32,38–41] Furthermore, the study of degermanation processes in germanosilicate zeolites also provided information on the chemical shifts of silicon atoms located within the *d4r* of ADORable zeolites – something also achieved through ^{11}B NMR and its preferential location within the **UTL** framework.[10,33,34,42] ^{27}Al NMR spectroscopy has been employed to the extension of the ADOR process to catalytic applications and ^{27}Al NMR studies have monitored both synthetic and post-synthetic incorporation of Al into the **UTL** structure, with time-resolved studies offering insight into rate of incorporation under different reaction conditions.[7,10,15,40,43] ^{19}F NMR spectroscopy has proven valuable in the characterisation of ADORable germanosilicate materials by identifying the proportion and location of germanium within the *d4r* units. The preference of Ge to organise in *4r* sheets within *d4r* of **UTL**, rather than randomly is postulated to be a driving factor for the success of **UTL**-derived ADOR processes.[4,16,31,39,43,44] Further, ^{17}O NMR spectroscopy experiments have shown a surprising level of exchange of framework oxygen sites within the bulk zeolite layers in ^{17}O-enriched hydrolyses and demonstrated how the hydrolysis mechanism followed depends on system treatment; *e.g.*, reflux hydrolysis vs. mechanochemistry.[18,19,21]

In this section, ^{29}Si MAS NMR spectroscopy is used to explore the changes to the local structure of hydrolytic intermediates as they disassemble and organise to form crystallographically distinct materials. Further, changes to the local structure of crystallographically same IPC-1P intermediates, during the ‘induction period’ are also investigated.

4.5.1 Effect of Reaction Sampling on End Product

Using information obtained from studies in Section 4.4.4, the end products of hydrolyses carried out using the standard method (Section 4.4.5.2) and filtrate discard hydrolyses (Section 4.4.5.4) were compared after eight hours of hydrolysis, using X-ray diffraction and ^{29}Si solid-state NMR spectroscopy. Example PXRD patterns and ^{29}Si NMR spectra are displayed in Figure 4.12.

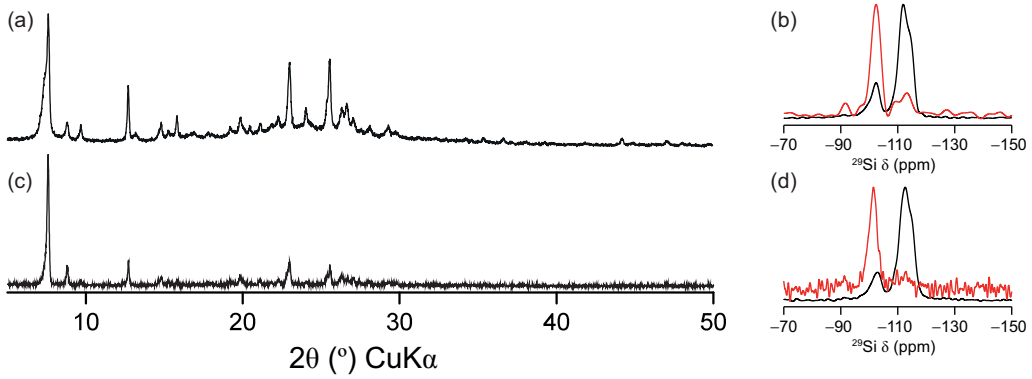

Figure 4.12: Comparison of (a,c) PXRD patterns and (b,d) (9.4 T, 14 kHz) ^{29}Si MAS NMR spectra of IPC-2P products obtained from the hydrolysis of **UTL** in water at 92 °C for eight hours using (a,b) standard hydrolyses and (c,d) filtrate discard hydrolyses. Red overlay in (b,d) corresponds to ^{1}H^{29}Si CP spectrum (5000 μs contact time).

Figure 4.12a,b show that both materials produced are the expected IPC-2P product and as such the ADOR transformation is complete. It is noted that a small amount of amorphous material has formed in (a), as shown by the slight broad feature in the baseline between $\approx$ 20-30 2θ. The solid-state NMR spectra in Figure 4.12b,d agree with the PXRD findings as the local structure of both materials appear as IPC-2P. Integration of ^{29}Si lineshapes using DMfit[45] produce Q^3:Q^4 ratios of 1:4.92 and 1:4.89 for standard and filtrare discard hydrolyses, respectively. It is interesting that both of these materials, which are fully organised to IPC-2P, exhibit Q^3:Q^4 significantly lower in Q^4 than that expected, when compared to idealised IPC-2P models derived from structural analyses. Further, the CP MAS spectra, shown overlaid, suggest that the two samples possess slightly different distributions of silanols. Both spectra show a significant peak in the Q^3 region for $Si(O-Si)_3O-H$, as expected, but the standard hydrolysis sample in Figure 4.12b also possesses a small amount of Q^2 $Si(O-Si)_2(O-H)_2$ species. Although a small amount of these Q^2 sites are present, this is not sufficient to indicate a vastly different mechanistic result is obtained when carrying out ADOR hydrolyses of **UTL** in water using either of these two methods, provided the temperature, time and initial solid : water remain consistent. Consequently they will both be used henceforth in this chapter to support NMR-spectroscopic investigations.

4.5.2 Intermediate Identification

To learn more about the changes to the local structure of ADOR intermediates formed during the hydrolysis of **UTL** in water, a series of standard hydrolysis reactions (see Section 4.4.5.2) were performed at 100 °C, taking samples after 1, 60, 240 and 480 minutes.[13] The kinetics of the ADOR hydrolysis reaction at this temperature mean that the expected products at each of these intervals are expected to be IPC-2P*, IPC-1P, IPC-2P and IPC-2P.[12] The PXRD patterns (Table 4.4 and Appendix Figure C.1) and ^{29}Si MAS NMR spectra (Figure 4.13) of the resulting materials are compared.

Hydrolysis Time / min	Expected Product	Expected d_{200} / Å	Experimental d_{200} / Å	Experimental Product
SM*	**UTL**	14.53	14.39	**UTL**
1	IPC-2P*	11.62	11.85	IPC-2P*
60	IPC-1P	10.40	10.58	IPC-1P
240	IPC-2P	11.62	11.58	IPC-2P
480	IPC-2P	11.62	11.60	IPC-2P

Table 4.4: Comparison of the (200) reflection position for products obtained by standard ADOR hydrolysis of Ge-**UTL** in water at 100 °C with their expected (200) peak positions.[13] * SM denotes Starting Material.

Table 4.4 shows that the isolated products of the 100 °C reactions have d_{200} reflection at positions similar to the ideal materials, so the reaction is deemed to have proceeded successfully. Furthermore, the ^{29}Si MAS NMR spectra (Figure 4.13) display a rapid spectral change from that of the parent **UTL** structure is seen after just one minute of hydrolysis, resulting in Q^3 and Q^4 signals as hydrolysis occurs. Normalising by Q^4 intensity in Figure 4.13 clearly shows how the proportion of Q^3 and Q^4 changes over time, with a maximum proportion of Q^3 sites seen after one hour for IPC-1P and the highest levels of disassembly and disorder. Following this, reorganisation and reintercalation processes occur to form IPC-2P at four and eight hours. Similar to that seen in Section 4.5.1, there is a discrepancy between the experimentally obtained Q^3:Q^4.

Hydrolysis Time / min	Structure-derived Q^3:Q^4	Experimentally-derived Q^3:Q^4
SM*	∞	∞
1	1:7.0	1:3.1
60	1:2.5	1:2.6
240	1:7.0	1:6.2
480	1:7.0	1:6.1

Table 4.5: Comparison of Q^3:Q^4 of materials obtained by standard ADOR hydrolyses of Ge-**UTL** in water at 100 °C with their expected Q^3:Q^4 derived from structural models. * SM denotes Starting Material.

Table 4.5 shows how, after 1 minute of hydrolysis, the level of germanium removal and silanol formation is significant with a lower Q^3:Q^4 than expected from structures indicated by PXRD. This corroborates with the idea that initial hydrolysis and germanium removal is incredibly rapid at 100 °C and shows that the separation of silica-rich layers happens at a slower rate than this initial germanium removal. Data for one hour shows a fairly good agreement for the highly disassembled intermediate, IPC-1P, before it reassembles to IPC-2P. The IPC-2P materials formed are more defective and silanol-rich than the structural models would predict. In reality, this persistently higher concentration of silanols may be caused by hydrolytic removal of germanium from within the silica-rich layers of the **UTL** material, or through incomplete reintercalation of silicon species from the reaction solution.

Whilst it is expected that the change in structure of the ADOR hydrolysis products will result in changes to the ^{29}Si MAS NMR lineshapes in Figure 4.13, it is interesting to observe that changes to the local structure of materials are observed even when the Q^3:Q^4 and PXRD-derived structures are the same. For example, IPC-2P* and IPC-2P (1 min *vs.* 4 hr *vs.* 8 hr samples all exhibit different lineshapes. Furthermore, there is evidence of a change in the local-environment of Q^4 species between 1 hr IPC-1P and the IPC-2P materials, even though the Q^4 species (present in the siliceous layers where ADOR processes are not expected), should be largely crystallographically similar in both of these materials. A subsequent study to explore this observation was carried out in Section 4.5.3.

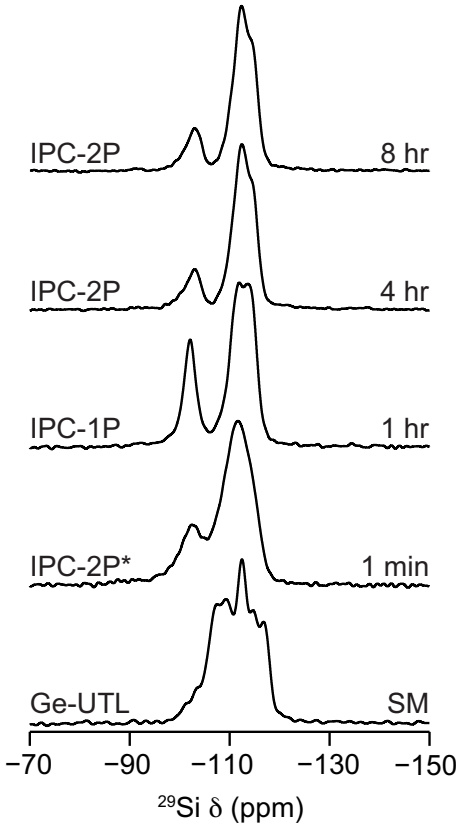

Figure 4.13: ^{29}Si (14 kHz MAS, 9.4 T) NMR spectra of products obtained from the hydrolysis of **UTL** in water at 100 °C using standard hydrolyses for varying amounts of time. Product identification from PXRD (left) and reaction time (right) are indicated on each spectrum trace.

4.5.3 The Induction Period

Within this section, the 'induction period' that takes place between disassembly and reassembly steps of the ADOR process is investigated. During this time, there are no visible changes to the long-range order of the disassembled IPC-1P intermediate, as shown in Figure 4.9, however, it is suspected that local structural changes occur that initiate silicon reintercalation, leading to the subsequent change in d_{200} and inter-layer spacing. The exact structural rearrangements occurring in the induction period are unclear, but it is clear that the rate at which they occur is dependent on the temperature of the reaction system. Lower reaction temperatures lengthen the lifetime of the IPC-1P phase dominance, following Avrami-Erofeev kinetics, with no change to d_{200} observed at all for reactions carried out below 70 °C.[12] A series of 92 °C standard hydrolysis reactions in water are investigated here, to explore the changes to the local structure occurring during **UTL** ADOR hydrolyses. The ^{29}Si MAS NMR spectra of the products are shown in Figure 4.14.

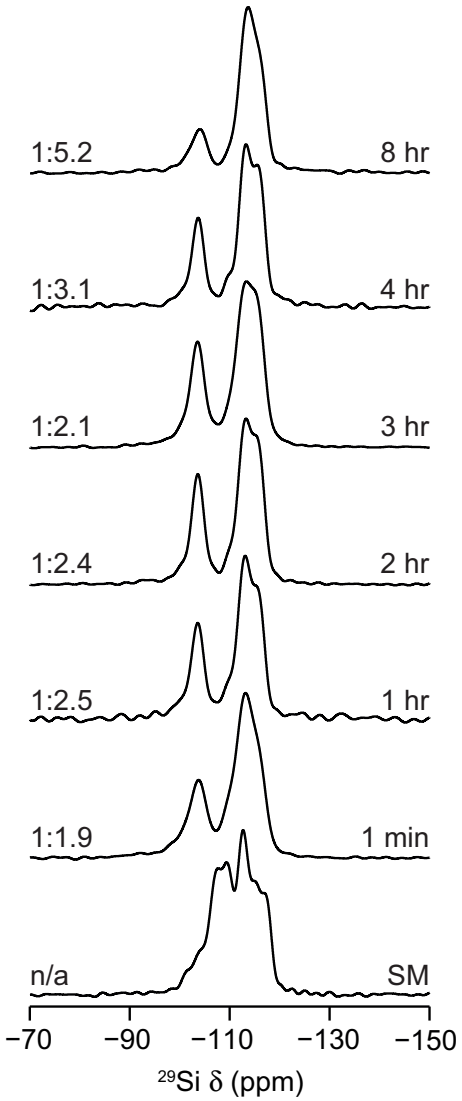

Figure 4.14: ^{29}Si (14 kHz MAS, 9.4 T) NMR spectra of products obtained from the hydrolysis of **UTL** in water at 92 °C using standard hydrolyses for varying amounts of time to study the induction period for reorganisation from IPC-1P. DMfit-derived Q^3:Q^4 (left) and reaction time (right) are indicated on each spectrum trace.

Figure 4.14, shows that the Q^3:Q^4 integral ratios for products isolated are as expected for ADOR hydrolyses taking place under these conditions with the dominant product in all reactions >1 hour being IPC-1P, with the exception of the eight hour experiment. Figure 4.9 shows that products present after one, two, three and four hours of reaction indicate a long induction period occurs and exhibit very similar long-range order. It is clear, however that during this time, the local structure of the intermediate materials constantly change, evidenced by the differences in lineshape and proportion of the Q^3 and Q^4 environments in the structures.

The highly disorganised nature of the IPC-1P intermediate makes it difficult to identify exactly which structural and environmental changes are observed when comparing the spectra in Figure 4.14, yet a few conclusions can be drawn. When comparing IPC-2P* materials at one minute with IPC-1P at times > 1 hour, the sharper lineshape in the latter makes it clear that the silanol (Q^3) distribution is more ordered here. This narrower lineshape persists again until the material changes phase by reorganisation to IPC-2P. More ordered silanols may be expected for IPC-1P materials as they occur dominantly at the interface of the inter-layer region of the silicon-rich 2D sheets.

The change in ^{29}Si chemical shift in spectra in Figure 4.14 indicate that there is a constant change of local structure of the Q^4 silicon environments in the siliceous IPC-1P structure, prior to any re-intercalation of aqueous silicate species occurring. Exactly what structural rearrangements happen during this period is unclear, but there appears to be the growth and loss or disordering and reordering of the local structure as the material remains as IPC-1P. The disordered nature of the IPC-1P structure and the large number of crystallographically-distinct silicon sites in the material make it difficult to identify exactly what these different Q^4 line-shape components are from ^{29}Si NMR spectra. It is possible that this is to do with the departure from and rearrangement to a material that contains *s4r*. Amongst the large-pore germanosilicates with *d4r*, Ge-**UTL** is unique for its tendency to form Ge *s4r*, or *4r* 'faces' of Ge_4O_4 rings within the *d4r*, which makes the 'inter-layer region' increasingly hydrolytically unstable and therefore ideal for ADOR-type transformations.[35,39,46] It it feasible to suggest that the local structure of defective IPC-1P, rich in germanium- or silicon-rich rings and an IPC-2P precursor where silicon-rich *s4r* are required may be somewhat similar, hence the similarity of the lineshapes produced by one hour and four hour samples in Figure 4.14. The changes observed between these timepoints at two and three hours may be part of the reorganisation process. Either way, it is clear that reorganisation of the material is necessary in order to form a product with the local structure as captured in the result at four hours, in order to kickstart silicon reintercalation and the 'organisation' step of the ADOR process.

There is a preference for germanium to locate in specific positions for Ge-**UTL**, particularly on the surface of the siliceous sheets, connected through T–O–T linkage to the *d4r*.[46] This position should not actively take part in the ADOR process, however germanium in this 'silicate layer' position will be hydrolysed upon contact with water. This may offer an explanation as to why the Q^3:Q^4 ratio observed is lower than that expected for IPC-1P as one germanium removed here will produce four Q^3 silanol groups. Yet further

hydrolysis or reintercalation at this position should not result in a change to the inter-layer spacing of the material. Reintercalation is in fact necessary to facilitate the production of an inter-layer species from which *s4r* in IPC-2P can grow. It is proposed therefore to be vital that silicon reintercalation at this T6 position occurs during the induction period in order to allow filling of the inter-layer space (organisation) and an increase in d_{200} to form IPC-2P structures.

4.6 Following the ADOR Process using ^{17}O NMR Spectroscopy

Previous sections in the chapter have highlighted the importance of PXRD and ^{29}Si MAS NMR spectroscopy techniques to study the ADOR process. The former underlined the effect of ADOR transformations on the long-range order of materials and intermediates formed and showed that through adaption of hydrolysis conditions the products of ADOR transformations of **UTL** can be controlled. The latter showed how the local structural disorder of these ADORable intermediates is also influenced by hydrolysis conditions how this can influence the next stages of the reactions, providing complementary information to X-ray diffraction.

The introduction of the ^{17}O isotope to the reaction and its subsequent study using ^{17}O NMR spectroscopy can provide a further insight into the mechanism of the ADOR process, by shining a light on specific zeolite reactivity. Employing ^{17}O-enriched reagents ($H_2{}^{17}O$, $^{17}O_{2(g)}$) in specifically-designed ADOR reactions enables the study of specific solid-liquid, solid-gas interactions and can provide information on how reversible kinetic bond lability and irreversible thermodynamic bond hydrolysis processes are facilitated in ADOR transformations.

4.6.1 Strategy

The high costs associated with the use of ^{17}O-enriched reagents mean their use in an extensive suite of experiments to explore the effect of the ADOR process on the local coordination environment of oxygen in **UTL** materials is not feasible. Instead, using the knowledge of ADOR process tunability and control as explored in Sections 4.4 and 4.5 it is possible to design a set of specific experiments that target specific materials generated in the ADOR process for further study. This in turn enables extraction of information from interesting structures, revealing information about the ADOR mechanism and the roles of different intermediates.

4.6.2 Enriched UTL Material Preparation

The following sections detail the synthetic protocols used to successfully enrich targeted **UTL** and **UTL**-derived materials in ^{17}O. The ratio of solid : water used in each reaction is indicated where appropriate.

4.6.2.1 $H_2{}^{17}O$ Continual Hydrolysis Reaction

Calcined zeolite **UTL** (Si/Ge = 4.5) (800 mg) was combined with a 3.5% solution of $H_2{}^{17}O$ (prepared from distilled water and 20% $H_2{}^{17}O$ enriched water) (64 mL). The mixture was heated to 92 °C for 24 hours under rotation at 400 rpm. Samples were taken from the reaction at 1 minute and 1, 2, 5 and 24 hours such that the solid : water ratio in the flask remains constant. The solids were filtered and washed with the minumum amount (< 5 mL) of distilled water and dried at 80 °C for 10 minutes. Solid : water = 1 : 80 (by mass).

4.6.2.2 $H_2{}^{17}O$ Low-volume Hydrolysis Reaction

Calcined zeolite **UTL** (Si/Ge = 4.5) (300 mg) was combined with a 20% solution of $H_2{}^{17}O$ made up from distilled water and 40% $H_2{}^{17}O$ enriched water (16 mL). The mixture was heated to 92 °C for 18 hours under rotation at 400 rpm. The reaction was cooled to room temperature, filtered and washed with 5 mL distilled water. The solid was dried at 80 °C for 10 minutes. Solid : water = 1 : 8 (by mass).

4.6.2.3 $H_2{}^{17}O$ Incipient Wetness Impregnation

Calcined zeolite **UTL** (Si/Ge = 4.5) (200 mg) was combined with a solution of hydrochloric acid (6 M, 40 mL). The mixture was heated to 92 °C for 18 hours under rotation at 400 rpm. The reaction was cooled to room temperature, filtered and washed with distilled water. The solid was dried at 80 °C for 10 minutes and found to be IPC-2P. Solid : water = 1 : 200 (by mass).

Isolated IPC-2P as prepared above was impregnated dropwise with 40% $H_2{}^{17}O$ (100 μL) at a rate slower than that rate at which the enriched water is absorbed into the pores of the material. In practice, addition of enriched water took $\approx$ 10 minutes at room temperature and produced a dry IPC-2P solid enriched in $H_2{}^{17}O$.

4.6.2.4 $H_2{}^{17}O$ Slurries

Calcined zeolite **UTL** of desired composition (25 mg) was placed in a PTFE HRMAS NMR 4 mm rotor insert and 40% $H_2{}^{17}O$ enriched water (25 μL) added gradually under mixing. The rotor insert was sealed using the accompanying plug and cap and was stored in a sample vial on the benchtop. Solid : Water = 1 : 1 (by mass). See also Section 3.5.4.

4.6.2.5 $^{17}O_{2(g)}$ Post-synthetic gas-exchange

Calcined zeolite **UTL** (Si/Ge = 4.5) ($\approx$ 50 mg) was dehydrated under vacuum overnight ($\approx 2.0x10^{-3}$ Torr) at 300 °C, cooled and sealed under argon. The sample was then sealed in a quartz tube before evacuation and exposure to an atmosphere of 200 mbar 70% $^{17}O_{2(g)}$. The material was sealed under the enriched gas atmosphere and heated in a tube furnace at 700 °C for 48 hours, using a positive and negative temperature ramp of 5 °/min. See also Section 3.5.5.

4.6.2.6 $H_2{}^{17}O$ Ball-milling

Calcined zeolite **UTL** (Si/Ge = 4.5) ($\approx$ 500 mg) was combined with 40% $H_2{}^{17}O$ enriched water (100 μL) in a PTFE bottle with yittria-stablized zirconia (YSZ) milling media of 3 mm diameter (250 g). The bottle was sealed and milled on rotary ball mill at 150 rpm for varying periods of time; 30, 120 an 240 minutes. The resulting materials were filtered and washed using ethanol (50 cm^3) and dried at 80 °C for 10 minutes. Procedure developed in reference 21.

4.6.2.7 Synthesis of $Ge^{17}O_2$

Germanium ethoxide (1.0 mL), distilled water (0.5 mL) and 40% $H_2{}^{17}O$ (0.5 mL) were stirred at 400 rpm at room temperature for 24 hours. The white gel formed upon completion of hydrolysis was dried at 80 °C under flowing nitrogen for five hours. The material was calcined under flowing nitrogen using a stepped ramping program of 300 °C for 2 hours and 575 °C for five hours, with a positive temperature ramp of 1 °C/min up and a negative 2 °C/min down. Procedure adapted from that in reference 47.

4.6.3 Hydrolysis Reactions

The results in this section follow on from previously published work that aimed to uncover the mechanism of the ADOR process under low volume (low solid : water) conditions.[19] In addition to finding the new mechanism for hydrolysis in low-volume conditions, the study revealed that the rearrangement and exchange of framework oxygen species with those in the hydrolysing solution was more extensive than first thought. Significant exchange of ^{17}O into framework sites in the two-dimensional zeolite layers was observed using ^{17}O solid-state NMR spectroscopy at high magnetic fields.[19] This result confirmed not only the expected presence of $Si-{}^{17}OH$ silanols formed irreversibly through hydrolysis but also the reversible kinetic formation of $Si-{}^{17}O-Si$ linkages that make up the zeolitic layers of hydrolysed IPC-*n*P intermediates.

By recreating and redeveloping standard hydrolysis reactions in the presence of $H_2{}^{17}O$, this section uncovers more about the rate at which reversible bond lability and irreversible bond hydrolysis processes occur in Ge-**UTL** and the related IPC-2P intermediate structure.

4.6.3.1 High-volume Continuous Hydrolysis

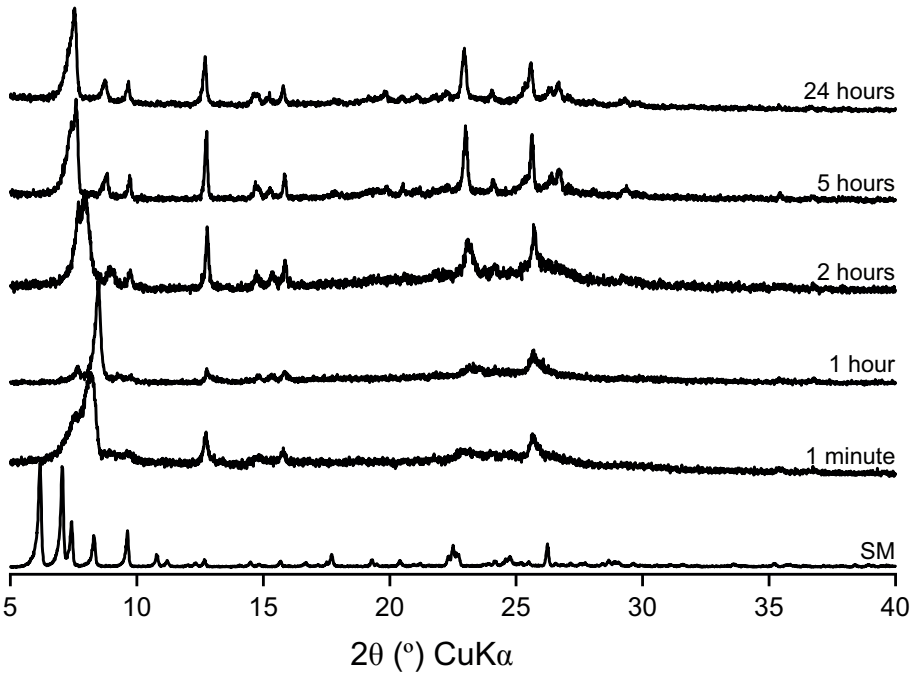

Figure 4.15: Powder X-ray diffraction patterns of products obtained from the continual hydrolysis of Ge-**UTL** in water (3.5% $H_2{}^{17}O$) at 92 °C. Hydrolysis time is indicated on each trace.

Hydrolysing Ge-**UTL** using the method outlined in Section 4.6.2.1 successfully resulted in the high-volume ADOR hydrolysis mechanistic pathway (see Section 4.4.4 for further details) with a solid : water of 1 : 80. This ratio and a 3.5% concentration of $H_2{}^{17}O$ provided an adequate amount of ^{17}O incorporated into disassembled materials to facilitate facile NMR spectroscopy study. The PXRD patterns and quantitative ^{17}O and ^{29}Si NMR spectra of the isolated products of this reaction are displayed in Figure 4.15 and Figure 4.16, respectively. Comparison of the identity of intermediates suggested from PXRD-derived long-range order structural assignment and NMR spectral intensities are detailed in Table 4.6.

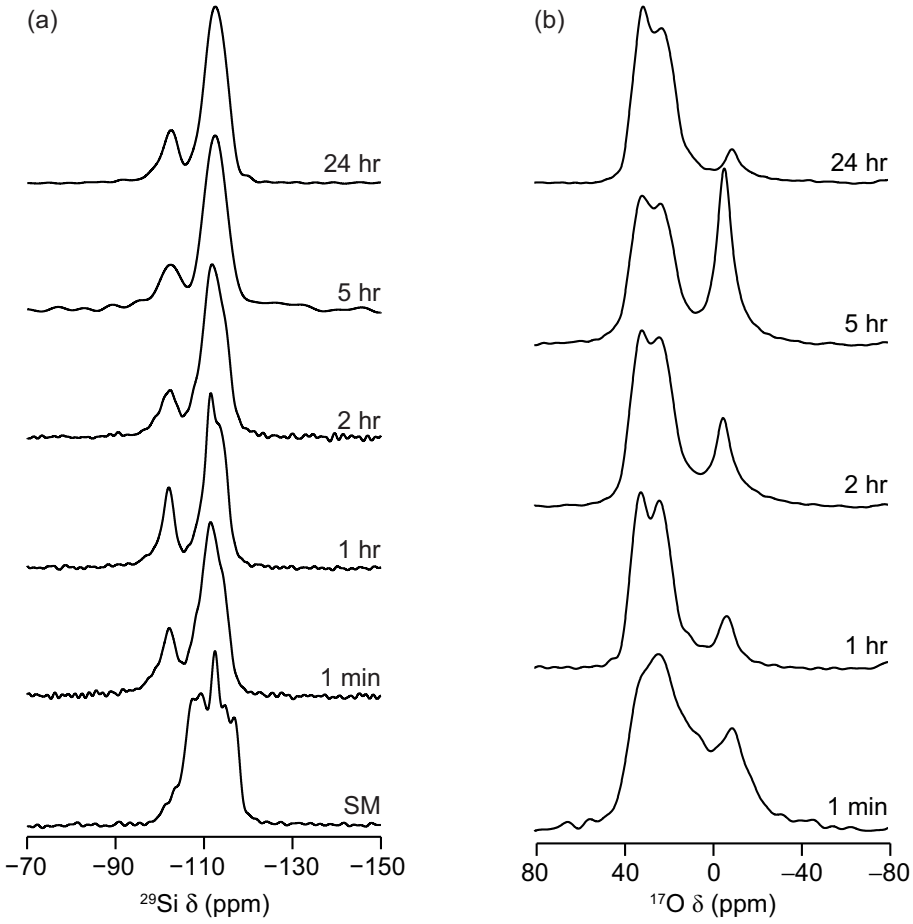

Figure 4.16: (a) ^{29}Si (14 kHz MAS, 9.4 T) quantitative and (b) ^{17}O (14 kHz MAS, 20.0 T) short flip angle NMR spectra of products obtained from the continual hydrolysis of Ge-**UTL** in water with a 3.5% $H_2{}^{17}O$ concentration at 92 °C. Hydrolysis time is indicated on each trace.

The diffraction patterns in Figure 4.15 confirm that the expected hydrolysis pathway is largely followed and in qualitative agreement with the observed Q^3:Q^4 ratio (Table 4.6) derived from ^{29}Si MAS NMR spectra in Figure 4.16a. In this instance, the induction period is shorter than typically expected for a 92 °C reaction under 'high-volume' conditions. This is likely caused by the lower solid : water ratio of 1:80 (previous studies based

on 4.4.5.2 used 1:200). This lower solid : water will produce a higher concentration of aqueous species, whilst still following the high-volume disassembly mechanism, which will likely result in a faster reintercalation / pre-assembly period.[14,19]

Hydrolysis Time / min	Expected Product	Experimental d_{200} / Å (product)	Experimental Q^3:Q^4 (product)
1	IPC-2P*	11.31 (IPC-2P*)	1:2.4 (IPC-1P)
60	IPC-1P	10.42 (IPC-1P)	1:3.1 (IPC-1P)
120	IPC-1P	11.23 (IPC-6P)	1:3.4 (IPC-1P-6P)
300	IPC-6P	11.65 (IPC-2P)	1:4.4 (IPC-6P)
1440	IPC-2P	11.73 (IPC-2P)	1:5.9 (IPC-2P)

Table 4.6: Comparison and characterisation of materials obtained from the continual hydrolysis of Ge-**UTL** in water with a 3.5% $H_2{}^{17}O$ concentration at 92 °C.

Alongside the hydrolysis taking place in the above reaction, the spectra, acquired at high field, provide evidence of additional processes taking place during ADOR hydrolysis that confirm exchange of **UTL** framework oxygen species. Both the nature of this enrichment and the rate at which it occurs is surprising; ^{17}O NMR signal can be acquired in these materials even within one minute of reaction in enriched water, which is comparable to the rate at which the rapid ADOR hydrolysis occurs under these conditions. In order to further understand the surprisingly rapid enrichment process observed, the short-flip ^{17}O MAS NMR spectra have been normalised in Figure 4.17.

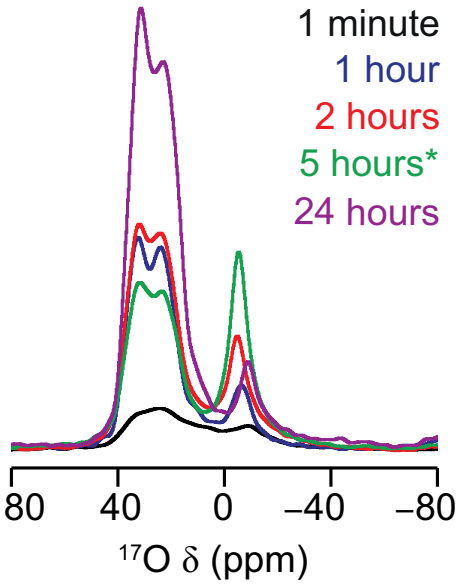

Figure 4.17: ^{17}O (14 kHz MAS, 20.0 T) short flip angle NMR spectra of products obtained from the continual hydrolysis of Ge-**UTL** in water with a 3.5% $H_2{}^{17}O$ concentration at 92 °C. Spectra are scaled to take account of the number of transients averaged and the mass of sample in the rotor. Hydrolysis time is indicated on each trace. The small amount of five hour sample recovered (*) was studied by packing into a 4 mm PTFE HRMAS NMR rotor insert.

From Figure 4.17, it is is clear that rapid framework enrichment takes place at short hydrolysis times, with a continued high rate of framework exchange up until IPC-1P becomes the dominant phase at 1-2 hours. As the reaction time increases and the material transforms to IPC-2P, exchange of the framework oxygens continues, producing a highly enriched material after 24 hours. The lower absolute level of enrichment obtained for the material at five h reaction time arises from the low volume of sample recovered from this reaction. This had to be packed with a 4 mm PTFE HRMAS insert within the rotor. Although this, in principle, can be accounted for in terms of the mass, it isn't clear if the measurement is strictly comparable. Furthermore, this sample also has a surprisingly high level of water present (signal at 0 ppm), which will lead to small differences after scaling for the sample mass.

In order to aid spectral deconvolution of the complex lineshapes in the ^{17}O MAS NMR spectra in Figure 4.17b and learn more about the local structural environment of the newly-exchanged oxygen species in the materials, two dimensional high-resolution solid-state NMR experiments were performed. $\{^{1}H\}^{17}O$ MQMAS NMR experiments for selected intermediates are displayed in Figure 4.18.

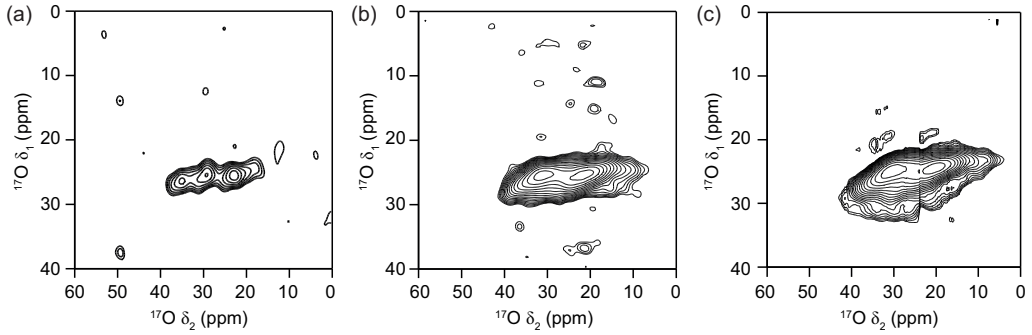

Figure 4.18: ^{17}O (14 kHz MAS, 20.0 T) $\{^{1}H\}^{17}O$ MQMAS NMR spectra of products obtained from the continual hydrolysis of Ge-**UTL** in water with a 3.5% $H_2{}^{17}O$ concentration at 92 °C. Spectra displayed correspond to samples hydrolysed for (a) 1 minute, (b) 2 hours and (c) 24 hours.

The spectra in Figure 4.18 show that as hydrolysis time increases, there is a qualitative increase in sensitivity of each MQMAS NMR experiment, which have been recorded using the same spectral parameters and similar sample masses. With the exception of Figure 4.18a, where a small amount of germanium is likely present, the materials in each spectrum are purely siliceous, taking the form of layered Q^4 tetrahedral silicate sheets terminated by Q^3 silanol groups. Therefore, potentially resolvable resonances in these spectra correspond to oxygen present in framework Si – ^{17}O – Si linkages and Si – ^{17}OH silanols.[19] Using published examples from the literature,[48–57] the resonance observed can be best assigned to Si-O-Si linkages within the structure of the intermediates. The crystal structure of the **UTL** framework contains 23 crystallographically-distinct oxygen sites, 21 of which are found in the siliceous layers.[29] However, the complexity of the **UTL** framework and the broadening of spectral lineshapes attributed to second-order quadrupolar effects, which are not removed in MQMAS, precludes the resolution and assignment of any specific crystallographic sites to regions within the observed resonance.[58,59]

Interestingly, no evidence of isotopically-enriched silanols are observed in the ^{17}O MQMAS spectra (despite clear evidence for silanol formation in ^{29}Si NMR spectra). Considering their role in the hydrolysis reaction and their interactions with aqueous species in this reaction system, possible reasons for this could include a back reaction with water in the air (unlikely given the sample handling), or more likely rapid relaxation arising from

proximity to, or exchange with, water in the pores. This was observed in previous work on ADOR layered intermediates where Si – ^{17}OH signal was not seen in MQMAS experiments unless very strong ^{1}H decoupling was used, and ^{1}H^{17}O CP signal was extremely poor unless at very low temperature.[19] ^{1}H^{17}O CP MAS NMR experiments at room temperature were also unsuccessful for the samples studied here, leading to the conclusion that the rapid relaxation and/or ongoing exchange with the water of the terminal silanol species is occurring in these samples.[19]

4.6.3.2 Low-volume Hydrolyses

To further understand the mechanistic pathway associated with the low-volume hydrolysis experiment carried out in reference 19, a ^{17}O-enriched hydrolysis experiment was devised using low-volume conditions (see Section 4.6.2.2). Contrary to the previous experiment however, this hydrolysis was carried out in the absence of hydrochloric acid, using distilled water (3.5 % $H_2{}^{17}O$) only. The NMR-spectra of the resulting IPC-2P product are displayed in Figure 4.19.

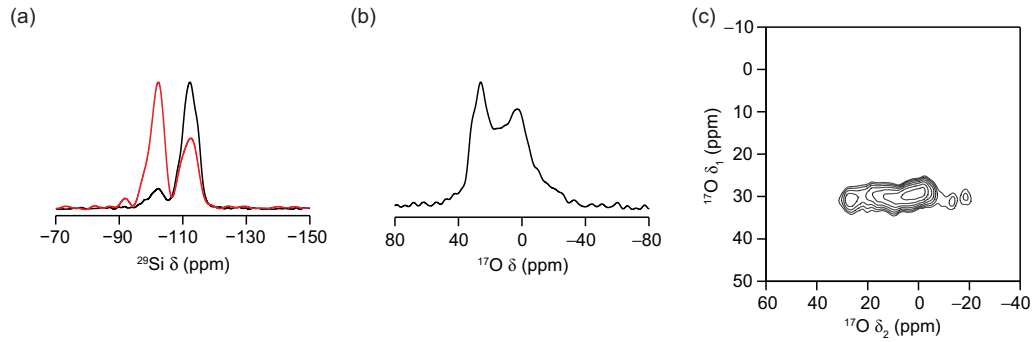

Figure 4.19: (a) ^{29}Si (14 kHz MAS, 9.4 T) quantitative and (b,c) ^{17}O (14 kHz MAS, 14.1 T) NMR spectra of Ge-**UTL** hydrolysed in 3.5% $H_2{}^{17}O$ at 92 °C under low volume conditions. (b) short flip angle and (c) $\{^{1}H\}^{17}O$ MQMAS NMR spectra. Red overlay in (a) corresponds to ^{1}H^{29}Si CP spectrum (5000 μs contact time).

Integration analysis of the quantitative ^{29}Si MAS NMR spectrum in Figure 4.19a yields a Q^3:Q^4 ratio of 1:4.1, indicating the local structure of the material is similar to IPC-2P, in agreement with the PXRD pattern and confirming that structural disassembly and hydrolysis has occurred. The $^{1}H^{29}Si$ CP MAS NMR spectrum overlaid in Figure 4.19a indicates the presence of both Q^3 and a low level of Q^2 defects present in the material following hydrolysis, as would be expected. In the absence of acid, it is anticipated that the mechanism for ADOR disassembly will differ; previous studies have shown how alteration of hydrochloric acid concentration can be used to control the products of the ADOR hydrolysis reaction with increasing concentrations of acid helping to push the products formed from IPC-1P to IPC-2P-like materials as this helps to aid reintercalation of aqueous silicate species.[14] Here however, as described above, the product formed resembles IPC-2P and so the effect of acid concentration on the ^{17}O-exchange of species into the zeolite framework can be compared to previously published data.[19]

The level of ^{17}O enrichment of ADOR intermediates found by Bignami *et al.* and the enrichment observed in 4.6.3.1 is very similar to that seen in Figure 4.19. Hydrolysing the material in this way once again results in the exchange of ^{17}O isotope into the Si – O – Si sites of the zeolite layers, forming an isotopically-enriched IPC-2P-like material (see Figure 4.19b,c). In comparison, the levels of enrichment observed in this experiment are likely to be lower than those seen in reference 19, owing to the lower proportion of $H_2{}^{17}O$ present in the reaction mixture (20% v.s. 3.5%).

Differences in the extent to which the material is enriched may also be caused by the differences in absolute concentration of zeolite and $H_2{}^{17}O$ in high- and low-volume hydrolyses. High (solid : water = 1:80) and low (solid : water = 1:8) hydrolysis reactions proceed through different mechanisms and so it may be expected that the framework enrichment observed in their corresponding spectra are affected by this. *i.e.*, the more extensive rearrangement observed under high-volume conditions may present the opportunity to access further Si – O – Si linkages for which a less complete rearrangement under low-volume conditions cannot.[19]

Once again unfortunately, the high structural similarity of oxygen environments within the structure of the **UTL** silicate layers and the second-order quadrupolar broadening effects present make difficult the assignment of resolved oxygen sites to any particular specific group within the IPC-2P structure and as several hypotheses cannot be confirmed on the basis of the current experiments. It remains clear, however that exchange of framework oxygen in Si – O – Si sites with $H_2{}^{17}O$ is a favourable process.

4.6.3.3 Incipient Wetness Impregnation of IPC-2P

It is desirable to distinguish whether the exchange of framework oxygens observed in previous hydrolyses and ^{17}O NMR studies is consequential of ADOR processes, or whether this exchange occurs independently from hydrolytic disassembly and rearrangement. Furthermore, as the ADOR mechanism is strongly temperature dependent, the effect of temperature on any the framework oxygen exchange will also be explored. To achieve this, a sample of IPC-2P was prepared using high-volume hydrolysis in 6M HCl. The material was dried before reintroduction of $H_2{}^{17}O$ by direct dropping of 40% enriched water onto the sample (see Section 4.6.2.3). ^{17}O NMR spectra of the post-synthetically treated ^{17}O-enriched material are shown in Figure 4.20.

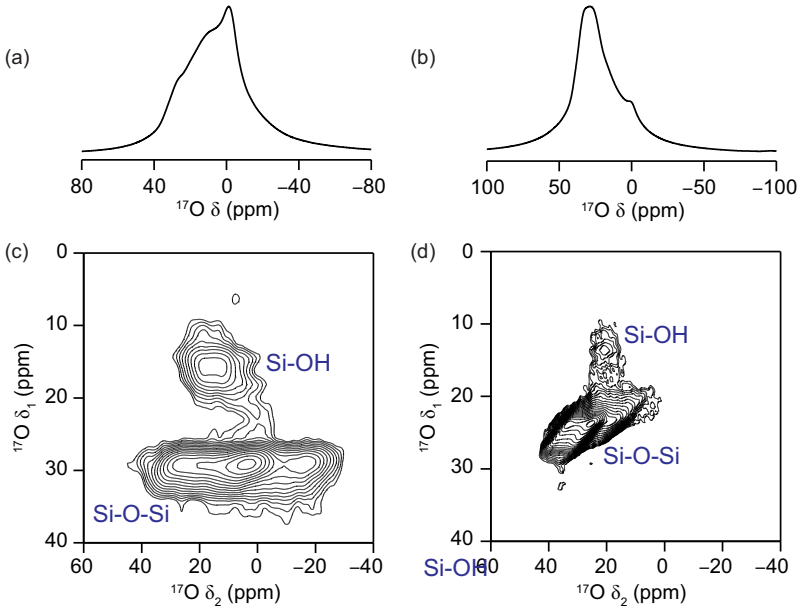

Figure 4.20: (a,c) (14 kHz MAS, 14.1 T) and (b,d) (14 kHz MAS, 23.5 T) (a,b) ^{17}O quantitative short flip angle and (c,d) $\{^1H\}^{17}O$ MQMAS NMR of IPC-2P post-synthetically enriched in ^{17}O by incipient wetness impregnation using $H_2{}^{17}O$.

From Figure 4.20 it is clear that this method of treatment also facilitates the framework exchange of oxygen atoms with those found in the $H_2{}^{17}O$ reagent. Extensive incorporation of ^{17}O isotope is observed for materials treated in this way, with evidence of both $Si-{}^{17}O-Si$ and $Si-{}^{17}OH$ resolvable in MQMAS spectra recorded at both fields (14.1 T (Figure 4.20c) and 23.5 T (Figure 4.20d). Resonances resolved at 14.1 T correspond roughly to $\delta_1 \approx$ 26-35 ppm ($Si-{}^{17}O-Si$) and $\delta_1 \approx$ 16-23 ppm ($Si-{}^{17}OH$).

The evidence of framework enrichment observed in this experiment provides a number of pieces of information that help to provide a better understanding of bond lability processes occurring in ADOR intermediates. Firstly, the extent of the enrichment observed here is significant, confirming that the process for this exchange is energetically favourable, even when at room temperature and in the absence of a solvent. The mechanism behind this enrichment therefore must not require a carrier phase or a large excess of water molecules in order to facilitate it. Secondly, as no ADOR processes are occuring in this sample, it is likely that more than just ADOR-reactive species are taking part in the framework oxygen exchange. Terminal silanol groups generated from the enrichment process are enriched as are silicate linkages, which are not expected to be reactive under these conditions. Furthermore, the extent to which the material is enriched overall points to the fact that a greater proportion of the silicate linkages than those involved in ADOR surface reintercalation processes have been exchanged, meaning those linkages within the two-dimensional silicate sheets are also reactive under these conditions, however further NMR experiments and lineshape fitting analysis would be required to confirm this. This would mean the mechanism of this room-temperature lability, is not constrained by steric effects under these conditions, which may prohibit mechanisms involving large amounts of water.

Whilst this experiment above confirms room-temperature lability in the disassembled IPC-2P intermediate by simple hydration with small amounts of water, several questions about the mechanism for this process remain. The IPC-2P material, although not compromised in the process is inherently defective, containing a large amount of silanol defects on its surface. The role of these in the structure and reactivity of the material is not fully understood. Secondly, despite significant washing with distilled water upon workup, the fact that the material was hydrolysed using 6 M HCl means that the presence of additional acidic proton species within the material framework cannot be completely ruled out. It may be possible that the presence of any excess hydrated acidic protons could facilitate the reversible bond cleavage and framework oxygen exchange observed in NMR studies.

To further understand the processes occurring that lead to the surprising framework oxygen exchange observed in Ge-**UTL** and its ADOR-derived daughter material, further experiments exploring alternative methods for framework enrichment are desired.

4.6.4 *In-situ* Slurrying Reactions

The successful enrichment of IPC-2P by room-temperature treatment with $H_2{}^{17}O$ in Section 4.6.3.3 prompted the study of pristine **UTL** starting materials, in an attempt to understand the effect of framework integrity on the observed oxygen exchange. As it has been shown that ^{17}O exchange takes place at low-volume and room temperature, it should be straightforward to study the mechanism using small amounts of zeolite and $H_2{}^{17}O$. This makes the reaction easily scalable, making it adaptable for *in-situ* solid-state NMR analysis (see 4.6.2.4). Provided the system remains sealed, this approach provides the additional possibility for time-resolution; giving an idea of any reactivity over time as other processes, *e.g.*, ADOR hydrolysis or framework degradation take place. The effect of framework composition on any bond lability has also been investigated in this study, with germanium and aluminium content of parent **UTL** material explored.

4.6.4.1 High-Ge Ge-UTL

A sample of high-germanium Ge-**UTL** was prepared with Si/Ge = 3. This material was combined in a slurry with either $H_2{}^{17}O$ (40%) or $H_2{}^{16}O$ and studied using solid-state NMR spectroscopy (as in Section 4.6.2.4).

The PXRD patterns are shown in Figure 4.21, revealing that even with these very low ratios of solid : water (1 : 1 by mass), framework hydrolysis is observed as the structure becomes similar to IPC-2P. The low relative proportion of water in the slurry and its confinement as an essentially sealed system within the HRMAS insert may make it difficult for a complete ADOR process to take place with insufficient opportunity for full cleansing if the inter-layer space that would allow disassembly and organisation to occur. Instead, it is most likely that both of these processes are incomplete in materials and that the identity of the intermediate is germanium-containing IPC-2P*.

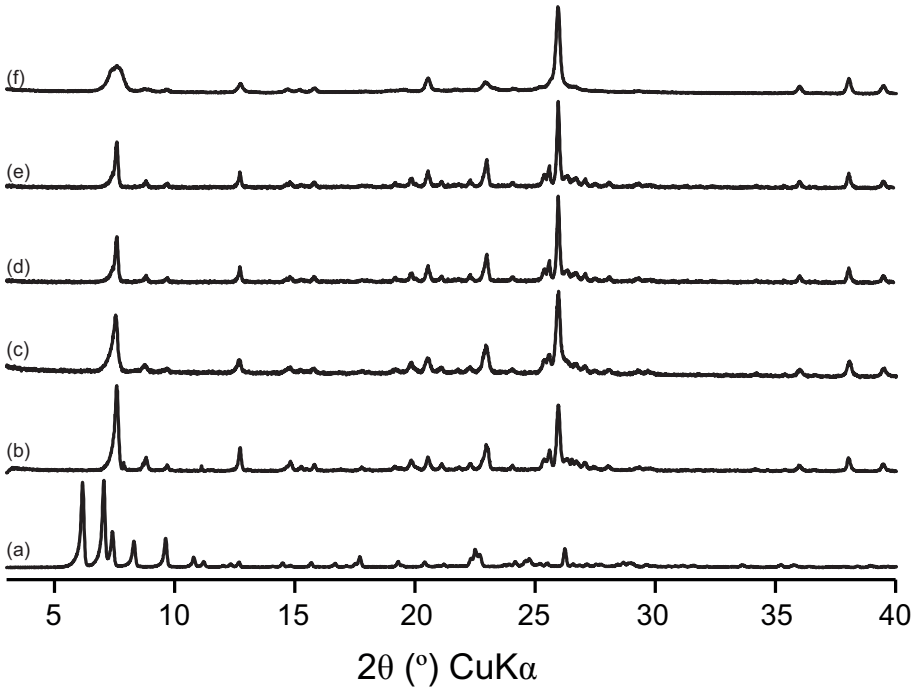

Figure 4.21: PXRD patterns of high-Ge Ge-**UTL**, slurried in $H_2{}^{16}O$ for varying amounts of time. (a) Starting Material (b) 7 days, (c) 50 days, (d) 100 days, (e) 300 days and (f) 500 days.

Analysing the extent of the disassembly occurring during this treatment, it can be seen that the **UTL** material is essentially broken down to IPC-2P* after seven days in the slurry (Figure 4.21b). The material stays this way under these conditions until 500 days (Figure 4.21f), where some broadening of the (200) reflection is observed. It may be expected that the material has started to degrade after this amount of time under these

conditions. The strong reflection at ≈ 26 °present strongly in all slurry diffraction patterns is assignable to α quartz phase GeO_2. This material is formed from the germanium removed during hydrolysis in the slurry and crystallises out as there is insufficient liquid to keep the metal solvated under these conditions.

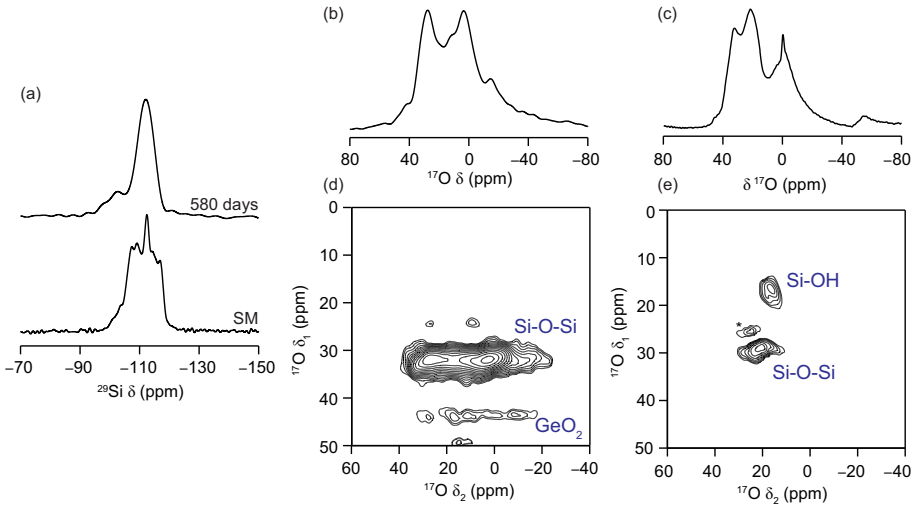

Figure 4.22: (a) ^{29}Si (14 kHz MAS, 9.4 T) quantitative, (b,d) ^{17}O (14 kHz MAS, 14.1 T) and (c,e) ^{17}O (14 kHz MAS, 20.0 T) time-resolved NMR spectra of high-Ge Ge-**UTL**, slurried in $H_2{}^{17}O$ for varying amounts of time. Oxygen spectra taken at slurry age (b,d) 583 and (c,e) 27 days using (b,c) short flip-angle and (d,e) $\{^1H\}^{17}O$ MQMAS NMR experiments.

NMR spectra of samples slurried with $H_2{}^{17}O$ (Figure 4.22) reveal evidence of two competing chemical processes. Firstly, ^{29}Si MAS NMR spectra (Figure 4.22a) show clear evidence of ADOR hydrolysis in water occurring on the small scale of the *in-situ* rotor insert experiment ≈ 50 mg and under very low-water conditions (solid : water = 1 : 1), producing a Q^3:Q^4 of 1:3.8. This is similar to that seen by Bignami *et al.* for the hydrolysis of **UTL** under similar conditions using 6 M HCl.[18,19] Secondly, surprisingly high levels of ^{17}O framework enrichment are observed in ^{17}O NMR experiments (Figure 4.22b-d). Resonances present in $\{^1H\}^{17}O$ MQMAS NMR spectra acquired at 20.0 T (Figure 4.22e) can be assigned to Si-OH and Si-O-Si species at δ_1 ≈ 12-18 ppm and 25-30 ppm, respectively. The high density of silanols present in the 27 day spectrum is attributed to the high germanium content of the framework, which has resulted in extensive disassembly and a highly disordered intermediate. As the slurry ages to 583 days (Figure 4.22d), Si-O-Si species are again present as well as the formation of a small amount of crystalline, quartz-phase $Ge^{17}O_2$ at δ_1 ≈ 28-38 ppm and 42-45 ppm, respectively. This small amount of $Ge^{17}O_2$ formed corroborates with the observation of a similar species in the PXRD patterns of Figure 4.21.[47]

4.6.4.2 Low-Ge Ge-UTL

A similar set of NMR and PXRD experiments was performed for a sample of low-germanium Ge-**UTL** (Si/Ge = 4.5).

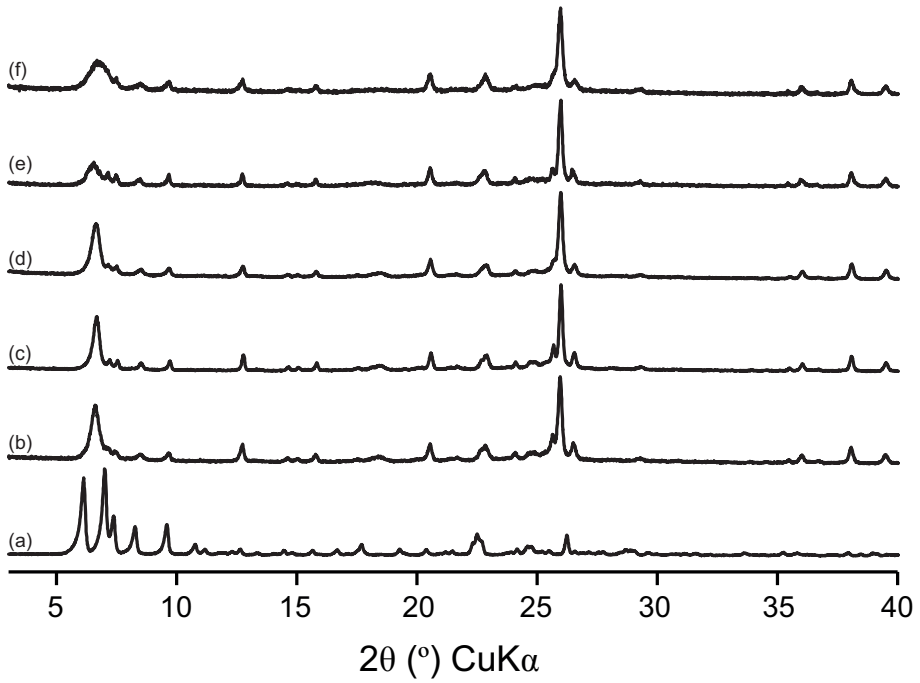

Figure 4.23: PXRD patterns of low-Ge Ge-**UTL**, slurried in $H_2{}^{16}O$ for varying amounts of time. (a) Starting Material (b) 7 days, (c) 50 days, (d) 100 days, (e) 300 days and (f) 500 days.

The PXRD patterns are shown in Figure 4.23, revealing again that even with these very low ratios of solid : water (1 :1 by mass), clear framework hydrolysis is observed as the structure becomes IPC-2P-like. Again, evidence of ADOR hydrolysis is observed for this material, at a similar rate to that of the high-Ge Ge-**UTL** material in Figure 4.21 as the IPC-2P* material is formed.

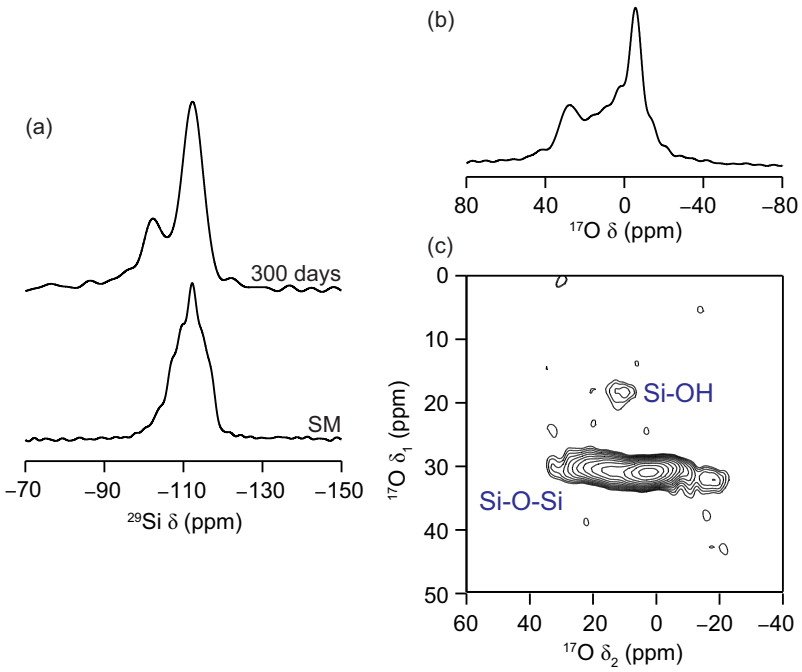

Figure 4.24: (a) ^{29}Si (14 kHz MAS, 9.4 T) quantitative and (b,c) ^{17}O (14 kHz MAS, 14.1 T) time-resolved NMR spectra of low-Ge Ge-**UTL**, slurried in $H_2{}^{17}O$ for varying amounts of time. Oxygen spectra taken at slurry age of 300 days using (b) short flip-angle and (c) $\{^1H\}^{17}O$ MQMAS NMR experiments.

NMR spectra of the sample slurried with $H_2{}^{17}O$ (Figure 4.24) again reveal evidence of two competing chemical processes; irreversible ADOR hydrolysis and reversible bond lability and ^{17}O framework enrichment. ^{29}Si MAS NMR spectra (Figure 4.24a) show clear evidence of ADOR process hydrolysis in water occurring on the small scale, producing a Q^3:Q^4 of 1:3.4. This is slightly slower than that seen for high-Ge Ge-**UTL** material in Figure 4.22, attributable to the lower germanium content of the material here. Moderate levels of ^{17}O framework enrichment are observed in ^{17}O NMR experiments (Figure 4.24b,c), but longer slurrying times are needed to get significant framework enrichment, which indicates that the germanosilicate ADOR hydrolysis process has an influence on the rate of reversible bond lability facilitated for a material. ADOR hydrolyses introduce defects and silanol species to the structure, which could facilitate reversible lability within the layers. Resonances present in $\{^1H\}^{17}O$ MQMAS NMR spectra at 14.1 T (Figure 4.24c) can be assigned to Si-OH and Si-O-Si species at $\delta_1 \approx$ 18-22 ppm and 26-34 ppm. Interestingly, the lower amount of germanium present in the starting material means that even at long slurry times it is not possible to resolve any $Ge^{17}O_2$ in the NMR spectra, even though some evidence is seen by the PXRD slurry study in (Figure 4.23b).

4.6.4.3 Si-UTL

A similar set of NMR and PXRD experiments was performed for a sample of post-synthetically de-germanated Si-**UTL** (Si/Ge = 120).

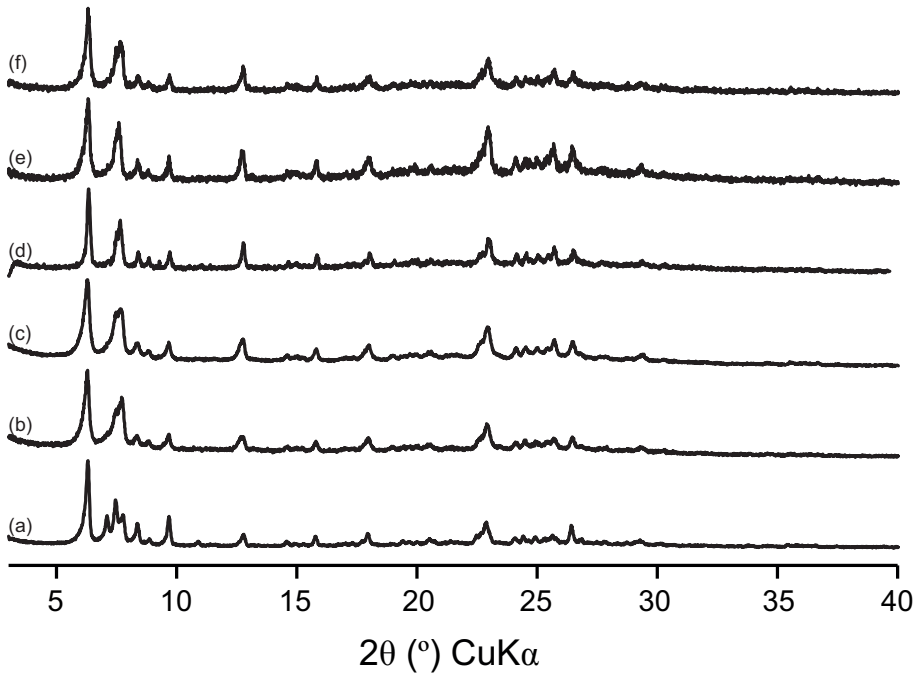

Figure 4.25: PXRD patterns of Si-**UTL**, slurried in $H_2{}^{16}O$ for varying amounts of time. (a) Starting Material (b) 7 days, (c) 50 days, (d) 100 days, (e) 300 days and (f) 500 days.

The PXRD patterns shown in Figure 4.25 and reveal the significance of germanium presence within the slurried framework. Although slightly defective, the Si-**UTL** framework appears to withstand the slurrying treatment and no changes to the long-range order crystallinity of the material are observed.

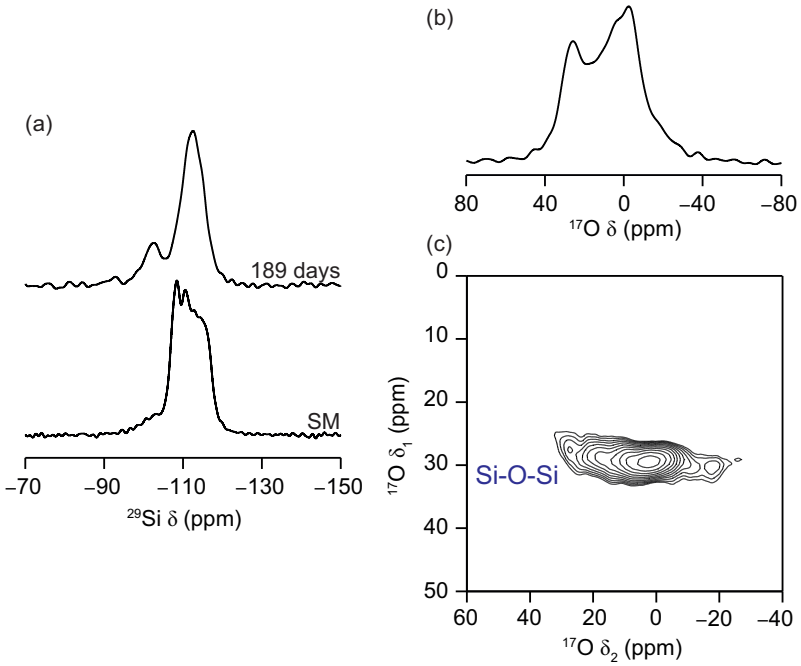

Figure 4.26: (a) ^{29}Si (14 kHz MAS, 9.4 T) quantitative and (b,c) ^{17}O (14 kHz MAS, 14.1 T) time-resolved NMR spectra of Si-**UTL**, slurried in $H_2{}^{17}O$ for varying amounts of time. Oxygen spectra taken at slurry age of 300 days using (b) short flip-angle and (c) $\{^1H\}^{17}O$ MQMAS NMR experiments.

NMR spectra of the slurry with 40% enriched water (Figure 4.26) again reveal evidence of two competing chemical processes; irreversible ADOR hydrolysis and reversible bond lability and ^{17}O framework enrichment. Despite the degermanation process, ^{29}Si MAS NMR spectra (Figure 4.26a) show clear evidence of ADOR process hydrolysis in water occurring on the small scale, producing a Q^3:Q^4 of 1:3.4. The surprisingly high concentration of Q^3 sites observed compared to the lack of change to the PXRD patterns of slurried intermediates indicates that germanium removal from the *d4r* units may introduce defects that cause a more extensive destruction of part of these units, without compromising the overall positioning and orientation of the two-dimensional zeolitic sheets. Moderate levels of ^{17}O framework enrichment are observed in ^{17}O NMR experiments (Figure 4.26b,c), which is surprising for a pure-silica zeolite (where there are, in principle, no hydrolytically accessible Ge atoms). However, exchange is likely enabled by the availability of silanol groups in the starting material, which would be expected to be resolved at $\delta_1 \approx$ 15-20 ppm in Figure 4.26c. The resonance present in $\{^1H\}^{17}O$ MQMAS NMR spectra at 14.1 T (Figure 4.26c) can be assigned to Si-O-Si species at $\delta_1 \approx$ 25-35 ppm.

4.6.4.4 Al,Ge-UTL

A similar set of measurements were also performed for a sample of hydrothermally synthesised Al,Ge-**UTL** (Si/Al/Ge = 90/5/1, (Si/Al = 17).

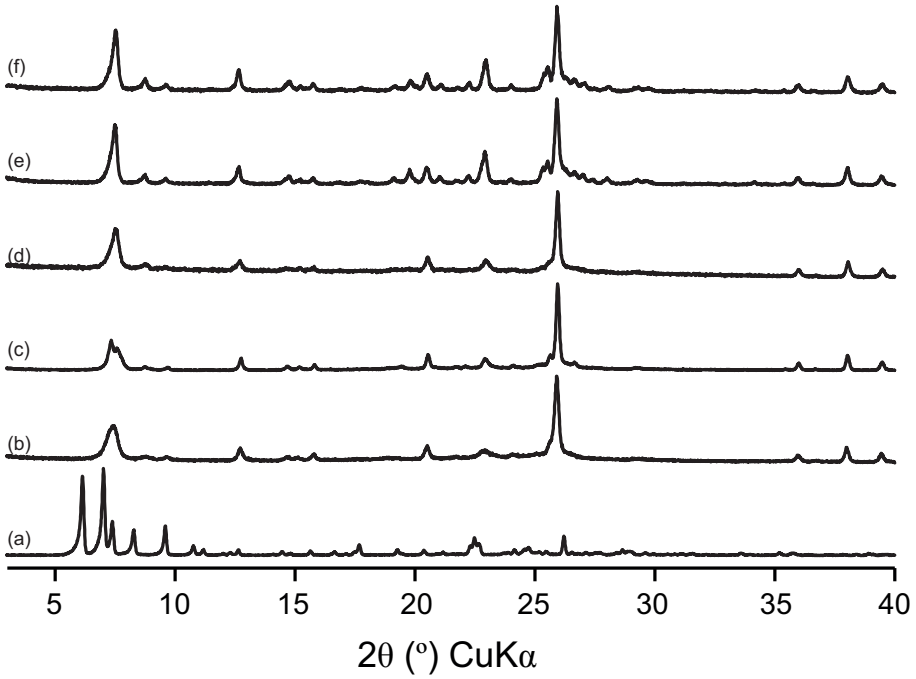

Figure 4.27: PXRD patterns of Al,Ge-**UTL**, slurried in $H_2{}^{16}O$ for varying amounts of time. (a) Starting Material (b) 7 days, (c) 50 days, (d) 100 days, (e) 300 days and (f) 500 days.

The PXRD patterns shown in Figure 4.23, reveal that even with these very low ratios of solid : water (1 : 1 by mass), distinct framework hydrolysis is observed as the structure becomes IPC-2P-like. It appears that the inclusion of aluminium and germanium in the structure in this instance has produced a highly hydrolytically unstable material, which breaks down to IPC-2P* as was seen for both high-Ge and low-Ge Ge-**UTL** samples.

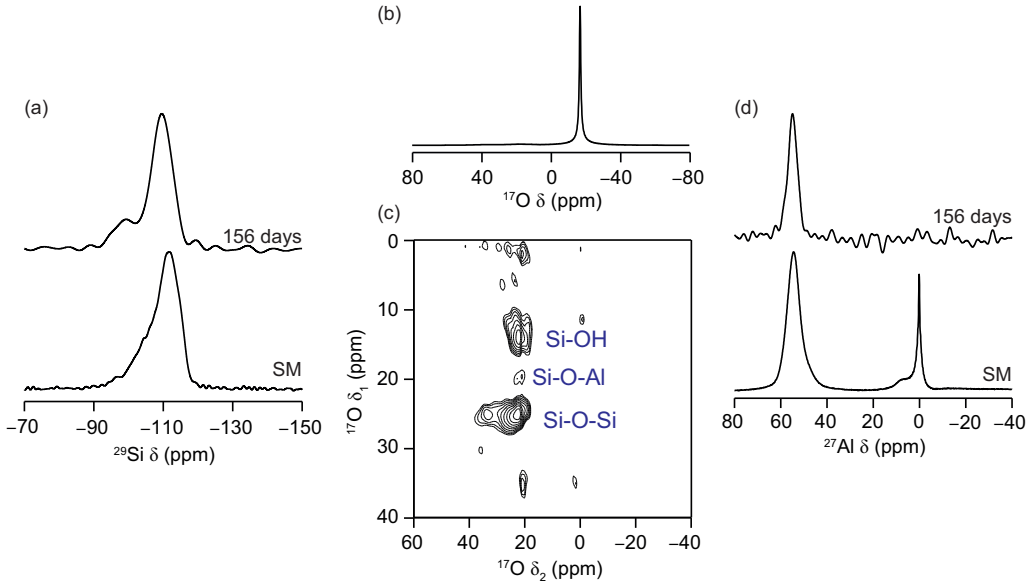

Figure 4.28: (a) ^{29}Si (14 kHz MAS, 9.4 T) quantitative, (b,c) ^{17}O (14 kHz MAS, 20.0 T) and (d) ^{27}Al (14 kHz MAS, 9.4 T) quantitative time-resolved NMR spectra of Al,Ge-**UTL**, slurried in $H_2{}^{17}O$ for varying amounts of time. Oxygen spectra taken at slurry age of 17 days using (b) short flip-angle and (c) $\{^1H\}^{17}O$ MQMAS NMR experiments.

NMR spectra of the sample slurried with enriched water (Figure 4.28) again reveal evidence of two competing chemical processes; irreversible ADOR hydrolysis and reversible bond lability, leading to ^{17}O framework enrichment. ^{29}Si MAS NMR spectra (Figure 4.28a) show clear evidence of ADOR hydrolysis in water occurring on the small scale, producing a Q^3:Q^4 of 1:3.6. It is unclear, however, whether this Q^3 site formation is completely attributable to ADOR hydrolysis or in fact is also to do with partial zeolite degradation. The idea of partial zeolite degradation is supported by considering the ^{27}Al MAS NMR spectra in Figure 4.28d. While tetrahedral aluminium is seen in slurried samples, there is a loss of octahedral aluminium when slurried and the significant decrease in the amount of signal obtained indicating that aluminium is lost from the structure of the zeolite and is now likely found in solution. In spite of this, some ^{17}O framework enrichment is observed in ^{17}O NMR experiments (Figure 4.28b,c). It is possible to observe this in $\{^1H\}^{17}O$ MQMAS NMR spectra recorded at 20.0 T (Figure 4.28c) resonances that can be assigned to Si-OH, Si-O-Al and Si-O-Si species at $\delta_1 \approx$ 11-15 ppm, 20-21 ppm and 25-28 ppm, respectively. Overall, however, information from silicon, aluminium and oxygen NMR spectra here would suggest that the calcined Al,Ge-**UTL** framework is effectively unstable to hydrolytic treatment even if some reversible bond lability processes are observed in ^{17}O NMR spectra.

4.6.5 GeO_2

To confirm the assignment of the resonance at $\delta_1 \approx$ 42-45 ppm in Figure 4.22 to quartz-phase $Ge^{17}O_2$, a sample of this material was prepared according to literature procedure (Section 4.6.2.7).[47] The resulting ^{17}O NMR spectra of the material are displayed in Figure 4.29.

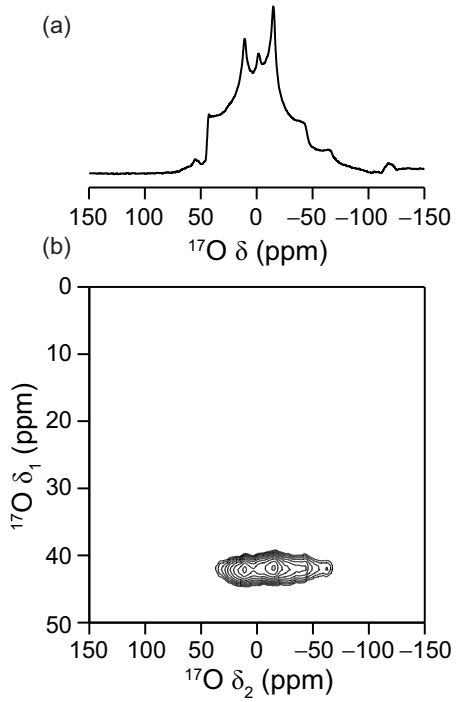

Figure 4.29: ^{17}O (14 kHz MAS, 14.1 T) NMR spectra of hydrothermally prepared $Ge^{17}O_2$. (a) quantitative short-flip angle and (b) $\{^1H\}^{17}O$ MQMAS NMR experiments.

Figure 4.29b shows a single environment as expected for $Ge^{17}O_2$, in agreement with reference 47, with a high C_Q (7.1 MHz) as expected for $Ge^{17}O_2$, along with a sharp line shape, centred at 0 ppm, attributed to water. Following this characterisation, the resonance at $\delta_1 \approx$ 42-45 ppm in slurried ADOR hydrolysis samples can be assigned to $Ge^{17}O_2$.

4.6.6 Gas-enriched Ge-UTL

Analysis of samples enriched using the slurrying method described above has provided information on the local structure of oxygen in IPC-2P*-type materials. For some of the ^{17}O MQMAS NMR spectra presented in Figure 4.22, Figure 4.24, Figure 4.26 and Figure 4.28, the Si−O−Si resonances often appear to comprise of more than one overlapped component, particularly in the region of 20 to −20 ppm δ_2, where the 'step' of the quadrupolar lineshape appears more significant than expected for a second-order broadened lineshape. To expand the knowledge of oxygen environments resolved in ^{17}O

NMR spectra of **UTL** materials, high-temperature framework oxygen exchange under a $^{17}O_{2(g)}$ atmosphere ($^{17}O_{2(g)}$ gas-enrichment) was performed (Section 4.6.2.5). This process should identify initial oxygen environments present in a standard Ge-**UTL** sample and may increase understanding of any highly overlapped resonances present in oxygen NMR spectra of the IPC-2P* slurry products.

4.6.6.1 Product Characterisation

^{17}O NMR spectra of Ge-**UTL** (Si/Ge = 4.5) post-synthetically exchanged with $^{17}O_{2(g)}$ are shown in Figure 4.30. The MQMAS NMR spectrum of the material (Figure 4.30b) shows signal in the region typically associated with Si – O – Si species, suggesting these have been enriched. The linkages present in this material however, also include Si-O-Ge and Ge – O$_G$e, which are known to possess similar characteristic NMR parameters.[47,60,61] It is possible therefore that the resonance observed at 14.1 T contains overlapped signals for different oxygen species. This is perhaps confirmed by the short-flip angle spectrum in Figure 4.30a, which clearly comprises more than one quadrupolar lineshape.

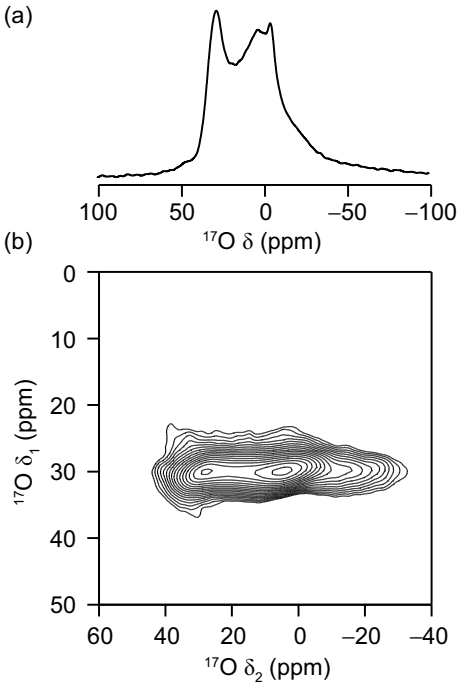

Figure 4.30: ^{17}O (14 kHz MAS, 14.1 T) NMR spectra of low-Ge Ge-**UTL**, post-synthetically oxygen exchanged in a 70% atmosphere of $^{17}O_{2(g)}$ by heating to 700 °C for 48 hours, following an initial 700 °C dehydration step overnight. (a) Quantitative short-flip angle and (b) $\{^1H\}^{17}O$ MQMAS NMR experiments.

4.6.6.2 Effect of Field Strength

The high similarity and overlap of the resonances present in Figure 4.30 mean it is not possible to fully determine the NMR parameters of the oxygen sites for a typical low Ge Ge-**UTL** material. To gain further insight, the effect of magnetic field strength on resonance position was investigated. ^{17}O NMR spectra were acquired at fields of 9.4, 14.1, 20.0 and 23.5 T and are displayed in Figure 4.31. For quadrupolar resonances possessing a very similar isotropic chemical shift, the NMR frequency is inversely dependent to the applied magnetic field[61] by:

$$\delta_{cg} = \delta_{iso} - \frac{3}{40}F(I)\frac{C_Q^2}{\nu_o^2}(1+\frac{\eta^2}{3}), \tag{4.1}$$

where δ_{cg} and δ_{iso} are the centre of gravity and isotropic chemical shift, respectively, *F(I)* is the spin-dependent factor of the central transition ($\frac{2}{25}$ for $I = \frac{5}{2}$ nucleus), $\mathrm{C_Q}$ and η_{Q} are the magnitude and asymmetry of the quadrupolar interaction, respectively and $\mathrm{v_0}$ is the magnetic field strength. The effect of this is such that the centre of gravity (COG) of the signal tends to their isotropic chemical shift. In this instance, where the lineshapes of Si−O−Si/Ge linkages will also be broadened by the local compositional disorder in the zeolite, considering the field dependence of the centres of gravity of the lineshape component will provide information on the NMR parameters and the different species present.

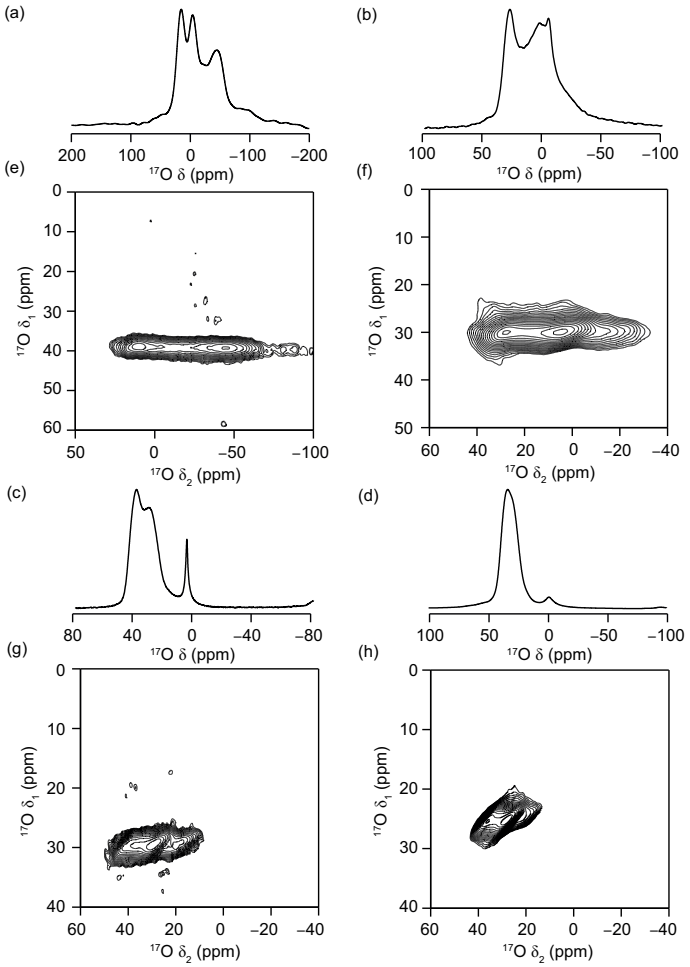

Figure 4.31: ^{17}O (14 kHz MAS) NMR spectra of gas-enriched Ge-**UTL** sample, acquired at (a,e) 9.4 T, (b,f) 14.1 T, (c,g) 20.0 T, (d,h) 23.5 T. (a-d) Quantitative short-flip angle and (e-h) $\{^1$H$\}^{17}$O MQMAS NMR experiments.

Figure 4.31 demonstrates how the magnetic field strength has an effect on the signal in the ^{17}O MQMAS NMR spectra for gas-enriched Ge-**UTL**. When field-strength is increased, there is evidence for the presence of two distinct resonances. The resonances are least resolved at 9.4 T, where a combination of the effect of field strength, chemical shift and the large C_Q of components present (expected C_Q of Si$-$O$-$Si/Ge $\approx$ 5.0-6.0 MHz) make resolution more difficult. In contrast, the MAS spectra at this field clearly cannot be explained by the presence of a single second-order broadened lineshape. By extracting individual rows from the sheared MQMAS, the COG of the individual lineshapes can be extracted in δ_2, giving some insight into the isotropic value of their chemical shift. By rearranging Equation 4.1 to:

$$\delta_{cg} = \frac{3C_Q^2 F(I)}{40}(1+\frac{\eta^2}{3}) \cdot \frac{1}{\nu_o^2} + \delta_{iso}, \tag{4.2}$$

it can be seen how the isotropic chemical shift can be estimated for these species for a linear plot, where the y-intercept is equal to the value of δ_{iso}. The resulting plot for gas-enriched Ge-**UTL** is displayed in Figure 4.32.

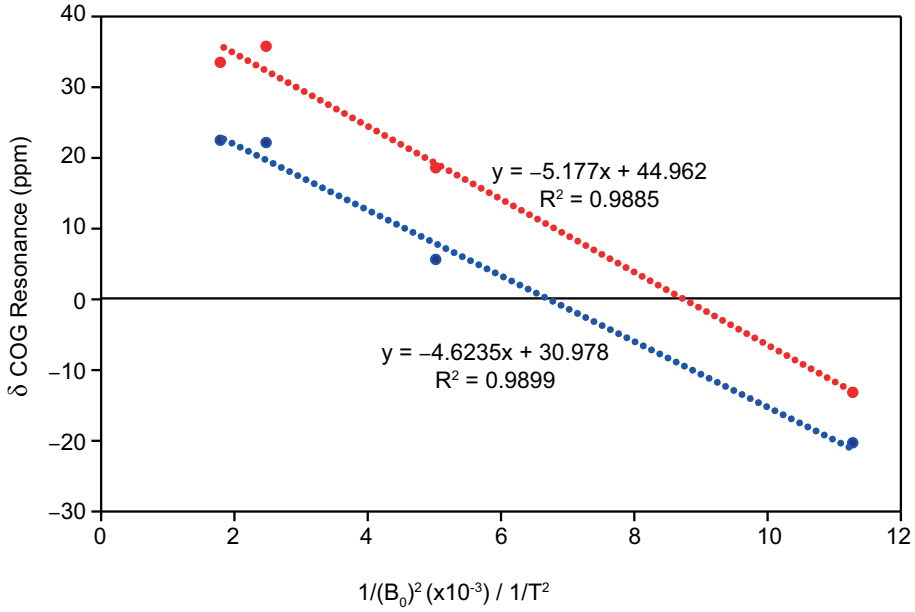

Figure 4.32: COG of resonances for gas-enriched Ge-**UTL** plotted as a function of the inverse square of the field strength at which they were recorded. Si−O−Si = red, Si−O−Ge = blue.

From Figure 4.32, evidence for two similar resonances in MQMAS NMR spectra is provided. These resonances have similar δ_{iso} of $\approx$ 31 and 45 ppm (error estimated to be $\pm$ 2 ppm), so may be overlapped at certain fields. Furthermore, it is observed that as the gradients of both lines observed are similar, significant changes in magnetic field will be needed to resolve these species. Considering the gradient of the lines produced is influenced by the C_Q of resonances (see Equation 4.2), this is unsurprising. The potential framework species observed in spectra of this gas-enriched Ge-**UTL** are likely limited to Si−O−Si/Ge, (as the prevalence of Ge−O−Ge in **UTL** materials is not always known, owing to Si/Ge content and Ge distribution throughout the framework) both of which will possess similar quadrupolar coupling constants in this material.[57,61–63] Based on the knowledge obtained and the results of DFT calculations, the strongly overlapped resonances in ^{17}O NMR spectra of gas-enriched Ge-**UTL** (Figure 4.31) and some related ^{17}O slurry end products are assigned as follows: Si−O−Si at $\delta_{\text{iso}} \approx$ 45 ppm (broadened over 40 - −20 ppm δ_2 in 14.1 T, 14 kHz MAS NMR spectra) and Si−O−Ge at $\delta_{\text{iso}} \approx$ 31 ppm (broadened over 20 - −40 ppm δ_2 in 14.1 T, 14 kHz MAS NMR spectra). From Equation

4.1, the value of P_Q for the Si–O–Si and Si–O–Ge resonances can be calculated from the plot in Figure 4.32, taking values of 5.2 and 5.1 MHz, respectively (expected error ± 0.2 MHz). P_Q can also be calculated from δ_1 and δ_2 positions, however owing to difficulties associated with estimating COG in both dimensions for overlapped lineshapes, the method calculating from δ_2 only was preferred.

4.6.7 Ball-milled Ge-UTL

There has been a high degree of interest recently in using facile, ambient and mechanochemical approaches to ^{17}O-enrich organic, inorganic and framework materials.[64–69] By combining efforts to increase the understanding of the ADOR process with the drive for sustainability and scalability of chemical processes, a mechanochemical approach to the ADOR process was developed (Section 4.6.2.6).[21] The approach resulted in successful hydrolysis of a parent Ge-**UTL** material to produce various daughter zeolites with reduced reaction and processing times and using less solvent under ambient conditions.[21] The conditions for hydrolysis used here can also provide an interesting view on the effect of mechanochemistry on the local structure of the zeolite material and as such, NMR spectroscopy may provide information on how the ADOR process proceeds under extremely low volume conditions (solid : water = 5 : 1 (mass)) and when significant external force is present.

4.6.7.1 Effect of Milling Time

The ball-milling reaction of Ge-**UTL** with $H_2{}^{17}O$ (40%) was performed for varying lengths of time lengths of time to gain insight into the rate at which framework hydrolysis proceeds, the level and position of framework enrichment and the local structure of the intermediates formed. Samples were isolated after 30, 120 and 240 mins of milling time. After just 30 mins of milling time the samples began to resemble a highly disordered IPC-2P* type intermediate by PXRD (from the position of the (200) reflection), however the Q^3:Q^4 from ^{29}Si MAS NMR spectroscopy of 1:3.2-3.8 indicate that the material has been hydrolysed and is highly defective and rich in silanols (see Appendix Figure D.1). In contrast to the end products of other non-sealed hydrolysis reactions systems, whose products are purely siliceous, the ball-milled materials have a Si/Ge of 10-20 (EDX).

Analysis of the ^{17}O NMR spectra of the materials provides no evidence of significant framework enrichment within the first 30 minutes of hydrolysis under mechanochemical conditions, with no significant signal observed in ^{17}O NMR spectra, despite some

evidence for ADOR hydrolysis from PXRD patterns and ^{29}Si MAS NMR spectra.[21] As mechanochemical treatment continues however, higher levels of framework enrichment of hydrolysed IPC-2P*-like materials can be seen (Figure 4.33), estimated to be in the region of 10%, when compared to levels of sensitivity seen for related ^{17}O-enriched materials.[70–73]

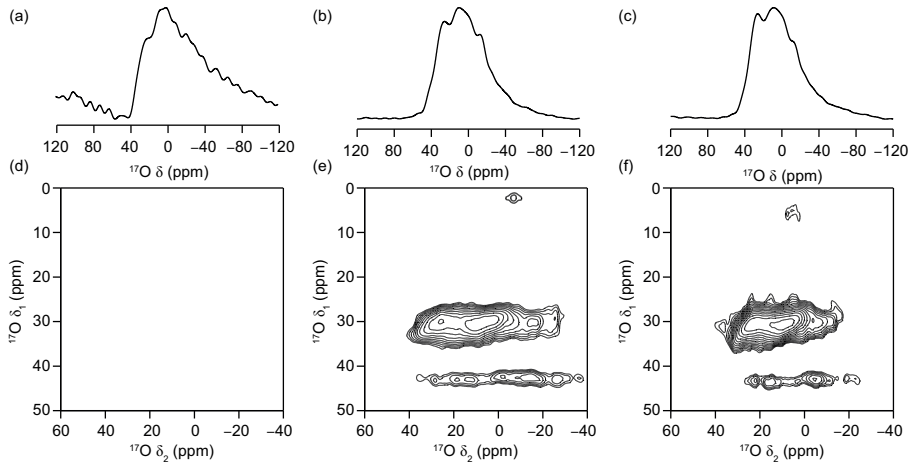

Figure 4.33: ^{17}O (14 kHz MAS, 14.1 T) NMR spectra of Ge-**UTL** samples, ball milled in $H_2{}^{17}O$ for (a,d) 20, (b,e) 120 and (c,f) 240 minutes. (a,b) Quantitative short-flip angle and (c,d) $\{^1H\}^{17}O$ MQMAS NMR experiments.

The ^{17}O spectra of the mechanochemically hydrolysed samples are similar to those of the enriched materials previously discussed. Some signals are similar to those seen for the gas-enriched starting material (Figure 4.30) with what appears to be two strongly overlapped components in the framework Si–O–Si/Ge region but also exhibit signals from $Ge^{17}O_2$ as seen in the low-volume *in-situ* slurrying experiments (Figure 4.22). The resolution of the latter of these species is not entirely surprising as the extremely low-volume conditions of the mechanochemical treatment provides little opportunity to remove any germanium hydrolytically extracted from the zeolite and the ethanolic washing of the end product has a reduced effect on pre-formed GeO_2. This does, however, raise a point of contention with regard to the proposed germanium content of the reaction end product and whether the non-zero Si/Ge measured by EDX is affected by the presence of $Ge^{17}O_2$ in the mixture or whether the zeolitic components of the product (IPC-2P*) do actually contain germanium within their framework. Although zeolite-type crystallites were selected specifically for EDX-analyses, it is not possible to confirm the exclusion of all $Ge^{17}O_2$ material in the measurements. Considering the level of hydrolysis observed here and the IPC-2P-type diffraction patterns produced,[21] it is conceivable to suggest that some Ge is still contained within the structure of the materials.

4.6.7.2 Effect of Field Strength

As the spectra recorded at 14.1 T (Figure 4.33) again provide evidence of strongly overlapped resonances for framework silicate and germanosilicate oxygen sites, the effect of the external field strength on the position of resonances was again investigated for the mechanochemically hydrolysed samples, as described for gas-enriched materials above. As the level and position of enrichment or level of ball-milled materials does not appear to change significantly after two hours treatment, the 120 minute sample was chosen for multi-field analyses (see Figure 4.34).

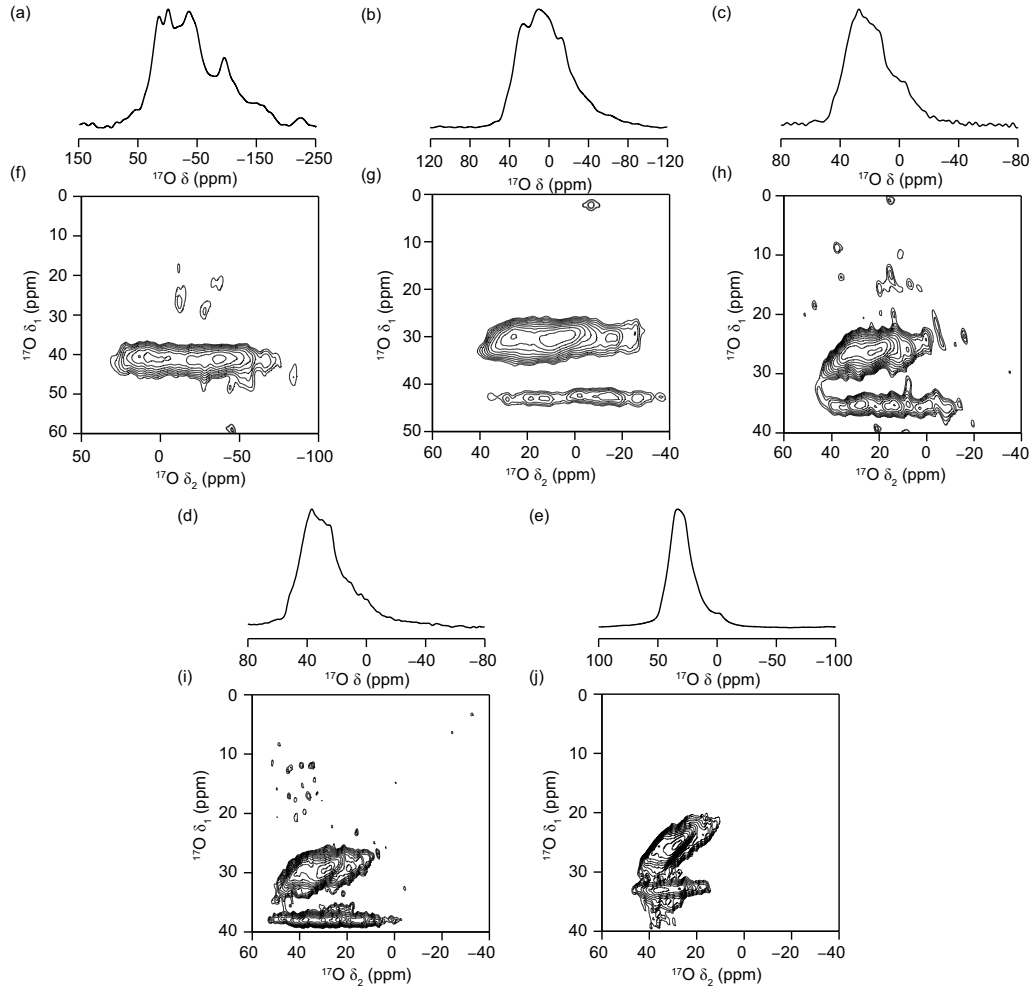

Figure 4.34: ^{17}O (14 kHz MAS) NMR spectra of Ge-**UTL**, ball milled in $H_2{}^{17}O$ for 120 minutes, acquired at (a,f) 9.4 T, (b,g) 14.1 T, (c,h) 18.8, (d,i) 20.0 T, (e,j) 23.5 T. (a-e) Quantitative short-flip angle and (f-j) $\{^1H\}^{17}O$ MQMAS NMR experiments.

Figure 4.34 shows two well resolved signals at all field strengths, but with evidence of a further signal being resolved at higher field. Figure 4.35 plots the variation of the centre of gravity of these signals as a function of field strength, allowing the NMR parameters to be determined.[61] Two of these signals are very similar to those seen in Ge-**UTL**, confirming them as Si–O–Si and Si–O–Ge, while the third matches well with GeO_2. Once again, the centre of gravity of the resonances is found to have a strongly linear correlation with the inverse square of the field strength. The resonances resolved in the MQMAS spectra in Figure 4.34 are assigned as follows: Si–O–Si at $\delta_{iso} \approx 44$ ppm (40 - −20 ppm δ_2 in 14.1 T, 14 kHz MAS NMR spectra), Si–O–Ge at $\delta_{iso} \approx 29$ ppm (20 - −40 ppm δ_2 in 14.1 T, 14 kHz MAS NMR spectra) and GeO_2 at $\delta_{iso} \approx 51$ ppm (40 - −40 ppm δ_2 in 14.1 T, 14 kHz MAS NMR spectra). Expected errors for δ_{iso} are $\pm$ 2 ppm. From Equation 4.1, the value of P_Q for the Si–O–Si and Si–O–Ge resonances can also be calculated from the plot in Figure 4.35, taking values of 5.4, 5.1 and 7.1 MHz, respectively (expected error $\pm$ 0.2 MHz) and agreeing with that seen for the gas-enriched **UTL** material.

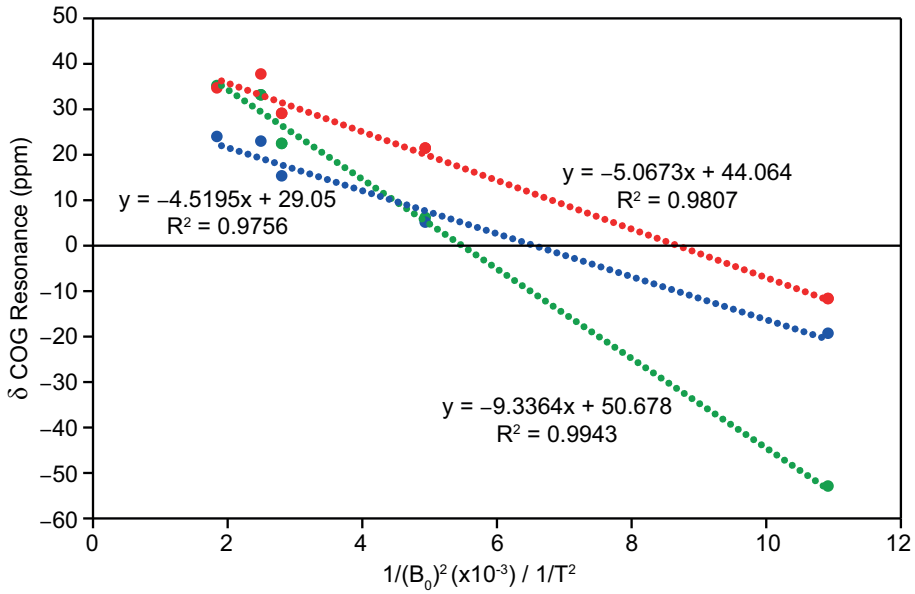

Figure 4.35: COG of resonances for 120 minute mechanochemically hydrolysed Ge-**UTL** plotted as a function of the inverse square of the field strength at which they were recorded. Si–O–Si = red, Si–O–Ge = blue, Ge–O–Ge = green.

The intensity of the signal attributed to Si–O–Ge in ^{17}O MQMAS NMR spectra of ball-milled materials indicates that although the material has been hydrolysed under the reaction conditions, actually not all germanium is removed from its position within the framework during this hydrolysis process. Furthermore, it demonstrates a surprising degree of reversibility and lability within the germanosilicate linkages, in addition to the lability of silicate linkages seen previously. The inclusion of germanium, which produces strongly hydrolytically unstable Ge-O bonds can still facilitate reversible Ge-O bond hydrolysis

that exchanges ^{16}O for ^{17}O under these conditions. This provides a degree of confidence in the EDX analyses that showed germanium presence in the zeolitic-type crystallites analysed and points to a truly dynamic and reversible disassembly pathway for ADOR materials under these conditions.

4.7 Summary and Conclusions

The work detailed in the chapter has studied the ADOR process for germanosilicate **UTL**, focusing on the interactions and reactivity of the zeolite with water. Using X-ray crystallography and NMR spectroscopy techniques, the effect of this treatment on the long-range order and local structure of the materials has been uncovered, building on published studies and on pre-existing knowledge.

The ADOR process is known to be strongly dependent on a number of reaction conditions, particularly temperature, overall reaction volume and composition (ratio of solid to solvent). Changing these variables has been shown previously to not only change the rate of reaction, but also the expected products and the mechanism for their formation. As this chapter aimed to build on these findings by studying the mechanism and processes for the formation of particular intermediates and to learn more about the synergy of their local and long-range structure, a series of initial experiments were first needed to develop protocols that would produce model materials for further analyses.

The rate of the ADOR processes under some conditions meant that accurately characterising certain intermediates of the ADOR process would be challenging. To obtain an overview of the standard ADOR reaction, *i.e.* one carried out at high-volume and elevated temperature, a high-throughput PXRD study was performed, taking samples at incremented times to determine the 'standard' reaction pathway and intermediates formed. In this instance, the solid : water ratio was kept as constant as possible by not replacing the filtrate when removing samples for filtration and subsequent PXRD analysis. Analysis of this data using PXRD confirmed the rapid formation of IPC-1P for ADOR species hydrolysed in water, before an induction period and gradual reintercalation, of silicon in solution to form IPC-2P and the stable aqueous product.

Using this reaction as a model and aiming to replicate the pathway under a range of conditions, the effect of removing and replacing filtrate from reactions when performed with varying solid : water ratios was explored using PXRD. This effectively demonstrated how the ratio of zeolite to reaction hydrolysing solution affects the products formed and the

rate at which this happens. By comparing continual hydrolyses like the high-throughput reaction to single hydrolysis reaction products, the effect of continual reaction sampling was found to be negligible provided solid : water remained roughly the same. It was found that decreasing the solid : water ratio from 1 : 200 to 1 : 80 was the limit if the desire is to form the same products (as determined by PXRD under the same conditions of a 92 °C reaction), provided the solvent used in sampling was returned to the reaction flask following filtration.

Having developed a subset of experimental conditions that, according to PXRD analyses can reliably produce the same ADOR products and intermediates, ^{29}Si NMR spectroscopy was employed to explore the effect of varying reaction conditions on the local structure of the material. ^{29}Si NMR spectroscopy of key intermediates indicates that changes to the local structure of the zeolite are much more significant and occur much more rapidly under hydrolysis than indicated by PXRD, particularly, the rate of germanium removal and generation of Q^3 silanols as seen in the silicon NMR spectra occurs noticeably before the change in d_{200} of the PXRD patterns do. Further, it was again observed that the Q^3:Q^4 does not reach the idealised ratio for the zeolite intermediate, as per previous reports. It is possible that the Q^3:Q^4 following reorganisation is adversely affected by the loss of single germanium atoms in the two-dimensional layers of **UTL**, which can generate four silanol sites when in completely isolated positions.

To learn more about the effect of ADOR hydrolyses on the local structure of the materials, ^{17}O NMR spectroscopic studies were performed, requiring the development of cost-effective enrichment protocols for starting materials and reaction intermediates. **UTL** materials were enriched using a variety of high temperature hydrolysis, slurrying, high-temperature gas exchange and mechanochemical hydrolysis approaches. It was found that the reaction of **UTL** frameworks at room temperature with water was sufficient to cause hydrolysis and degermanation of the framework. Furthermore, during this period, surprising levels of reversible room-temperature bond lability, evidenced by the exchange of ^{17}O isotope into the framework picked up in ^{17}O NMR spectroscopy studies are observed. It was found that Si–O–Si sites within different **UTL** frameworks are reversibly cleaved, enriching without specific detriment to this aspect of the framework. The level of enrichment observed does appear to be affected by the germanium content (and overall hydrolytic stability) of the material, with germanium-rich materials enriching more and producing both Si–^{17}OH and quartz-phase Ge$^{17}O_2$. Enrichment of **UTL** materials in this manner has been seen before under elevated-temperature or room-temperature acidic conditions, but for of room-temperature water alone.

Further ^{17}O NMR spectroscopic investigations of the ADOR process have identified the location and nature of Si−O−Ge linkages within pristine and partially hydrolysed Ge-**UTL** materials. Through development of a more environmentally friendly $H_2{}^{17}O$ hydrolysis process utilising mechanochemistry, partially hydrolysed IPC-2P* intermediates were formed, enriched and analysed at a range of magnetic fields. The results reveal how the local structure of materials changed from their pristine form under mechanochemical hydrolysis, when compared to a ^{17}O gas-enriched starting material. The strong overlap of framework Si−O−Si and Si−O−Ge linkage resonances in ^{17}O MQMAS NMR spectra at intermediate field strengths meant a multi-field analysis approach was targeted with δ_{iso} extracted for individual resonance groups achieved by exploiting the variation of position as a function of external magnetic field strength.

Together, the results presented in this chapter have increased our understanding of the mechanism, reactivity and physical interactions that underpin the ADOR process for germanosilicate **UTL** in water. The results obtained have implications for the kinetics and mechanism of the ADOR process and the manipulation of germanosilicate zeolites; variation of the reaction conditions observed a change in rate for hydrolytic rearrangement when solvent solutions are manipulated. This reinforces the importance of solid : water ratio in ADOR transformations and highlights the importance of the concentration of aqueous silicate species in solution for promoting re-intercalation organisation steps. The versatility of the ADOR hydrolysis reaction with water was also demonstrated by the wide range of hydrolysis techniques employed. In particular, the use of mechanochemistry here was particularly successful for the formation of novel structural intermediates. This highlights the importance of this technique as a research tool but also demonstrates its aptitude in performing both solid-state hydrolysis reactions and economical ^{17}O framework enrichment in short reaction times with relative ease. Finally, this work has revealed the surprising ease with which non-destructive bond lability can take place in ADORable zeolite frameworks. Although this often took place in frameworks with an inherent weakness and increased flexibility, there is evidence that continual bond lability, particularly involving Si−O linkages can proceed without requiring or causing any loss of a pristine tetrahedrally coordinated zeolite framework structure.

4.8 References

[1] W. J. Roth, O. V. Shvets, M. Shamzhy, P. Chlubná, M. Kubů, P. Nachtigall and J. Čejka, *J. Am. Chem. Soc.*, 2011, **133**, 6130–6133.

[2] W. J. Roth, P. Nachtigall, R. E. Morris, P. S. Wheatley, V. R. Seymour, S. E. Ashbrook, P. Chlubná, L. Grajciar, M. Položij, A. Zukal, O. Shvets and J. Čejka, *Nat. Chem.*, 2013, **5**, 628–633.

[3] W. J. Roth, P. Nachtigall, R. E. Morris and J. Čejka, *Chem. Rev.*, 2014, **114**, 4807–4837.

[4] M. Shamzhy, M. Opanasenko, Y. Tian, K. Konysheva, O. Shvets, R. E. Morris and J. Čejka, *Chem. Mater.*, 2014, **26**, 5789–5798.

[5] R. E. Morris and J. Čejka, *Nat. Chem.*, 2015, **7**, 381–388.

[6] P. Eliášová, M. Opanasenko, P. S. Wheatley, M. Shamzhy, M. Mazur, P. Nachtigall, W. J. Roth, R. E. Morris and J. Čejka, *Chem. Soc. Rev.*, 2015, **44**, 7177–7206.

[7] M. Mazur, P. S. Wheatley, M. Navarro, W. J. Roth, M. Položij, A. Mayoral, P. Eliášová, P. Nachtigall, J. Čejka and R. E. Morris, *Nat. Chem.*, 2016, **8**, 58–62.

[8] J. Přech, P. Pizarro, D. P. Serrano and J. Čejka, *Chem. Soc. Rev.*, 2018, **47**, 8263–8306.

[9] M. Opanasenko, M. Shamzhy, Y. Wang, W. Yan, P. Nachtigall and J. Čejka, *Angew. Chemie Int. Ed.*, 2020, **59**, 19380–19389.

[10] O. V. Shvets, P. Nachtigall, W. J. Roth and J. Čejka, *Microporous Mesoporous Mater.*, 2013, **182**, 229–238.

[11] M. Trachta, O. Bludský, J. Čejka, R. E. Morris and P. Nachtigall, *ChemPhysChem*, 2014, **15**, 2972–2976.

[12] S. E. Henkelis, M. Mazur, C. M. Rice, P. S. Wheatley, S. E. Ashbrook and R. E. Morris, *J. Am. Chem. Soc.*, 2019, **141**, 4453–4459.

[13] S. E. Henkelis, M. Mazur, C. M. Rice, G. P. M. Bignami, P. S. Wheatley, S. E. Ashbrook, J. Čejka and R. E. Morris, *Nat. Protoc.*, 2019, **14**, 781–794.

[14] P. S. Wheatley, P. Chlubná-Eliášová, H. Greer, W. Zhou, V. R. Seymour, D. M. Dawson, S. E. Ashbrook, A. B. Pinar, L. B. McCusker, M. Opanasenko, J. Čejka and R. E. Morris, *Angew. Chemie Int. Ed.*, 2014, **53**, 13210–13214.

[15] J. Zhang, O. Veselý, Z. Tošner, M. Mazur, M. Opanasenko, J. Čejka and M. Shamzhy, *Chem. Mater.*, 2021, **33**, 1228–1237.

[16] M. Mazur, A. M. Arévalo-López, P. S. Wheatley, G. P. M. Bignami, S. E. Ashbrook, Á. Morales-García, P. Nachtigall, J. P. Attfield, J. Čejka and R. E. Morris, *J. Mater. Chem. A*, 2018, **6**, 5255–5259.

[17] V. Kasneryk, M. Shamzhy, J. Zhou, Q. Yue, M. Mazur, A. Mayoral, Z. Luo, R. E. Morris, J. Čejka and M. Opanasenko, *Nat. Commun.*, 2019, **10**, 1–8.

[18] S. A. Morris, G. P. M. Bignami, Y. Tian, M. Navarro, D. S. Firth, J. Čejka, P. S. Wheatley, D. M. Dawson, W. A. Slawinski, D. S. Wragg, R. E. Morris and S. E. Ashbrook, *Nat. Chem.*, 2017, **9**, 1012–1018.

[19] G. P. M. Bignami, D. M. Dawson, V. R. Seymour, P. S. Wheatley, R. E. Morris and S. E. Ashbrook, *J. Am. Chem. Soc.*, 2017, **139**, 5140–5148.

[20] M. Navarro, S. A. Morris, Á. Mayoral, J. Čejka and R. E. Morris, *J. Mater. Chem. A*, 2017, **5**, 8037–8043.

[21] D. N. Rainer, C. M. Rice, S. J. Warrender, S. E. Ashbrook and R. E. Morris, *Chem. Sci.*, 2020, **11**, 7060–7069.

[22] Y. Ma, H. Xu, X. Liu, M. Peng, W. Mao, L. Han, J. Jiang and P. Wu, *Chem. Commun.*, 2019, **55**, 1883–1886.

[23] M. V. Shamzhy, O. V. Shvets, M. V. Opanasenko, P. S. Yaremov, L. G. Sarkisyan, P. Chlubná, A. Zukal, V. R. Marthala, M. Hartmann and J. Čejka, *J. Mater. Chem.*, 2012, **22**, 15793.

[24] M. Mazur, V. Kasneryk, J. Přech, F. Brivio, C. Ochoa-Hernández, A. Mayoral, M. Kubů and J. Čejka, *Inorg. Chem. Front.*, 2018, **5**, 2746–2755.

[25] M. Jin, O. Veselý, C. J. Heard, M. Kubů, P. Nachtigall, J. Čejka and L. Grajciar, *J. Phys. Chem. C*, 2021.

[26] Y. Zhang, M. Kubů, M. Mazur and J. Čejka, *Microporous Mesoporous Mater.*, 2019, **279**, 364–370.

[27] O. Veselý, P. Eliášová, R. E. Morris and J. Čejka, *Mater. Adv.*, 2021, **2**, 3862–3870.

[28] R. A. Doyle, S. E. Russell and R. E. Morris, *Microporous Mesoporous Mater.*, 2019, **280**, 367–371.

[29] J.-l. Paillaud, B. Harbuzaru, J. Patarin and N. Bats, *Science (80-.).*, 2004, **304**, 990–993.

[30] A. Corma, M. J. Díaz-Cabañas, F. Rey, S. Nicolopoulus and K. Boulahya, *Chem. Commun.*, 2004, 1356–1357.

[31] V. Kasneryk, M. Shamzhy, M. Opanasenko, P. S. Wheatley, S. A. Morris, S. E. Russell, A. Mayoral, M. Trachta, J. Čejka and R. E. Morris, *Angew. Chemie Int. Ed.*, 2017, **56**, 4324–4327.

[32] D. S. Firth, S. A. Morris, P. S. Wheatley, S. E. Russell, A. M. Z. Slawin, D. M. Dawson, A. Mayoral, M. Opanasenko, M. Položij, J. Čejka, P. Nachtigall and R. E. Morris, *Chem. Mater.*, 2017, **29**, 5605–5611.

[33] H. Xu, J.-g. Jiang, B. Yang, L. Zhang, M. He and P. Wu, *Angew. Chemie Int. Ed.*, 2014, **53**, 1355–1359.

[34] H. Xu, J.-g. Jiang, B. Yang, L. Zhang, M. He and P. Wu, *Angew. Chemie*, 2014, **126**, 1379–1383.

[35] S. A. Morris, P. S. Wheatley, M. Položij, P. Nachtigall, P. Eliášová, J. Čejka, T. C. Lucas, J. A. Hriljac, A. B. Pinar and R. E. Morris, *Dalt. Trans.*, 2016, **45**, 14124–14130.

[36] S. E. Henkelis, S. A. Morris, M. Mazur, P. S. Wheatley, L. N. McHugh and R. E. Morris, *J. Mater. Chem. A*, 2018, **6**, 17011–17018.

[37] S. E. Russell, S. E. Henkelis, S. M. Vornholt, D. N. Rainer, K. W. Chapman and R. E. Morris, *Mater. Adv.*, 2021.

[38] E. Verheyen, L. Joos, K. Van Havenbergh, E. Breynaert, N. Kasian, E. Gobechiya, K. Houthoofd, C. Martineau, M. Hinterstein, F. Taulelle, V. Van Speybroeck, M. Waroquier, S. Bals, G. Van Tendeloo, C. E. A. Kirschhock and J. A. Martens, *Nat. Mater.*, 2012, **11**, 1059–1064.

[39] N. Kasian, A. Tuel, E. Verheyen, C. E. A. Kirschhock, F. Taulelle and J. A. Martens, *Chem. Mater.*, 2014, **26**, 5556–5565.

[40] V. Kasneryk, M. Opanasenko, M. Shamzhy, Z. Musilová, Y. S. Avadhut, M. Hartmann and J. Čejka, *J. Mater. Chem. A*, 2017, **5**, 22576–22587.

[41] V. Kasneryk, M. Shamzhy, M. Opanasenko, P. S. Wheatley, R. E. Morris and J. Čejka, *Dalt. Trans.*, 2018, **47**, 3084–3092.

[42] O. V. Shvets, M. V. Shamzhy, P. S. Yaremov, Z. Musilová, D. Procházková and J. Čejka, *Chem. Mater.*, 2011, **23**, 2573–2585.

[43] M. V. Shamzhy, P. Eliašová, D. Vitvarová, M. V. Opanasenko, D. S. Firth and R. E. Morris, *Chem. - A Eur. J.*, 2016, **22**, 17377–17386.

[44] X. Liu, U. Ravon, F. Bosselet, G. Bergeret and A. Tuel, *Chem. Mater.*, 2012, **24**, 3016–3022.

[45] D. Massiot, F. Fayon, M. Capron, I. King, S. Le Calvé, B. Alonso, J.-o. Durand, B. Bujoli, Z. Gan and G. Hoatson, *Magn. Reson. Chem.*, 2002, **40**, 70–76.

[46] S. O. Odoh, M. W. Deem and L. Gagliardi, *J. Phys. Chem. C*, 2014, **118**, 26939–26946.

[47] R. Hussin, R. Dupree and D. Holland, *J. Non-Cryst. Solids*, 1999, **246**, 159–168.

[48] L. M. Bull, A. K. Cheetham, T. Anupold, A. Reinhold, A. Samoson, J. Sauer, B. Bussemer, Y. Lee, S. Gann, J. Shore, A. Pines and R. Dupree, *J. Am. Chem. Soc.*, 1998, **120**, 3510–3511.

[49] U. T. Pingel, J. P. Amoureux, T. Anupold, F. Bauer, H. Ernst, C. Fernandez, D. Freude and A. Samoson, *Chem. Phys. Lett.*, 1998, **294**, 345–350.

[50] J. P. Amoureux, F. Bauer, H. Ernst, C. Fernandez, D. Freude, D. Michel and U. T. Pingel, *Chem. Phys. Lett.*, 1998, **285**, 10–14.

[51] L. M. Bull, B. Bussemer, T. Anupõld, A. Reinhold, A. Samoson, J. Sauer, A. K. Cheetham and R. Dupree, *J. Am. Chem. Soc.*, 2000, **122**, 4948–4958.

[52] D. Freude, T. Loeser, D. Michel, U. Pingel and D. Prochnow, *Solid State Nucl. Magn. Reson.*, 2001, **20**, 46–60.

[53] H. Ernst, D. Freude, J. Kanellopoulos, T. Loeser, D. Prochnow and D. Schneider, *Stud. Surf. Sci. Catal.*, 2004, **154 B**, 1173–1179.

[54] L. Peng, Y. Liu, N. Kim, J. E. Readman and C. P. Grey, *Nat. Mater.*, 2005, **4**, 216–219.

[55] L. Peng, H. Huo, Z. Gan and C. P. Grey, *Microporous Mesoporous Mater.*, 2008, **109**, 156–162.

[56] H. Huo, L. Peng, Z. Gan and C. P. Grey, *J. Am. Chem. Soc.*, 2012, **134**, 9708–9720.

[57] S. E. Ashbrook, Z. H. Davis, R. E. Morris and C. M. Rice, *Chem. Sci.*, 2021, **12**, 5016–5036.

[58] S. E. Ashbrook and S. Sneddon, *J. Am. Chem. Soc.*, 2014, **136**, 15440–15456.

[59] S. E. Ashbrook, D. M. Dawson and J. M. Griffin, in *Local Struct. Characterisation*, ed. D. O'Hare and R. I. Walton, John Wiley & Sons, Ltd, 1st edn., 2014, pp. 1–88.

[60] L.-s. Du, L. Peng and J. F. Stebbins, *J. Non. Cryst. Solids*, 2007, **353**, 2910–2918.

[61] K. J. D. Mackenzie and M. E. Smith, *Multinuclear Solid-State Nuclear Magnetic Resonance of Inorganic Materials*, Pergamon, Oxford, 1st edn., 2002.

[62] P. J. Grandinetti, J. H. Baltisberger, I. Farnan, J. F. Stebbins, U. Werner and A. Pines, *J. Phys. Chem.*, 1995, **99**, 12341–12348.

[63] T. H. Sefzik, T. M. Clark and P. J. Grandinetti, *Solid State Nucl. Magn. Reson.*, 2007, **32**, 16–23.

[64] T.-X. Métro, C. Gervais, A. Martinez, C. Bonhomme and D. Laurencin, *Angew. Chemie Int. Ed.*, 2017, **56**, 6803–6807.

[65] J. G. Schiffmann, F. Emmerling, I. C. Martins and L. Van Wüllen, *Solid State Nucl. Magn. Reson.*, 2020, **109**, 101687.

[66] C.-H. Chen, E. Gaillard, F. Mentink-Vigier, K. Chen, Z. Gan, P. Gaveau, B. Rebière, R. Berthelot, P. Florian, C. Bonhomme, M. E. Smith, T.-X. Métro, B. Alonso and D. Laurencin, *Inorg. Chem.*, 2020, **59**, 13050–13066.

[67] C.-H. Chen, F. Mentink-Vigier, J. Trébosc, I. Goldberga, P. Gaveau, E. Thomassot, D. Iuga, M. E. Smith, K. Chen, Z. Gan, N. Fabregue, T.-X. Métro, B. Alonso and D. Laurencin, *Chem. – A Eur. J.*, 2021, **27**, 12574–12588.

[68] J. Mei, A. Duan and X. Wang, *Materials*, 2021, **14**, 788–801.

[69] D. N. Rainer and R. E. Morris, *Dalt. Trans.*, 2021, **50**, 8995–9009.

[70] G. P. M. Bignami, Z. H. Davis, D. M. Dawson, S. A. Morris, S. E. Russell, D. McKay, R. E. Parke, D. Iuga, R. E. Morris and S. E. Ashbrook, *Chem. Sci.*, 2018, **9**, 850–859.

[71] A. Fernandes, R. F. Moran, S. Sneddon, D. M. Dawson, D. McKay, G. P. M. Bignami, F. Blanc, K. R. Whittle and S. E. Ashbrook, *RSC Adv.*, 2018, **8**, 7089–7101.

[72] C. J. Heard, L. Grajciar, C. M. Rice, S. M. Pugh, P. Nachtigall, S. E. Ashbrook and R. E. Morris, *Nat. Commun.*, 2019, **10**, 4690–4967.

[73] S. M. Pugh, P. A. Wright, D. J. Law, N. Thompson and S. E. Ashbrook, *J. Am. Chem. Soc.*, 2020, **142**, 900–906.

Chapter 5

Bond Lability in Zeolite Frameworks

5.1 Acknowledgements

Parts of the work detailed in this chapter have been carried out in collaboration with researchers at the University of St Andrews, the University of Warwick, Charles University (Prague) and Chevron Corporation (USA). The molecular dynamics simulations on the SSZ-13(H) **CHA** zeolite were carried out by Dr Christopher Heard, Dr Lukas Grajciar and Professor Petr Nachtigall of Charles University in Prague. The SSZ-13(H) zeolite used for slurrying experiments and enriched by post-synthetic gas exchange was provided by Dr Stacey Zones of Chevron Corp.. DFT calculations for **CHA** materials were performed by Professor Sharon Ashbrook. Selected ^{17}O NMR spectra were carried out at the UK High-Field Solid-state NMR Spectroscopy Facility, based at the University of Warwick. High-field experiments were enabled by collaborative assistance from Dr Daniel Dawson, Dr Dinu Iuga and Dr Trent Franks.

5.2 Introduction

The work in Chapter 4 uncovered a surprisingly facile bond lability exhibited by Ge-**UTL** and related ADOR-derived materials when treated with $H_2{}^{17}O_{(l)}$. Through a range of experiments, signals from Si–O–Si, Si–O–Ge, Si–O–Al, Si–OH and Ge–O–Ge species were resolved in ^{17}O NMR spectra of materials treated with $H_2{}^{17}$O-enriched reagents under mild conditions. These results have extended the understanding of a previously observed flexibility of zeolites under mild conditions, characterising unexpected framework oxygen exchange and reversible, extensive bond lability in zeolites.[1–3]

Whilst framework flexiblity and dynamics are undoubtedly observed under these conditions, the exact reasons for the reversible bond lability are unknown. Indeed, for almost all cases of mild-condition-facilitated ^{17}O-enrichment discussed in Chapter 4, the framework was either defect-rich; having a large amount of silanols in a layered or heavily defective structure, or is hydrolytically unstable due to the presence of germanium. Despite this, there is some evidence that exchange of framework oxygens for ^{17}O occurs in some zeolite framework linkages and sites (particularly intra-layer Si – O – Si) considered to be more isolated from defective sites or unresponsive to ADOR transformation processes. Exchange at these sites is therefore of great interest and further exploration of how similar framework sites in related zeolites behave is desired. If these sites are easily exchangeable, it should be possible to propose the mechanistic pathway for how this exchange proceeds.

In order to probe when zeolite frameworks are able to be enriched and at which specific sites, a series of experiments were devised, predominantly focussed on studying the exchange that occurs by slurrying with water aluminosilicate zeolite frameworks that are known to be stable under harsh conditions, particularly where water is present. The interactions of aluminosilicates with water under a range of conditions is a topic of significant interest within the scientific community as zeolite instability in hot aqueous or steaming conditions can have detrimental consequences for industrial zeolite applications.[4–20] This study is to our knowledge one of the first that aims to understand the interactions of zeolites with water under ambient conditions.[21,22] As such, it was desired that frameworks considered in this study would be topologically simple, have industrial relevance and be able to be prepared with varying aluminium and/or heteroatom content. This led us to the chabazite (**CHA**) and faujasite (**FAU**) frameworks, both of which possess only a single T site and four O sites.

5.3 Bond Lability in SSZ-13(H) CHA

As outlined in Section 1.6.1, **CHA** is an example of a naturally occurring zeolite that has a crystallographically simple framework topology. The $T_{36}O_{72}$ unit cell has only one and four crystallographically distinct T and O sites, respectively.[23] Furthermore, the synthetic production of **CHA** frameworks is well established and many examples of silicate, aluminosilicate and other heteroatomic (B, Ti, Zn...) framework preparations exist in the literature.[24–38] Combined with its industrially relevant uses as a MTO and ammonia-SCR catalyst, the above reasons make the chabazite topology an excellent choice of starting framework for further exploration of the bond lability of zeolites.[39–43]

As a model system to start exploring bond lability in **CHA**, an SSZ-13-type material in the Brønsted-acid (H^+ form (SSZ-13(H)) was selected. The aluminosilicate material has a Si/Al of 11 and was first documented by the Chevron corporation in 1985.[43] The specific SSZ-13(H) sample used in this thesis was provided by Dr Stacey Zones of Chevron.

5.3.1 Characterisation of the Starting Material

The SSZ-13(H) was received in its calcined form. Prior to the investigation of bond lability the material was again calcined (see Section 5.8.1) and characterised by PXRD (Figure 5.1), solid-state NMR spectroscopy (Figure 5.2) and EDX spectroscopy.

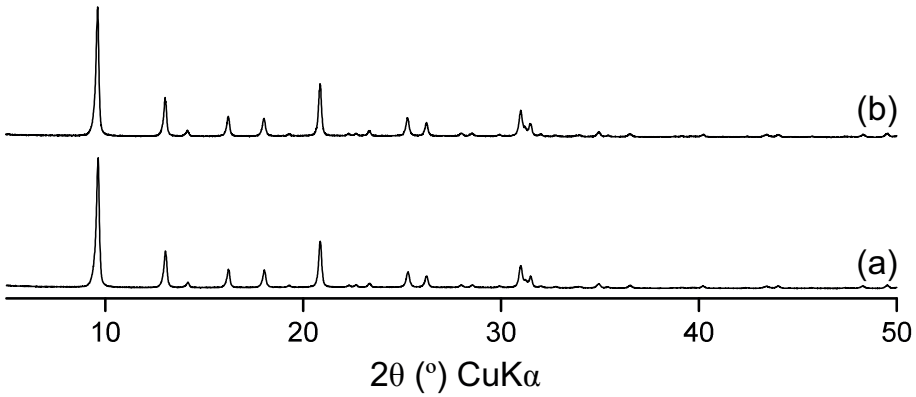

Figure 5.1: Powder X-ray diffraction pattern of (a) the reference SSZ-13(H) material[44] and (b) the calcined SSZ-13(H) material used in this work.

Figure 5.1 demonstrates that the in-house calcination of the zeolite has not been detrimental to the structure of the material and the long-range order of the zeolite still resembles that of the starting **CHA** material.

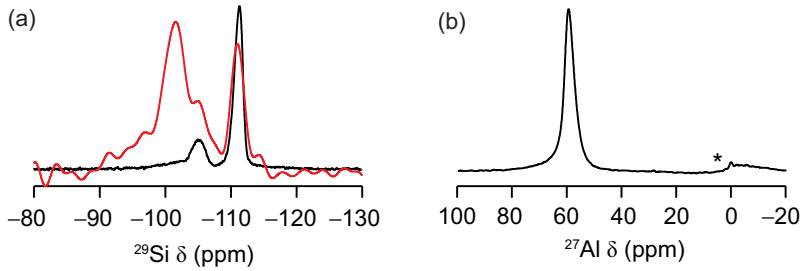

Figure 5.2: (9.4 T, 14 kHz) (a) ^{29}Si and (b) ^{27}Al MAS single-pulse NMR spectra of calcined Chevron SSZ-13(H). Red overlay in (a) is the ^{1}H^{29}Si CP NMR spectrum (5000 μs contact time). Asterisk (*) in (b) denotes a spinning sideband.

Solid-state NMR characterisation of SSZ-13(H) confirms the framework as a good example of a tetrahedrally coordinated aluminosilicate zeolite (Figure 5.2). The ^{27}Al NMR spectrum in Figure 5.2b shows almost exclusively tetrahedral coordination of aluminium

within the framework, whilst ^{29}Si NMR spectra in Figure 5.2a show evidence of a high proportion of Q^4 framework coordinated Si atoms within the structure. Deconvoluting the lineshapes allows assignment of specific resonances in the single-pulse (black) spectrum for Figure 5.2a, that can be made as follows: $Si(O-Si)_4$ (-112 ppm), $Si(O-Si)_3(O-Al)$ (-106 ppm), $Si(O-Si)_2(O-Al)_2$ (-100 ppm) and $Si(O-Si)_3(OH)$ (-102 ppm).[45–47] Due to their low prevalence, the latter two resonances are difficult to distinguish in the single-pulse NMR spectrum alone and cross-polarisation spectra were acquired particularly to investigate the presence of silanol defect sites within the material. It is clear from the red trace in Figure 5.2b that the parent calcined SSZ-13(H) does have some silanol defects, but the intensity of these is thought not to be above that of standard expected defect levels (typically <5%). Using DMfit, the ^{29}Si MAS NMR spectrum was fitted to produce a Si/Al of 10.2. This is comparable to the Si/Al value of 11 obtained from EDX measurements. As the unit cell of **CHA** contains 36 T sites, these values of Si/Al correspond to approximately three aluminium atoms per unit cell in the material.

5.3.2 Characterisation of $^{17}O_{2(g)}$-enriched Products

To aid the understanding of any bond lability observed using ^{17}O-enriched reagents in the SSZ-13(H) material, a $^{17}O_{2(g)}$-enriched sample was first prepared. As mentioned in Section 1.5.2, post-synthetic gas exchange is thought to be the most effective way of producing uniformly ^{17}O-enriched for zeolite material.[48] SSZ-13(H) was dehydrated and post-synthetically exchanged with $^{17}O_{2(g)}$ as detailed in Section 5.8.3. The gas-enrichment process did not result in any apparent change to the crystallinity and the long range order of the material (see Figure 5.3).

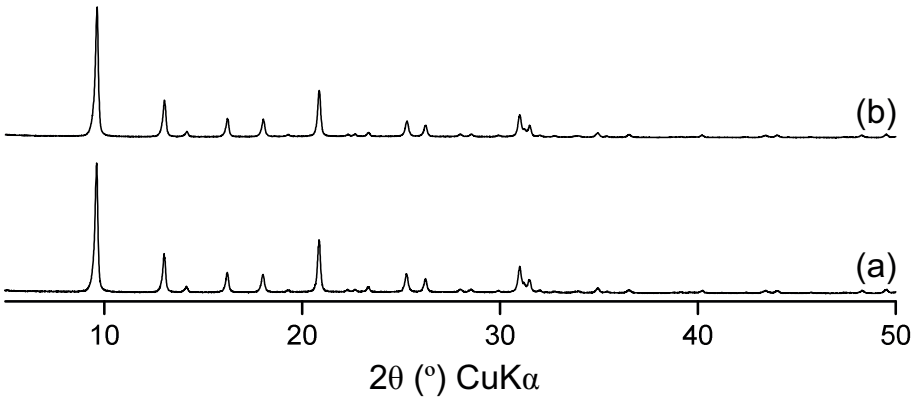

Figure 5.3: Powder X-ray diffraction pattern of (a) the calcined SSZ-13(H) material and (b) $^{17}O_{2\,(g)}$-enriched SSZ-13(H).

Characterisation of the framework in the gas-enriched sample (Figure 5.4) using ^{29}Si and ^{27}Al NMR spectroscopy shows some slight differences to the starting material. Although the local structure is largely preserved during the gas-enrichment procedure, there are some changes to the relative intensities of silicon environments, as shown in Figure 5.4a. Comparison with Figure 5.2a shows the gas-enriched material has relatively slightly fewer $Si(O-Si)_3(O-Al)$ sites. Interestingly however, there does not seem to be a greatly increased intensity of silanols in the red CP trace of the same figure. It is possible therefore that something other than loss of some aluminium atoms has occurred in the SSZ-13(H) material during the high-temperature gas-enrichment process. This is perhaps confirmed in Figure 5.4b, which shows both an increased linewidth for the peak corresponding to tetrahedral aluminium, indicating a slight increase in disorder for Al species and the growth of octahedral aluminium species at ≈ 0 ppm. It is proposed therefore that during the high temperature enrichment process, the coordination of aluminium atoms within the zeolite framework is altered, having an impact on its local connectivity to oxygen and bonds to silicon. Despite this it is clear that the structure of the **CHA** framework is preserved throughout the gas-enrichment process and the majority of T site coordination in the zeolite remains tetrahedral. Thus, the sample is still suitable for further study.

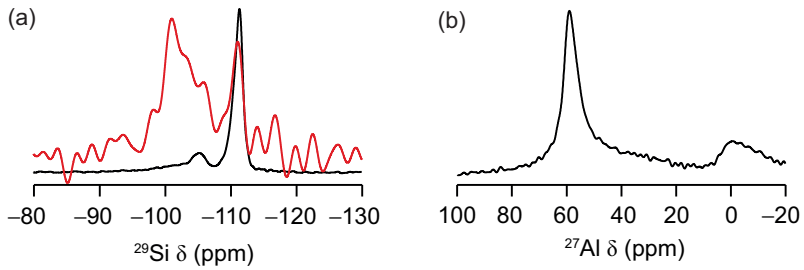

Figure 5.4: (9.4 T, 14 kHz) (a) ^{29}Si and (b) ^{27}Al MAS single-pulse NMR spectra of of $^{17}O_{2\,(g)}$-enriched SSZ-13(H). Red overlay in (a) is the $^{1}H^{29}$Si CP NMR spectrum (5000 μs contact time).

The ^{17}O NMR spectra in Figure 5.5 reveals the successful incorporation of ^{17}O into the framework sites of SSZ-13(H) **CHA** by post-synthetic exchange with $^{17}O_{2(g)}$. The quantitative short-flip angle spectrum in Figure 5.5a shows a complex lineshape composed of multiple overlapped quadrupolar broadened resonances. Separation of these resonances in the MQMAS spectrum in Figure 5.5b resolves three main regions of interest (see Table 5.1), which can be assigned[22,49–52] as two distinct Si–O–Si resonances at $\delta_1 \approx 32$ ppm, 27 ppm and a third, broad region at $\delta_1 \approx 17$ ppm, assigned to Si–O–Al environments.

Oxygen Site	Location (ppm) δ_1, δ_2	δ_{iso} (ppm)	$\lvert C_Q \rvert$ / MHz	η_Q
Si–O–Si 1	32.6, 19.1	45.5	5.2	0.21
Si–O–Si 2	28.0, 10.2	35.9	5.4	0.19
Si–O–Al 1	19.4, 18.3	29.1	3.7	0.52

Table 5.1: NMR parameters and tentative assignments for SSZ-13(H) **CHA** enriched in ^{17}O, using high-temperature $^{17}O_{2(g)}$ exchange.

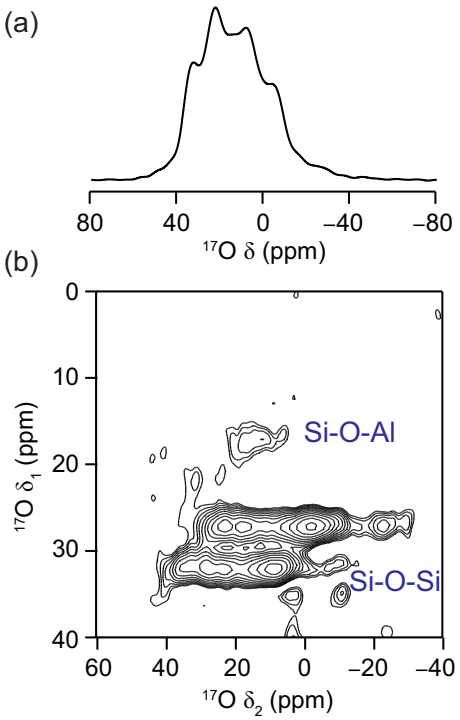

Figure 5.5: (14.1 T, 14 kHz) ^{17}O MAS NMR spectra of of $^{17}O_{2(g)}$-enriched Chevron SSZ-13(H). (a) Quantitative short flip-angle and (a) $\{^1H\}^{17}$O MQMAS NMR spectra.

Considering the framework sites within the **CHA** unit cell for the SSZ-13(H) material of this composition (Si/Al = 11) with completely isolated aluminium atoms, there are to be six times as many Si–O–Si sites as Si–O–Al (0.167 Si–O–Al per Si–O–Si). It might

be unsurprising therefore that the Si−O−Al linkage region in this spectrum is broad and not fully resolved as their expected abundance is small compared to that of the Si−O−Si linkages. Despite this, and the inherent non-quantitivity of the MQMAS experiment, rough integration of Si−O−Si and Si−O−Al linkages produce a Si−O−Si : Si−O−Al of 8 : 1, pointing to a fairly uniform, if slightly preferential enrichment of Si−O−Si linkages in this experiment (ideal uniform value 6 : 1). Within the resolved Si−O−Si signals, the relative integral intensities of the two are approximately 1 : 1, indicating similar levels of enrichment. The ^{17}O-enrichment level of this material is predicted to be $\approx 10\%$.

It is perhaps surprising that two distinct O signals environments are resolved for Si−O−Si linkages in SSZ-13(H). Considering that the topology should have four distinct O environments, one might expect better resolution of four different oxygen resonances at the moderate magnetic field used, as is the case for ^{17}O NMR spectra for other crystallographically simple zeolites, such as aluminosilicates A (**LTA**),[51,52] X / Y (**FAU**)[50,53] and sodalite (**SOD**),[54,55] or of siliceous ferrierite (**FER**).[56]

For this reason, DFT calculations were performed on a dehydrated, siliceous **CHA** structure, to predict the expected NMR parameters for oxygen atoms. The results are detailed in Table 5.2. The environments detailed in Table 5.2 correspond to the three ring structures that each oxygen atom is found to be at the intersection of in **CHA**.

Oxygen Site	Environment	δ_{iso} (ppm)	$\lvert C_Q \rvert$ / MHz
O1	*4r*, *4r*, *6r*	40.8	5.58
O2	*4r*, *8r*, *8r*	26.2	5.85
O3	*4r*, *6r*, *8r*	28.3	5.81
O4	*4r*, *4r*, *8r*	38.2	5.68

Table 5.2: DFT Calculated NMR parameters for oxygen environments within an idealised, dehydrated SiO_2 **CHA** framework structure.[57]

From the calculation results above it is evident that isotropic chemical shifts and quadrupolar couplings for both O1 and O4 are similar as is O2 and O3. It may be expected then that the NMR signals for crystallographically different oxygen atoms with similar parameters will therefore overlap. It follows therefore, that the experimental NMR spectrum of ^{17}O-enriched **CHA** materials contain two separate resonances for each of the Si−O−Si and Si−O−Al linkages. This certainly appears to be the case for Si−O−Si resonances in $^{17}O_{2(g)}$-enriched SSZ-13(H) Si−O−Si resonances. Further exploration is needed however to confirm this is the case for Si−O−Al sites.

The computational results detailed in Table 5.2 are for an idealized, dehydrated silica zeolite and so will be affected by any changes to the local coordination environment upon Al incorporation and the addition of a Brønsted proton (which could be located on the framework or on the water within the pores) and the presence of water itself. This is in contrast to the results obtained from the $^{17}O_{2(g)}$ exchanged sample (Table 5.1), which was considered to be 'air-hydrated' when acquisition of NMR spectra took place. This increase in the local disorder in the hydrated sample will result in small changes of chemical shift and quadrupolar splitting and will likely lead to a broadening of the ^{17}O signals. In instances where the aluminium content is very high *e.g.*, Si/Al = 3-5, the appearance of 'two distinct signals' for each of Si – O – Si and Si – O – Al may be less apparent.

5.3.3 Effect of Slurrying with $H_2{}^{17}O$

After characterization of a uniformly ^{17}O enriched SSZ-13(H) **CHA**, the enrichment of SSZ-13(H) by simply slurrying with isotopically enriched water was investigated using ^{17}O NMR spectroscopy, $H_2{}^{17}O$, following the protocol outlined in Section 5.8.2. The initial (unenriched) zeolite was combined with small amounts of 40%-enriched $H_2{}^{17}O$ (1 : 1 solid : water (mass)), producing surprisingly rapid framework ^{17}O-enrichment as detailed in Figure 5.6.

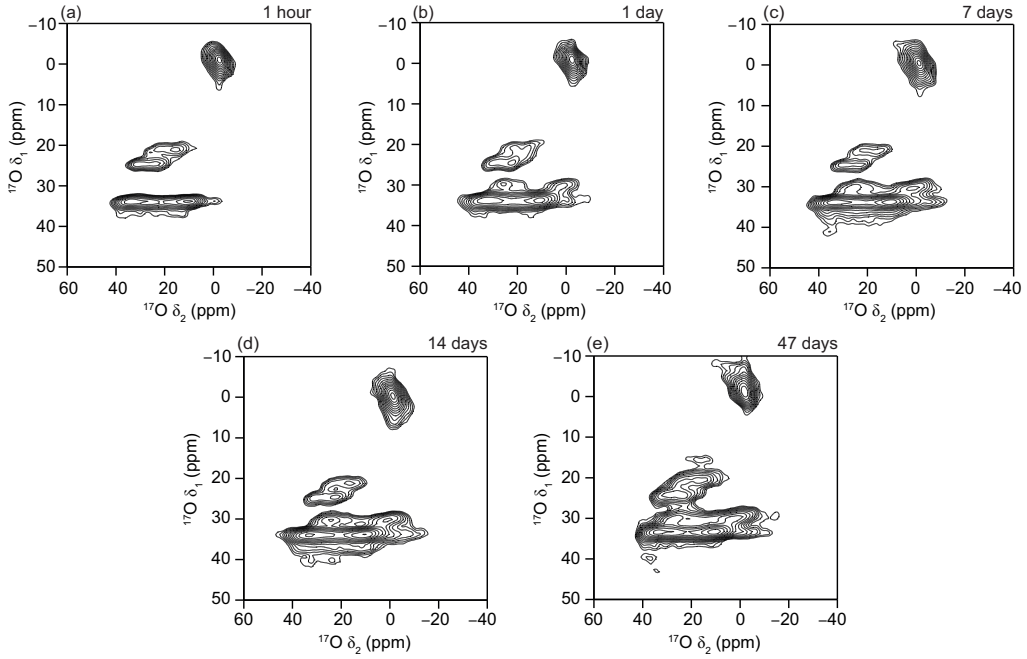

Figure 5.6: (14.1 T, 14 kHz) $\{^1H\}^{17}O$ MQMAS NMR spectra of calcined Chevron SSZ-13(H), slurried with small amounts of 40% $H_2{}^{17}O$. NMR spectra taken after (a) 1 hour, (b) 1 day, (c) 7 days, (d) 14 days and (e) 47 days of reaction.

From Figure 5.6 it is clear that there has been significant exchange of framework oxygen atoms in SSZ-13(H) with the ^{17}O atoms in the $H_2{}^{17}O$ reagent. Furthermore, the exchange occurs rapidly and under ambient conditions with good levels of signal seen even in an MQMAS spectrum even after just a few hours of hydration (typical MQMAS experiment length 14-16 h at 14.1 T). In Figure 5.6, the growth of signals associated with the **CHA** framework can be identified, in addition to the presence of water (0 ppm). Although signal from water itself should not be seen in an MQMAS spectrum, any restricted rotation as a result of hydrogen bonding to other water molecules or to the framework, will result in water oxygen with a slight quadrupolar moment, allowing it to pass through the triple-quantum filter. The four framework resonances resolved are attributed to two different sets of Si–O–Si and Si–O–Al signals, with NMR parameters extracted from the spectrum of the 47 day slurry (Figure 5.6e) given in Table 5.3.

Oxygen Site	Location (ppm) δ_1, δ_2	δ_{iso} (ppm)	$\lvert C_Q \rvert$ / MHz	η_Q	Likely O site
Si–O–Si 1	33.4, 21.5	46.5	5.2	0.24	O1, O4
Si–O–Si 2	30.4, 17.0	40.9	5.4	0.26	O2, O3
Si–O–Al 1	23.9, 26.1	37.6	3.5	0.45	O1, O4
Si–O–Al 2	20.5, 19.4	32.6	3.9	0.49	O2, O3

Table 5.3: NMR parameters and tentative assignments for SSZ-13(H) **CHA** slurried with 40% $H_2{}^{17}O$ for 47 days.

These signals can be tentatively assigned by comparison with the NMR parameters predicted using DFT calculations. For these, a set of four structures were constructed from the idealized SiO_2 **CHA** structure considered above, with one Si replaced by an Al, and the charge-balancing ^1H placed on each of the four crystallographically different O sites in the framework (given in Table 5.2), although the different hydration states of the materials should be noted. Figure 5.7 shows the centre-of-gravity of each O signal in an ^{17}O MQMAS spectrum (at 14.1 T) using the DFT-calculated parameters. This figure shows that two sets of Si–O–Al and Si–O–Si linkages are likely to be seen (with differing δ_1 positions) in good agreement with experiment, allowing the signals to be tentatively assigned to those from O1/O4 at higher δ_1 and those from O2/O3 at lower δ_1. There is no evidence in the experiment of signals that could be attributable to Brønsted acid sites (these would have much lower δ_2 as a result of larger C_Q values). However, this likely reflects the different hydration state of the real material, which has substantial numbers of water molecules in the pores. Although studies have shown that Brønsted acid protons in SSZ-13(H) sit preferentially on O3 and O4,[58,59] it is likely that hydrated materials may have H located partially or fully on the water molecules in the pore, or perhaps even dynamic on the NMR timescale. This difference in hydration state may also cause small

structural changes in the framework and small shifts in the expected position of ^{17}O signals associated with the framework oxygens between experiment and calculation.

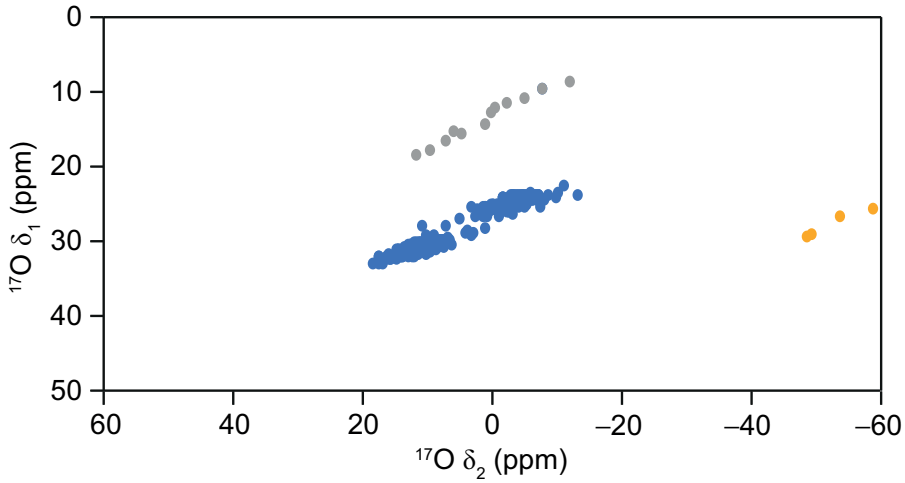

Figure 5.7: (14.1 T) Predicted centre-of-gravity (from DFT calculated NMR parameters for 4 models of Al-substituted **CHA**) of resonances in ^{17}O MQMAS NMR spectra for SSZ-13(H). The colour denotes the type of framework linkage, with Si–O–Si linkages (blue), Si–O–Al linkages (silver) and Si–O(H)–Al linkages (orange).

The spectra in Figure 5.6 show extensive ^{17}O enrichment of the framework, although quantifying this in absolute terms in *in-situ* reactions is difficult. The relative level of enrichment does vary with hydration time, as shown in the (normalised) ^{17}O MAS NMR spectra in Figure 5.8, which have been acquired with a short flip angle. At short slurrying times the spectra are dominated by the signal from water (δ = 0 ppm) although signals at higher shift (at 0-60 ppm) suggest framework O species are now enriched. The relative enrichment of the framework clearly increases with increasing hydration time, although the overlap of all signals makes accurate deconvolution challenging.

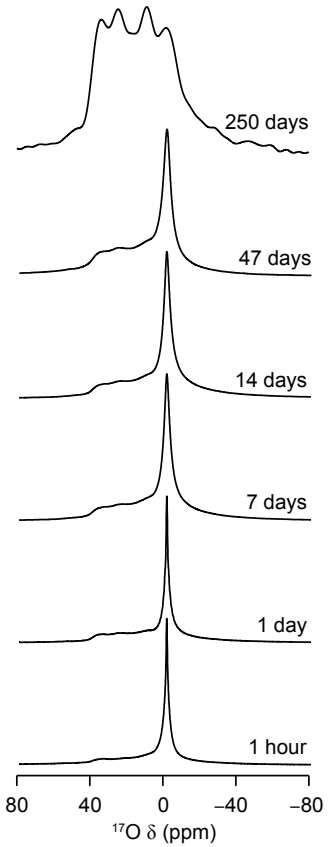

Figure 5.8: (14.1 T, 14 kHz) ^{17}O short flip-angle NMR spectra for Chevron SSZ-13(H), slurried for varying amounts of time. All experiments displayed are normalised by the number of scans.

The observed framework enrichment in SSZ-13(H) **CHA** that occurs at room temperature must do so in a continual and reversible exchange process. Further to this, there is evidence in Figure 5.6 to suggest that the rate at which oxygens are exchanged in the material is dependent on the nature of the linkage (*i.e.* silicate or aluminosilicate) and also that the location of that linkage within the framework may also affect its exchange ability. From Figure 5.6 two Si−O−Al signals and a single Si−O−Si signal is present at very short enrichment times (1 hour), before the gradual increase in intensity of a second Si−O−Si site over the subsequent seven days. Whilst it is not easy to determine absolute intensities from the overlapped and non-quantitative MQMAS data, it does appear qualitatively, at least that Si−O−Al linkages in the material enrich preferentially over Si−O−Si linkages at short hydration times, with a lower Si−O−Si : Si−O−Al ratio than expected. Furthermore, the second Si−O−Si signal appears to enrich more slowly, appearing with increased intensity at longer slurrying times. These observations are further confirmed through analysis of the δ_1 sum projections of the MQMAS NMR spectra of Figure 5.6, displayed in Figure 5.9.

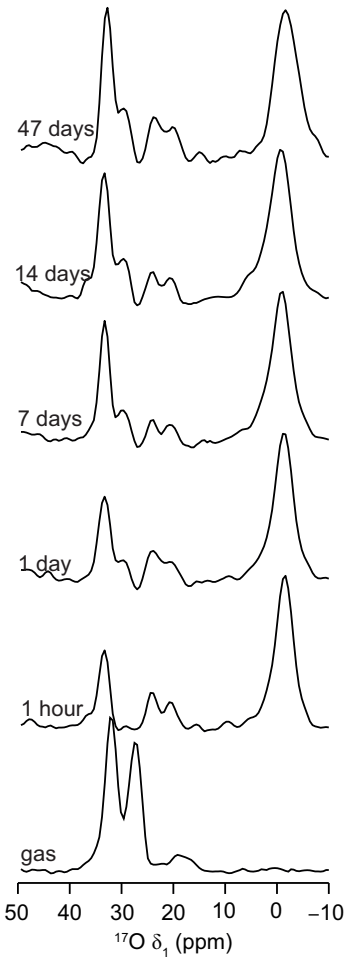

Figure 5.9: (14.1 T, 14 kHz) δ_1 positive projections of $\{^1\mathrm{H}\}^{17}$O MQMAS NMR spectra for Chevron SSZ-13(H), slurried for varying amounts of time.

Assuming the projection of the sample post-synthetically enriched using exchange with $^{17}O_{2(g)}$ in Figure 5.9 is representative of uniformly enriched SSZ-13(H), it can be seen that the two Si−O−Si signals with δ_1 = 40-25 ppm have approximately equal intensity, *i.e.* it is likely that of the four crystallographically distinct sites present in the **CHA** framework, two contribute to each Si−O−Si signal, as proposed earlier. Combining with the aluminosilicate linkages, which appear at δ_1 = 25-10 ppm, the relative ratio of Si−O−Si : Si−O−Al within the gas-enriched spectrum is slightly below the ideal ratio of 8 : 1 expected for this Si/Al.

Figure 5.9 also shows sum projections onto δ_1 of ^{17}O MQMAS spectra of SSZ-13(H) zeolites slurried with water for different times. Although the hydration states of the two materials are likely to be different, these do show some differences to that of the gas-exchanged sample. The Si−O−Al linkages account for a far greater proportion of the overall signal intensity, with two distinguishable peaks present, as can also be seen in MQMAS spectra (Figure 5.6). Interestingly, the same is not true for Si−O−Si linkages.

Here, one Si – O – Si signal increases in intensity much more slowly with slurrying time, first visible after one day. Furthermore, this signal never exhibits the same intensity as the Si – O – Si resonance at higher δ_1, in comparison to the gas-enriched material, where both have approximately equal integrated intensities. This implies that there may be a barrier to obtaining uniform enrichment for the second Si – O – Si resonance. The relative intensities of the two Si – O – Si peaks after 47 days are between 2 : 1 and 3 : 1. However as equal intensities are observed for the gas-enriched framework, it is possible that only one of the two types of linkage expected to contribute to the second Si – O – Si signal is significantly enriched (resulting in a ratio of 2 : 1; similar to what is seen experimentally).

The exchange of framework oxygen atoms for those in the aqueous solvent in the slurry must involve the cleavage of Si – O and Al – O bonds. It is of interest therefore, to study the effects of this oxygen exchange on the local structure and connectivity of the Si and Al T atoms that make up the framework. Figure 5.10 shows ^{29}Si MAS NMR spectra of SSZ-13(H) after slurrying. Even after long slurrying times, there is no significant effect of the framework oxygen exchange on the local structure and connectivity, with Al content and distribution (as determined by the relative intensities of Q^4 Si species) remaining consistent. The Si/Al of the framework remains at $\approx$ 10 as for the starting material. Further, the ^{1}H^{29}Si CP MAS NMR spectra (red traces in Figure 5.10) also show no significant changes to the starting material. There is a slight change in the ^{1}H^{29}Si CP MAS NMR spectra after 137 days, (Figure 5.10a) with the loss of the shoulder at ≈ -106 ppm. Similarly, the ^{27}Al MAS NMR spectra in Figure 5.10b,d show no changes at all with slurrying time. At approximately 200 days later the coordination of the aluminium remains tetrahedral with no losses of intensity or the visibility of any penta- or octa-hedral coordination.

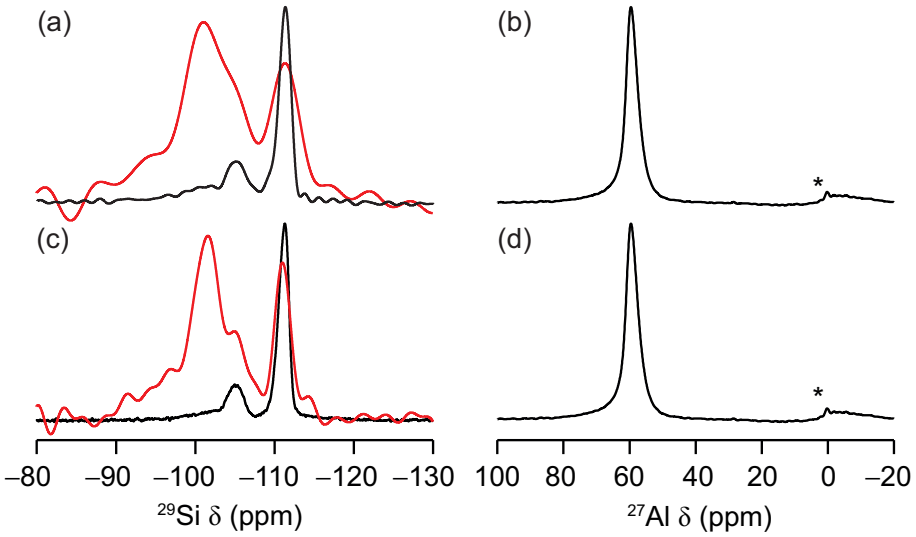

Figure 5.10: (9.4 T, 14 kHz) (a,c) ^{29}Si and (b,d) ^{27}Al single-pulse MAS NMR spectra for Chevron SSZ-13(H), for (b,d) starting material, (a) 137 days and (b) 202 days. Red overlay in (a,c) is the ^{1}H^{29}Si CP MAS NMR spectra (5000 μs contact time). Asterisk (*) in (b,d) denotes spinning sideband.

The long-range order of the zeolite structure was also assessed through a PXRD study, with samples prepared identically to those used in $H_2{}^{17}O$ slurry experiments (5.8.2), but instead using $H_2^{16}O$. Recording diffraction patterns for materials after set amounts of time (Figure 5.11) shows that the reaction of the zeolite with water, as in slurrying and framework-enrichment process has no effect on the long-range order or crystallinity of the SSZ-13(H).

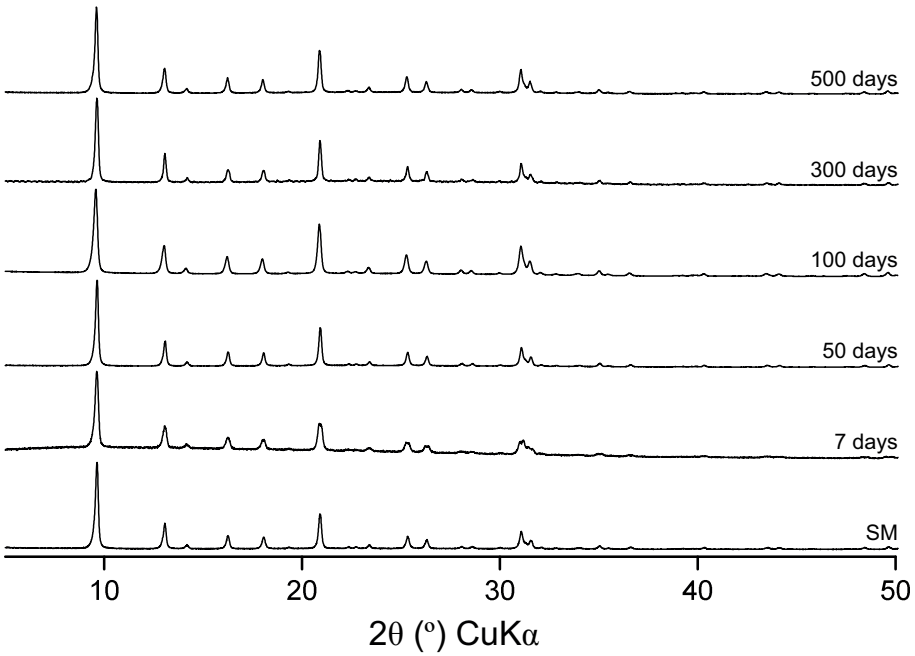

Figure 5.11: PXRD patterns for SSZ-13(H) slurried with $H_2{}^{16}O$ in a 1 : 1 (mass) ratio for different durations.

Clearly then, the oxygen exchange with the framework is happening continually and rapidly at room temperature, with bond cleavage a reversible and sustainable process within the material. Furthermore, it also appears that the exchange is easier for some oxygen atoms within the framework than for others, with some signals appearing more rapidly than others as a function of hydration time. As yet, the exact mechanism for this process is not clear.

5.3.4 Mechanistic Study

Whilst several mechanisms for bond-cleavage of Si – O and Al – O bonds exist in the literature, most are not applicable to the work carried out here. For example, those describing Al – O bond hydrolysis take place with the presence of the Brønsted proton on the framework throughout the reaction;[14,60] something unlikely here, considering the aqueous environment of the slurring conditions, which should solvate the Brønsted protons. Proposed Si – O reaction mechanisms require either higher activation energies than attainable at room temperatures, or are both thermodynamically and kinetically infeasible.[4,14,20,61–65]

In an attempt to increase the understanding of the lability taking place within the SSZ-13(H) **CHA** structure, *ab-initio* molecular dynamics (AIMD) simulations were performed in collaboration with researchers at Charles University in Prague, which aimed to provide insight into possible mechanistic pathways that facilitate bond cleavage upon

the interaction with water. The MD simulations carried out are therefore specific to the **CHA** framework however, the simplicity and applicability of the **CHA** topology to that of a model system means it is possible that similar types of bond cleavage processes may occur in other zeolites.

The MD simulations reveal two novel mechanisms for the initial bond cleavage in SSZ-13(H) **CHA** that support the possibility of framework bond cleavage (and subsequent oxygen exchange) under ambient conditions. The mechanisms found differ for Si – O – Si and Si – O – Al linkages, but have energy barriers that appear accessible at room temperature, *i.e.*, between 30 and 60 kJmol^{-1} (see Figure 5.12).

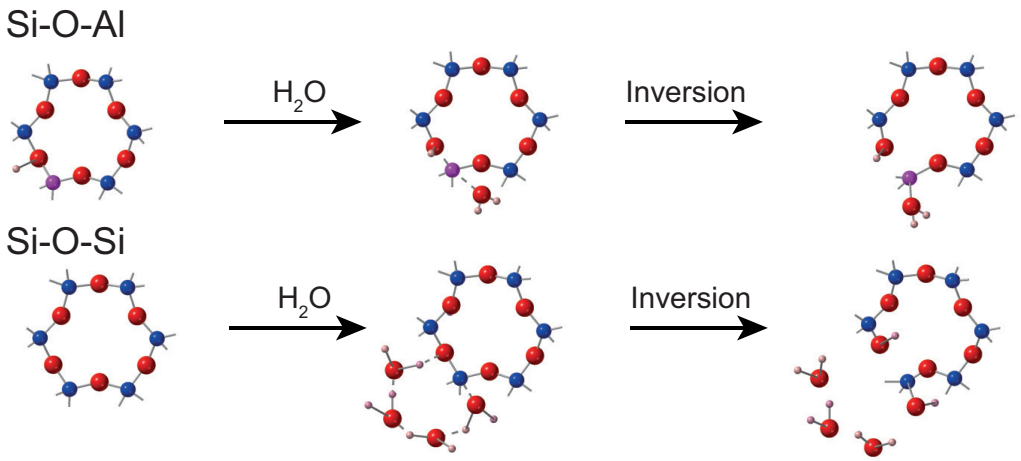

Figure 5.12: Mechanisms for bond cleavage in SSZ-13(H) **CHA** as predicted by AIMD simulations. Atom colours: oxygen = red, silicon = blue, aluminium = purple and hydrogen = pink.

For Si – O – Al bond cleavage, the framework bond can be broken by interaction with a single water molecule attacking the aluminium on which the Brønsted proton resides. This then results in inversion of the AlO_4 tetrahedron, cleaving the framework Al – O bond. Bond cleavage is possible for each of the four distinct Si – O(H) – Al sites that may surround the Al, provided they are bound in some way to the Brønsted acid proton at the time of attack. Interestingly, the mechanism shows that addition of the acidic proton from solution is possible during this mechanism, yet the solvation state of the protons in this ensemble is predicted to be 99%. This would indicate that the acidic proton in hydrated SSZ-13(H) is associated closely to the framework at some point, allowing bond cleavage to be possible at room temperature.

For Si – O – Si linkages the mechanism is slightly more complex, as can be seen in Figure 5.12. To facilitate Si – O bond cleavage here, simulations show that the formation of a chain of hydrogen-bonded water molecules, typically with a chain length of four is

required. This is initiated by the attack of a water molecule at the silicon centre at an angle to the Si – O bond, forming a pentacoordinate silicon. Following this, the hydrogen bonded water chain forms, encompassing the initial water and ending at the oxygen adjacent to silicon that is now pentacoordinate. A proton is then shuttled in a Grotthuss-type mechanism from the initial water molecule to the framework oxygen, cleaving the Si – O bond.[66,67] As shown in Table 5.4, calculations predict that this type of mechanism leads to low energy barriers for the bonds containing O1 and O4 oxygens. Although calculations were performed only for O1 and O4, a low barrier is also predicted for bonds involving O3. This is not the case for O2, owing to steric hindrance caused by the framework topology, which prevents the formation of the hydrogen bonded chain and the backside attack. Interestingly, the formation of the required hydrogen bonded chain would not be possible if water molecules were in free space. Under these conditions water molecule oxygens would typically form two hydrogen bonds, making the formation of a chain of this manner unfeasible. In the confines of the zeolite framework however, the pore and channel architectures restrict this value of hydrogen bonds to 0.86, allowing water molecules to spread out and assemble in the correct orientation. The predicted activation energies for bond scission at different O sites are detailed in Table 5.4.[21]

Oxygen Site	$\Delta A^{\ddagger}$ kJmol^{-1}	ΔA_{rxn} kJmol^{-1}
Si – O_1 – Si 1	63	1
Si – O_4 – Si 2	63	24
Si – O_1 – Al 1	32	17
Si – O_4 – Al 2	24	16

Table 5.4: Calculated activation energies ($\Delta A^{\ddagger}$) and overall reaction (ΔA_{rxn}) enthalpies derived from AIMD simulations for bond cleavage at O1 and O4 Si – O – Si and Si – O – Al sites in SSZ-13(H) **CHA** at 300 K.[21]

The simulations performed describe only the first cleavage of the framework bonds, and so do not explain the complete enrichment process. There must be subsequent mechanistic steps that then facilitate the exchange of ^{17}O oxygen into the framework, reforming the bonds broken initially. All in all, the complete exchange of oxygen from water into the zeolite framework will require the breaking and reformation of four bonds. Whilst it is unclear how these proceed mechanistically in detail, it is suggested that due to the lack of significant signals that can be attributed to silanol defects *etc.* in the NMR spectra, these subsequent steps are likely not to be rate determining, and the largest barriers to reaction are associated with initial bond cleavage.

5.4 Effect of the Countercation in SSZ-13(M) CHA

The mechanistic studies described in Section 5.3.4 provide evidence to support the surprising framework oxygen exchange observed for SSZ-13(H) **CHA** using ^{17}O NMR spectroscopy. The computational work suggests that, at least for the mechanism proposed, the presence of the Brønsted proton on the framework is important for Si−O−Al scission and the availability of protons for the Grotthuss-type proton shuffle mechanism is needed to enable Si−O−Si cleavage. It is of interest therefore, to explore the reactivity under slurrying conditions for zeolites for which acidic protons are absent. To do this and to ensure a degree of comparability, the calcined Chevron SSZ-13(H) was ion-exchanged (see Section 5.8.4) to a variety of different metal cationic forms (Na^+, K^+, Cu^{2+}, Zn^{2+}) and ^{17}O enrichment using a slurrying approach then studied.

5.4.1 Characterisation of the Exchanged Starting Materials

Metal cation-exchanged materials were first prepared by ion-exchange with the appropriate Na^+, K^+, Cu^{2+} or Zn^{2+} ionic salts as detailed in Section 5.8.4. Retention of the crystallinity of the materials was confirmed by PXRD characterisation (Figure 5.13), showing that all materials still exhibit the **CHA** structure.

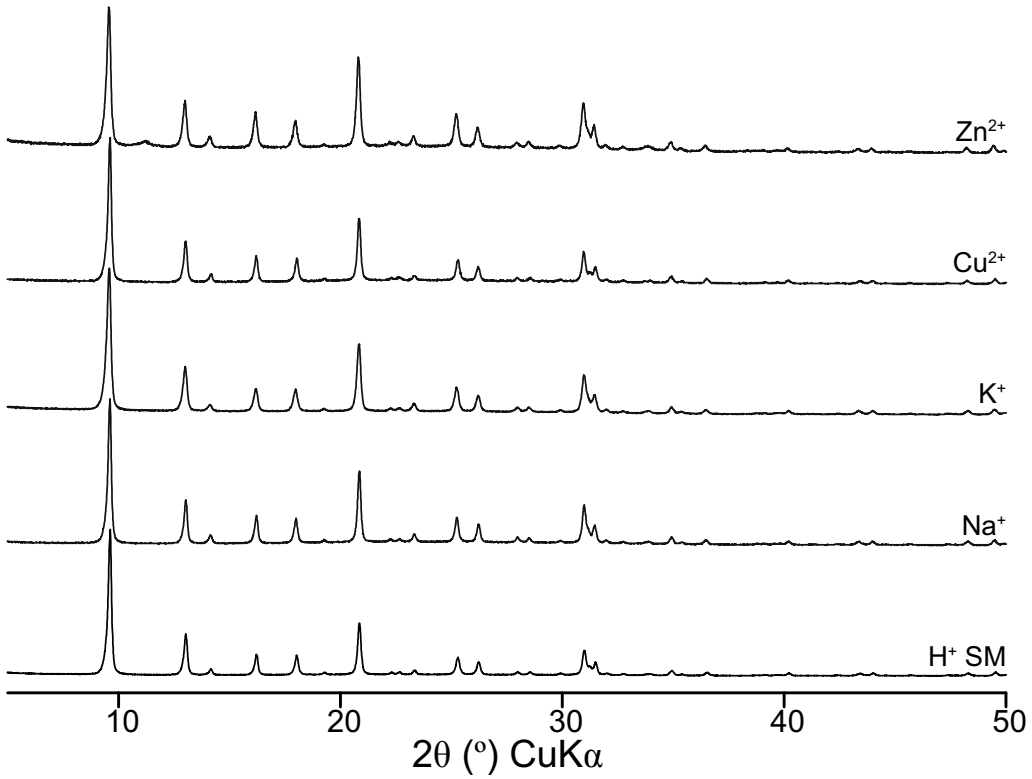

Figure 5.13: Powder X-ray diffraction patterns of metal-exchanged SSZ-13(M) **CHA** materials.

^{29}Si and ^{27}Al MAS NMR spectra of the ion-exchanged samples are shown within Figure 5.15 and Figure 5.16, respectively. ^{29}Si NMR spectra show no significant changes when compared to the SSZ-13(H) starting material, indicating that no significant increase in silanol defects has occurred and that the aluminium content or distribution has not changed significantly. Similarly, no significant changes are seen in the ^{27}Al MAS NMR spectra, although for K^+ (Figure 5.16bii) and Zn^{2+} (Figure 5.16dii) materials, a small amount of octahedral aluminium is observed. This however, is not thought to impact the integrity of the material. For the Cu^{2+}-exchanged material (Figure 5.16cii), the ^{27}Al lineshape appears broadened, most likely due to the paramagnetic copper centre on the framework.[68] Details of the Si/Al of exchanged materials are given in Table 5.5 along with values of Si/Al for subsequently $^{17}O_{2\,(g)}$-enriched materials, which will be discussed in the next section.

Cationic Form	EDX-derived Si/Al SM	Fit-calculated Si/Al SM	EDX-derived Si/Al $^{17}O_{2\,(g)}$ enriched	Fit-calculated Si/Al $^{17}O_{2\,(g)}$ enriched
H	11	10	12	11
Na	15	11	15	14
K	12	11	12	11
Cu	14	11	15	13
Zn	14	12	14	13

Table 5.5: Comparison of the EDX-derived and fit-calculated Si/Al for SSZ-13(X) **CHA** materials studied in this project. SM = starting materials, $^{17}O_{2\,(g)}$ = $^{17}O_{2\,(g)}$ gas-enriched.

5.4.2 Characterisation of $^{17}O_{2\,(g)}$-enriched Products

As for the Brønsted acidic SSZ-13(H) material (Section 5.3.2), post-synthetic $^{17}O_{2\,(g)}$ gas-enrichment of the ion-exchanged materials was performed. Once again, the observed exchange of oxygen atoms in these samples is thought to show uniform enrichment of framework oxygen and hence provide an overview of oxygen coordination environment within these materials.

The enrichment conditions used for the ion-exchanged materials are detailed in Section 5.8.6. Interestingly, the experimental conditions needed for satisfactory levels of ^{17}O exchange into framework oxygen sites are far less extreme than those for the proton form of the same material. *i.e.* similar levels of framework enrichment for the cation-exchanged zeolites here could be achieved with lower temperatures, far shorter heating times and generally easier sample handling and preparation. Furthermore, although the ^{17}O NMR spectra of the gas-enriched metal-form materials presented in this thesis are dehydrated prior to the gas-enrichment procedure, framework hydration is found to have far less of an

effect on the success of high-temperature $^{17}O_{2(g)}$ gas-enrichment than it does for H-form materials. Although the reasons behind why high-temperature oxygen exchange is more facile for SSZ-13(M) materials than for SSZ-13(H) is not known, the findings seem to be relatively consistent with that seen in other zeolites.[48] Successful ^{17}O-enrichment of SSZ-13(M) materials is achieved as evidenced by ^{17}O NMR spectra displayed in Figure 5.14.

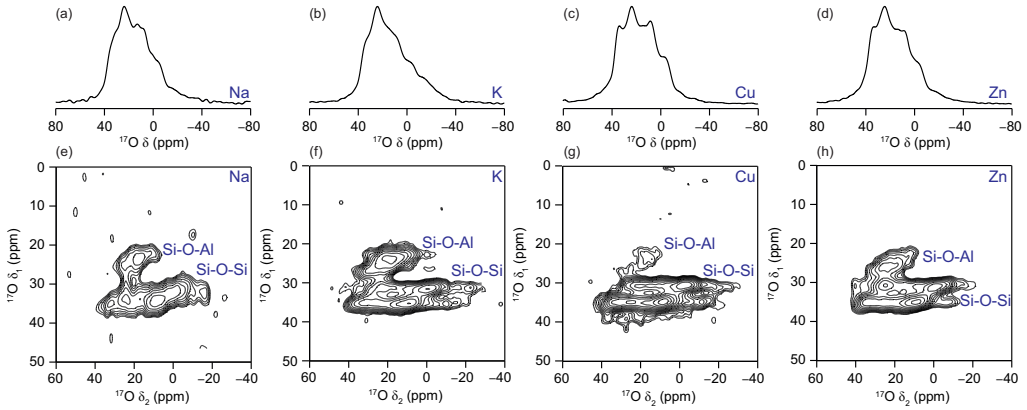

Figure 5.14: (14.1 T, 14 kHz) ^{17}O MAS NMR spectra of of $^{17}O_{2(g)}$-enriched Chevron SSZ-13(M). (a-d) quantitative short flip-angle and (e-h) $\{^1H\}^{17}O$ MQ-MAS NMR spectra. M = (a,e) Na^+, (b,f) K^+, (c,g) Cu^{2+}, (d,h) Zn^{2+}.

Post synthetic gas-enrichment of cation-exchanged SSZ-13 materials show the nature of the extra-framework cation (and potentially the enrichment procedure used) have a pronounced effect on the ^{17}O signals seen in the spectrum, and potentially on the local oxygen coordination environments. By comparison to ^{17}O NMR spectra of SSZ-13(H) (Figure 5.5), all spectra (with the exception of SSZ-13(Na)) show two distinct signals for Si−O−Si linkages, yet the extent to which the signals from Si−O−Al sites are resolved differs. Overall, the ^{17}O NMR spectra of the Cu^{2+} exchanged material most closely resembles that of the parent SSZ-13(H), which is surprising considering the presence of the paramagnetic Cu^{2+} cation in the framework. K^+ (Figure 5.14b,f) and Zn^{2+} (Figure 5.14d,h) exchanged materials both exhibit ^{17}O MQMAS spectra with two distinct Si−O−Si signals but also show higher levels of enrichment of Si−O−Al linkages. It is thought that the SSZ-13(K) material has the highest level of ^{17}O enrichment of Si−O−Al linkages within the SSZ-13(M) series and spectra show the best resolution of two Si−O−Al signals, as was seen for the SSZ-13(H) enriched via slurrying (Figure 5.6). The ^{17}O NMR spectra of the Na^+-exchanged material (Figure 5.14a,e) show only a single signal for both Si−O−Si and Si−O−Al species, the former of which is reasonably broad and covers much of the region seen for the two Si−O−Si signals in the other materials. In order to determine whether the method used for ^{17}O enrichment (*i.e.*, the high-temperature gas exchange), or the nature of the extra-framework cation (and subsequent structural changes) is affecting the number and type of ^{17}O signals seen, ^{29}Si

and ^{27}Al NMR spectra were recorded (Figure 5.15 and Figure 5.16) for all ion-exchanged materials.

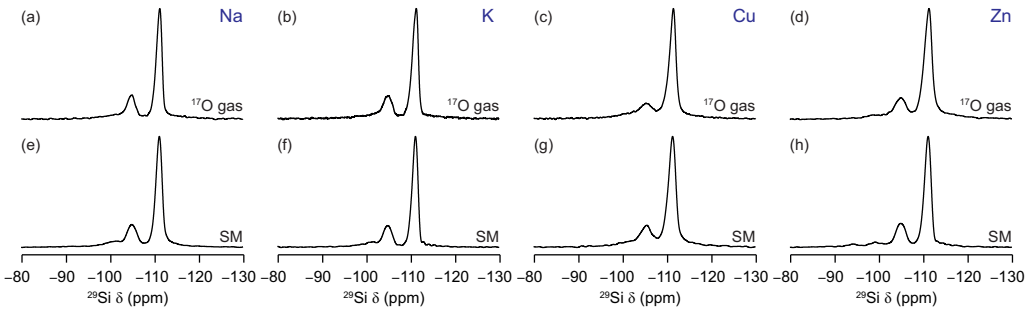

Figure 5.15: (9.4 T, 14 kHz) ^{29}Si MAS NMR spectra of (a-d) $^{17}O_{2(g)}$-enriched Chevron SSZ-13(M) and (e-h) each corresponding starting material. M = (a,e) Na^+, (b,f) K^+, (c,g) Cu^{2+}, (d,h) Zn^{2+}.

The enrichment is confirmed to proceed with relatively little effect on the overall framework structure, with similar ^{29}Si MAS NMR spectra (Figure 5.15) seen prior to and post enrichment. Comparing the spectra of the starting and ^{17}O-enriched materials of each SSZ-13(M), there appears little change in the connectivity of silicon in the materials and limited generation of silanol defects. Analysis of the Si/Al ratio in the products does reveal there may be a slight loss of aluminium associated with the high-temperature gas-exchange procedure, as evidenced by the values derived from analytical fitting in Table 5.5. The values obtained for Si/Al pre- and post- gas-enrichment procedure are closely related for all materials, however it is likely that there are some errors associated with these measurements. For EDX-derived Si/Al, the sensitivity of the technique to only the surface layers of the material likely introduces an error of $\pm$ 1-2 for this measurement. Likewise, Si/Al calculated from analytical fitting suffers from inaccuracies associated with peak fitting, resulting in an estimated error of $\pm$ 1.

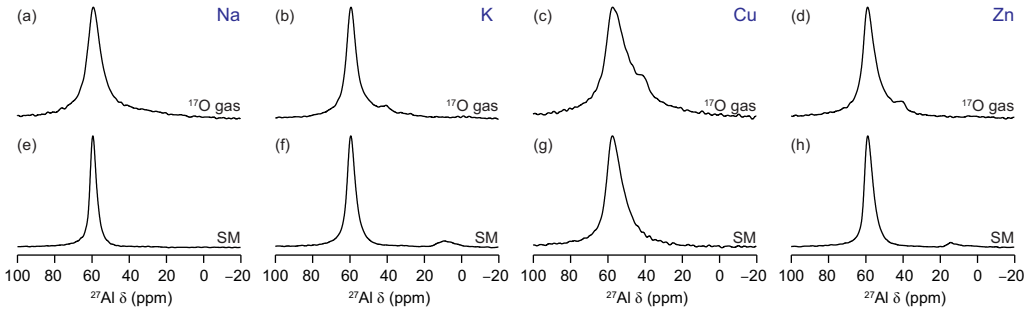

Figure 5.16: (9.4 T, 14 kHz) ^{27}Al MAS NMR spectra of (a-d) $^{17}O_{2(g)}$-enriched Chevron SSZ-13(M) and (e-h) each corresponding starting material. M = (a,e) Na^+, (b,f) K^+, (c,g) Cu^{2+}, (d,h) Zn^{2+}.

The ^{27}Al NMR spectra of the ion-exchanged materials (Figure 5.16) show that the high-temperature enrichment process has resulted in some changes in the coordination environment of aluminium within the SSZ-13(M) frameworks. For all zeolites, the signal from tetrahedral aluminium appears broader following high-temperature $^{17}O_{2(g)}$ treatment, which could result from either a small increase in quadrupolar coupling, higher levels of disorder (*i.e.*, an increase in defects or presence of different charge-balancing mechanisms) or potentially increased couplings to the NMR-active ^{17}O. For all materials with the exception of SSZ-13(Na), the presence of a shoulder on the Al(IV) peak is observed at $\approx$ 45 ppm.

^{27}Al NMR spectra (Figure 5.16) show that the high-temperature enrichment process has resulted in a change in the coordination of aluminium within the SSZ-13(M) series. For all zeolites, the tetrahedral aluminium peak appears broader following high-temperature $^{17}O_{2(g)}$ treatment and for all materials with the exception of SSZ-13(Na), the presence of a 4/5-coordinate species is observed at $\approx$ 45 ppm. This observed change in coordination may account for the differences seen between ^{17}O spectra of $^{17}O_{2(g)}$-enriched materials and is likely a result of slight weakening of the integrity of the framework around aluminium T sites. Interestingly however, this aluminium species is generated without any significant influence on the local structure around silicon (where the NMR spectra do not change significantly upon enrichment) but the formation of these new Al species may have an effect on the reaction of the frameworks with water and on ^{17}O enrichment. Based on these data, the structure of this aluminium species is unknown and it is difficult to say whether this is true 5-coordinate zeolite aluminium or another unknown aluminium species, such as broad distorted tetrahedron 4-coordinate.[69,70] To investigate this further, $\{^1H\}^{27}$Al MQMAS NMR studies were performed for the SSZ-13(H) and SSZ-13(M) materials. The spectra, displayed in Appendix E.1 reveal that distorted tetrahedral coordinated Al is present in the samples, following high temperature gas-exchange. This distorted aluminium species has been observed in zeolites previously, with its formation attributed to distortion of the tetrahedral environment of the Al centre.[71–74] This distortion has been proposed to be caused by polarisation by nearby octahedral Al sites or residual Brønsted protons, which will be more closely associated with the framework following their high-temperature gas enrichment. It has also been seen to be formed reversibly from ordered octahedral Al. Octahedral Al is seen only in the SSZ-13(H) samples, from which all the SSZ-13(M) materials were ion-exchanged. It is therefore likely that the material history and heat treatments are responsible for producing these distorted aluminium species.

5.4.3 Effect of Slurrying with $H_2{}^{17}O$

1 : 1 slurries (by mass) of 40% $H_2{}^{17}O$ and calcined and air-hydrated ion-exchanged SSZ-13(M) zeolite were prepared (Section 5.8.2) in an analogous manner to those of SSZ-13(H) (Section 5.3.3). Once again, facile, room-temperature bond lability was observed for the **CHA** materials. ^{17}O MAS NMR spectra, recorded at 20.0 T after 30 days of slurrying time are shown in Figure 5.17.

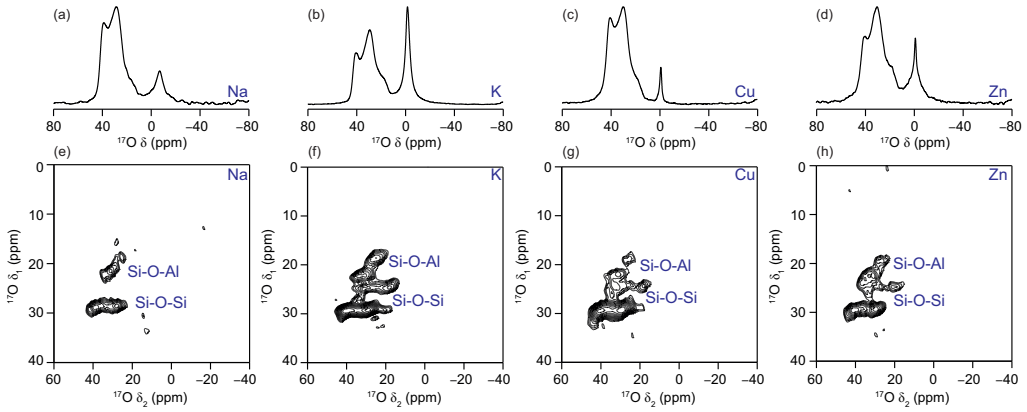

Figure 5.17: (20.0 T, 14 kHz) (a-d) quantitative short flip-angle and (e-h) $\{^1H\}^{17}O$ MQMAS NMR spectra of calcined Chevron SSZ-13(M), slurried with small amounts of 40% $H_2{}^{17}O$ for 30 days. M = (a,e) Na^+, (b,f) K^+, (c,g) Cu^{2+}, (d,h) Zn^{2+}.

Owing to the reduced second-order quadrupolar broadening at increased magnetic field, acquisition at 20.0 T has the advantage of increasing the resolution of the ^{17}O signals from the Si−O−Si and Si−O−Al resonances and the water peak at 0 ppm (Figure 5.14) and further increases the separation of resonances in the indirect dimension of $\{^1H\}^{17}O$ MQMAS NMR spectra (Figure 5.17e-h).

The increased line separation achieved at high field helps to distinguish the individual signals resolved for the slurried samples of SSZ-13(M). Overall, it appears that Si−O−Al sites are once again preferentially enriched at these hydration times, by comparison to spectra of SSZ-13(H) (Figure 5.6). Furthermore, the resolution of two signals for aluminosilicate linkages is greater for all SSZ-13(M) than in the analogous gas-enriched materials, although these materials have slight structural differences caused by the state of framework hydration, which could affect ^{17}O NMR signals. A possible mechanistic reason for the relatively enhanced intensity of Si−O−Al signals in SSZ-13(M) materials (where the Brønsted proton is absent) is that the computationally predicted bond cleavage mechanism did not require interactions with multiple water molecules and a Grotthus-type proton shuttle, as is the case for Si−O−Si (see Section 5.3.4). It is possible then that the role (if any) that the Brønsted proton plays in Si−O−Al scission in SSZ-13(H)

slurries is also fufilled by M in SSZ-13(M) slurries (or by the more likely association of this O with any remaining H defects), or that the energy barriers for Al – O bond cleavage are still accessible at room temperature for these weaker bonds even when the interaction with water/protons is reduced.

Two signals for Si – O – Si linkages are seen for all materials with the exception of SSZ-13(Na), where only a single signal (similar to that which enriched more rapidly in SSZ-13(H)) is seen. In all subsequent ^{17}O NMR spectra acquired for the slurry of the sodium-exchanged zeolite, a second Si – O – Si site is never seen. Generally however, the intensity of the 'second' Si – O – Si signal (*i.e.*, that at lower δ_1) in SSZ-13(M) spectra is of lower intensity than that for the corresponding signal in SSZ-13(H), as confirmed by the δ_1 MQMAS projections in (Figure 5.18). This could reflect poorer levels of enrichment (perhaps owing to a reduced interaction with water and/or reduced availability of protons) or possibly a structural change which would result in different NMR parameters and δ_1 shifts for the different oxygen species. It is possible to comment qualitatively on the relative rates of enrichment observed. Across the series, the following rate trend is observed: H^+, $Cu^{2+} > K^+ > Zn^{2+} > Na^+$ for SSZ-13 materials, determined from qualitative analysis of signal-to-noise levels in short-flip angle single pulse and MQMAS spectra recorded with an identical number of scans. It must be considered however that other factors, such as the exact experimental set up and multiple quantum transfer efficiency between samples with different countercations and hydration states may lead to a greater uncertainty, particularly when spectra are acquired many days apart and where absolute signal is difficult to measure.

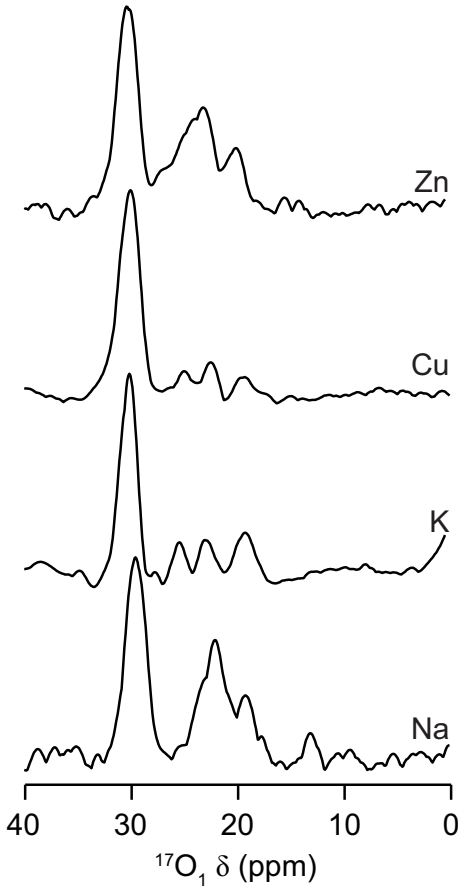

Figure 5.18: (20.0 T, 14 kHz) δ_1 sum projections of $\{^1H\}^{17}O$ MQMAS NMR spectra for SSZ-13(M), slurried for 30 days.

The exact reasons for the difference in overall and relative enrichment rates for SSZ-13(M) CHA materials are unknown and even speculation would likely require a more detailed structural characterization of the fully hydrated material which is challenging for the small scale *in-situ* experiments. It is probable that the nature of the cation plays an important role. The relative efficiency of oxygen exchange cannot be explained simply by counterion charge. Although the **CHA** framework can facilitate high diffusivity of guest molecules, it is still a small-pore zeolite with a relatively low pore volume and small ring windows.[75,76] Considering this and the enrichment behaviour observed, it is plausible that the size of the countercation and also its hydration sphere may play a role in facilitating (or hindering) bond cleavage and oxygen exchange. The estimated radius of hydration is expected to be: $Zn^{2+} > Cu^{2+} > Na^+ > K^+ > H^+$.[77–80] Of these, the divalent Zn^{2+} and Cu^{2+} cations are predicted to site within hydrated **CHA** frameworks at the base of the *cha* cages above the *d6r* in hydrated materials.[26,81,82] This position (SII in Figure 1.14) is more spacious than others and therefore the bulk of the cation size may have a lesser steric effect on any bond lability. This is particularly crucial if bond cleavage for oxygen exchange requires the formation of a hydrogen bonded chain of water molecules. Further, the larger

size of the Zn^{2+} hydration sphere and hence greater steric effect may be responsible for the overall lower enrichment level seen in this material. The alkali metal cations, K^+ and Na^+ are predicted to site closer to the *cha* (SIII) and in the *cha* cages, near the *4r* windows (SIII').[58,83,84] Cations near these positions are likely to place a greater steric hindrance to any bond cleavage processes taking place, particularly around the O2 site. It follows, therefore, that the hydrated metal cations, particularly hydrated Na^+ may block access of water molecules to specific oxygen sites in the framework, limiting the hydrolytic bond lability and preventing or reducing the framework oxygen exchange processes from occurring. Whilst this theory is based on the computational prediction that Si–O–Si sites in SSZ-13(H) slurries need the interaction with protons and a H-bonded chain of water molecules to facilitate bond cleavage, it is plausible that these steric effects will also hamper the mechanism of action in SSZ-13(M) slurries, which may too utilise H-bonded water. Additionally, the availability of water molecules to interact with the zeolite framework or contribute to any H-bonded chains may also be affected by the strength with which the water molecules are held by the extra-framework cation.

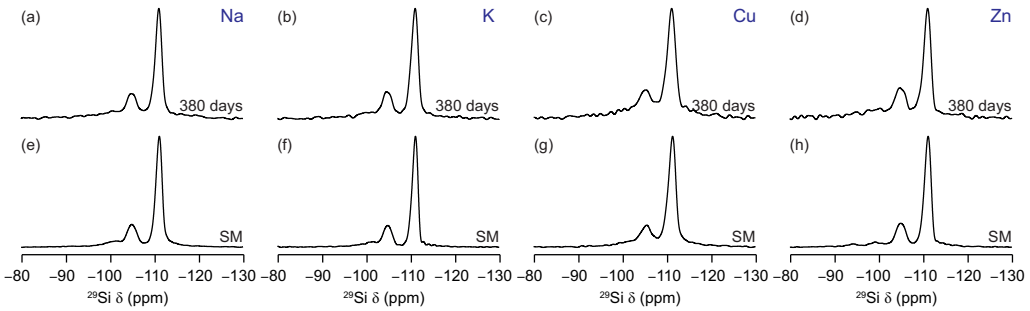

Figure 5.19: (9.4 T, 14 kHz) ^{29}Si MAS NMR spectra of (a-d) $H_2{}^{17}O$ slurried Chevron SSZ-13(M) and (e-h) the corresponding starting material. M = (a,e) Na^+, (b,f) K^+, (c,g) Cu^{2+}, (d,h) Zn^{2+}. Slurry ages indicated on plot.

During slurrying of these materials, the silicon and aluminium sites remain tetrahedrally coordinated and no significant changes to the Si/Al ratio and their respective framework T site distributions occur (see Figure 5.19 and Figure 5.20). This means, once again, the room-temperature bond lability and framework oxygen exchange process occur without detriment to the overall framework structure. Small amounts of distorted tetrahedral aluminium are again seen in $\{^1H\}^{27}Al$ MQMAS NMR spectra, displayed in Appendix E.2.

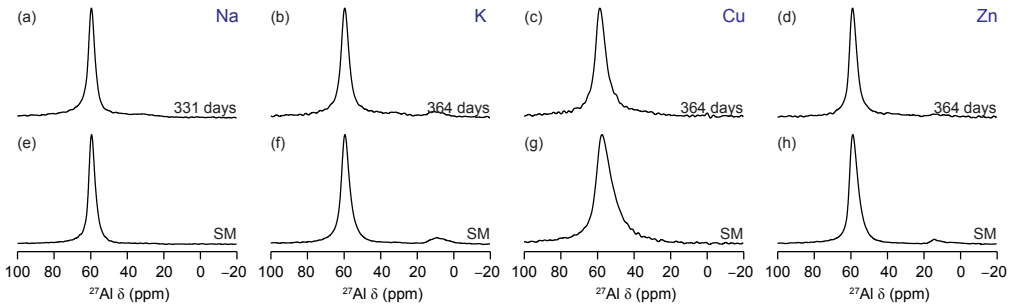

Figure 5.20: (9.4 T, 14 kHz) ^{29}Si MAS NMR spectra of (a-d) $H_2{}^{17}O$ slurried Chevron SSZ-13(M) and (e-h) the corresponding starting material. M = (a,e) Na^+, (b,f) K^+, (c,g) Cu^{2+}, (d,h) Zn^{2+}. Slurry ages indicated on plot.

5.5 Effect of Framework Composition in CHA

The low concentration of aluminium in SSZ-13 mean these atoms are often isolated in the framework, resulting in strongly acidic Brønsted protons. Further, the introduction of aluminium into the framework results in increased framework hydrophilicity and average bond polarity and a decreased average bond enthalpy. Aluminium, however, is not the only dopant element that can be incorporated into the **CHA** framework and that can have an effect on its stability and structure. It is of interest therefore to investigate the effect of framework composition on the room-temperature bond lability seen above by varying the Al content or substituting Al^{3+} for other T-atoms, such as B^{3+}, Ti^{4+} and Zn^{2+}.

These cations will have a different effect on the overall framework charge, compared to Al^{3+}. B^{3+}, having the same valence as aluminium in zeolites will produce the most similar effect. However the reduced acidity of borosilicate zeolites will result in changes to the charge distribution, bond polarity and reactivity. Substitution for Ti^{4+} will produce a charge-neutral framework that possesses a degree of polarity as the single T site of the **CHA** framework will not be populated in a uniform manner. It is desired to characterise the reactivity of this material with water against a purely siliceous **CHA** framework, where all T sites are crystallographically equivalent. **CHA** is one of only a handful of frameworks where substitution of aluminium for a divalent cation has been achieved. exchange for Zn^{2+} here provides a great opportunity to study how materials with increased framework charge and Brønsted acidity behave under aqueous conditions.

5.5.1 Characterisation of the Substituted Starting Materials

In keeping with the previous work on SSZ-13(H), **CHA** materials of varied composition and negative framework charge were prepared directly in the proton-form using published literature methods.[24,28,29,34,85,86] Materials prepared in this manner and those prepared with neutral frameworks for this study are: Si-**CHA**, B-**CHA**(H), Ti-**CHA** and Zn-**CHA**(H). Syntheses are detailed in Section 3.3. These materials are known to display a degree of framework flexibility based on the heteroatom selected, showing variations in pore geometry and host-guest interaction efficacy, having implications for CO_2/CH_4 separation efficiency.[87] Additionally, a low silica (Si/Al = 5) **CHA** material was prepared in the K^+-form,[88] and ion-exchanged (to NH_4^+-form). However, the low thermal stability of the resulting material meant it was not possible to produce the H^+ form without compromising the framework structure. Instead, the bond lability of an Al-**CHA**(K) material was investigated, as described in Chapter 5 as part of an investigation into post-synthetic transformations (PST). The PXRD patterns of synthesised heteroatomic **CHA** materials are presented in Figure 5.21, confirming the **CHA** framework has successfully been formed in each case.

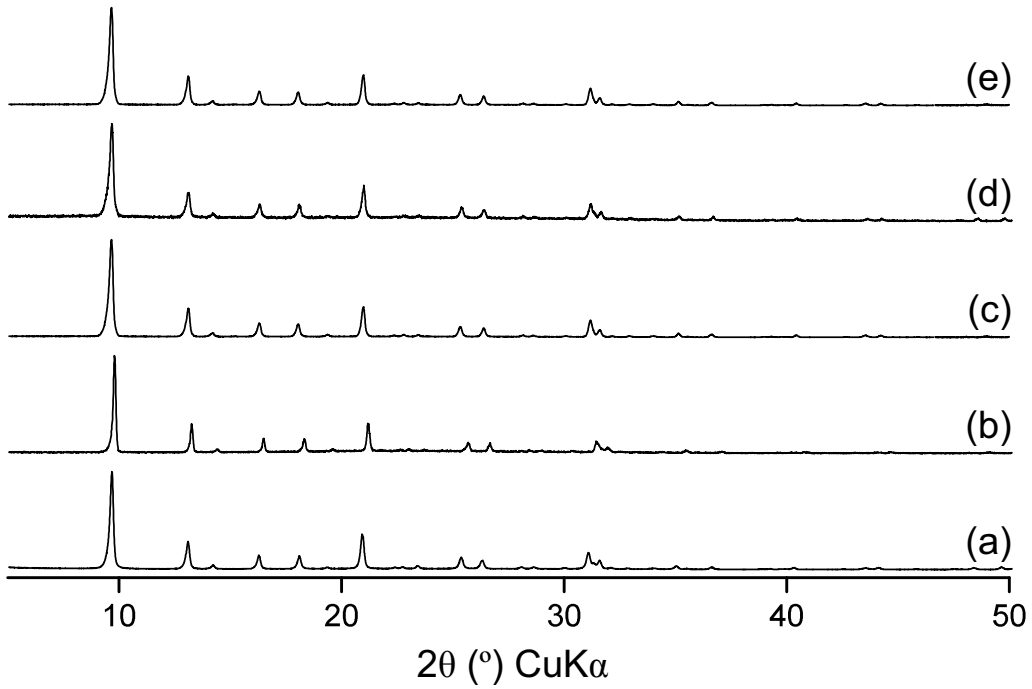

Figure 5.21: Powder X-ray diffraction pattern of (a) SSZ-13(H), (b) Si-**CHA**, (c) B-**CHA**(H), (d) Ti-**CHA** and (e) Zn-**CHA**(H).

The local structure of the frameworks was characterised by performing ^{29}Si NMR experiments for calcined heteroatomic materials, as shown in Figure 5.22. Generally, all materials show small amounts of Q^3 framework silanol defects ($\delta \approx -102$ ppm) as evidenced by CP MAS NMR spectra, alongside the Q^4 framework site at $\delta \approx -102$ ppm. For B-

CHA(H) it is proposed the overlapped signals/shoulders at δ −113, −110 and −106 ppm are attributed to boron in neighbouring T sites, which experiences lattice distortion. The Q^4 $Si(O-Si)_3(O-B)$ and Q^3 silanol defect peaks are found overlapped between −102 and −99 ppm.[29,38] In the case of Si-**CHA** an increased number of transients had to be averaged to achieve the signal-to-noise seen in Figure 5.22a and as such this material is considered almost non-defective. It was not possible to perform accurate lineshape fitting on ^{29}Si MAS NMR spectra of heteroatomic materials to determine the Si/X ratio (X = B, Ti, Zn), however EDX measurements indicate that materials have heteroatom contents (Si/X) of 8 (B-**CHA**(H)), 22 (Ti-**CHA**) and 18 (Zn-**CHA**(H)), or a total of 4, <2 and <2 per crystallographic unit cell, respectively.

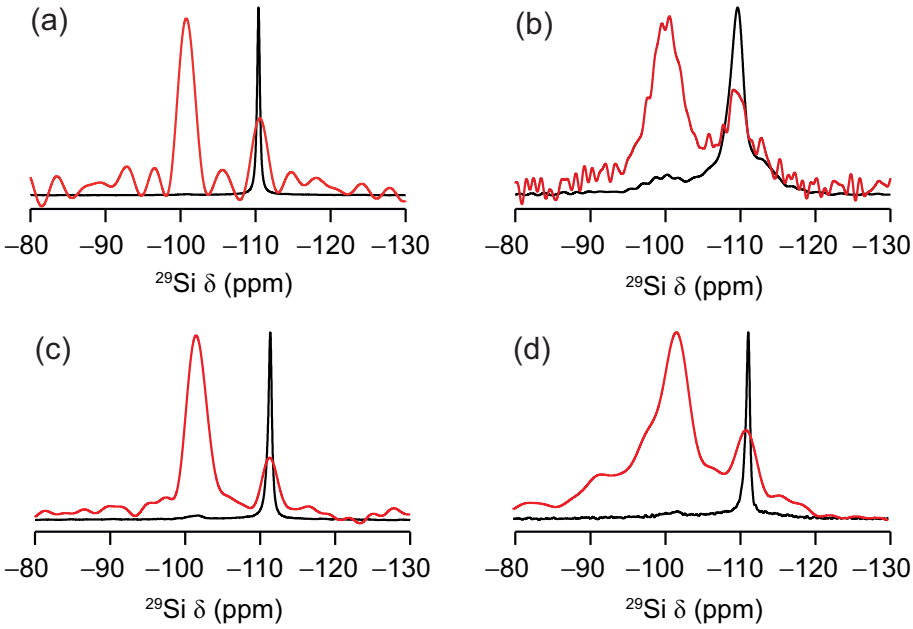

Figure 5.22: (9.4 T, 14 kHz) ^{29}Si single-pulse MAS NMR spectra for calcined heteroatom-substituted **CHA** materials. (a) Si-**CHA**, (b) B-**CHA**(H), (c) Ti-**CHA** and (d) Zn-**CHA**(H). Red overlay on spectra is the ^{1}H^{29}Si CP NMR spectrum (5000 μs contact time).

Elemental boron is 80.1% ^{11}B, which has I = 3/2, reasonably good NMR sensitivity and NMR parameters (both chemical shift and quadrupolar coupling) that are very sensitive to the coordination number.[89] The study of borosilicate zeolites using ^{11}B NMR is therefore relatively straightforward and potentially informative, provided a boron nitride (BN)-free probe is available. Insight into the ^{11}B local environment in B-**CHA**(H) will also provide information on the effect of any reversible bond lability processes on the framework. ^{11}B MAS NMR spectra of two forms of the starting material are shown in Figure 5.23. The sharp signal at − 3.5 ppm is assigned as tetrahedrally coordinated B(IV), within the **CHA** framework itself, with the small C_Q reflecting the symmetric coordination environment. In the as-synthesised material, the presence of the neighbouring peak at − 2 ppm is inter-

esting. Tetrahedrally coordinated peaks like this have been reported previously, however no definitive assignment to a particular chemical species has been made. These tetrahedral species are predicted to be partially hydrated and capable of transitioning between tetrahedrally coordinated B(IV) species associated with acidic water (H_3O^+) to trigonally bound framework species fully coordinated to a water molecule as a function of material hydration.[90,91] This is cited as a reason for why this species at -2 ppm is less prominent in the calcined sample (Figure 5.23b), where overall framework hydration is expected to be lower. During the calcination process however, a trigonal species with higher C_Q, with a higher δ_{iso}, most likely attributable to non-framework boron, formed during calcination.[38,91,92] Although occasionally a reversible process, the leeching of boron in this manner is a known problem for borosilicate zeolites in the proton form as hydrolysis of framework linkages under high-temperature conditions (*e.g.*, those of the calcination temperature) is increasingly favourable, compared to analogous aluminosilicate materials.[38,90–92]

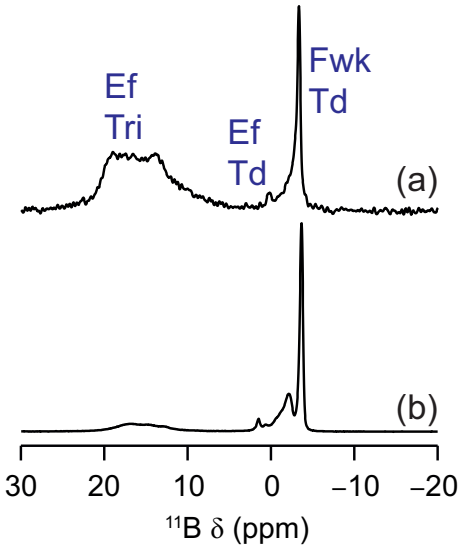

Figure 5.23: (14.1 T, 14 kHz) ^{11}B single-pulse NMR spectra for B-**CHA**(H). (a) calcined and hydrated and (b) as-synthesised materials.

5.5.2 Effect of Slurrying with $H_2{}^{17}O$

Despite the increased defects present in some heteroatomic materials, the enrichment of the zeolite frameworks using $H_2{}^{17}O$ slurrying was studied using the same approach for SSZ-13(H) and SSZ-13(M) (see Section 5.8.9).

It was only possible to successfully enrich Si-**CHA** using post-synthetic exchange with $^{17}O_{2(g)}$ (see Section 5.8.8). The absence of any dopant elements in Si-**CHA** means that

^{17}O NMR spectra, particularly of the $^{17}O_{2(g)}$ enriched sample (which is expected to have higher levels or more uniform enrichment) should produce the highest resolution spectrum and the greatest chances of resolving signals from the four distinct O species (if this is indeed possible). The ^{17}O NMR spectra gas-enriched spectra are shown in Figure 5.24.

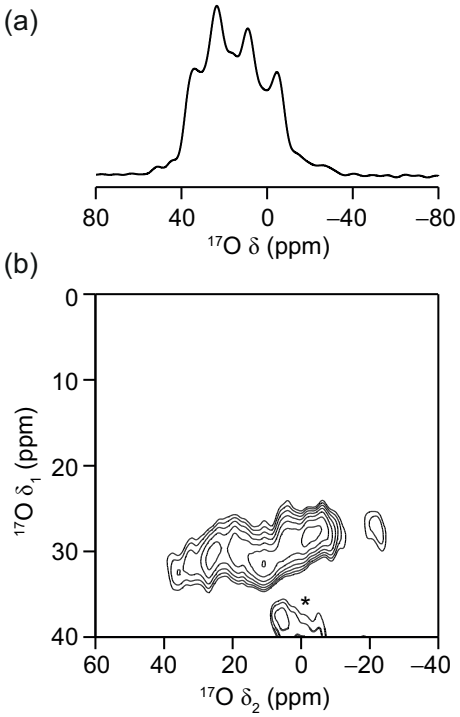

Figure 5.24: (14.1 T, 14 kHz) ^{17}O MAS NMR spectra of of $^{17}O_{2(g)}$-enriched Si-**CHA**. (a) Quantitative short flip-angle and (b) $\{^1H\}^{17}$O MQMAS NMR spectra.

Considering the ^{17}O NMR spectra of SSZ-13(H) and SSZ-13(M) seen previously, one may expect two separate Si – O – Si resonances for the gas-enriched Si-**CHA**. In Figure 5.24a, the presence of more than one quadrupolar lineshape is evident, yet complete separation of the four signals in the MQMAS NMR spectrum (Figure 5.24b) has not been fully achieved, but the resonance positions agree well with those predicted previously using DFT (for a dehydrated material) in Figure 5.7. In order to unambiguously determine whether the Si – O – Si signal can be resolved into signals from the distinct Si – O – Si linkages, a spectrum at a higher magnetic field is needed.

Exposure of unenriched Si-**CHA** to $H_2{}^{17}O$ in a slurry results in some framework enrichment, as shown in Figure 5.25. When comparing the enrichment rate to those of the aluminosilicate slurries discussed previously, it is apparent that the pure silica material exchanges framework oxygens far more slowly, or in much lower quantities (see large free water peak at 0 ppm), possibly due to the increased hydrophobicity of the material. Nonetheless, the fact that framework enrichment is observed for Si-**CHA**, in the absence of any polar bonds, negative framework charge or any extraframework charge-balancing

cations, is particularly surprising. Whilst possibly less energetically favourable than the breaking of bonds in acidic zeolites, the mechanism for Si-**CHA** bond cleavage is likely to be similar to that seen for Si – O – Si bonds in SSZ-13(H) and SSZ-13(M) materials. Although the exact mechanism for this exchange is unknown, and although the material will contain a very low level of silanol defects, it is clear that it is not only these that are being enriched (as the signal seen is too intense for that). It may be, however, that even low levels of defects can act as points of weakness in a framework, increasing the lability of the entire material. Loss of ^{17}O signal is not seen in enriched materials exposed to air, which suggests that an interaction with the strongly hydrogen bonded water provided by the exposure to $H_2^{17}O_{(l)}$ is required for O exchange.

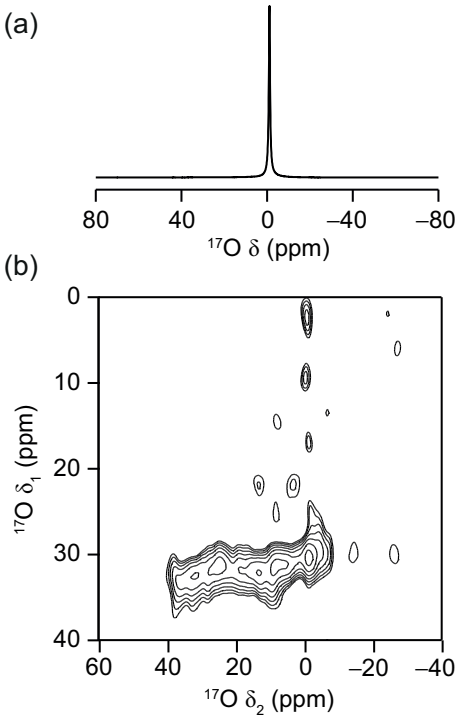

Figure 5.25: (14.1 T, 14 kHz) ^{17}O MAS NMR spectra of Si-**CHA**, slurried with small amounts of 40% $H_2{}^{17}O$ for 10 days. (a) quantitative short flip-angle and (a) $\{^1H\}^{17}$O MQMAS NMR spectra.

Interestingly, the resonance resolved in the ^{17}O MQMAS experiment overlays most well with the Si−O−Si signal at higher δ_1 in SSZ-13(H) spectra. Unfortunately it is unclear from the spectra in Figure 5.24 and Figure 5.25, whether the local atomic structure of the aluminosilicate **CHA** will cause any change in the position of NMR resonances or whether there is more preferential enrichment of some O sites in a Si-**CHA** slurry.

Whichever mechanism is followed to exchange framework oxygen with those in free water within the slurry, the local coordination environment of Si and the overall long-range order of the material is not compromised, for materials enriched using either a slurry or gas-exchange, as shown using ^{29}Si MAS NMR (Figure 5.26) and PXRD (not shown).
The ^{17}O enrichment of titanosilicate and zincosilicate **CHA** frameworks in a slurry was subsequently studied using ^{17}O NMR spectroscopy. Titanosilicate frameworks are well suited to this NMR-based investigation as the direct coordination of Ti to O produces a very significant change in chemical shift. Oxygens in Ti−O bonds in this study are predicted to have δ_{iso} between 600-800 ppm.[89] As a result, enrichment of any Ti−O linkage should be easily identified in ^{17}O NMR spectra. As for zincosilicate frameworks, introduction of Zn^{2+} should result in a double negative charge on the framework, creating two Brønsted acidic sites. The suggested need for a Brønsted proton to facilitate the rate of framework oxygen exchange for **CHA** materials makes study of this framework compo-

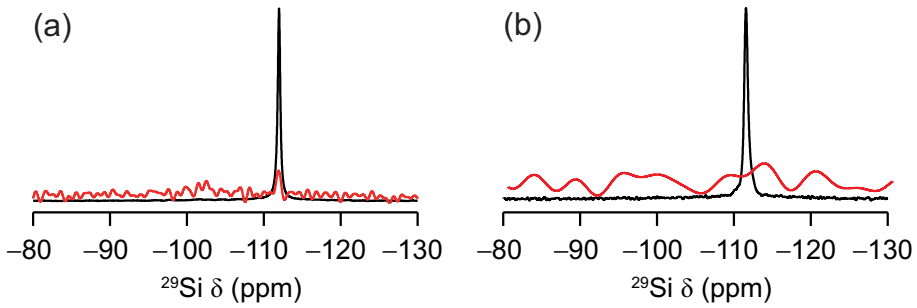

Figure 5.26: (14.1 T, 14 kHz) ^{29}Si MAS NMR spectra of Si-**CHA**, (a) slurried with small amounts of 40% $H_2{}^{17}O$ for 10 days and (b) gas-enriched in 70% $^{17}O_{2(g)}$ at 600 °C for 18 hours. Red overlay on spectra is the $^{1}H^{29}Si$ CP NMR spectrum (5000 μs contact time).

sition particularly interesting. ^{17}O NMR spectra of Ti-**CHA** and Zn-**CHA**(H) materials, enriched using a slurry, are shown in Figure 5.27.

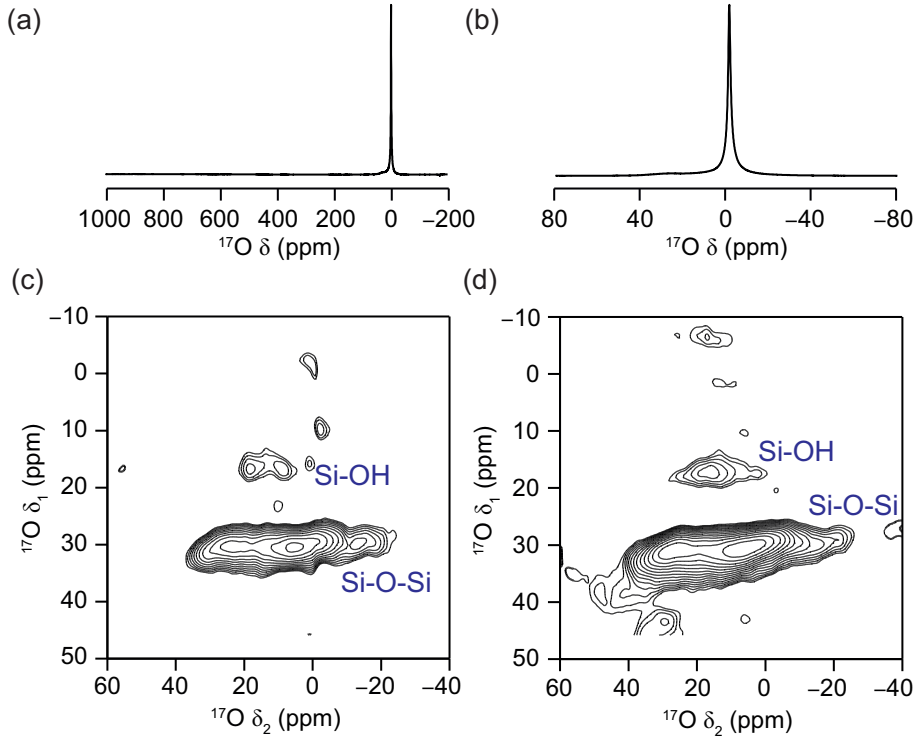

Figure 5.27: (14.1 T, 14 kHz) ^{17}O MAS NMR spectra of of (a,c) Ti-**CHA** and (b,d) Zn-**CHA**(H) slurried with small amounts of 40% $H_2{}^{17}O$ for 7 days. (a,b) Quantitative short flip-angle and (c,d) $\{^{1}H\}^{17}O$ MQMAS NMR spectra.

For the titano- and zinco-silicate materials, a broad signal corresponding to Si–O–Si is seen at $\delta_1 \approx 32$ ppm, however, there is no evidence of Ti–O or Zn–O resonances in Figure 5.27. Furthermore, both MQMAS NMR spectra exhibit a resonance at $\delta_1 \approx 18$ ppm, attributable to Si–OH silanols.[93] The extent of the silanol defects resolved indicates the frameworks are most likely unstable to slurrying processes and are highly defective. For this reason their study within this experiment was not continued.

Protonated borosilicate zeolites are generally less Brønsted acidic than their aluminosilicate analogues, owing to the reduced polarity of the B–O bond. It is of interest, therefore, to understand the effect this has on the room-temperature bond lability of these frameworks. The B-**CHA**(H) material was slurried in an identical manner to those materials studied previously. Additionally, high magnetic field experiments (23.5 T) were carried out on a sample of the same borosilicate material that had been treated with $H_2{}^{17}O$ through an incipient-wetness enrichment procedure (Section 5.8.10). The procedure is similar to the slurry enrichment procedure, except that the system is not sealed and so the isotopically-enriched water is either fully absorbed into the material or is able to evaporate from the surface of the sample. ^{17}O NMR spectra are shown in Figure 5.28.

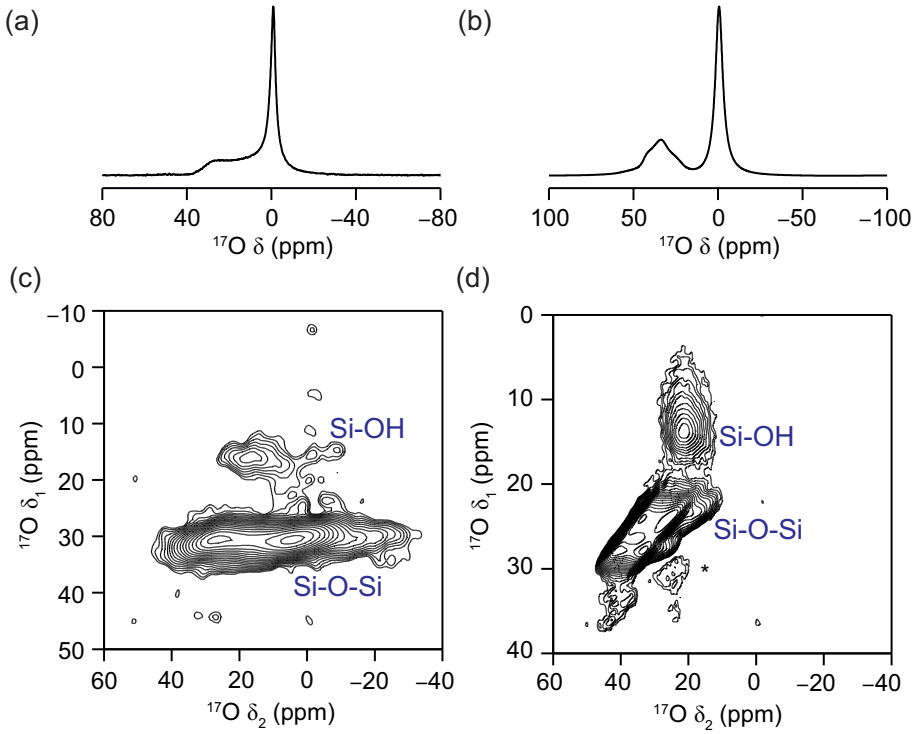

Figure 5.28: ^{17}O MAS NMR spectra of B-**CHA**(H), (a,c) slurried in $H_2{}^{17}O$ for 89 days, recorded at 14.1 T, 14 kHz MAS. (b,d) Incipient wetness treated with $H_2{}^{17}O$ and left for 89 days, recorded at 23.5 T, 20 kHz MAS. (a,b) quantitative short flip-angle and (c,d) $\{^1H\}^{17}O$ MQMAS NMR spectra.

Clearly, room-temperature bond lability facilitates the framework oxygen exchange in B-**CHA**(H), as shown in Figure 5.28. Significant quantities of the ^{17}O isotope are found sited within Si–O–Si linkages for both the slurry and incipient wetness treated materials. The mechanism of bond lability (and therefore the rate and positon of enrichment) is expected to be similar for both of these materials, owing to the similarities in their preparation, however the time during which exchange can take place is expected

to be shorter for the samples enriched using incipient-wetness as these will be more susceptible to ambient evaporation. As such, the bond lability in B-**CHA**(H) is judged to be facile and to take place on a rapid timescale. The 23.5 T ^{17}O MQMAS spectrum (Figure 5.28d shows evidence for two Si – O – Si resonances (δ_1 of 20-30 ppm) and an intense resonance centred at $\delta_1 \approx$15 ppm, which can be assigned to Si – OH. A similar picture is seen for the slurried sample in Figure 5.28c, with high levels of enrichment but only one clear Si – O – Si signal seen is resolved. It is likely that this resonance is the sum of the two seen at 23.5 T, which has become overlapped in the lower field (14.1 T) experiment. Interestingly, Si – O – B linkages could not be seen in either spectra. At 14.1 T, these are predicted to be centred in the region (δ_1, δ_2) $\approx$ (40, 20) ppm.

Three main conclusions can be drawn from the 17O enrichment of B-CHA(H). Firstly, when compared to the aluminosilicate materials, the presence of the heteroatom in the framework does not significantly impact the ability for, or rate of, Si – O – Si enrichment. Secondly, it is interesting that the substitution of aluminium by boron does extensively change the local structural environment of the oxygen atoms in the material, with two signals attributed to Si – O – Si resonances resolved in similar positions to that of ^{17}O-enriched SSZ-13 samples. It is proposed that a similar effect occurs for other heteroatomic T sites, *e.g.* Ti^{4+} and Zn^{2+}, such that the MQMAS spectra recorded for these materials at 14.1 T (see Figure 5.27) may contain two strongly overlapped Si – O – Si sites. Finally and more generally, the flexibility of boron coordination in these calcined B-**CHA**(H) materials can become irriversible at the levels of water exposure used in slurry and incipient wetness studies. In the case of the incipient wetness sample; which was considered dry at time of acquisition; ^{11}B NMR spectra (Figure 5.29a,c,e) show that for both approaches, boron is fully hydrolysed from the framework and a dynamic, solution-type lineshape for a $B(OH)_3$ species (high chemical shift but little quadrupolar broadening) is observed. This is accompanied by an increased Si – OH concentration and broadening of the Q^4 signal in the ^{29}Si MAS NMR spectra (Figure 5.29b,d,f).

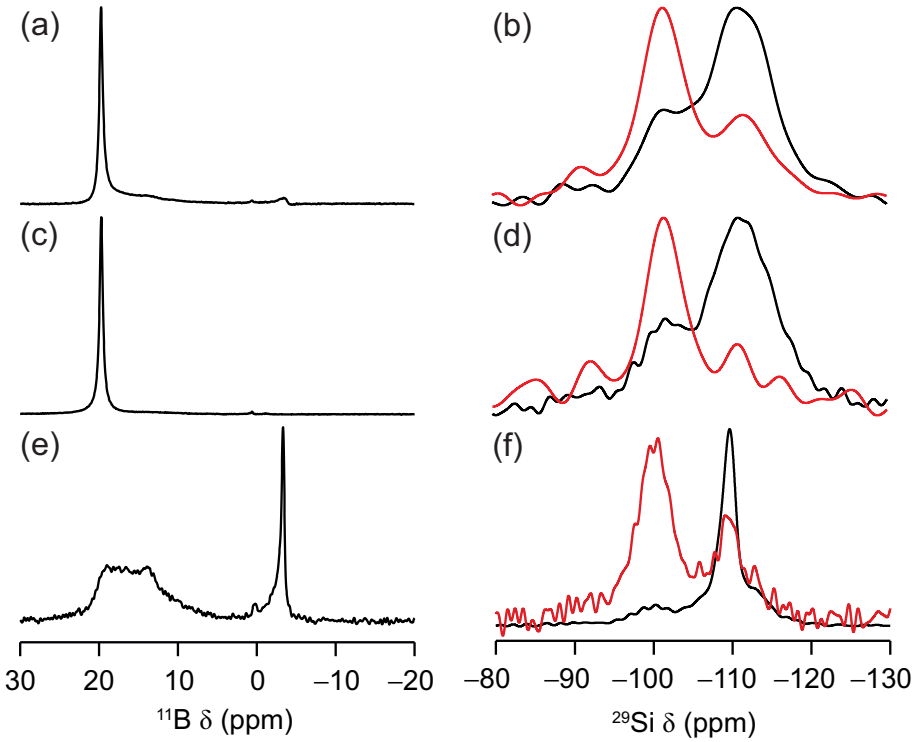

Figure 5.29: (a,c,e) (14.1 T, 14 kHz) ^{11}B and (b,d,f) (9.4 T, 14 kHz) ^{29}Si MAS NMR spectra of B-**CHA**(H). (a,b) Incipient wetness treated with $H_2{}^{17}O$ and left for 30 days, (c,d) slurried in $H_2{}^{17}O$ for (c) 87 days, (d) 28 days, (e,f) calcined starting material. Red overlay on spectra for (b,d,f) is the $^{1}H^{29}Si$ CP NMR spectrum (5000 μs contact time).

Considering the enrichment of Brønsted acidic **CHA** frameworks with varying heteroatom substitution, it is clear that the efficiency of framework oxygen exchange within these materials is not dependent on a single factor *e.g.*, availability of a Brønsted proton, framework charge, defect prevalence or acidity strength. Without a doubt, however, is the ability of **CHA** framework materials to readily exchange oxygen atoms in framework Si–O–Si sites at room temperature. The overall trend for framework enrichment in M-**CHA**(H) observed is roughly as follows: Al > B > Zn ≈ Ti > Si. Interestingly, this trend does not seem to follow the one seen by Yue *et al.* in reference 87, when assessing the distortion and flexibility of the *8r* window in **CHA**: Ga > Ti ≈ B > Si > Al.[87] This suggests that other descriptors of zeolite framework flexibility may not necessarily indicate whether a zeolite framework is susceptible to aqueous-mediated framework flexibility and bond lability processes. It is interesting, yet unclear why of all Si–O–X (X = Al, B, Ti, Zn) linkages present in the **CHA** materials studied, evidence of bond lability was seen for the Si–O–Al linkage only.

5.6 Effect of Framework Topology - Expansion to FAU

The need for hydrogen-bonded chains of water molecules to facilitate the lability of bonds with attack at specific orientations relative to a bond in the **CHA** topology was predicted computationally to be an important factor in the ability of the framework to readily undergo ^{17}O exchange.[21] However, it has been shown that other zeolite topologies, specifically **MOR** and **FER**, also demonstrate such facile framework oxygen exchange, albeit qualitatively speaking at a slightly slower rate.[22] To further understand lability processes ongoing in zeolites, the study above was expanded to the **FAU** topology. This framework was chosen due to its structural similarity to the **CHA** framework; particularly as the materials can be interconverted (see Chapter 6); and as in-depth ^{17}O NMR spectroscopic investigations and spectral assignments exist in the literature for dehydrated frameworks.[50]

5.6.1 Characterisation of the Starting Material

Sodium-form Linde type-Y **FAU** (Si/Al = 1.7) was prepared using literature methods (see Section 3.3.12).[94] The material was characterised using PXRD (Figure 5.30) and ^{27}Al and ^{29}Si NMR spectroscopy (Figure 5.31).

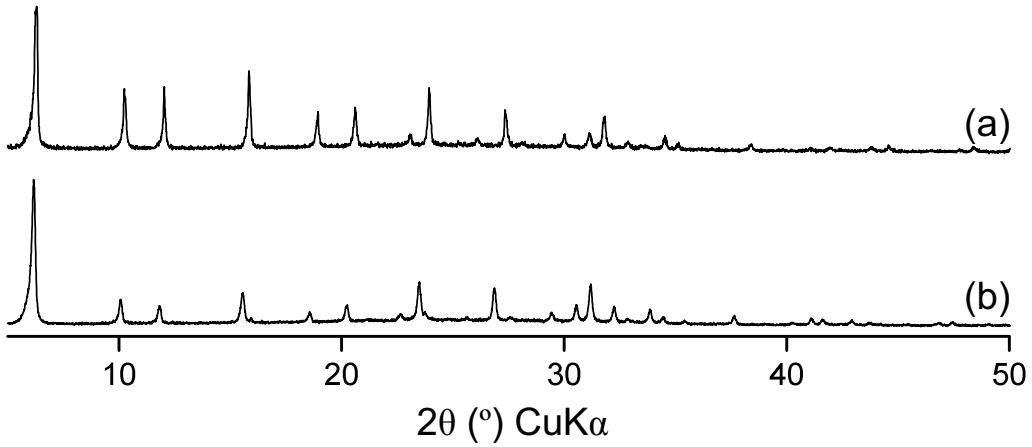

Figure 5.30: Powder X-ray diffraction pattern of (a) reference **FAU** material[95] and (b) synthesised Al-**FAU**(Na).

Figure 5.30 confirms a **FAU** structure material has been obtained. Figure 5.31 shows how the material, which possesses only a single crystallographic T site has a fully tetrahedrally-coordinated framework, with only signals from tetrahedrally coordinate Al seen (Figure 5.31b). Additionally, a Q^4 local structure with minimal defects is seen for the ^{29}Si NMR spectrum in (Figure 5.31a), containing $Si(O-Si)_4$, $Si(O-Si)_3(O-Al)$, $Si(O-Al)_2(O-Si)_2$, $Si(O-Si)(O-Al)_3$ and $Si(O-Al)_4$ at -97 ppm, -93 ppm, -88 ppm, -84 ppm and -79 ppm, respectively.

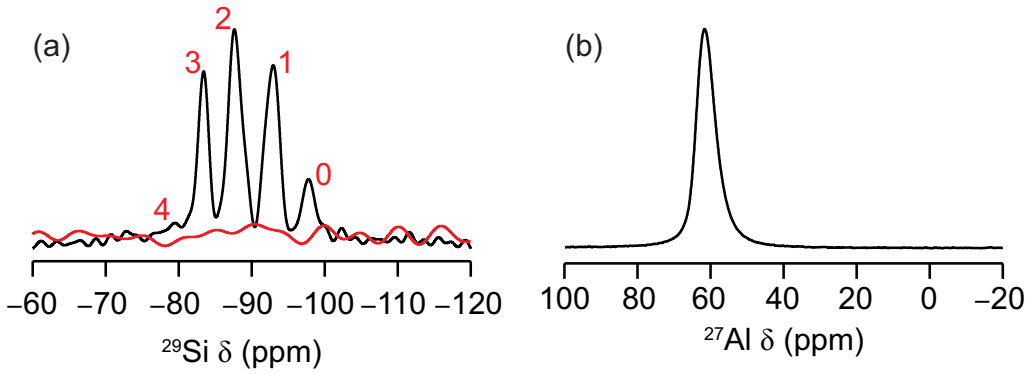

Figure 5.31: (9.4 T, 14 kHz) (a) ^{29}Si and (b) ^{27}Al MAS single-pulse NMR spectra of as-synthesised Al-**FAU**(Na). Red overlay in (a) is the ^{1}H^{29}Si CP NMR spectrum (5000 μs contact time). Number of NNN silicon atoms (n) for Si(O−Si)$_{4-n}$(O−Al)$_n$, indicated in red on figure in (a).

5.6.2 Characterisation of $^{17}O_{2(g)}$-enriched Products

It was possible to successfully $^{17}O_{2(g)}$-enrich the Al-**FAU**(Na) material to a good level, provided prior dehydration procedures were carried out (see Section 6.9.5). Combined with a lower target enrichment temperature, the known high-temperature degradation of aluminium-rich zeolite frameworks was minimised and material crystallinity was retained. ^{17}O NMR spectra of the resulting material are shown in Figure 5.32.

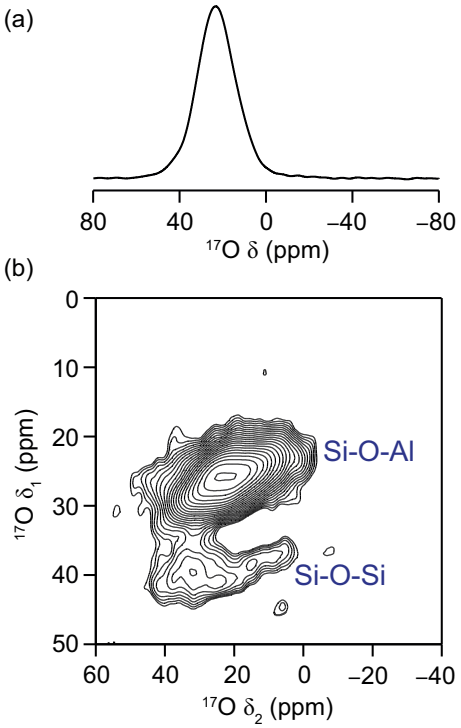

Figure 5.32: (14.1 T, 14 kHz) ^{17}O MAS NMR spectra of $^{17}O_{2(g)}$-enriched Al-**FAU**(Na). (a) Quantitative short flip-angle and (b) $\{^{1}H\}^{17}$O MQMAS NMR spectra.

Unsurprisingly, the observed enrichment of this material is dominated by Si−O−Al linkages, owing to the lower Si/Al, when compared to the other framework materials discussed in this Chapter. At this field, one broad Si−O−Al signal is seen, centred at (δ_1, δ_2) ≈ (25, 21) ppm. Some Si−O−Si signal is also seen between δ_1 of 37 and 45 ppm. Although not possible to confirm unambiguously, extracting rows from the MQMAS spectrum provides evidence that this spectral feature may contain two separate Si−O−Al and Si−O−Si signals at ≈ 22 and ≈ 28 (Si−O−Al) and ≈ 39 and ≈ 42 ppm (Si−O−Si), respectively. MAS NMR spectra acquired with a short flip angle in Figure 5.32a show little resolution of distinct signals.

From the ^{27}Al and ^{29}Si NMR spectra of the $^{17}O_{2(g)}$-enriched product (Figure 5.33), there is evidence that the enrichment procedure did result in some changes to the framework. Figure 5.33a shows a slight broadening and change in distribution of silicon species (from relative intensities) following the high-temperature treatment, accompanied by an increase in $^{1}H^{29}$Si CP signal; indicating the formation of silanol species. Figure 5.33b also demonstrates an increase in disorder of the aluminium species in the material, with some broadening of the ^{27}Al signal at low frequency. No formation of octahedral extra-framework aluminium is observed.

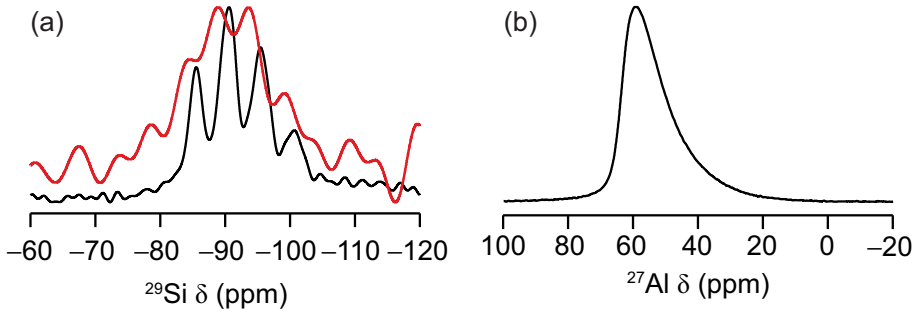

Figure 5.33: (9.4 T, 14 kHz) (a) ^{29}Si and (b) ^{27}Al MAS NMR spectra of $^{17}O_{2\,(g)}$-enriched Al-**FAU**(Na). Red overlay on spectra for (b) is the $^{1}H^{29}$Si CP NMR spectrum (5000 μs contact time).

5.6.3 Effect of Slurrying with $H_2{}^{17}O$

Based on the results of the $^{17}O_{2\,(g)}$ enrichment, enrichment of Al-**FAU**(Na) was performed using a slurry (see Section 5.8.11). From Figure 5.34, it can be seen that treating the **FAU** material in this way does result in some enrichment. The ^{17}O MQMAS spectrum (acquired after 7 days of slurrying time) shows significant signal only for Si – O – Al linkages, with little evidence of Si – O – Si signals in spectra. Furthermore, the level of enrichment seen for Al-**FAU**(Na) is noticeably lower than that seen for **CHA** frameworks. The observation that non-uniform framework enrichment is observed in this Al-**FAU**(Na) material is particularly interesting, considering that the extraframework countercation is sodium. It is therefore unclear whether the presence of sodium in the pores and channels of the **FAU** framework is causing the slower and non-uniform enrichment as it did for **CHA** (Section 5.4), or whether this is attributed to the differences between the **CHA** and **FAU** frameworks.

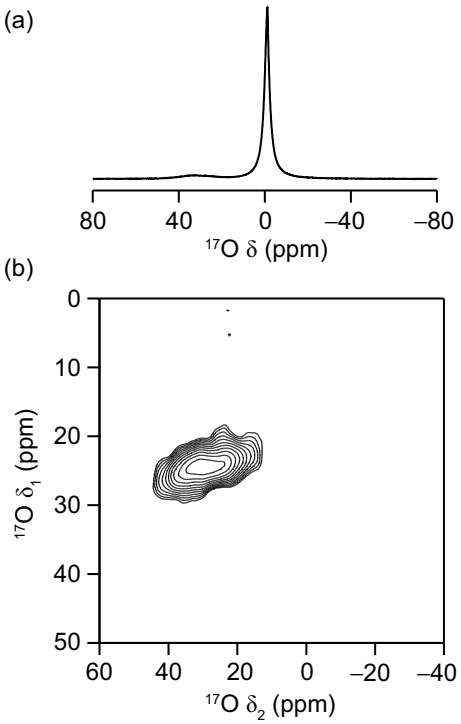

Figure 5.34: (14.1 T, 14 kHz) ^{17}O MAS NMR spectra of Al-**FAU**(Na) slurried with small amounts of $H_2{}^{17}O$ for 7 days. (a) quantitative short flip-angle and (a) $\{^1H\}^{17}$O MQMAS NMR spectra.

The Al-**FAU**(Na) material however is stable to the slurrying procedure as evidenced by ^{27}Al and ^{29}Si NMR spectra in Figure 5.35. The local structure of the silicon and aluminium species is largely unaffected, with spectra obtained resembling those of the initial starting material displayed in Figure 5.31. The small volumes of sample used for these slurrying experiments mean that the presence of a ^{29}Si probe background signal is more pronounced between -95 and -120 ppm.

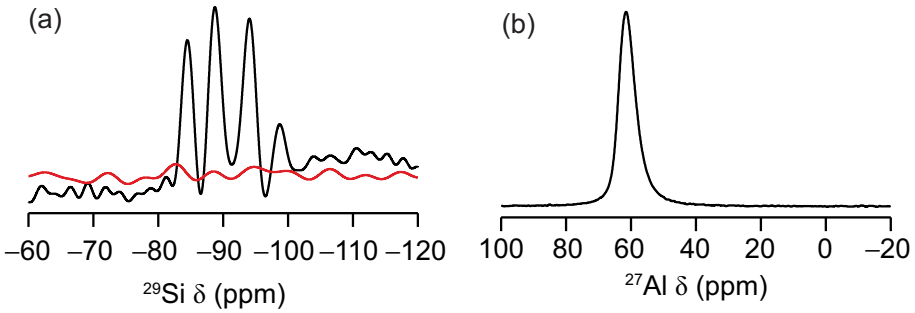

Figure 5.35: (9.4 T, 14 kHz) (a) ^{29}Si and (b) ^{27}Al MAS NMR spectra of of Al-**FAU**(Na) slurried with small amounts of $H_2{}^{17}O$ for 575 days. Red overlay on spectra for (b) is the $^1H^{29}$Si CP NMR spectrum (5000 μs contact time).

5.7 Summary and Conclusions

The work presented in this chapter builds on findings from Chapter 4, where facile, reversible room-temperature bond lability processes were uncovered in germanosilicate (and related) framework materials, using ^{17}O NMR spectroscopy. In an attempt to further understand the molecular-level interactions of the zeolitic frameworks and the enriched water that enabled framework oxygen exchange to take place, related studies were performed on a model chabazite system; Al-SSZ-13(H).

The results uncovered that surprisingly extensive framework oxygen exchange occurs when this material is simply placed in contact with water under ambient conditions and that this exchange occurs rapidly (evidence of framework enrichment observed by ^{17}O NMR < 1 hour after contact), without detriment to the local atomic coordination environment of the T sites, overall framework composition or the long-range crystalline order of the material. A possible explanation for the rapid and reversible bond lability observed in this material was suggested through a MD study, which revealed a potential mechanism for bond cleavage in the material, with energy barriers accessible at room temperature. Mechanistic investigations suggest that targeted attack of the aluminium atom within the Si−O(H)−Al linkage by water anti to the bond results in bond scission. For Si−O−Si linkages, the ability to form a hydrogen-bonded chain of four water molecules in the zeolite pore between neighbouring silicon atoms, one of which is adjacent to the Brønsted proton enables Si−O−Si linkage cleavage, mediated by the Grotthus-type shuffle of the acidic proton. The formation of the hydrogen bonded water chain might not be possible at certain sites within this (or indeed other) frameworks, resulting in more facile enrichment of Si−O−Al over Si−O−Si. While this doesn't prevent completely enrichment of Si−O−Si by another route, it may be that this is significantly slower.

To further understand the mechanism of bond lability, ion-exchange of Al-SSZ-13(H) was performed. Surprisingly however, extensive framework enrichment was seen in SSZ-13(M) slurries (M = Na, K, Cu, Zn) in the absence of significant Brønsted protons. Whilst the exact reasons for the bond lability observed in these materials are unknown, it is clear that the presence of different countercations have an effect on the efficacy of this bond lability in **CHA**. Changing countercation produces different preferences for framework enrichment, with the most stark differences obtained when the Na^+ cation is present; something which is thought to indicate a solvation sphere mediated blocking effect on the bond cleavage mechanism. Further work using larger cations *e.g.* Cs^+ is proposed to investigate this trend.

Further to this, the effect of framework composition on framework oxygen exchange was investigated. It was found that all heteroatomic frameworks studied, where T sites have been substituted for Si, B, Ti and Zn also exhibited extensive framework oxygen exchange. Of these, the pure-silica Si-**CHA** material was of most interest. Being a non-polar framework with no extraframework cations and minimal defects, the material still exhibited framework oxygen exchange with $H_2{}^{17}O$. Whilst the exact mechanism is not yet clear, it demonstrates the ability for zeolite frameworks to act dynamically and flexibly under ambient conditions. The studies of other heteroatomic materials were unsuccessful in enriching any heteroatomic linkages and instead tended to break down under reaction conditions. For B-**CHA**(H) this was accompanied by the irreversible sequestration of boron from the framework, evidenced through ^{11}B NMR studies.

Finally, the ability of the **FAU** framework to exhibit reversible bond lability was also examined. Experiments on the Na^+ form of a Linde-Y type framework revealed framework oxygen exchange is still possible, despite a change in topology and an increased aluminium content. Interestingly, slurry-enrichment of Si – O – Al sites only was observed for this material, although it is not yet known whether this is a consequence of the change in topology from **CHA** or due to the unique behaviour of sodium-exchanged frameworks. Further investigations of the **FAU** framework are presented in Chapter 6 alongside a post-synthetic framework transformation study.

Some further work which may help increase understanding of mechanism(s) of framework lability can be identified. It is necessary to understand the relative importance of both topology and aluminium content of the framework on the efficiency of enrichment within a slurried zeolite sample. Preparation of **CHA** frameworks with varying Si/Al ratio and preparation of zeolites with other framework topologies, particularly purely

siliceous analogues, would be desired. The importance of the chemical history of a framework is also of interest. For example, do materials prepared directly in a certain form enrich differently to similar materials prepared using ion exchange? Will materials that have once been in a proton form always exchange more efficiently than those that have not, due to even very small amounts of residual protons? Finally, does this framework exchange also apply to T sites, *e.g.*, silicon? Whilst more involved than ^{17}O NMR studies, could analogous ^{29}Si NMR studies using ^{29}Si-enriched TEOS or colloidal silica reagent also be performed to possible highlight reversible T site exchange?

Despite the questions that remain about the more general lability of all zeolite topologies and compositions, it is clear that for the industrially-relevant zeolites studied here, these processes are widespread and facile. The use of zeolite frameworks in commercial applications is widespread, particularly for size- and shape-selective processes. Although these results do not change the ability of currently employed zeolites to perform these reactions, they do perhaps raise questions on how these reactions proceed and whether water content in feedstocks for future zeolite-based processing applications should be considered in process design. A particular sector where this work may be of relevance is in biomass processing, where water-rich feedstocks can now be processed using zeolites.[96] There may be conflicting points of view on whether enhanced framework flexibility under aqueous conditions would be of use here. For example, the performance of more labile zeolite frameworks may be advantageous, facilitating greater access to the active site of the catalyst for more substrates. However, the continual lability exercised by some frameworks may reduce the shape selectivity surrounding an active site, making reaction turnover less efficient.

5.8 Sample Preparation

5.8.1 Calcination of SSZ-13(H) CHA

As-received zeolite was calcined at 550 °C for six hours in air. The positive and negative temperature ramp rates used were 1 and 2 °C, respectively.

5.8.2 Preparation of SSZ-13(H) CHA Slurries

Calcined zeolite (25 mg) was combined with $H_2{}^{17}O$ (40%, 25 μL) in a Bruker 4 mm HRMAS NMR rotor insert as detailed in Section 3.5.4.

5.8.3 Preparation of $^{17}O_{2(g)}$-enriched SSZ-13(H) CHA

Calcined zeolite ($\approx$ 100 mg) was dehydrated (300 °C, 16 hours) under vacuum and sealed under argon before being heated (600 °C, 72 hours) in an atmosphere of $\approx$ 200 mbar $^{17}O_{2(g)}$ in a manner described in Section 3.5.5.

5.8.4 Preparation of Ion-exchanged SSZ-13(M) CHA

Calcined zeolite (200 mg) was combined with a 3 M solution of selected metal salt (NaCl, KNO_3, $CuSO_4$ or $ZnCl_2$ (50 cm^3) and heated to 80 °C for 16 hours whilst stirring. The product was filtered and the process repeated with a fresh metal solution. The product was again filtered and washed with distilled water. When exchanging using $CuSO_4$ the pH of the exchange solution is adjusted to 3.5 using HNO_3.

5.8.5 Preparation of SSZ-13(M) CHA Slurries

Calcined zeolite (25 mg) was combined with $H_2{}^{17}O$ (40%, 25 μL) in a Bruker 4 mm HRMAS NMR rotor insert as detailed in Section 3.5.4.

5.8.6 Preparation of $^{17}O_{2(g)}$-enriched SSZ-13(M) CHA

Calcined zeolite ($\approx$ 100 mg) was dehydrated (300 °C, 16 hours) under vacuum and sealed under argon before being heated (600 °C, 18 hours) in an atmosphere of $\approx$ 200 mbar $^{17}O_{2(g)}$ in a manner described in Section 3.5.5.

5.8.7 Preparation of Si-CHA Slurries

Calcined zeolite (25 mg) was combined with $H_2{}^{17}O$ (40%, 25 μL) in a Bruker 4 mm HRMAS NMR rotor insert as detailed in Section 3.5.4.

5.8.8 Preparation of $^{17}O_{2(g)}$-enriched Si-CHA

Calcined zeolite ($\approx$ 100 mg) was dehydrated (300 °C, 16 hours) under vacuum and sealed under argon before being heated (550 °C, 48 hours) in an atmosphere of $\approx$ 200 mbar $^{17}O_{2(g)}$ in a manner described in Section 3.5.5.

5.8.9 Preparation of M-CHA(H) Slurries

Calcined zeolite (25 mg) was combined with $H_2{}^{17}O$ (40%, 25 μL) in a Bruker 4 mm HRMAS NMR rotor insert as detailed in Section 3.5.4.

5.8.10 Preparation of B-CHA(H) Incipient Wetness Sample

$H_2{}^{17}O$ (90%, 35 μL) was dropped onto the surface of calcined B-**CHA**(H) zeolite (70 mg) and mixed. The mixture is left to stand in air for 30 minutes before being sealed in a sample vial.

5.8.11 Preparation of Linde Y FAU(Na) Slurries

Calcined zeolite (25 mg) was combined with $H_2{}^{17}O$ (40%, 25 μL) in a Bruker 4 mm HRMAS NMR rotor insert as detailed in Section 3.5.4.

5.8.12 Preparation of $^{17}O_{2(g)}$-enriched Linde Y FAU(Na)

Calcined zeolite ($\approx$ 100 mg) was dehydrated (300 °C, 16 hours) under vacuum and sealed under argon before being heated (500 °C, 48 hours) in an atmosphere of $\approx$ 200 mbar $^{17}O_{2(g)}$ in a manner described in Section 3.5.5.

5.9 References

[1] N. E. R. Zimmermann, S. Jakobtorweihen, E. Beerdsen, B. Smit and F. J. Keil, *J. Phys. Chem. C*, 2007, **111**, 17370–17381.

[2] V. Kapko, C. Dawson, M. M. J. Treacy and M. F. Thorpe, *Phys. Chem. Chem. Phys.*, 2010, **12**, 8531.

[3] R. E. Morris and L. Brammer, *Chem. Soc. Rev.*, 2017, **46**, 5444–5462.

[4] M. Nielsen, A. Hafreager, R. Y. Brogaard, K. De Wispelaere, H. Falsig, P. Beato, V. Van Speybroeck and S. Svelle, *Catal. Sci. Technol.*, 2019, **9**, 3721–3725.

[5] R. A. Beyerlein, C. Choi-feng, J. B. Hall, B. J. Huggins and G. J. Ray, *Top. Catal.*, 1997, **4**, 27–42.

[6] G. N. Kalantzopoulos, F. Lundvall, K. Thorshaug, A. Lind, P. Vajeeston, I. Dovgaliuk, B. Arstad, D. S. Wragg and H. Fjellvåg, *Chem. Mater.*, 2020, **32**, 1495–1505.

[7] L. Zhang, K. Chen, B. Chen, J. L. White and D. E. Resasco, *J. Am. Chem. Soc.*, 2015, **137**, 11810–11819.

[8] S. Prodinger, M. A. Derewinski, A. Vjunov, S. D. Burton, I. Arslan and J. A. Lercher, *J. Am. Chem. Soc.*, 2016, **138**, 4408–4415.

[9] E. Nusterer, P. Blöchl and K. Schwarz, *Chem. Phys. Lett.*, 1996, **253**, 448–455.

[10] L. M. Parker, D. M. Bibby and G. R. Burns, *Zeolites*, 1991, **11**, 293–297.

[11] N. Mizuno, H. Mori, K. Mineo and M. Iwamoto, *J. Phys. Chem. B*, 1999, **103**, 10393–10399.

[12] Z. Xu and J. F. Stebbins, *Geochim. Cosmochim. Acta*, 1998, **62**, 1803–1809.

[13] R. Von Ballmoos and W. M. Meier, *J. Phys. Chem.*, 1982, **86**, 2698–2700.

[14] M. C. Silaghi, C. Chizallet, J. Sauer and P. Raybaud, *J. Catal.*, 2016, **339**, 242–255.

[15] E. Brunner, H. Ernst, D. Freude, M. Hunger, C. B. Krause, D. Prager, W. Reschetilowski, W. Schwieger and K. H. Bergk, *Zeolites*, 1989.

[16] R. M. Ravenelle, F. Schü, A. D. Amico, N. Danilina, J. A. V. Bokhoven, J. A. Lercher and C. W. Jones, *J. Phys. Chem. C*, 2010, **114**, 19582–19595.

[17] A. Filippidis, A. Godelitsas, D. Charistos and A. Kassoli-fournaraki, *Appl. Clay Sci.*, 1996, **11**, 199–209.

[18] D. Olson, W. Haag and W. Borghard, *Microporous Mesoporous Mater.*, 2000, **35-36**, 435–446.

[19] C. J. Heard, L. Grajciar, F. Uhlík, M. Shamzhy, M. Opanasenko, J. Čejka and P. Nachtigall, *Adv. Mater.*, 2020, **32**, 2003264.

[20] D. E. Resasco, S. P. Crossley, B. Wang and J. L. White, *Catal. Rev.*, 2021, **00**, 1–61.

[21] C. J. Heard, L. Grajciar, C. M. Rice, S. M. Pugh, P. Nachtigall, S. E. Ashbrook and R. E. Morris, *Nat. Commun.*, 2019, **10**, 4690–4967.

[22] S. M. Pugh, P. A. Wright, D. J. Law, N. Thompson and S. E. Ashbrook, *J. Am. Chem. Soc.*, 2020, **142**, 900–906.

[23] L. S. Dent and J. V. Smith, *Nature*, 1958, **181**, 1794–1796.

[24] M.-J. Díaz-Cabañas, P. A. Barrett and M. A. Camblor, *Chem. Commun.*, 1998, 1881–1882.

[25] E. A. Eilertsen, B. Arstad, S. Svelle and K. P. Lillerud, *Microporous Mesoporous Mater.*, 2012, **153**, 94–99.

[26] D. W. Fickel and R. F. Lobo, *J. Phys. Chem. C*, 2010, **114**, 1633–1640.

[27] S. Imasaka, H. Ishii, J. Hayashi, S. Araki and H. Yamamoto, *Microporous Mesoporous Mater.*, 2019, **273**, 243–248.

[28] N. Koike, K. Iyoki, S. H. Keoh, W. Chaikittisilp and T. Okubo, *Chem. Eur. J.*, 2018, **24**, 808–812.

[29] J. Liang, J. Su, Y. Wang, Z. Lin, W. Mu, H. Zheng, R. Zou, F. Liao and J. Lin, *Microporous Mesoporous Mater.*, 2014, **194**, 97–105.

[30] R. Martínez-Franco, M. Moliner, J. R. Thogersen and A. Corma, *ChemCatChem*, 2013, **5**, 3316–3323.

[31] M. Miyamoto, Y. Fujioka and K. Yogo, *J. Mater. Chem.*, 2012, **22**, 20186.

[32] G. A. Nasser, M. A. Sanhoob, I. A. Bakare, N. Alyassir, M. Vyas, Z. Malibari, Z. H. Yaman and O. Muraza, *Microporous Mesoporous Mater.*, 2021, **326**, 111375.

[33] Y. Shan, X. Shi, J. Du, Z. Yan, Y. Yu and H. He, *Ind. Eng. Chem. Res.*, 2019, **58**, 5397–5403.

[34] L. A. Villaescusa, I. Bull, P. S. Wheatley, P. Lightfoot and R. E. Morris, *J. Mater. Chem.*, 2003, **13**, 1978–1982.

[35] X. Wang, Q. Wu, C. Chen, S. Pan, W. Zhang, X. Meng, S. Maurer, M. Feyen, U. Müller and F.-s. Xiao, *Chem. Commun.*, 2015, **51**, 16920–16923.

[36] X. Wang, R. Zhang, H. Wang and Y. Wei, *Catal. Surv. Asia*, 2020, **24**, 143–155.

[37] J. Wang, L. Wang, D. Zhu, W. Cui, P. Tian and Z. Liu, *Chem. Commun.*, 2021.

[38] S. I. Zones and S. J. Hwang, *Microporous Mesoporous Mater.*, 2011, **146**, 48–56.

[39] F. Bleken, M. Bjørgen, L. Palumbo, S. Bordiga, S. Svelle, K.-P. Lillerud and U. Olsbye, *Top. Catal.*, 2009, **52**, 218–228.

[40] I. Bull, R. S. Boorse, W. M. Jaglowski, G. S. Koermer, A. Moini, J. A. Patchett, W.-M. Xue, P. Burk, J. C. Dettling and M. T. Caudle, *U.S. Patent US2008/0226545A1*, 2008.

[41] J. Tang, Y. Zhou, W. Su, X. Liu and Y. Sun, *Adsorpt. Sci. Technol.*, 2013, **31**, 549–558.

[42] L.-T. Yuen, S. Zones, T. Harris, E. Gallegos and A. Auroux, *Microporous Mater.*, 1994, **2**, 105–117.

[43] S. I. Zones, *U.S. Patent 4544538*, 1985.

[44] M. Calligaris, G. Nardin and L. Randaccio, *Zeolites*, 1983, **3**, 205–208.

[45] S. I. Zones and R. A. V. Nordstrand, *Zeolites*, 1988, **8**, 166–174.

[46] S. Li, Z. Zhao, S. Li, Y. Xing and W. Zhang, *Acta Phys. - Chim. Sin.*, 2019, **36**, 1–10.

[47] K. Mlekodaj, J. Dedecek, V. Pashkova, E. Tabor, P. Klein, M. Urbanova, R. Karcz, P. Sazama, S. R. Whittleton, H. M. Thomas, A. V. Fishchuk and S. Sklenak, *J. Phys. Chem. C*, 2019, **123**, 7968–7987.

[48] S. E. Ashbrook, Z. H. Davis, R. E. Morris and C. M. Rice, *Chem. Sci.*, 2021, **12**, 5016–5036.

[49] L. Peng, Y. Liu, N. Kim, J. E. Readman and C. P. Grey, *Nat. Mater.*, 2005, **4**, 216–219.

[50] L. Peng, H. Huo, Z. Gan and C. P. Grey, *Microporous Mesoporous Mater.*, 2008, **109**, 156–162.

[51] P. S. Neuhoff, P. Zhao and J. F. Stebbins, *Microporous Mesoporous Mater.*, 2002, **55**, 239–251.

[52] J. E. Readman, N. Kim, M. Ziliox and C. P. Grey, *Chem. Commun.*, 2002, **2**, 2808–2809.

[53] L. M. Bull, A. K. Cheetham, T. Anupold, A. Reinhold, A. Samoson, J. Sauer, B. Bussemer, Y. Lee, S. Gann, J. Shore, A. Pines and R. Dupree, *J. Am. Chem. Soc.*, 1998, **120**, 3510–3511.

[54] D. Freude and T. Loeser, *Lect. Notes Phys.*, 2004, **634**, 163–183.

[55] T. Loeser, D. Freude, G. T. Mabande and W. Schwieger, *Chem. Phys. Lett.*, 2003, **370**, 32–38.

[56] L. M. Bull, B. Bussemer, T. Anupõld, A. Reinhold, A. Samoson, J. Sauer, A. K. Cheetham and R. Dupree, *J. Am. Chem. Soc.*, 2000, **122**, 4948–4958.

[57] C. J. Heard, L. Grajciar and P. Nachtigall, *Chem. Sci.*, 2019, **10**, 5705–5711.

[58] B. Civalleri, A. M. Ferrari, M. Llunell, R. Orlando, M. Mérawa and P. Ugliengo, *Chem. Mater.*, 2003, **15**, 3996–4004.

[59] L. J. Smith, A. Davidson and A. K. Cheetham, *Catal. Lett.*, 1997, **49**, 143–146.

[60] M.-c. Silaghi, C. Chizallet, E. Petracovschi, T. Kerber, J. Sauer and P. Raybaud, *ACS Catal.*, 2015, **5**, 11–15.

[61] C. Hühn, A. Erlebach, D. Mey, L. Wondraczek and M. Sierka, *J. Comput. Chem.*, 2017, **38**, 2349–2353.

[62] O. Tamada, G. V. Gibbs, M. B. Boisen and J. Donald Rimstidt, *J. Mineral. Petrol. Sci.*, 2012, **107**, 87–98.

[63] A. Pelmenschikov, J. Leszczynski and L. G. Pettersson, *J. Phys. Chem. A*, 2001, **105**, 9528–9532.

[64] M. Jin, M. Liu, P. Nachtigall, L. Grajciar and C. J. Heard, *Chem. Mater.*, 2021, **33**, 9202–9212.

[65] T. Sun, S. Xu, D. Xiao, Z. Liu, G. Li, A. Zheng, W. Liu, Z. Xu, Y. Cao, Q. Guo, N. Wang, Y. Wei and Z. Liu, *Angew. Chemie Int. Ed.*, 2020, **59**, 20672–20681.

[66] C. J. T. de Grotthuss, *Ann. Chim.*, 1806, **58**, 54–73.

[67] S. Cukierman, *Biochim. Biophys. Acta - Bioenerg.*, 2006, **1757**, 876–885.

[68] J. H. Kwak, D. Tran, S. D. Burton, J. Szanyi, J. H. Lee and C. H. Peden, *J. Catal.*, 2012, **287**, 203–209.

[69] Z. Wang, Y. Jiang, O. Lafon, J. Trébosc, K. Duk Kim, C. Stampfl, A. Baiker, J. P. Amoureux and J. Huang, *Nat. Commun.*, 2016, **7**, 7–11.

[70] S. Xin, Q. Wang, J. Xu, Y. Chu, P. Wang, N. Feng, G. Qi, J. Trébosc, O. Lafon, W. Fan and F. Deng, *Chem. Sci.*, 2019, **10**, 10159–10169.

[71] B. H. Wouters, T. H. Chen and P. J. Grobet, *J. Am. Chem. Soc.*, 1998, **120**, 11419–11425.

[72] J. A. Van Bokhoven, A. L. Roest, D. C. Koningsberger, J. T. Miller, G. H. Nachtegaal and A. P. Kentgens, *J. Phys. Chem. B*, 2000, **104**, 6743–6754.

[73] A. Omegna, J. A. Van Bokhoven and R. Prins, *J. Phys. Chem. B*, 2003, **107**, 8854–8860.

[74] K. Chen, S. Horstmeier, V. T. Nguyen, B. Wang, S. P. Crossley, T. Pham, Z. Gan, I. Hung and J. L. White, *J. Am. Chem. Soc.*, 2020, **142**, 7514–7523.

[75] A. J. O'Malley, I. Hitchcock, M. Sarwar, I. P. Silverwood, S. Hindocha, C. R. A. Catlow, A. P. E. York and P. J. Collier, *Phys. Chem. Chem. Phys.*, 2016, **18**, 17159–17168.

[76] A. J. O'Malley, M. Sarwar, J. Armstrong, C. R. A. Catlow, I. P. Silverwood, A. P. E. York and I. Hitchcock, *Phys. Chem. Chem. Phys.*, 2018, **20**, 11976–11986.

[77] J. Barrett, *Inorganic Chemistry in Aqueous Solution*, Royal Society of Chemistry, Cambridge, 2007.

[78] P. M. Dove and C. J. Nix, *Geochim. Cosmochim. Acta*, 1997, **61**, 3329–3340.

[79] W. Grzybkowski, *Polish J. Environ. Stud.*, 2006, **15**, 655–663.

[80] J. Mähler and I. Persson, *Inorg. Chem.*, 2012, **51**, 425–438.

[81] L. A. M. M. Barbosa, R. A. van Santen and J. Hafner, *J. Am. Chem. Soc.*, 2001, **123**, 4530–4540.

[82] Q. Guo, F. Fan, D. A. J. M. Ligthart, G. Li, Z. Feng, E. J. M. Hensen and C. Li, *ChemCatChem*, 2014, **6**, 634–639.

[83] L. J. Smith, H. Eckert and A. K. Cheetham, *J. Am. Chem. Soc.*, 2000, **122**, 1700–1708.

[84] L. J. Smith, H. Eckert and A. K. Cheetham, *Chem. Mater.*, 2001, **13**, 385–391.

[85] J. R. Di Iorio and R. Gounder, *Chem. Mater.*, 2016, **28**, 2236–2247.

[86] Q. Yue, J. Zhang, M. Shamzhy and M. Opanasenko, *Microporous Mesoporous Mater.*, 2019, **280**, 331–336.

[87] Q. Yue, J. Halamek, D. N. Rainer, J. Zhang, R. Bulánek, R. E. Morris, J. Čejka and M. Opanasenko, *Chem. Eng. J.*, 2022, **429**, 131277.

[88] D. E. Akporiaye, I. M. Dahl, H. B. Mostad and R. Wendelbo, *J. Phys. Chem.*, 1996, **100**, 4148–4153.

[89] K. J. D. Mackenzie and M. E. Smith, *Multinuclear Solid-State Nuclear Magnetic Resonance of Inorganic Materials*, Pergamon, Oxford, 1st edn., 2002.

[90] R. de Ruiter, A. Kentgens, J. Grootendorst, J. Jansen and H. van Bekkum, *Zeolites*, 1993, **13**, 128–138.

[91] S. J. Hwang, C. Y. Chen and S. I. Zones, *J. Phys. Chem. B*, 2004, **108**, 18535–18546.

[92] C. Fild, D. F. Shantz, R. F. Lobo and H. Koller, *Phys. Chem. Chem. Phys.*, 2000, **2**, 3091–3098.

[93] G. P. M. Bignami, D. M. Dawson, V. R. Seymour, P. S. Wheatley, R. E. Morris and S. E. Ashbrook, *J. Am. Chem. Soc.*, 2017, **139**, 5140–5148.

[94] *Verified Syntheses of Zeolitic Materials*, ed. S. Mintova, Elsevier, 3rd edn., 2016.

[95] E. G. R., D. P. Shoemaker and K. J. G., *J. Phys. Chem.*, 1967, **71**, 1812–1819.

[96] T. Ennaert, J. Van Aelst, J. Dijkmans, R. De Clercq, W. Schutyser, M. Dusselier, D. Verboekend and B. F. Sels, *Chem. Soc. Rev.*, 2016, **45**, 584–611.

Chapter 6

Tracking Zeolite Framework Interconversions

6.1 Acknowledgements

Selected ^{17}O NMR experiments were carried out at the UK High-Field Solid-state NMR Spectroscopy Facility, based at the University of Warwick. High-field experiments were enabled by collaborative assistance from Dr Dinu Iuga and Dr Trent Franks.

6.2 Introduction

The limited number of known zeolite framework topologies that have been prepared experimentally has led to a focus on the development of methods for their synthesis, aiming to find novel zeolite topologies or novel routes to topologies with real-world value. Of interest are 'non-conventional' routes to zeolites using pre-crystallised units, which negate the need to start from lower-energy primary reagent sources and whose subsequent reactions have a greater degree of product control. A previously discussed example of this is the ADOR process, (see Chapter 4). Synthetic developments have led to the production of a number ($\approx$ 10%) of zeolites, on which commercial applications are now dependent. Many more framework topologies and/or material compositions also exist, with potentially commercially-relevant properties. Whilst many zeolites may exhibit desirable properties or activity, their implementation into industrial or commercial processes is often hampered by aspects of their synthesis, *e.g.* reaction time, nature of reagents, impurity phases or waste generated and control of local structure/defects, which negatively affect associated costs and sustainability factors.

One method that addresses some of the concerns above is the zeolite framework interconversion or post-synthetic transformation (PST) route.[1–4] PST methods are well-established within the literature and work, as the name suggests, by converting one fully-formed zeolite framework into another. The PST itself often takes the form of a short hydrothermal reaction under basic conditions, sometimes in the presence of a small amount of an additional silica or alumina source and/or SDA. The ability to tune a PST reaction based upon the starting material and desired reaction product means that the synthesis of some zeolite frameworks can be achieved far more economically and sustainably than traditional hydrothermal methods starting from silicas and aluminas. PST reactions are characterised by reduced reaction preparation and heating times, provided the starting zeolite is formed and tend to use safer and less expensive reagents when compared to their syntheses from primary reagent sources.

6.3 Application to Framework Bond Lability Study

PST methods are popular within the literature, yet the exact mechanistic conditions required to evoke PST more generally remain unclear. Whilst some reports describe the feasibility of PST reactions in terms of factors that relate the two zeolites, such as shared types of building units, recrystallisation compatibility, competing reaction syntheses, framework condensation reactions or graph similarity, whether this is a single factor that determines if two frameworks are able to interconvert remains unknown.[3] Outside of using previously used reaction conditions for other interconvertible framework pairs, the development of a topological conversion reaction between any two given zeolite frameworks therefore remains largely down to trial and error, with an unpredictable chance of success.

Despite the challenges described above, it is clear that conversion between a pair of frameworks during PST is likely to require each zeolite to exhibit a degree of framework flexibility and bond lability. The PST reaction therefore becomes an interesting example of how aluminosilicate zeolite frameworks can selectively, yet non-destructively, undergo structural rearrangement in mild aqueous conditions, where they would otherwise be predicted to act as stable, inert scaffolds.

Considering the results for framework lability under slurrying documented in Chapter 5, it may be unsurprising that both **FAU** and **CHA** regularly appear in PST reactions. Furthermore, both frameworks exist as a related PST pair, with the conversion of **FAU** frameworks to **CHA** well-documented.[4–19] As this reaction is described within the lit-

erature, both PXRD and solid-state NMR (^{27}Al, ^{29}Si) studies have been performed to characterise changes seen in the long- and short-range structure. To our knowledge however, no spectroscopic studies on the effect of PST on the local-structural environment of oxygen throughout the transformation have been reported. The knowledge obtained from prior slurrying studies (Chapter 5) and the widespread documentation on the **FAU**-**CHA** transformation provides a unique opportunity not only to increase understanding of the related PST reaction, but also the possibility to improve the understanding of the lability of framework linkages under different reaction conditions.

6.4 Development of Reaction System

Building on the bond lability and slurrying studies previously described, this chapter aims to uncover the activity and reactivity of the bonds within zeolite frameworks during the PST. Consequently, the PST reaction followed for the **FAU**-**CHA** transformation needs to be suitable for cost-effective isotopic enrichment, using $H_2{}^{17}O$. Due to the large number of reports of **FAU** to **CHA** transformations in the literature, existing protocols were surveyed and the most appropriate then adapted for ^{17}O-enrichment.[4–19]

6.4.1 Practical Considerations

Several key factors may help identify whether a hydrothermal reaction is feasible for adaption to facilitate ^{17}O-enrichment.[20] Firstly, the reaction needs to be able to be scaled such that a relatively low volume of aqueous solvent is required. Owing to the high cost of the isotopically-enriched $H_2{}^{17}O$, small reactions and the ability to use reagents with higher levels of enrichment are needed. For the specific PST reaction studied here, it is desirable to have a system for which a gradual conversion of **FAU** to **CHA** may be observed over several days, such that reaction intermediates can easily be isolated and studied, without the possibility of missing the transformation completely, but enabling information on the mechanistic pathway to be obtained. Furthermore, in order to ensure maximum comparability and negate the possibility of further interfering factors, it is essential that the PST reaction system developed does not change the overall composition of the zeolite formed, and as such, only transformations that require no additional SDAs, silica or alumina reagents will be considered. The lability of any framework linkages should therefore only be determined by the interaction of the basic reaction solvent with the zeolite framework.

6.4.2 Reaction Selection

Based on the criteria described above, a selection of PST reactions from the literature were trialled.[5–11]

It was found that several protocols could be successfully replicated in-house, yielding the desired transformation of the Linde Y-type **FAU** material (see Section 3.3.12) to one of the **CHA** structure. Of these, the protocol published by Muraoka *et al.*[8] was found to be reproducible and effected the PST reaction in the presence of hot KOH only, without the need for any additional silica, alumina or SDA sources. Furthermore, as this reaction takes place over a five day period, with relatively concentrated reagent solutions (*i.e.* low volumes of basic solution), it was deemed as the most suitable for use in this study.

6.4.3 Reaction Optimisation

The original reaction by Muraoka *et al.* in reference 8 involves the ion-exchange of the Al-**FAU**(Na) with Si/Al = 2.7 to the K^+ form, before hydrothermal treatment of the Al-**FAU**(K) in KOH to form Al-**CHA**(K). As the Si/Al of the material used in this work is slightly lower (Si/Al = 1.7), the effect of ion-exchange and the concentration of base used was investigated. Following this, the reaction conditions as well as the effect of changing the overall reaction volume was investigated, in an attempt to make the reaction as economical as possible for isotopic enrichment using $H_2{}^{17}O$.

6.4.4 Original Protocol

For reference, the original protocol as detailed in reference 8 is briefly summarised here:

The starting Al-**FAU**(Na) (Si/Al = 2.69) (1.0 g) was dispersed in KCl solution ((4 g KCl in 80 g of deionized water), (0.67 M, 84 cm^3)) and agitated at 333 K for 2 h. The solid sample was recovered *via* filtration and washed with deionised water. This procedure was repeated three times.

The solid product was dispersed in KOH solution. This mixture had a chemical composition of:

$$2.2KOH : 1.0Al(OH)_3 : 2.7SiO_2 : 150H_2O, \tag{6.1}$$

equivalent to zeolite (0.5 g) in KOH ($\approx$ 5.2 cm^3 of 0.55 M solution). The mixture was heated to 423 K under autogenous pressure for 110 h in a Teflon reactor encapsulated in a stainless-steel autoclave tumbled at 20 rpm. Products were filtered, washed with distilled water and left to dry at 353 K.

6.4.5 Effect of Ion-exchange Reactions

To minimise loss of material associated with consecutive ion-exchange procedures, temperature, length and number of these exchanges were optimised. Maintaining the concentration of KCl solution at 0.66 M, it was found that an increase of ion-exchange temperature to 353 K resulted in amorphisation of the framework. Repeating ion-exchanges only once but each with a length of 16 hours also caused framework degradation. By keeping the ion-exchange temperature at 333 K with a 0.66 M ion-exchange solution, a subsequent successful PST reaction (determined by PXRD) was achieved with the original 2 hour exchanges but repeating these only twice.

6.4.6 Concentration of Base

Owing to the higher concentration of aluminium in the starting zeolite used in this work, the effect of varying the concentration of KOH used was studied. The amount of KOH used in the reaction in Equation 6.1 is in excess for a standard zeolite framework (2.2 K^+ for every negative charge imparted by Al^{3+}). Although an aim of this study is to destabilise the **FAU** framework to promote inter-zeolite conversion (IZC), zeolites are susceptible to complete degradation in the presence of strong base, especially those that are aluminium-rich. An effort therefore was made to reduce the required concentration of this reagent, whilst keeping total reaction volume constant. As reactions were taking place at lower concentrations of KOH, reaction times were extended up to 14 days to allow for any changes to reaction rate. Results are summarised in Table 6.1.

Reaction	KOH Concentration (M)	Reaction Time (days)	PST Success?	Comments
Initial	0.55	5	Yes	Complete in 3 days
Reduced OH^-	0.50	5	Yes	Success
Reduced OH^- 2	0.45	5	Yes	Success
Increased Time Reduced OH^-	0.45	14	Yes	Reduced crystallinity
Increased Time Reduced OH^- 2	0.42	14	Yes	Reduced crystallinity

Table 6.1: Effect of varying hydroxide concentration and reaction length on the conversion of **FAU** to **CHA** in the PST reaction. Reaction success determined by PXRD.

It was found that the KOH concentration could be decreased by 0.1 M and still produce a complete **FAU**-**CHA** PST transformation within five days. The completeness of the reaction was determined to be the point at which no reflections from the **FAU** framework were visible in PXRD patterns. Interestingly, although this still resulted in a complete framework conversion, increasing the reaction time upwards to 10-14 days resulted in a reduction in crystallinity of the predominantly **CHA** phase formed after about 10 days. As indicated in Table 6.1, reducing the concentration of KOH further had no effect on the outcome of the longer reaction. Reaction times of 10-14 days therefore may have a negative effect on the stability of the material.

6.4.7 Hydrothermal Conditions

Several options exist for the incorporation of ^{17}O into the PST reaction, using commercially available isotopically-enriched reagents. Of these, the use of $H_2{}^{17}O$ is once again most useful here. Whilst the literature details many examples of enrichment of zeolites with ^{17}O, this is almost always achieved post-synthetically using high-temperature exchange with $^{17}O_{2(g)}$.[20] As the characterisation of any framework exchange occurring during synthesis is desired here and incorporation of ^{17}O into materials is desired to take place during the PST reaction, this method is not appropriate here in the first instance. Instead, inspiration from the metal-organic framework (MOF) world is taken, utilising dry-gel conversion (DGC) / solvent free reactions.

Using the optimised KOH concentrations determined above, DGC reactions were attempted by having either (i) zeolite and KOH solid mixed and separated from distilled water, or (ii) by having zeolite separated from an aqueous KOH solution. Unfortunately, in both cases, the product PXRD patterns showed the presence of a poorly crystalline phase, without the expected primary reflections for **FAU** and **CHA** frameworks.

Attempts to recreate solvent-free **FAU**-**CHA** reactions,[7,11] were unsuccessful as reaction products were resolved to be of the **FAU** (starting material) structure. This prevented the opportunity to exploit these protocols to enrich during the synthesis with an *in-situ* steaming approach by first dehydrating the required reagents and replacing the lost mass of coordinated water with a similar amount of $H_2{}^{17}O$.

From the reactions carried out above it appears, at least for this PST reaction, that dispersion of the zeolite within basic solution and direct interaction of the KOH with the **FAU** framework is essential for successful interzeolite conversion. Consequently, the initial reaction method that uses this approach was followed.

6.4.8 Reaction Scale and % ^{17}O-content

When attempting to enrich a material in ^{17}O, it is useful to explore potential syntheses, particularly those that utilise $H_2{}^{17}O$ by varying the percentage $H_2{}^{17}O$ content of the solvent to see what level is needed for practical NMR spectroscopic studies.[20] It was seen in Chapter 4 for isotopically-enriched ADOR hydrolyses that a $H_2{}^{17}O$ content of $\approx 5\%$ was sufficient to effect good levels of framework enrichment in high volume reactions, however the enrichment level used in slurrying reactions for **CHA** in Chapter 5 is 40%.

In the current format, the overall reaction requires ≈ 5.2 cm^3 of water reagent, to yield $\approx$ 400 mg product. This volume is too high for any useful level of $H_2{}^{17}O$ incorporation at reasonable cost, however only approximately 150 mg product is needed for subsequent characterisation and analysis. It was found that halving the overall reaction volume (250 mg zeolite and 2.6 cm^3 of water) successfully produced the desired PST, according to PXRD patterns of the products. Further attempts to decrease the overall solvent volume by reducing this by half again (*i.e.* 250 mg zeolite and 1.3 cm^3 of water) were not successful in producing the PST product.

In a test reaction for ^{17}O-enrichment for a **FAU**-**CHA** PST with total solvent volume of 2.6 cm^3, the substitution of 0.5 cm^3 $H_2$16O for 20% $H_2{}^{17}O$ (*i.e.*, an overall percentage ^{17}O concentration in the water = 3.85%) was found to give a level of ^{17}O-isotope incorporation sufficient to obtain good sensitivity in ^{17}O NMR spectra (see Figure 6.1) on a reasonable timescale. The cost of 20% $H_2{}^{17}O$ reagent is $\approx$ £200 / mL, giving an enrichment cost for each PST reaction in the region of £100. This is comparable, if not more economical, than the cost of *in-situ*-enrichment techniques for other framework materials using $H_2{}^{17}O$, *e.g.*, MIL-53 MOF, where 130 μL of 90% $H_2{}^{17}O$ (@ £1600 / mL), was used, costing $\approx$ £200 worth of $H_2{}^{17}O$ per synthesis.[21,22]

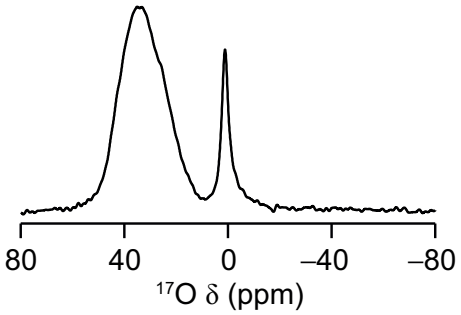

Figure 6.1: (14.1 T, 14 kHz) ^{17}O MAS NMR spectrum of ^{17}O-enriched Al-**CHA**(K), formed through the PST of Al-**FAU**(K) in $H_2{}^{17}O$-doped KOH solution for five days. Spectrum acquired with 4096 transients with a recycle interval of 1 s (total experiment time $\approx$ 1.2 hours).

6.4.9 Finalised Protocol

The reaction optimisations and evaluation of isotopic enrichment level discussed above led to the development of a new protocol for the PST of a **FAU** topology material to one of **CHA** topology.

Ion-exchange: Al-**FAU**(Na) zeolite (Si/Al = 1.7) (5.0 g) was dispersed in KCl (0.66 M, 250 cm^3) and heated under stirring at 333 K for 2 hours. The mixture was cooled and filtered. The ion-exchange was repeated twice further using identical quantities of the same KCl solution. The three-times exchanged material was washed with distilled water and dried at 80 °C for 1 hour, obtaining Al-**FAU**(K) with Si/Al = 1.6 (^{29}Si NMR).

PST reaction: Al-**FAU**(K) zeolite (Si/Al = 1.6) (0.25 g) was combined with a solution of KOH (0.55 M, 2.14 cm^3). $H_2{}^{16}O$ or $H_2{}^{16}O$ with a 20% $H_2{}^{17}O$ (0.5 cm^3) was added, forming an overall unenriched / 3.85% enriched KOH solution (2.64 cm^3, 0.45 M). This provides an overall reaction composition of,

$$1.67KOH : 1.0Al(OH)_3 : 1.6SiO_2 : 81H_2O. \tag{6.2}$$

The mixture is fully dispersed, sealed in a Teflon-lined steel autoclave and heated statically for up to five days. Autoclaves are removed from the oven, cooled and the solids filtered and washed with the minimum volume of distilled water before drying at 80 °C for 5 minutes.

Steaming Reaction: To assess the effect of the hydrothermal treatment only on the zeolite material, a PST-style reaction in the absence of KOH was performed.
Al-**FAU**(K) zeolite (Si/Al = 1.6) (0.25 g) was combined with distilled water (2.14 cm^3). $H_2{}^{16}O$ or $H_2{}^{16}O$ with 20% $H_2{}^{17}O$ (0.5 cm^3) was added, forming an overall unenriched / 3.85% enriched aqueous solution (2.64 cm^3, 0.45 M). This provides an overall reaction composition of,

$$1.0Al(OH)_3 : 1.6SiO_2 : 81H_2O. \tag{6.3}$$

The mixture is fully dispersed, sealed in a Teflon-lined steel autoclave and heated statically for three days. Autoclaves are removed from the oven, cooled and the solids filtered and washed with the minimum volume of distilled water before drying at 80 °C for 5 minutes.

6.5 PST Reaction in ^{16}O

The **FAU**-**CHA** PST reaction developed in Section 6.4.9 was used to prepare a series of PST products and intermediates with natural abundance levels of ^{17}O. The prepared materials: Al-**FAU**(Na) (Na^+ SM), Al-**FAU**(K) (K^+ SM, from ion-exchange), three-day steamed Al-**FAU**(K) (3 days SM) and five PST products (1-5 days reaction time); obtained by sequential quenching of reactions at 24 hour intervals from the reaction start time to five days; were studied using PXRD, lineshape fitting and ^{27}Al and ^{29}Si NMR analysis. Powder X-ray diffraction patterns for obtained materials are shown in Figure 6.2.

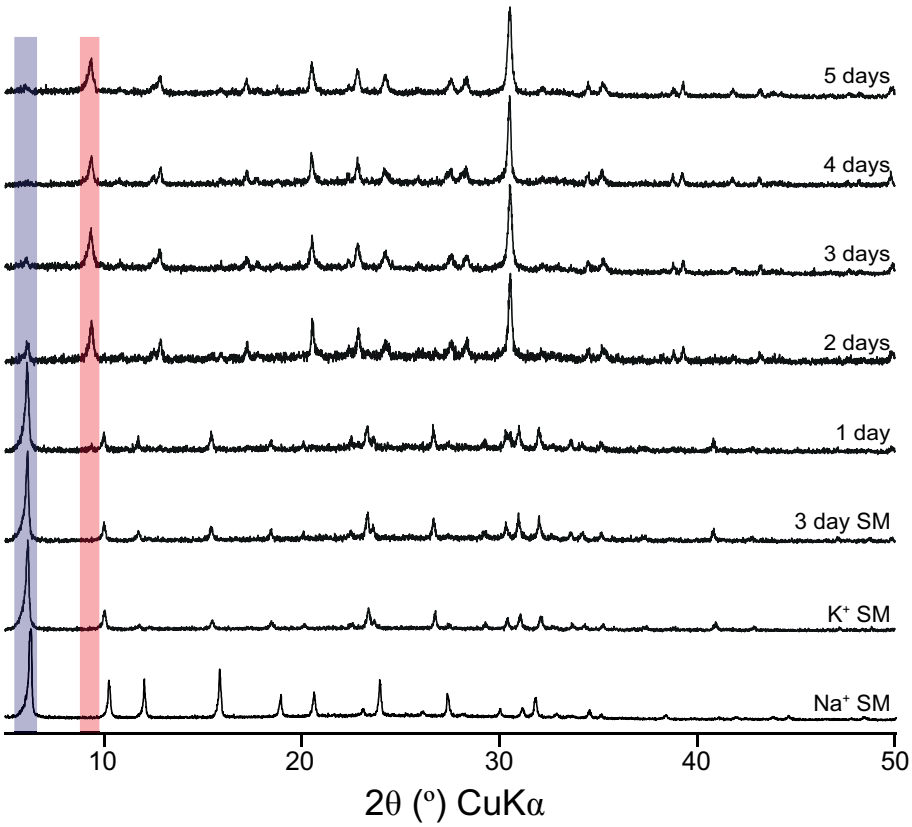

Figure 6.2: PXRD patterns of selected samples, isolated from a **FAU**-**CHA** PST reaction, carried out as described in Section 6.4.9. Identity of isolated material detailed on figure. Primary reflections of frameworks: **FAU** (111) and **CHA** (100), highlighted in blue and red, respectively.

PXRD patterns of the obtained intermediates show that the main structural PST phase change takes place between 1-3 days, with the 2 day sample (48 hours reaction time) showing a clear mix of **FAU** and **CHA** reflections (primary reflections of each material present at 6.1°and 9.4°(2θ), respectively). Between 3 and 4 days the material becomes predominantly **CHA** with very little evidence of the primary **FAU** reflection present thereafter, at which point the transformation is considered complete.

The 3 day 'hydrothermal steaming' reaction (3 day SM) on Al-**FAU**(K), performed in the absence of KOH retains an almost identical PXRD pattern to the K^+-form starting material. For this reason, the patterns in Figure 6.2 confirm that the key factor promoting the PST reaction within this system is the presence of the KOH and that hydrothermal (in)stability of the material in hot aqueous conditions alone is not affecting the PST reaction. In order to verify the transformation between phases, Le Bail fits were performed for the initial Al-**FAU**(K), 3-day hydrothermally steamed **FAU** and day 5 product **CHA** materials.

6.5.1 Structural Characterisation

Whole diffraction pattern fitting analysis was achieved using the Le Bail method to confirm the crystal topology of the initial and formed PST phases, **FAU** and **CHA**.[23–25] Lineshape analysis was performed using GSAS within the EXPGUI interface. Verified[26] models for **FAU** and **CHA** were taken from Olson *et al.*[27] (hydrated Al-**FAU**(Na)) and Calligaris *et al.*[28] (hydrated Al-**CHA**(K)).

The Le Bail fits of **FAU**-**CHA** PST **FAU** starting material, **FAU** 3 day PST steamed material and **CHA** 5 day PST end product, are shown in the Appendix, in Figure F.1, Figure F.2 and Figure F.3, respectively. By comparing to the structural models, it is confirmed that the desired **CHA** material is formed through PST methods (Figure F.3). Furthermore, it is confirmed that the 3 day PST steamed material (Figure F.2), heated in the absence of KOH, remains as **FAU** starting material (Figure F.1). Details of the cell parameters obtained from Le Bail fitting are shown in Table 6.2, Table 6.3 and Table 6.4. The far smaller unit cell volume for **CHA** is attributed to its significantly smaller number of unit cell atoms (120 atoms) *vs.* 576 for **FAU**.

a / Å	b / Å	c / Å	α °	β °	γ °	cell volume / Å^3
24.90(4)	24.90(4)	24.90(4)	90.000	90.000	90.000	15442(8)

Table 6.2: Le Bail fit results for Al-**FAU**(K) PST starting material (**FAU** space group F d −3 m). χ^2 = 2.468.

a / Å	b / Å	c / Å	α °	β °	γ °	cell volume / Å^3
24.98(8)	24.98(8)	24.98(8)	90.000	90.000	90.000	15587(8)

Table 6.3: Le Bail fit results for Al-**FAU**(K) PST 3 day steamed material (**FAU** space group F d −3 m). χ^2 = 3.763.

a / Å	b / Å	c / Å	α °	β °	γ °	cell volume / Å^3
13.78(1)	13.78(1)	15.46(7)	90.000	90.000	120.000	2544(1)

Table 6.4: Le Bail fit results for Al-**CHA**(K) 5 day PST product (**CHA** space group R −3 m). χ^2 = 1.634.

6.5.2 NMR Spectroscopic Characterisation

Assessment of the local structure of the starting, intermediate and product materials of the PST reactions was performed using ^{27}Al and ^{29}Si NMR spectroscopy.

A factor critical to this PST study was the condition that the PST reaction proceed without any change to the composition of the material, enabling a degree of comparability between the amount/type of local structural species (*e.g.* any Si – O – Si / Si – O – Al linkages) observed when ^{17}O NMR studies are performed. For this reason, ^{29}Si MAS NMR spectra (Figure 6.3) are of interest as they will reveal any changes in T-site connectivity during the PST and provide the opportunity to calculate the Si/Al of the starting material, intermediate or product.

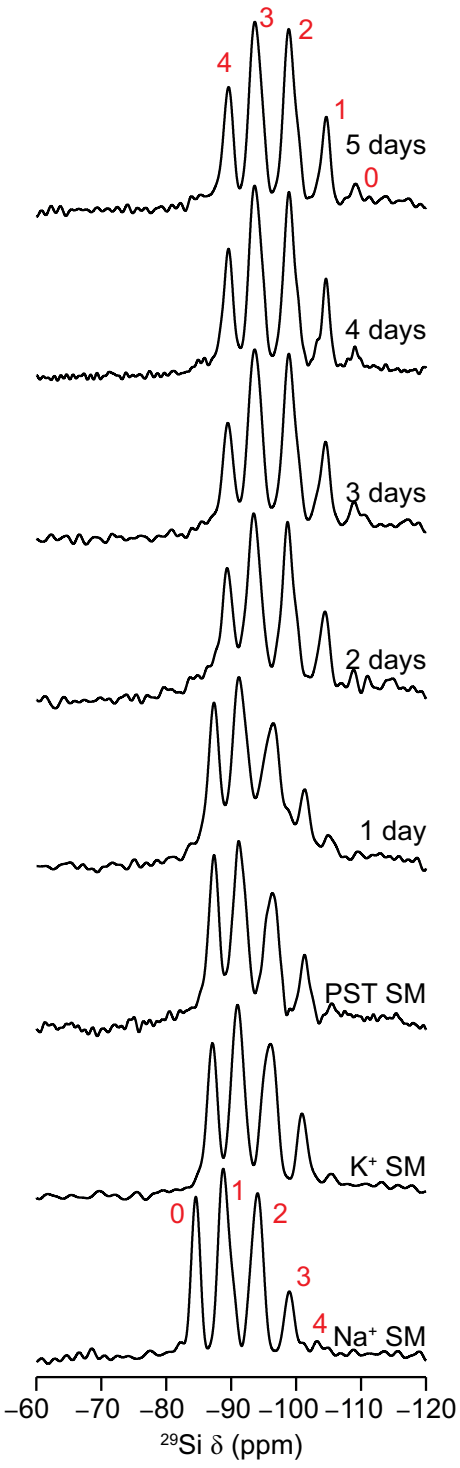

Figure 6.3: (9.4 T, 14 kHz) ^{29}Si MAS NMR spectra of selected samples, isolated from an optimised **FAU**-**CHA** PST reaction. Identity of isolated material detailed on figure. Number of NNN silicon atoms (n) for $Si(O-Si)_n(O-Al)_{4-n}$, indicated in red on figure for selected materials.

From Figure 6.3 it is clear that the various treatments applied to the initial Al-**FAU**(Na) material have had differing effects on the local atomic structure of silicon throughout the material. Firstly, the transition between **FAU** and **CHA** topologies is most obvious in samples transformed for 1-2 days, where the most disordered silicon distributions occur. This is slightly earlier than the changes observed in PXRD patterns (2-3 days) (see Figure 6.2), indicating that local structural changes may pre-date the changes to the long-range order of the material. Ion-exchange to the K^+ form and the change of topology to **CHA** both result in a slight increase in ^{29}Si shielding, evidenced by the net upfield shift in peaks as the starting **FAU** is transformed to **CHA**. The effect observed for ion-exchange of Al-**FAU**(Na) to Al-**FAU**(K) may be explained by a slight increase in shielding experienced by T-site silicon atoms as the larger hydrated K^+ cation fills the pores of **FAU** in place of hydrated Na^+. The further shift to lower frequency as **FAU** transforms to **CHA** is also shown by the verified NMR spectra[26,29,30] and is likely due to the increase in shielding experienced as the 'smaller-pore' **CHA** material is formed.

To verify whether the composition of the materials isolated had changed over the course of the reactions, analytical fitting analysis was performed for the ^{29}Si MAS NMR spectra in Figure 6.3. The results of the fitting analysis are displayed in Table 6.5.

Material	Calculated Si/Al
Na^+ SM	1.71
K^+ SM	1.63
3 day SM	1.58
1 day PST	1.61
2 day PST	1.55
3 day PST	1.56
4 day PST	1.58
5 day PST	1.61

Table 6.5: Si/Al of materials isolated from a **FAU**-**CHA** PST reaction, determined from their respective ^{29}Si MAS NMR spectra. Estimated error in values is ± 0.1

The fitting results reveal that no specific changes to the Si/Al occur following ion-exchange from Al-**FAU**(Na) to Al-**FAU**(K). This signals a great success in terms of reaction development and indicates that subsequent PST products produced using this method should be comparable using ^{29}Si NMR spectroscopy. It is interesting that during the PST reaction there appears to be a change to the aluminium distribution, demonstrated by differences in the intensities of the five resolved $(Si(O-Si)_n(O-Al)_{4-n}$ peaks in each ^{29}Si NMR spectrum. The effect is most pronounced for the leftmost $Si(O-Al)_4$ peak, which decreased in intensity during the course of the reaction. As Si/Al remains constant, this peak intensity must be distributed elsewhere within the material, having the net effect

that silicon atoms in these PST-formed **CHA** will have a greater probability of being connected to at least one further silicon atom *via* direct oxygen linkage than in the parent **FAU** material. This is perhaps best illustrated by comparing the relative intensities of each signal between samples, as shown in Figure 6.4.

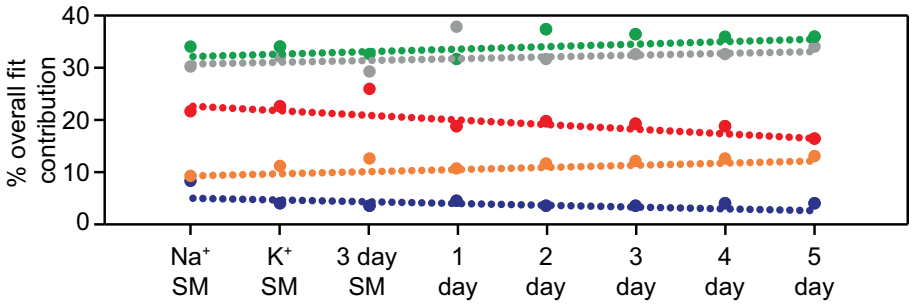

Figure 6.4: Percentage contribution of each type of silicon environment to the spectrumfor each product isolated from the optimised **FAU** to **CHA** PST reaction. 4 Si NNN (blue), 3 Si NNN (orange), 2 Si NNN (grey), 1 Si NNN (green) and 0 Si NNN (red). Percentage background contribution excluded from calculation. Least-squares line of best fit shown.

Within Figure 6.4, the gradient of the lines of best fit indicate any net change in prevalence of types of silicon NNN linkage, within the isolated intermediates. From these data, excluding for $Si(O-Si)_4$ (blue), which stays fairly constant when excluding the first Na^+ SM point, a significant decrease in the amount of $Si(O-Al)_4$ (red) is seen, whilst the relative prevalence of all other signals increase, especially that of $Si(O-Si)_3O$-Al (orange), indicating a shift in the distribution of aluminium throughout the materials formed.

The exact reasons behind this change in aluminium distribution is unknown, yet this finding may challenge one major theory for IZC reactions that they simply proceed through the rearrangement of pre-crystallised units. As mentioned in Section 1.6, both **FAU** and **CHA** materials have a common *d6r* building unit, so could feasibly interconvert through a SBU rearrangement, which would result in only a very small amount of aluminium rearrangement. A similar conclusion was reached by Muraoka *et al.* in reference 8, the PST study on which the synthetic procedure used in this work was initially based. The authors used Monte-Carlo methods, determining that whilst the *d6r* motif remains intact during PST, the organisation of aluminium within the *d6r* common building units rearranges, in order to site Al in an energetically preferred location within the framework. This hypothesis was tested by comparing distributions of Si NNN from ^{29}Si NMR spectra between hydrothermally synthesised **FAU** and **CHA** and PST synthesised (from **FAU**) **CHA**. Recently, the first evidence of PST reactions taking place between the rearrangements of non-SBU zeolite fragments has been observed.[19]

Here, the authors suggest that zeolitic fragments, common to **FAU**, **LTA** and **MFI** and often chains of five T-atoms consisting of at least three aluminium atoms rearrange to form **CHA** materials with more energetically preferred locations of aluminium. These fragments are formed through stepwise disintegration of parent zeolites–SBU–fragments. Mechanistically it is still unclear how these fragments rearrange. It would be possible for a mechanism of this nature to produce the ^{29}Si NNN result observed above, but to satisfy Figure 6.4 it would require a specific set of rearrangements to occur, primarily involving fragmentation at $Si(O-Al)_4$ junctions and rearrangement of those aluminium into $Si(O-Si)_3(O-Al)$ environments.

To investigate changes to the T site environments further, ^{27}Al MAS NMR spectra were recorded for the same intermediates. The resultant spectra are shown in Figure 6.5 and show throughout that there is no observable change in chemical shift and no significant change to the local tetrahedral coordination environment of aluminium within the isolated zeolite at any stage of the transformation. Further, the overall intensity of the aluminium signal resolved is also unchanged, indicating that there is no significant loss of the number of Al atoms as indicated by calculated Si/Al.

This appears to contradict some observations made for ^{29}Si MAS NMR spectra, where it seems aluminium species must relocate or change coordination during the PST. As it is not expected that the PST reaction would continue for the isolated intermediates in the *ex-situ* NMR measurements performed here, intermediate phase aluminium species are expected. Based on this, it is most likely that any aluminium intermediate species must be coordinated tetrahedrally, but the MAS NMR performed is insensitive to the specific connectivity. To investigate this $^{1}H-^{27}Al$ CP NMR experiments could be performed. A further, alternative explanation is that, owing to the cease in reactivity upon isolation from hydrothermal conditions, the consistently crystalline material formed is more closely reminiscent of an intergrowth of crystalline **FAU** and **CHA** phases. This would mean that there is a preference to crystallise a mixture of stable tetrahedrally-coordinated framework materials over that of any transient, partially amorphous reactive state. This points to the idea that this PST never approaches extensive zeolite framework digestion and re-nucleation to form a new phase from disordered, amorphous species.

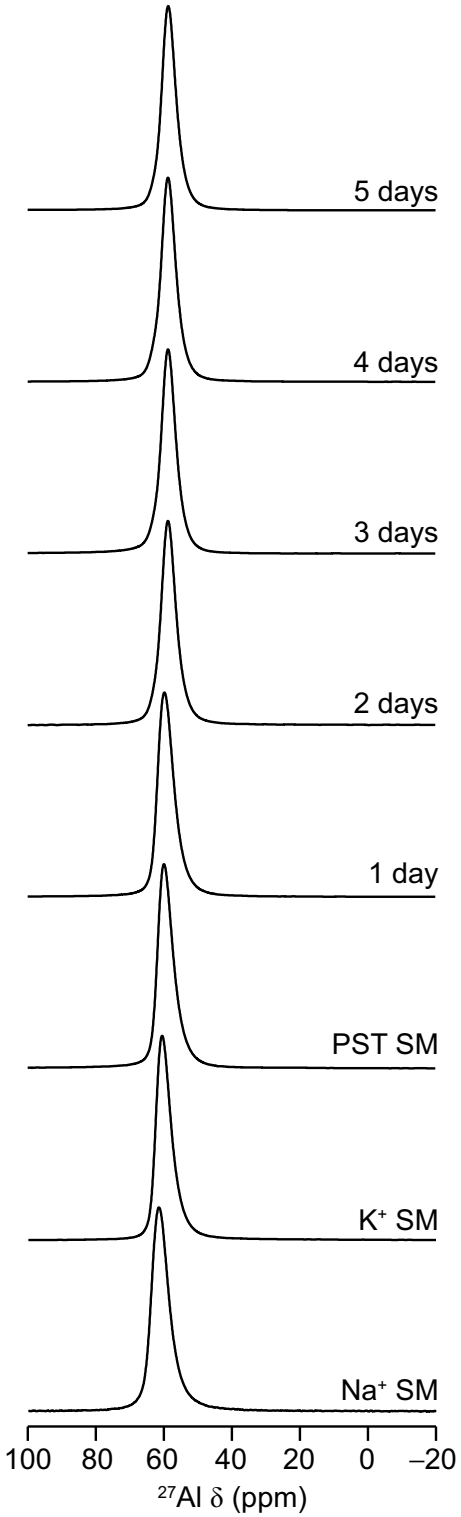

Figure 6.5: (9.4 T, 14 kHz) ^{27}Al MAS NMR spectra of selected samples, isolated from an optimised **FAU**-**CHA** PST reaction. Identity of isolated material detailed on figure.

Structural characterisation of products and intermediates of the **FAU**-**CHA** PST reaction confirm that the reaction proceeds as a 'pure' PST, with retention of framework composition throughout. Interestingly, PXRD patterns show that at all points reflections assignable to either **FAU**, **CHA** or both materials are present, indicating the state of materials present throughout the transformation retain a degree of crystallinity and do not completely fragment. This is supported by ^{27}Al MAS NMR experiments, which show aluminium coordination in all isolated intermediates retains its tetrahedral coordination. However, ^{29}Si MAS NMR experiments show, similar to observations in some other PST studies, that during framework transformation, the distribution of aluminium changes in materials. This was evidenced by ^{29}Si NMR spectra, which show an average increase in number of silicon NNN for any one given silicon atom.

6.6 PST Reaction with ^{17}O Enrichment

Having characterised the effect of the PST reaction on the long-range order and local structural coordination of T-site atoms in the zeolitic materials, a ^{17}O NMR study was performed on an analogous suite of PST-derived materials, which were synthesised using the procedure in Section 6.4.9.

6.6.1 Structural Characterisation

The materials obtained from the reactions using ^{17}O-enriched water were first characterised by PXRD to ensure that the desired **FAU**-**CHA** transformation had also been successful. Diffraction patterns are plotted in Figure 6.6.

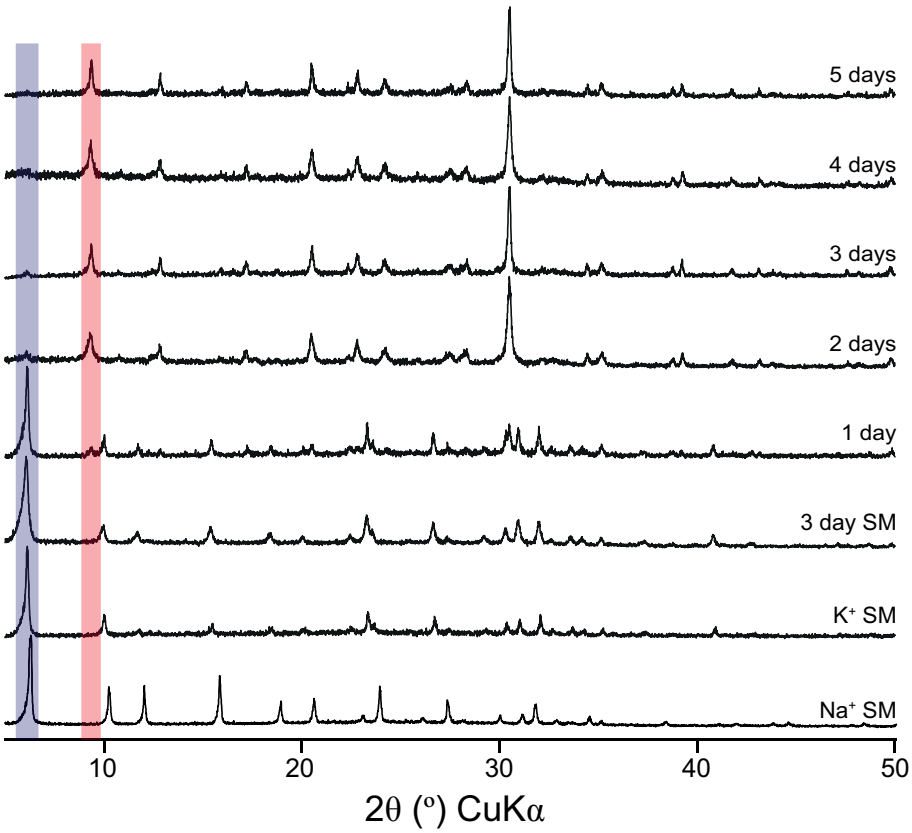

Figure 6.6: PXRD patterns of selected samples, isolated from an optimised ^{17}O-enriched **FAU**-**CHA** PST reaction. Identity of isolated material detailed on figure. Primary reflections of frameworks: **FAU** (111) and **CHA** (100), highlighted in blue and red, respectively.

The similarity of the obtained diffraction patterns to those of the previous materials with natural-abundance levels of ^{17}O (Figure 6.2) shows that the ^{17}O-enriched PST reaction has proceeded successfully, forming the desired **CHA** phase. It is noted that this particular set of reactions has proceeded slightly more rapidly than the previous set as the sample from the 2-day reaction in Figure 6.6 is resolved as an almost pure **CHA** phase, rather than the mixed phase product seen at the same time point in Figure 6.2.

6.6.2 NMR Spectroscopic Characterisation

Once again, ^{27}Al and ^{29}Si MAS NMR spectra were collected for all isolated materials from the PST. ^{29}Si NMR spectra are shown in Figure 6.7.

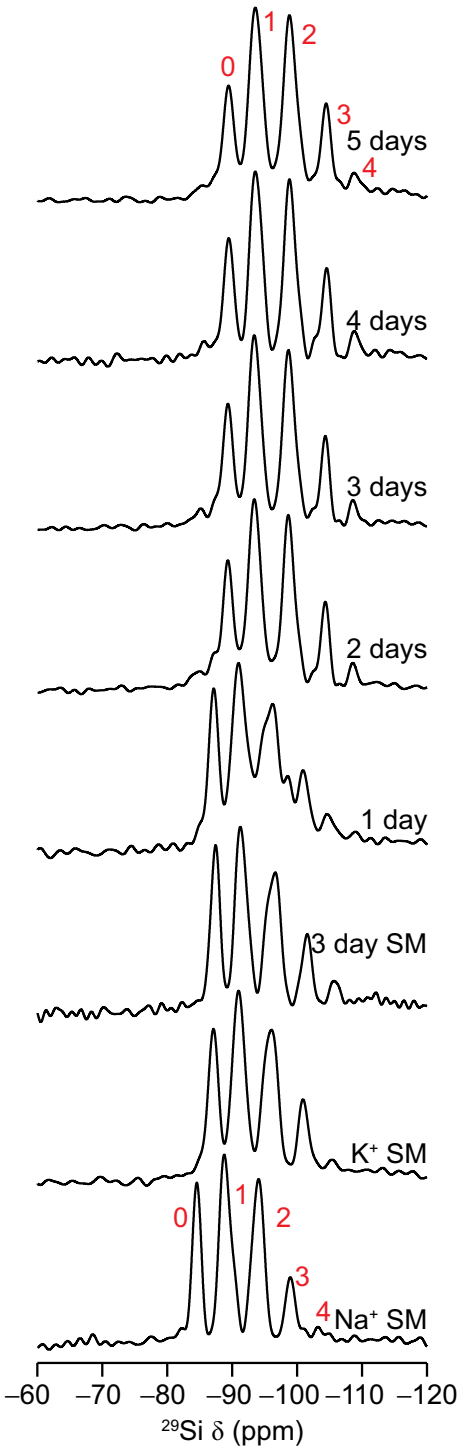

Figure 6.7: (9.4 T, 14 kHz) ^{29}Si MAS NMR spectra of selected samples, isolated from an optimised ^{17}O-enriched **FAU**-**CHA** PST reaction. Identity of isolated material detailed on figure. Number of NNN silicon atoms (n) for $\mathrm{Si(O-Si)}_n\mathrm{(O-Al)}_{4-n}$, indicated in red on figure for selected materials.

As for the natural-abundance samples (Figure 6.3), the ^{29}Si MAS NMR spectra for the ^{17}O-enriched reaction show both a small decrease in chemical shift for each signal and a change in the distribution of different silicon NNN linkages, evidenced by the relative change in intensities of each peak in the spectrum. Once again, it is visible that there is a decrease in the prevalence of the $Si(O-Al)_4$ linkage at times greater than two days; when the phase transformation is shown to be complete by PXRD. Further, the slightly increased rate of this PST reaction, as indicated by PXRD patterns (Figure 6.6) is also captured by NMR spectroscopy. Here, disruption to silicon local coordination environment is evident for 1 day and 2 day PST samples, which is once again slightly ahead of the changes observed by PXRD.

The change in the relative proportions of silicon NNN environments following phase transformation to **CHA** is again evident for materials of this reaction set. In Figure 6.4, the relative intensity of the $Si(O-Si)_4$ signal is increased, with a complementary, observable loss in intensity of the $Si(O-Al)_4$ signal. Determination of Si/Al again confirms that no aluminium is lost from the structure and ^{27}Al MAS NMR spectra (Figure 6.8) also indicate no significant changes to the aluminium coordination through PST transformation to **CHA**.

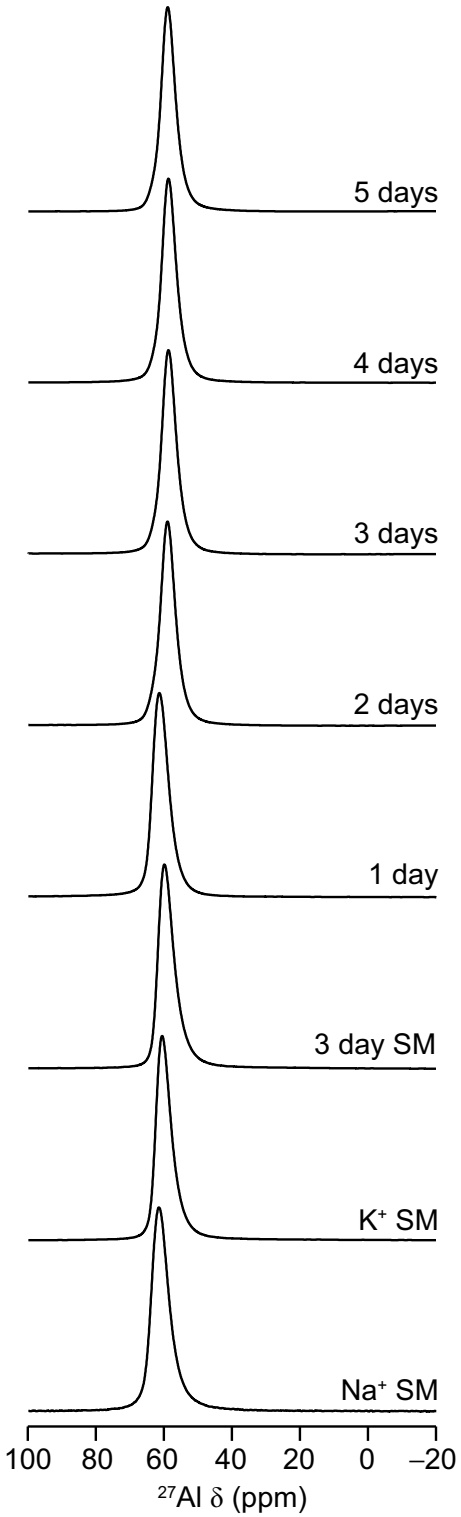

Figure 6.8: (9.4 T, 14 kHz) ^{27}Al MAS NMR spectra of selected samples, isolated from an optimised ^{17}O-enriched **FAU**-**CHA** PST reaction. Identity of isolated material detailed on figure.

It appears therefore that the optimised PST reaction has been repeated successfully using $H_2{}^{17}O$. It is also suggested that the reaction has proceeded using the same mechanism as similar results are observed for ^{27}Al and ^{29}Si NMR spectra. This result is, of course, expected as the only change to the reaction system is the isotopic molecular weight of the solvent.

Evidence of any ^{17}O isotopic incorporation to the materials was then studied using high-field solid-state NMR spectroscopy. Resulting spectra are shown in Figure 6.9.

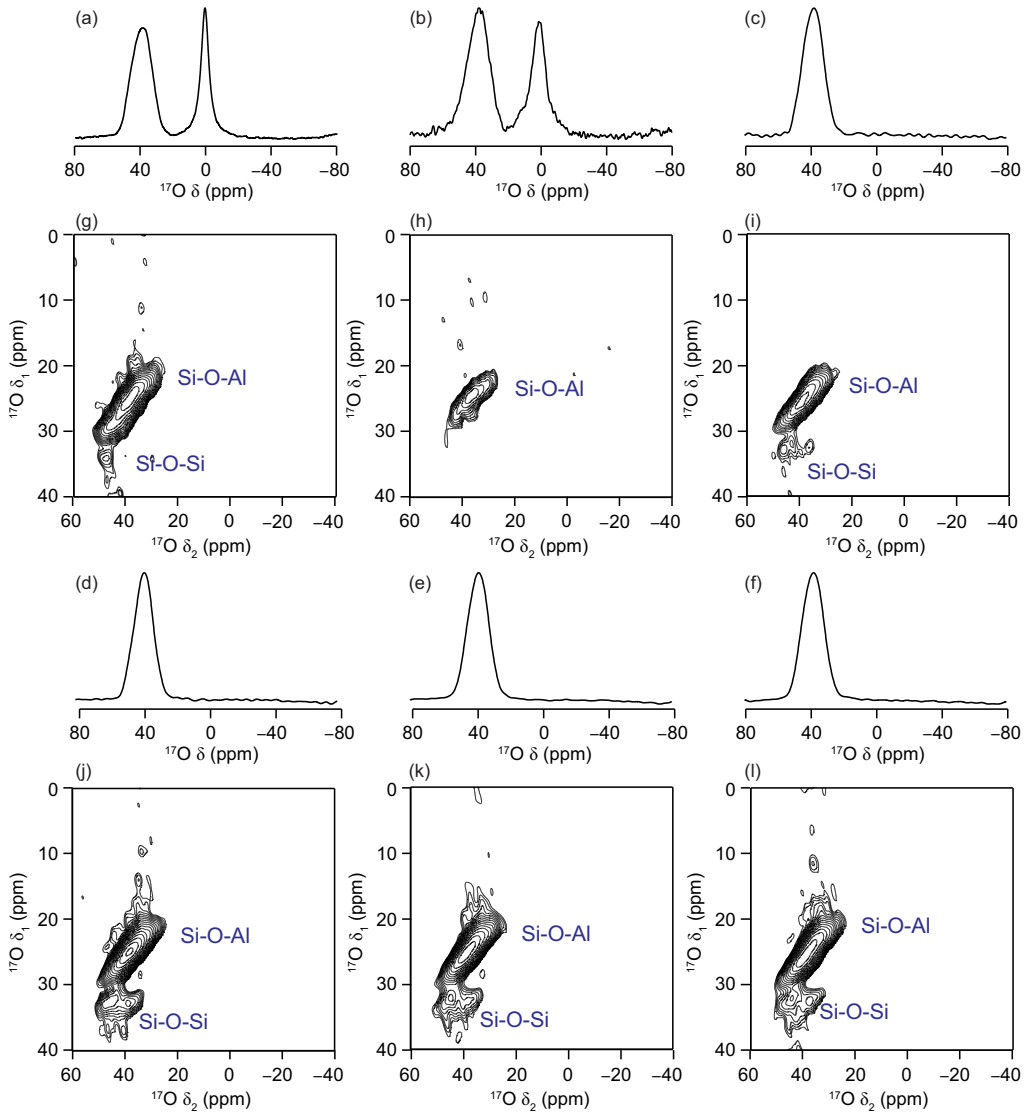

Figure 6.9: (20.0 T, 14 kHz) ^{17}O MAS NMR spectra of selected samples, isolated from an optimised ^{17}O-enriched **FAU**-**CHA** PST reaction. (a-f) quantitative short flip-angle and (g-l) $\{^{1}H\}^{17}O$ MQMAS NMR spectra for (a,g) 3-day SM, (b,h) 1 day PST, (c,i) 2 days PST, (d,j) 3 days PST, (e,k) 4 days PST and (f,l) 5 days PST.

Evidently, the use of $H_2{}^{17}O$ as the solvent these PST reactions has resulted in good incorporation of ^{17}O into the structure of the zeolitic materials, with good levels of enrichment, considering the percentage ^{17}O content of the reaction solution. To investigate the observed enrichment, the spectra were first compared to those of previously published ^{17}O NMR studies for protonated Linde Y-type zeolite (Si/Al = 2.6) (Al-**FAU**(H), referred to as HY herein).[31–36] Specifically, the assignments of ^{17}O MQMAS NMR spectra for a dehydrated, $^{17}O_{2(g)}$-enriched HY in reference 35 by Peng *et al.* are used to aid assignment. *n.b.* the isotropic dimension of MQMAS spectra in this thesis are referenced according to the convention outlined by Pike *et al.*[37] following shearing transformation. For all materials, strong evidence of Si−O−Al linkage enrichment is observed, as seen for a broad region between ≈ 20-32 ppm δ_1.[35] The width of the signal in $\delta_1$indicates a distribution of local environments, but there are only four crystallographic O sites in the **FAU** framework, which are proposed to cluster in a 3 : 1 ratio.

Focusing first on **FAU** materials (Figure 6.9a,g (3 day SM) and Figure 6.9b,h (1 day PST)), we see that the only ^{17}O-enriched linkages present at significant intensity are Si−O−Al. Although this material (as indeed do all the materials for this PST), has a low Si/Al (≈ 1.6), given the prevalence of Si−O−Si linkages in the materials (≈ 60% linkages are Si−O−Si) the resolution of some these would be expected if they were enriched (predicted ≈ 30-50 ppm δ_1).[35] This may indicate that, as for the Al-**FAU**(Na) slurrying experiments in Chapter 5, siliceous linkages within the **FAU** topology are also challenging to enrich under these elevated temperature conditions. It is not known whether this lack of enrichment is caused by inefficient reversible bond lability processes in alkali metal-exchanged **FAU**, even at 150 °C, or whether this stage of the PST mechanism does not involve the cleavage of Si−O−Si linkages, or both. The observation of only enriched Si−O−Al linkages in the 1 day PST is interesting however, as it supports the previously published ideas that aluminium, or aluminium-containing species are the reactive and mobile species within a PST reaction.[8] However, for the material to remain crystalline and tetrahedrally coordinated, some Si−O−Si linkages would also have to re-form. It is likely then, that at the early stages of the PST reaction, limited bond breakage takes place and the **FAU** framework bond lability at elevated temperature is similar to that of the reversible lability seen in **FAU** slurry experiments.

Taking into account the understanding of bond lability mechanisms in zeolites gathered so far in this thesis, some conclusions can be drawn from the **FAU** materials. Firstly, it appears that **FAU** frameworks in (Figure 6.9a,b,g,h) are less willing to interact with water than the **CHA** materials, owing to their persistent 'free water' peak at 0 ppm in

the short flip-angle experiments (Figure 6.9a,b). The analogous peak disappears from the materials from 2 days onwards (Figure 6.9c) when **CHA** materials are formed, which is less time than for the 3 day SM **FAU** material where it is still present. Secondly, at the one day stage in the PST (Figure 6.9b,h), it is highly unlikely that bonds within Si−O−Si linkages are labile in the PST reaction as they are unresolved in ^{17}O NMR spectra. This finding is interesting, considering that the ^{29}Si MAS NMR spectra in Figure 6.7 show a change to their local coordination even at this point and while the material is crystalline **FAU** in PXRD. It may be suggested then that after 1 days PST time, the local-structure of silicon reflects a varied state of T-site coordination, where some aluminosilicate linkages have been enriched (possibly through non-PST processes) and some Si−O bonds are beginning to break within the structure. Spectra of attempted ^{1}H^{29}Si CP NMR experiments showed no significant signal gains for this time point, possibly due to the *ex-situ* nature of the study, or a lack of proton proximity in the materials. It would be interesting, though, to try ^{1}H^{17}O CP experiments to see if any Si−O oxygen species, within the proximity to protons can be resolved.

Following the crystallographic transformation to **CHA** at 2-3 days reaction time, Si−O−Si linkages are more clearly seen in ^{17}O NMR spectra (Figure 6.9c-l). The observation of Si−O−Si linkages in NMR spectra of **CHA** materials could once again be caused by either, or a combination of, PST processes or by bond lability processes. Owing to their absence in the 3 day SM, or 1 day PST (Figure 6.9a,b,g,h), it could be suggested that framework oxygen exchange in **CHA** materials is thought to be primarily a consequence of **CHA** topology-specific lability processes. This observation is supported by the continued growth of the Si−O−Si framework resonance region at days four and five of PST reaction (Figure 6.9e,f,k,l), where the PST reaction is thought to be complete (by PXRD). Owing to the composition of the reaction mixture, the effect of the extra K^+ (or OH^- in the reaction solvent is not fully known, however as seen in Chapter 5, potassium-exchanged **CHA** materials do enrich by lability processes at room temperature, so the effect of the hot KOH solution is not predicted to be fundamental to bond lability here. This result once again reinforces the apparent favour of bond lability processes in **CHA** over **FAU**.

6.6.3 ^{17}O NMR Spectral Assignment

Having gained a qualitative understanding of the types of framework linkage enriched during the **FAU**-**CHA** PST, spectra are compared against that of published and previously obtained **FAU** and previously obtained **CHA** ^{17}O NMR spectra.

Firstly, δ_1 and δ_2 values from ^{17}O MQMAS NMR spectra for PST materials recorded at 20.0 T (Figure 6.9) were used to determine δ_{iso} and P_Q. It was found that for all spectra, the Si – O – Al region could be separated into two overlapping ridges in the δ_1 dimension and that either one or two Si – O – Si ridges could be resolved. The results are detailed in Table 6.6.

Material	Linkage	δ_1 (ppm)	δ_2 (ppm)	δ_{iso} (ppm)	P_Q / MHz
3 day SM	Si-O-Al 1	24.5	37.7	42.1	3.1
	Si-O-Al 2	28.1	43.4	48.3	3.3
	Si-O-Si 1	34.3	47.6	34.3	4.5
1 day PST	Si-O-Al 1	23.2	34.4	39.3	3.3
	Si-O-Al 2	26.0	38.7	44.2	3.5
2 day PST	Si-O-Al 1	23.7	35.9	40.5	3.2
	Si-O-Al 2	27.2	41.3	46.5	3.4
	Si-O-Si 1	33.4	42.7	54.2	5.0
3 day PST	Si-O-Al 1	22.5	34.1	38.5	3.1
	Si-O-Al 2	27.8	41.0	47.1	3.6
	Si-O-Si 1	32.7	42.3	53.2	4.9
	Si-O-Si 2	36.7	44.1	58.5	5.6
4 day PST	Si-O-Al 1	22.5	34.7	38.6	3.0
	Si-O-Al 2	26.7	42.7	46.5	2.9
	Si-O-Si 1	32.3	41.3	52.3	5.0
	Si-O-Si 2	36.7	42.5	57.9	5.8
5 day PST	Si-O-Al 1	22.9	35.5	39.4	3.0
	Si-O-Al 2	26.5	41.1	45.6	3.2
	Si-O-Si 1	32.5	41.2	52.6	5.0
	Si-O-Si 2	35.4	42	56.2	5.6

Table 6.6: ^{17}O NMR parameters for signals in ^{17}O MQMAS (20.0 T) NMR spectra of isolated ^{17}O-enriched PST products, shown in Figure 6.9.

The NMR parameters detailed in Table 6.6 are reasonably self-consistent and extracted values of δ_{iso} and P_Q fall within the ranges expected for ^{17}O NMR parameters for silicate and aluminosilicate zeolite linkages.[20,33–35,38,39] Generally those NMR parameters obtained experimentally for **FAU** and **CHA** materials are quite similar in magnitude, reinforcing the similarity between the two frameworks and the similarity in local environments between the two frameworks and the similarity in their resolved NMR spectra. This provides a degree of confidence in the results obtained, such that they can be compared to related and published ^{17}O NMR parameters for **FAU** and **CHA** materials.

The ^{17}O NMR parameters of selected **FAU** PST intermediates are compared to those of published parameters for dehydrated $^{17}O_{2(g)}$ gas-enriched HY[35] and a slurried and a $^{17}O_{2(g)}$ gas-enriched (see Section 5.6) starting material prepared in this project. Spectra are shown in Figure 6.10) and NMR parameters detailed in Table 6.7.

Material	Linkage	δ_1 (ppm)	δ_2 (ppm)	δ_{iso} (ppm)	P_Q / MHz
3 day PST SM	Si-O-Al 1	25.0	29.4	39.5	3.4
	Si-O-Al 2	29.6	36.4	47.5	3.5
$^{17}O_{2(g)}$ gas-enriched SM	Si-O-Al 1	29.3	19.9	41.1	4.8
	Si-O-Al 2	32.8	24.4	46.7	5.0
	Si-O-Si	44.1	44.1	55.0	5.0
Al-**FAU**(Na) 7 day slurry	Si-O-Al 1	23.5	26.4	36.8	3.4
	Si-O-Al 2	27.5	31.7	43.3	3.6
	Si-O-Si 1	37.0	33.7	55.0	4.8
Published HY	Si-O-Al 2,3,4	-	-	27.5	2.7
	Si-O-Al 1	-	-	33.3	3.6
	Si-O-Si 2,3,4	-	-	44.0	5.3
	Si-O-Si 1	-	-	50.0	5.2

Table 6.7: ^{17}O NMR parameters for resonances extracted from ^{17}O MQMAS NMR spectra of ^{17}O-enriched **FAU** materials recorded at 14.1 T (Figure 6.10) and published dehydrated HY.

By comparing the values presented in Table 6.7, it can be seen that there are few similarities, especially between the PST SM and published HY data. This result is initially surprising, considering the consistency of the NMR parameters obtained for these ^{17}O-enriched PST intermediates and that the published experimental data is also supported by the results of DFT calculations on the dehydrated structure.[35] The differences between the experimental results presented for **FAU** materials enriched in this project in Table 6.7 is surprising, considering they all originate from the same batch of starting material, however the effect of the charge balancing cation and their method of ^{17}O-enrichment will most likely affect the observed resonances.

Furthermore, the hydration state of the materials will also affect the resonances observed within ^{17}O NMR spectra. The published HY parameters correspond to a fully dehydrated zeolite, where the Brønsted proton is found on the framework, which will cause lengthening of bonds in the Si – O(H) – Al linkage and distortion of the local oxygen environment. In contrast, the PST and slurry materials studied here can expect to be extensively hydrated, owing to their method of preparation. Here, the Brønsted proton is fully solvated from the framework, causing lesser framework distortions and hence differing δ_{iso} and P_Q values, as observed. The sample enriched in-house by high-temperature exchange with $^{17}O_{2(g)}$ here is 'air hydrated', having been left on the experimental bench, following high-temperature treatment. Its hydration state is expected to be between the published HY and the slurried and PST materials. Unfortunately in this case, an exact comparison to published assigned HY oxygen resonances has not been possible for this system.

Direct comparison of spectra in Figure 6.10 shows how different the enrichment profiles observed for the **FAU** materials are, with their main difference being their levels of hydration. The hydrated spectra for slurry (Figure 6.10a,d) and PST (Figure 6.10c,f) materials are the most similar. It is possible that the effect of the cation (Na for slurry and K for PST) may have a slight influence on the small differences seen between these two spectra, although this could also be caused by their enrichment method.

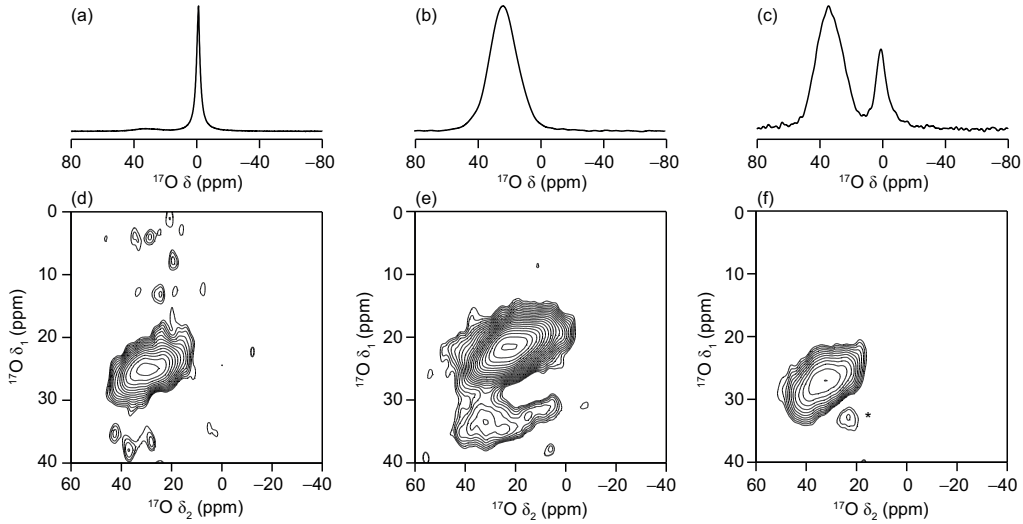

Figure 6.10: (14.1 T, 14 kHz) ^{17}O MAS NMR spectra of Si/Al = 1.6 Linde Y-type Al-**FAU**(M), ^{17}O-enriched using different methods. (a,d) M = Na, slurried for 7 days 1 : 1 (mass) 40% $H_2{}^{17}O$, (b,e) M = Na, dehydrated and $^{17}O_{2(g)}$ gas-enriched at 500 °C for 48 hours and (c,f) M = K, 3 day PST SM from optimised ^{17}O-enriched **FAU**-**CHA** PST reaction. (a-c) quantitative short flip-angle and (d-f) $\{^1H\}^{17}O$ MQMAS NMR spectra.

Similar observations for PST-synthesised **CHA** materials, when compared to other enrichment methods are also observed. As a fully assigned ^{17}O NMR spectrum for aluminosilicate **CHA** is not published in the literature, other examples of ^{17}O-enriched **CHA** materials are presented here (see Figure 6.11).

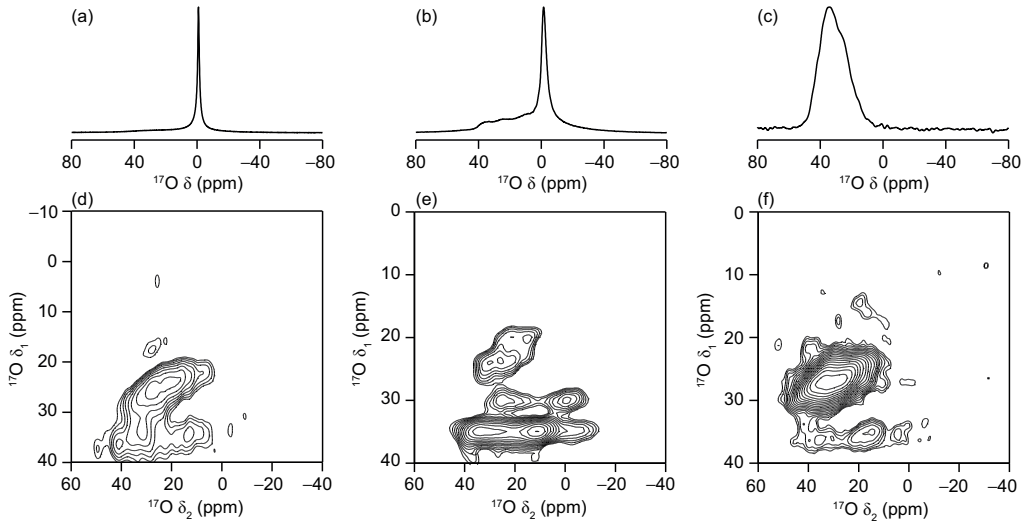

Figure 6.11: (14.1 T, 14 kHz) ^{17}O MAS NMR spectra of Al-**CHA**(K) materials with varying Si/Al, ^{17}O-enriched using different methods. (a,d) Si/Al = 5, slurried for 7 days 1 : 1 (mass) 40% $H_2{}^{17}O$, (b,e) Si/Al = 11 (SSZ-13), slurried for 14 days 1 : 1 (mass) 40% $H_2{}^{17}O$ and (c,f) Si/Al = 1.6, 5 day PST from optimised ^{17}O-enriched **FAU**-**CHA** PST reaction. (a-c) quantitative short flip-angle and (d-f) $\{^1H\}^{17}O$ MQMAS NMR spectra.

The isotropic chemical shifts and P_Q values for the **CHA** materials ^{17}O-enriched using PST and slurry methods (Figure 6.11) are shown in Table 6.8 and compared to published data.[38]

Material	Linkage	δ_1 (ppm)	δ_2 (ppm)	δ_{iso} (ppm)	P_Q / MHz
5 day PST product	Si-O-Al 1	24.6	26.8	38.2	3.5
	Si-O-Al 2	29.0	33.7	45.8	3.7
	Si-O-Si 1	35.9	29.3	52.1	5.0
Al-**CHA**(K) 7 day slurry	Si-O-Al 1	23.7	25.2	36.5	3.5
	Si-O-Si 1	34.4	24.8	48.7	5.1
SSZ-13(K) 14 day slurry	Si-O-Al 1	20.8	18.7	30.8	3.7
	Si-O-Al 2	23.3	24.8	35.9	3.5
	Si-O-Si 1	28.4	11.7	36.8	5.3
	Si-O-Si 2	33.2	20.7	45.8	5.3
Published SSZ-13(H)	Si-O-Al 1	20.5	19.4	32.6	3.9
	Si-O-Al 2	23.9	26.1	37.6	3.5
	Si-O-Si 1	30.4	17.0	40.9	5.4
	Si-O-Si 2	33.4	21.5	46.5	5.2

Table 6.8: ^{17}O NMR parameters for resonances extracted from ^{17}O MQMAS NMR spectra of ^{17}O-enriched **CHA** materials recorded at 14.1 T (Figure 6.11) and published slurried SSZ-13(H).

Comparing the results of NMR parameter extraction for **CHA** materials ^{17}O-enriched by slurry methods with those of the ^{17}O-enriched PST reaction, there are again both similarities and differences for the materials with similar hydration states. Generally, the resolved δ_{iso} and P_Q of PST-derived resonances agree with those seen for materials enriched using slurrying techniques, indicating that the PST products are ^{17}O-enriched **CHA**. There are, however some differences in the position of individual Si−O−Al and Si−O−Si signals, when compared to the results from SSZ-13(M) **CHA** materials and the resolved ^{17}O NMR parameters resemble more closely that of the more poorly-enriched, lower Si/Al Al-**CHA**(K) slurry and the low Si/Al **FAU** PST and slurry materials characterised earlier. It is possible that the differing Si/Al of these PST **CHA** materials and the SSZ-13(H) may cause the large difference in δ_{iso}. However, as one Si−O−Si linkage resonance is consistently resolved with good resolution in PST materials, it is thought that the PST-produced materials themselves are not uniformly enriched, making it difficult to draw comparisons of resolved sites between samples as no clear picture of the expected uniformly enriched zeolite material is known.

In order to learn more about the local atomic oxygen coordination at different sites in PST-formed **CHA** materials, a hydrated **CHA** material of low Si/Al, with a more uniform level of ^{17}O-framework enrichment is desired. This could be achieved by successful $^{17}O_{2(g)}$ gas-enrichment of a **CHA**, which has so far not proven possible, owing to low framework stability. Alternative enrichment techniques involving aqueous processes, such as incipient wetness, mechanochemistry or prolonged hydrolytic treatments could also be considered.[20]

Although it is not easy to assign specific signals in ^{17}O NMR spectra to specific O sites in **FAU** and **CHA** materials formed though PST reactions, it is possible that the transformation has an effect on the selectivity of the framework enrichment, owing to the differences in NMR spectra of some of the resolved linkages in ^{17}O-enriched PST **CHA** materials and hydrothermally synthesised and ^{17}O-enriched materials. One further piece of evidence in support of a different enrichment method under aqueous PST conditions is found when considering the relative integrated intensities of signals from framework linkages extracted as rows from ^{17}O MQMAS NMR spectra of PST products. Although a non-quantitative experiment, the similarity in P_Q values for like-linkages obtained from MQMAS NMR experiments allows this comparison to be drawn. Peng *et al.*[35] determined a 3:1 ratio between each of the two Si–O–Si and Si–O–Al signals seen in NMR spectra of HY, determining them to be split as Si–$O_{2,3,4}$–X and Si–O_1–X, where X = Si, Al. As seen in Chapter 5, a different intensity ratio is seen, with each of the two Si–O–X signals for X = Si and Al having a 1:1 ratio; Si–$O_{1,4}$–X and Si–$O_{2,3}$–X. When signals from the same type of linkage have been resolved in PST-enriched materials in this study, the resolved integrated intensities have been roughly 1 : 1 for **FAU** Si–O–Al linkages, 1.5 : 1 for **CHA** Si–O–Al linkages and 2 : 1 for **CHA** Si–O–Si linkages, indicating that the enrichment observed in the PST process may have a slight degree of selectivity. Working out exactly which, if any crystallographically distinct oxygen sites these correspond to will help greatly in understanding the mechanism of the PST reaction and the role of framework-water interaction. This however, is beyond the scope of the current work as the NMR signals resolved in spectra discussed here have been found to depend on how samples have been prepared and enriched, and also differ depending on their framework composition (Si/Al, hydration state and extra-framework cation).

6.7 Further Approaches to ^{17}O-enrichment

An ideal strategy to aid any spectral assignment is to perform ^{17}O enrichment processes on natural-abundance synthesised PST materials. This, in effect, should eliminate any reactivity-related issues for bond liability and exchange and focus only on the effect that material framework structure has on the local oxygen coordination environment and / or ability to exhibit bond lability processes under aqueous conditions.

Using the natural abundance PST materials characterised in Section 6.5, the K^+-exchanged SM, 2 day and four day PST materials were selected for further study as they represent a good selection of **FAU** starting material, intermediate phase and **CHA** end product (see Figure 6.2). The materials were subject to a washing procedure (Section 6.9.1) in an effort to remove any excess potassium species in their pores and channels, before being either slurried with $H_2{}^{17}O$ or enriched by high-temperature gas-exchange with $^{17}O_{2(g)}$.

The ^{29}Si and ^{27}Al MAS NMR spectra for high-temperature post-synthetic gas-exchange and slurrying processes for natural abundance PST materials are documented in the Appendix Section G.1 and Section G.2, respectively.

6.7.1 $^{17}O_{2(g)}$-enrichment of PST Materials

As for previous investigations, ^{17}O NMR spectra of high-temperature $^{17}O_{2(g)}$-exchanged PST materials were desired to give an idea of spectra resulting from potentially 'uniform' enrichment. Owing to the small sample volumes generated in the PST reactions, the success of this particular method here was limited, as only a few trial enrichment procedures to optimise reaction conditions were possible. Figure 6.12 shows that for all samples; K^+-exchanged SM, 2 day PST intermediate and 4 day PST product, it was possible to incorporate some ^{17}O isotope into the structure of the zeolite – as evidenced by the signal resolved between 20-60 ppm. Enrichment conditions used for the washed materials are detailed in Sections 6.9.6-6.9.8.

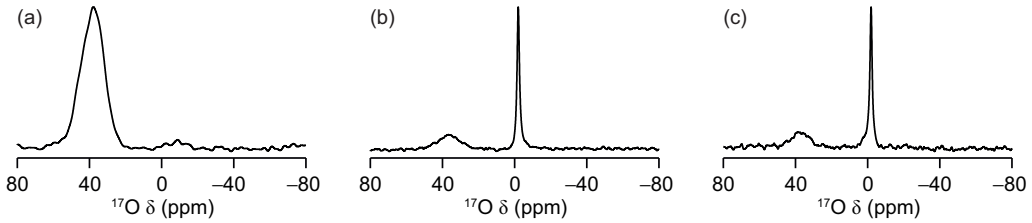

Figure 6.12: (20.0 T, 14 kHz) ^{17}O MAS quantitative short flip-angle NMR spectra of $^{17}O_{2(g)}$-enriched PST materials (a) K^+-exchanged **FAU** SM, (b) 2 day PST **FAU**-**CHA** intermediate and (c) 4 day PST-formed **FAU** product.

When considering the signal-to-noise ratio of the ^{17}O spectra and taking into account sample mass and experiment time, generally, the levels of ^{17}O incorporation into the framework here are lower (30-50 % of others) when compared to other $^{17}O_{2(g)}$-enriched zeolite frameworks characterised in this thesis. From Figure 6.12 it can be seen that the only material for which a useful amount of ^{17}O isotope has been incorporated is the Al-**FAU**(K) pre-PST SM (Figure 6.12a). It is not known why the 2 day intermediate and 4 day end product materials were not successfully $^{17}O_{2(g)}$-enriched and may possibly just be due to selection of non-ideal enrichment parameters for the phases present. However, ^{17}O NMR spectra for both of these materials exhibit a signal, centred at 0 ppm. It is possible that this hydration peak is attributed to $H_2{}^{17}O$ water stuck in the pores of the zeolite framework, following the dehydration and high-temperature gas-enrichment heating processes. The sign that this water is trapped may hinder the passage of $^{17}O_{2(g)}$ through the pores and channels of the framework, making successful framework oxygen exchange processes at high temperature difficult. Surface area measurements, such as BET analysis, or TGA analysis to gauge the level of residual water may prove useful here to indicate why enrichment using $^{17}O_{2(g)}$ was not very successful.

It was possible only to record the $\{^1H\}^{17}$O MQMAS NMR spectrum for K^+-exchanged **FAU** SM. This is shown in Figure 6.13.

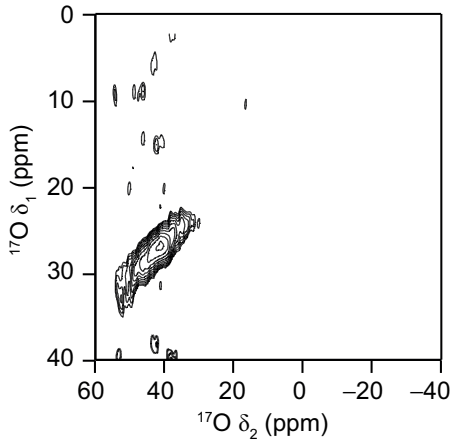

Figure 6.13: (20.0 T, 14 kHz) $\{^1H\}^{17}O$ MQMAS NMR spectrum of $^{17}O_{2(g)}$-enriched K^+-exchanged **FAU** PST SM.

Even for frameworks that did not enrich here using $^{17}O_{2(g)}$-enrichment techniques, no significant changes in the crystalline long-range order were observed and ^{27}Al MAS NMR spectra (Appendix Figure G.2) did not show significant changes. The ^{29}Si NMR spectra in Appendix Figure G.1, however do show that the heat treatment has slightly disrupted the local coordination environment of silicon in the material, with peak broadening seen. This may result in a slight weakening of the structural integrity of the framework overall, without disrupting the crystallinity. Owing to the small sample volumes obtained from gas-enrichment, the ^{29}Si NMR spectra are slightly disrupted by the broad resonance attributed to ^{29}Si in the probe background (see Appendix Figure A.1).

6.7.2 $H_2{}^{17}O$ Slurrying of PST Materials

1 : 1 (mass) zeolite : $H_2{}^{17}O$ slurries were prepared for K^+-exchanged SM, 2 day PST intermediate and 4 day PST products in a similar manner to previous slurries discussed in this thesis. Specific preparation details are given in Sections 6.9.9-6.9.11. ^{17}O NMR spectra of the resulting materials were taken after a period of approximately two weeks and are shown in Figure 6.14.

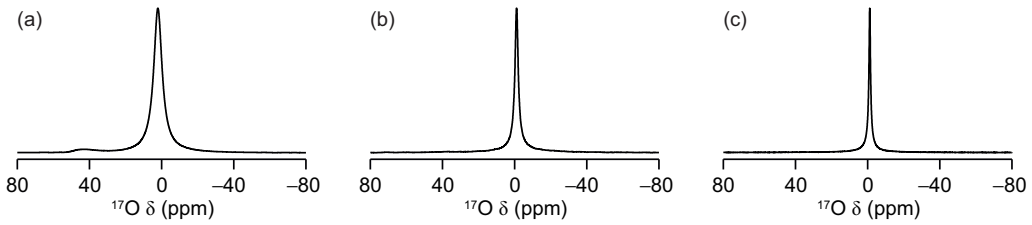

Figure 6.14: (20.0 T, 14 kHz) ^{17}O MAS quantitative short flip-angle NMR spectra of $H_2{}^{17}O$-slurried PST materials (a) K^+-exchanged **FAU** SM, slurried for 12 days, (b) 2 day PST **FAU**-**CHA** intermediate, slurried for 13 days and (c) 4 day PST-formed **FAU** product, slurried for 14 days.

Generally, the level of framework enrichment within the slurried PST materials is poor, when compared to similar **FAU** or **CHA** materials discussed previously in this thesis. Once again, the K^+-exchanged SM (Figure 6.14a) is the only material for which some ^{17}O isotope incorporation into the framework structure (signal between 20-60 ppm) is clear, but even this is on a low level (similar to that seen for gas-enrichment, above). Consequently, once again it was only possible to record the $\{^1H\}^{17}O$ MQMAS NMR spectrum for K^+-exchanged **FAU** SM, as shown in Figure 6.15.

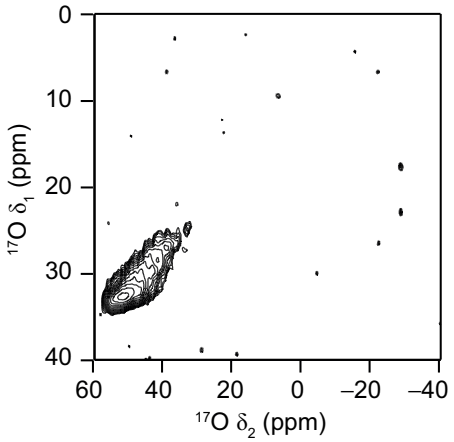

Figure 6.15: (20.0 T, 14 kHz) $\{^1H\}^{17}O$ MQMAS NMR spectrum of $^{17}O_{2(g)}$-enriched K^+-exchanged **FAU** PST SM.

It was perhaps expected that a low level and Si – O – Al-selective framework enrichment is observed for the Al-**FAU**(K) as this is what was observed for the pre ion-exchanged Al-**FAU**(Na) material, characterised in Chapter 5 (and Figure 6.10). What is perhaps more surprising is that both the 2 day intermediate and the 4 day product, both of which contain **CHA** phase materials, do not appear to enrich significantly using this approach. This is in contrast to what was seen for **CHA** materials of similar Si/Al or containing the H^+ extra-framework cation, which would have predicted that these PST-synthesised **CHA** materials would have displayed reversible bond lability under these conditions. The exact reason for the lack of observable bond lability in the PST-formed **CHA** materials is unknown, but it is possible that this is for reasons similar to those responsible for the poor $^{17}O_{2(g)}$ enrichment of PST materials in Section 6.7.1, *i.e.* extra-framework cations blocking the pores may hamper the ability of these materials to slurry. Further work is needed to explore these differences.

For slurried samples of PST materials, the overall framework integrity is preserved, as evidenced from the crystalline long-range order and ^{29}Si and ^{27}Al MAS NMR spectra (Appendix Figure G.4) did not show significant changes. Only for the ^{29}Si MAS NMR spectrum of the Al-**FAU**(K) slurry in Appendix Figure G.3a, is an increase in $^1H^{29}Si$

observed, indicating some slight hydrolysis processes have occurred here. Owing to the small sample volumes used in slurries, the ^{29}Si NMR spectra are once again slightly disrupted by the broad resonance attributed to ^{29}Si in the probe background (see Appendix Figure A.1).

6.8 Summary and Conclusions

This chapter has described an exploratory study into the **FAU**-**CHA** zeolite post-synthetic topology conversion. It was hoped that studying the PST reaction using ^{17}O NMR would characterise the reactivity of different zeolite framework linkages in **FAU** and **CHA** materials under aqueous conditions, shedding light on any irreversible PST and reversible bond lability processes, and whether these two processes are synergetic under reaction conditions.

The wealth of published studies on PST transformations, including those on the **FAU**-**CHA** system of interest meant that many variations of successful reactions in the literature exist. In order to be suitable for this study, it was desired that the transformation would be 'pure'; requiring no extra source of T-site reagent (silicas, aluminas, *etc.*) or additional organic SDAs. The published example in Muraoka *et al.*[8] was chosen as successful transformation from K^+-exchanged Linde Y-type **FAU** to **CHA** is performed in small amounts of KOH only. Through optimisation of the synthetic approach, the required amount of preparatory ion-exchanges, KOH concentration and total volume of reaction solution for the PST was decreased, enabling the effect of water on any topology conversion or bond lability processes to be studied more easily. Furthermore, the decrease in the overall amount of water solvent required for the reaction meant that an efficient and economical approach to *in-situ* ^{17}O enrichment was developed, involving dilution of small amounts of 20% $H_2{}^{17}O$ directly into the reaction solvent.

Analysis of the materials produced using PXRD and Le Bail fitting confirmed that **CHA** successfully forms from the starting **FAU** framework. Following this, ^{29}Si MAS NMR spectra uncovered how the distribution of silicon NNN atoms changes throughout PST reaction from **FAU** to **CHA**, without alteration of the overall Si/Al. This tendency has been observed previously for the **FAU**-**CHA** transformation, with aluminium distributions of the **CHA** materials formed also being different to those of hydrothermally synthesised **FAU**.[8] The reasons behind this apparent framework reorganisation during PST are still not fully understood, however ^{17}O NMR spectra of mid-conversion PST intermediates show enrichment only of Si – O – Al linkages, indicating that these are the

most (or only) mobile reactive species during the conversion of **FAU** to **CHA**. Only when **CHA** is the predominant phase and changes to ^{29}Si MAS NMR spectra have ceased are signals from Si – O – Si linkages observed in ^{17}O NMR spectra. Whilst it is not possible to confirm unequivocally from these data, this points to the idea that **FAU** framework Si – O – Si linkages are resistant to bond lability even under hydrothermal conditions and that lability in Al – O bonds are very important to the success of PST reactions. Furthermore, the results demonstrate the surprising favourable lability of Si – O – Si linkages under aqueous conditions. Interestingly however, post-PST slurrying of Al-**CHA**(K) materials did not provide any evidence of significant room-temperature lability processes in the synthesised materials. Together with a lack of ability to enrich the materials using $^{17}O_{2(g)}$, this indicates that the pores and channels of the formed materials may be blocked, perhaps by additional K^+ ions from the synthesis, which could play a templating role in the PST. Further study of produced materials, using surface area, EDX or TEM methods may help explain this finding.

Throughout the PXRD and NMR studies for ^{17}O-enriched PST reactions, no evidence of (temporarily) formed amorphous or defective material was observed. At all points, isolated intermediates resembled either crystalline **FAU**, **CHA** or both, with order and tetrahedral coordination of T-sites also preserved. Owing to the *ex-situ* nature of this study, this points to the idea that the PST reaction mechanism does not involve extensive fragmentation and reorganisation of the zeolite structure and that pathways to access higher framework energy, crystalline, ordered snapshots are favourable.

Building on the ^{17}O NMR work on **CHA** in Chapters 4 and 5 in this thesis and together with published ^{17}O NMR spectra, it was hoped that the favourable conversion of **FAU** to **CHA** under these reaction conditions would aid spectral assignment for specific oxygen linkages of **CHA**. Further, it was hoped that any ability to 'follow' specific oxygen linkages throughout the PST would open the possibility of effectively tracking the movement of oxygen atoms from one zeolite framework to another. Unfortunately however, the hydration state of the dehydrated model published HY **FAU** system was not compatible with the highly hydrated PST **FAU** materials isolated from the PST reaction. This largely precluded the assignment of different framework linkages to specific resonances in ^{17}O NMR spectra. However, going forward this could be remedied by producing an appropriate Si/Al **FAU** material, $^{17}O_{2g}$-enriching and then dehydrating it to match the published HY (Al-**FAU**(H)) material. Furthermore, the same strategy could be employed for **CHA** materials by the hydrothermal production of an appropriate low Si/Al Al-**CHA**(K) material, uniformly enriching it in ^{17}O using $^{17}O_{2(g)}$ and either dehydrating it to match the state of the HY sample or hydrating it to match the state of PST-synthesised Al-**CHA**(K) materials, or both. This strategy would also help to understand whether the NMR parameters of resonances resolved from PST-formed **CHA** materials were more closely related to that of the parent PST **FAU** material than to that of similar, hydrated, hydrothermally synthesised **CHA** materials.

The results in this chapter have once again uncovered the widespread lability of framework zeolite linkages under aqueous conditions. Although previous chapters have also described this phenomenon, something particularly evident here is the selectivity with which these bond lability mechanisms operate, even at elevated temperatures as seen in the PST reaction. Observable framework oxygen exchange is seen again to be strongly dependent on framework topology, with differences in observed framework enrichment seen for **FAU** and **CHA** materials at elevated temperatures in basic conditions. Observing framework enrichment throughout a PST reaction where known structural changes are occurring and yet limited to no framework degradation or compositional alteration is observed, indicates that certain zeolites can display both structural stability and flexibility at the same time, shedding light into how these materials behave in industrial processes involving aqueous elevated temperature conditions. Further, this provides weight to the argument that the PST mechanism of zeolites must not involve extensive framework fragmentation.

6.9 Sample Preparation

Further material preparations required, following PST reaction for selected samples are detailed here.

6.9.1 Washing Procedure

PST-synthesised zeolite materials (50 mg) were dispersed in distilled water (5 cm^3) and stirred at room temperature for 2 hours. Samples were filtered and the process repeated with the same volume of fresh distilled water. The samples are filtered again, washed with distilled water and dried at 80 °C for 10 minutes.

6.9.2 Al-CHA(H) Preparation

Calcined Al-**CHA**K (750 mg) was combined with a 3 M solution of NH_4Cl and heated to 80 °C for 16 hours whilst stirring. The product was filtered and the process repeated with a fresh solution. The product was again filtered and washed with distilled water. The ammonium form material was then calcined to 550 °C for 6 hours as described in Section 3.5.1.

6.9.3 Al-CHA(H) Slurry Preparation

Calcined zeolite (25 mg) was combined with $H_2{}^{17}O$ (40%, 25 μL) in a Bruker 4 mm HRMAS NMR rotor insert as detailed in Section 3.5.4.

6.9.4 SSZ-13(K) CHA Slurry Preparation

Calcined zeolite (25 mg) was combined with $H_2{}^{17}O$ (40%, 25 μL) in a Bruker 4 mm HRMAS NMR rotor insert as detailed in Section 3.5.4.

6.9.5 Linde Y FAU(Na) $^{17}O_{2(g)}$-enrichment Preparation

Calcined zeolite ($\approx$ 100 mg) was dehydrated (300 °C, 16 hours) under vacuum and sealed under argon before being gas-enriched (500 °C, 48 hours) in an atmosphere of $\approx$ 200 mbar $^{17}O_{2(g)}$ as described in Section 3.5.5.

6.9.6 PST SM Al-FAU(K) $^{17}O_{2(g)}$-enrichment

Ion-exchanged Al-**FAU**(K) SM ($\approx$ 100 mg) was dehydrated (300 °C, 16 hours) under vacuum and sealed under argon before being gas-enriched (500 °C, 48 hours) in an atmosphere of $\approx$ 200 mbar $^{17}O_{2(g)}$ as described in Section 3.5.5.

6.9.7 PST Intermediate $^{17}O_{2(g)}$-enrichment

Two day PST intermediate zeolite ($\approx$ 100 mg) was dehydrated (300 °C, 16 hours) under vacuum and sealed under argon before being gas-enriched (500 °C, 72 hours) in an atmosphere of $\approx$ 200 mbar $^{17}O_{2(g)}$ as described in Section 3.5.5.

6.9.8 PST End Product Al-CHA(K) $^{17}O_{2(g)}$-enrichment

Four day PST Al-**CHA**(K) ($\approx$ 100 mg) was dehydrated (300 °C, 16 hours) under vacuum and sealed under argon before being gas-enriched (500 °C, 72 hours) in an atmosphere of $\approx$ 200 mbar $^{17}O_{2(g)}$ as described in Section 3.5.5.

6.9.9 PST SM Al-FAU(K) Slurry Preparation

Ion-exchanged Al-**FAU**(K) SM (25 mg) was combined with $H_2{}^{17}O$ (90%, 25 μL) in a Bruker 4 mm HRMAS NMR rotor insert as detailed in Section 3.5.4.

6.9.10 PST Intermediate Slurry Preparation

Two day PST intermediate zeolite (25 mg) was combined with $H_2{}^{17}O$ (90%, 25 μL) in a Bruker 4 mm HRMAS NMR rotor insert as detailed in Section 3.5.4.

6.9.11 PST End Product Al-CHA(K) Slurry Preparation

Four day PST Al-**CHA**(K) (25 mg) was combined with $H_2{}^{17}O$ (90%, 25 μL) in a Bruker 4 mm HRMAS NMR rotor insert as detailed in Section 3.5.4.

6.10 References

[1] K. Honda, M. Itakura, Y. Matsuura, A. Onda, Y. Ide, M. Sadakane and T. Sano, *J. Nanosci. Nanotechnol.*, 2013, **13**, 3020–3026.

[2] C. Li, M. Moliner and A. Corma, *Angew. Chemie Int. Ed.*, 2018, **57**, 15330–15353.

[3] D. Schwalbe-Koda, Z. Jensen, E. Olivetti and R. Gómez-Bombarelli, *Nat. Mater.*, 2019, **18**, 1177–1181.

[4] S. Goel, S. I. Zones and E. Iglesia, *Chem. Mater.*, 2015, **27**, 2056–2066.

[5] M. Bourgogne, J.-L. Guth and R. Wey, *US Patent 4,503,024*, 1985.

[6] J. R. Di Iorio and R. Gounder, *Chem. Mater.*, 2016, **28**, 2236–2247.

[7] S. Miyagawa, K. Miyake, Y. Hirota, N. Nishiyama, M. Miyamoto, Y. Oumi and S. Tanaka, *Microporous Mesoporous Mater.*, 2019, **278**, 219–224.

[8] K. Muraoka, Y. Sada, A. Shimojima, W. Chaikittisilp and T. Okubo, *Chem. Sci.*, 2019, **10**, 8533–8540.

[9] L. V. Tendeloo, E. Gobechiya, E. Breynaert, J. A. Martens and C. E. Kirschhock, *Chem. Commun.*, 2013, **49**, 11737–11739.

[10] S. I. Zones, *J. Chem. Soc. Farady Trans*, 1991, **87**, 3709–3716.

[11] X. Wang, Q. Wu, C. Chen, S. Pan, W. Zhang, X. Meng, S. Maurer, M. Feyen, U. Müller and F.-s. Xiao, *Chem. Commun.*, 2015, **51**, 16920–16923.

[12] J. Devos, M. L. Bols, D. Plessers, C. V. Goethem, J. W. Seo, S. J. Hwang, B. F. Sels and M. Dusselier, *Chem. Mater.*, 2020, **32**, 273–285.

[13] J. Devos, S. Robijns, C. Van Goethem, I. Khalil and M. Dusselier, *Chem. Mater.*, 2021, **33**, 2516–2531.

[14] W. Qin, R. Jain, F. C. Robles Hernández and J. D. Rimer, *Chem. – A Eur. J.*, 2019, **25**, 5893–5898.

[15] T. Tanigawa, N. Tsunoji, M. Sadakane and T. Sano, *Dalt. Trans.*, 2020, **49**, 9972–9982.

[16] L. Van Dang, T. T. M. Nguyen, D. Van Do, S. T. Le, T. D. Pham and A. T. M. Le, *J. Anal. Methods Chem.*, 2021, **2021**, 1–10.

[17] X. Xiong, D. Yuan, Q. Wu, F. Chen, X. Meng, R. Lv, D. Dai, S. Maurer, R. McGuire, M. Feyen, U. Müller, W. Zhang, T. Yokoi, X. Bao, H. Gies, B. Marler, D. E. De Vos, U. Kolb, A. Moini and F.-S. Xiao, *J. Mater. Chem. A*, 2017, **5**, 9076–9080.

[18] J. Devos, M. A. Shah and M. Dusselier, *RSC Adv.*, 2021, **11**, 26188–26210.

[19] K. Mlekodaj, M. Bernauer, J. E. Olszowka, P. Klein, V. Pashkova and J. Dedecek, *Chem. Mater.*, 2021, **33**, 1781–1788.

[20] S. E. Ashbrook, Z. H. Davis, R. E. Morris and C. M. Rice, *Chem. Sci.*, 2021, **12**, 5016–5036.

[21] G. P. M. Bignami, Z. H. Davis, D. M. Dawson, S. A. Morris, S. E. Russell, D. McKay, R. E. Parke, D. Iuga, R. E. Morris and S. E. Ashbrook, *Chem. Sci.*, 2018, **9**, 850–859.

[22] C. M. Rice, Z. H. Davis, D. McKay, G. P. M. Bignami, R. G. Chitac, D. M. Dawson, R. E. Morris and S. E. Ashbrook, *Phys. Chem. Chem. Phys.*, 2020, **22**, 14514–14526.

[23] A. Le Bail, H. Duroy and J. L. Fourquet, *Mat. Res. Bull.*, 1988, **23**, 447–452.

[24] A. Le Bail, H. Duroy and J. Fourquet, *Mater. Res. Bull.*, 1988, **23**, 447–452.

[25] A. Le Bail, *Powder Diffr.*, 2005, **20**, 316–326.

[26] C. Baerlocher and L. B. McCusker, *Database of Zeolite Structures*, http://www.iza-structure.org/databases/.

[27] D. H. Olson, D. H. Olson, L. Broussard, D. P. Shoemaker, J. A. C. Soc, H. W. King, L. F. Vassmillet, A. X.-r. Anal, W. M. Mueller, G. R. Mallett, M. J. Fox, W. R. Busing, K. O. Martin and H. A. Levy, *J. Phys. Chem.*, 1970, **74**, 2758–2764.

[28] M. Calligaris, G. Nardin and L. Randaccio, *Zeolites*, 1983, **3**, 205–208.

[29] D. E. Akporiaye, I. M. Dahl, H. B. Mostad and R. Wendelbo, *J. Phys. Chem.*, 1996, **100**, 4148–4153.

[30] S. Greiser, M. Hunger and C. Jäger, *Solid State Nucl. Magn. Reson.*, 2016, **79**, 6–10.

[31] H. Huo, L. Peng and C. P. Grey, *Stud. Surf. Sci. Catal.*, 2007, **170**, 783–789.

[32] H. Huo, L. Peng and C. P. Grey, *J. Phys. Chem. C*, 2011, **115**, 2030–2037.

[33] L. Peng, Y. Liu, N. Kim, J. E. Readman and C. P. Grey, *Nat. Mater.*, 2005, **4**, 216–219.

[34] L. Peng, H. Huo, Y. Liu and C. P. Grey, *J. Am. Chem. Soc.*, 2007, **129**, 335–346.

[35] L. Peng, H. Huo, Z. Gan and C. P. Grey, *Microporous Mesoporous Mater.*, 2008, **109**, 156–162.

[36] L. Shen and L. Peng, *Chinese J. Catal.*, 2015, **36**, 1494–1504.

[37] K. J. Pike, R. P. Malde, S. E. Ashbrook, J. McManus and S. Wimperis, *Solid State Nucl. Magn. Reson.*, 2000, **16**, 203–215.

[38] C. J. Heard, L. Grajciar, C. M. Rice, S. M. Pugh, P. Nachtigall, S. E. Ashbrook and R. E. Morris, *Nat. Commun.*, 2019, **10**, 4690–4967.

[39] S. M. Pugh, P. A. Wright, D. J. Law, N. Thompson and S. E. Ashbrook, *J. Am. Chem. Soc.*, 2020, **142**, 900–906.

Chapter 7

Summary & Outlook

Although perceived as stable inorganic scaffolds, this work has added to the evidence that zeolites possess a degree of structural dynamics and flexibility through studying their interactions with water. ^{17}O NMR spectroscopy has revealed the reactivity of zeolite linkages and how the local coordination environment of zeolite frameworks continually changes as framework oxygen species exchange with the oxygen atoms of water. NMR spectroscopic studies of T site zeolite nuclei (^{29}Si, ^{27}Al, ^{11}B, *etc.*) and diffraction studies of the long range order provide evidence that this framework oxygen exchange can occur in both reactive and non-reactive regions of zeolites undergoing structural rearrangements as well as in zeolites whose frameworks would appear otherwise unaffected by interaction with water. The underlying reasons behind this chemical reactivity are not yet fully understood but these studies on 'model' zeolites provide a foundation for a more general understanding of this bond lability in zeolites and also open up new opportunities for study of oxygen structure in framework materials using ^{17}O NMR spectroscopy.

The ADOR process for zeolites, in which hydrolytically unstable germanosilicate zeolites are selectively disassembled and organised in aqueous conditions for the formation of novel zeolite frameworks, was studied, aiming to extend the knowledge of the effect of hydrolysis of parent **UTL** germanosilicate in acid on the local structure to include the effect of water alone. Analysis of products from ^{17}O-doped hydrolysis reactions revealed that ^{17}O exchanges with framework oxygen into Si – O – Si linkages that are not thought to be disrupted by ADOR hydrolysis processes. Further, this framework exchange is observed to have taken place even when no long-range structural changes to the material are happening; in slurries with purely siliceous **UTL** and during the induction period, where structural rearrangements of silicon atoms in IPC-1P are seen. Low-volume hydrolysis of **UTL** using mechanochemical methods was also realised, providing an efficient, lower energy, scalable alternative to the disassembly step in the

ADOR process. Mechanochemical treatment in the presence of $H_2{}^{17}O$ also produced efficient ^{17}O-enrichment of the material, something to our knowledge has not been used extensively for the enrichment of zeolites and producing the first evidence of Si−O−Ge linkages present in **UTL**-derived hydrolysis products. The ease with which mechanochemically-assisted ^{17}O-enrichment was obtained for **UTL**-derived materials makes this a promising method for further ^{17}O-enrichment studies of hydrolytically stable and unstable zeolites.

The SSZ-13 zeolite with **CHA** framework was chosen as a model system to study the effect of room-temperature framework oxygen exchange with water in an industrially-relevant, hydrolytically stable aluminosilicate zeolite. NMR and PXRD studies showed evidence of rapid oxygen exchange using the slurry method with no effect on the long range order of the structure, its composition or the local coordination environment of its T site atoms, even when the charge balancing cation was altered. By comparing ^{17}O NMR spectra of slurried zeolite frameworks, it is seen that the nature of the charge balancing cation has an effect on observed enrichment. Indeed, different extraframework cations appeared to dictate selective enrichment of specific crystallographic oxygen sites and different types of linkage (Si−O−Si or Si−O−Al). Evidence for selectivity in enrichment of specific sites is supported by comparison to the $^{17}O_{2\,(g)}$-enriched materials, indicating that, in general, Si−O−Al linkages are more labile and preferentially enriched using slurrying. An AIMD study carried out on the SSZ-13(H) material, for which particularly favourable oxygen exchange was observed, verifies this, showing that only one water molecule is needed to cleave Si−O−Al bonds with low energetic barriers. The Brønsted proton is considered to be important for Si−O−Si bond scission, with the formation of a hydrogen bonded chain of water molecules encompassing the Brønsted acid site predicted to facilitate bond breaking on the adjacent Si−O−Si linkage. This however, is clearly not the only mechanism facilitating bond lability in **CHA** as evidence of 'slower' exchanging sites where sterics preclude the formation of H-bonded chains and the enrichment of the SSZ-13(M) frameworks where only residual acidic protons remain, are also observed.

Framework enrichment was also observed for **FAU** framework materials treated in a similar manner to **CHA**. This once again challenges the applicability of the predicted mechanisms of the **CHA** material, pointing to the need for a greater understanding of lability processes in zeolites in the hope that a more general mechanistic understanding can be resolved. Whilst the occurrence of aqueous oxygen exchange processes with zeolites do not to our knowledge determine their ability to act as catalysts, absorbents, inert

scaffolds, *etc.*, it is beneficial to understand the processes by which this lability occurs and the factors that may affect them (topology, framework composition, extra-framework cations, *etc.*). Going forward, a greater understanding of the factors that influence bond lability pocesses for zeolite in aqueous conditions is beneficial and could be used to help design reaction systems where framework flexibility is either desirable or to be avoided. From a research point of view, the knowledge that one can enrich zeolites in ^{17}O isotope by simple dropping water on to them at room temperature is very useful, providing a simple method to help characterisation of local atomic structure in these commercially relevant materials. It is of interest to extend the understanding of the applicability of this slurrying method to other inorganic or hybrid materials, such as ALPOs, SAPOs, ZIFs and MOFs.

The known lability of framework linkages in **FAU** and **CHA** frameworks was exploited in an attempt to increase understanding of the inter-zeolite conversion, or post-synthetic transformation process between the two closely related topologies. Despite the widespread use of the PST method for the economical conversion of zeolites, the underlying mechanism by which many framework topologies convert is not fully understood. A reaction system was developed, producing Al-**CHA**(K) from Al-**FAU**(K) by heating only in aqueous KOH. In an attempt to increase understanding of the PST process, adaption of the synthesis for economical ^{17}O-enrichment was successful, with incorporation of ^{17}O from the water reagent very favourable under hydrothermal reaction conditions. Unfortunately however, from the data generated it was not possible to formulate a mechanism of how the transformation proceeds, although, owing to the retention of crystallinity and T site coordination throughout, it was possible to rule out that the transformation proceeds with extensive structural fragmentation. Furthermore, the rearrangement of T site distribution observed and the extensive Si – O – Al linkage resolution in ^{17}O NMR spectra does add weight to previously published arguments that aluminium atoms are the mobile phase in the PST. Interestingly, selectivities in framework site enrichment were seen within the PST transformation, with Si – O – Al-only enrichment seen for **FAU** as in previous slurry experiments and Si – O – Si sites only enriched when the material long range order resembles **CHA**. This indicates that some types of framework linkage may remain non-labile in aqueous conditions, even at elevated temperatures. This observed discrepancy between the lability of some different types of linkage is incredibly interesting.

Further studies to deepen the understanding of bond lability during the PST process are desired, especially ones that highlight the importance of water in the transformation. This could be achieved by substitution of the water solvent, changing conditions from hydrothermal to solvothermal. Analysis of ^{17}O NMR spectra of PST intermediates was made difficult by the strong overlap of many signals attributed to framework linkages and due to the lack of an applicable, fully assigned ^{17}O NMR spectrum for **FAU**. A uniformly enriched, hydrated ^{17}O NMR spectrum bearing similar Si/Al and counteraction is desired for both **FAU** and **CHA** to help with the assignment of observed resonances to different species within the zeolites. This information would be greatly useful to unpicking the structural conversions taking place during the transformation, hopefully providing an insight into the mechanism. It is possible that this understanding would then be more widely applicable to other known PST transformations, even helping to predict whether a pair of framework topologies are convertible.

The use of ^{17}O NMR spectroscopy in this thesis has revealed how extensive the interactions between zeolites and water are, and how water is capable of both supporting structural conversions of zeolites and reacting with pristine, fragmented and defective zeolite frameworks to exchange oxygen atoms with those of the zeolite structures. The results discussed reflect only a very small portion of the reactivity of water with zeolites, but make clear that accounting for this interaction is very important when considering the deployment of zeolites in aqueous conditions.

Looking forward, this thesis has implications for the field of zeolite science and for structure-reactivity studies in of materials chemistry. The results detail the reactivity and the sensitivity of aluminosilicate zeolites and silicate, germanosilicate, borosilicate, titanosilicate and zincosilicate zeolite materials to water under a variety of conditions. The products produced have shed light on novel reactivity pathways, with some interesting and potentially useful crystalline products produced. Further, in cases where non-crystalline products have been obtained from reaction with water or for cases where no structural changes to a material are seen, *e.g.* ^{17}O bond lability studies, the surprising reactivity and flexibility of zeolite frameworks has been demonstrated. For industrially relevant zeolites, such as **FAU** and **CHA**, although it is unlikely that reactivity with water is responsible for their catalytic properties, this behaviour should be considered when these materials are selected for a particular application. This consideration is particularly relevant as the scientific community seeks to address society's needs, for example in finding renewable energy sources. Zeolites are well suited to biomass refinery processes, however the feedstocks for these are often aqueous.

A large proportion of the work in this thesis has been dedicated to finding novel routes for studying crystalline microporous materials and their reactivity processes. To that end, effort has been invested in designing processes that allow simple study of otherwise complex reactivity pathways through analysis of the long-range order of isolated intermediates, or through the design of isotopic enrichment processes for solid-state NMR spectroscopy. Isolating intermediates of the ADOR process and analysing using both long-range and local-structural characterisation techniques has greatly deepened the understanding of the reactive processes occurring during disassembly and organisation steps. The ^{17}O NMR techniques developed for aluminosilicates highlight changes to the local structure in zeolites that are otherwise silent when diffraction-based techniques only are considered. When designing these experiments an effort has been made to keep them as simple as possible and specific to the material of study, whilst still making them applicable to zeolite materials in general. In particular, it is hoped that room-temperature slurrying and mechanochemical approaches to ^{17}O-enrichment using $H_2{}^{17}O$ are applicable to a wide range of zeolites. If approaches similar to these are utilised in the future and can enable a greater understanding of framework material structure and reactivity, then the exercise will have been worthwhile.

Appendix A

^{29}Si Probe Background

A.1 ^{29}Si Probe Background

All ^{29}Si MAS NMR spectra presented in this thesis have been recorded on a Bruker 4.0 mm low-γ wide bore probe at 9.4 T. This probe is known to contain a ^{29}Si background signal, which can overlap with expected zeolite resonances. To characterise the level of background present in the probe, a ^{29}Si MAS NMR spectrum was acquired for NaCl. The resulting spectrum is shown in Figure A.1.

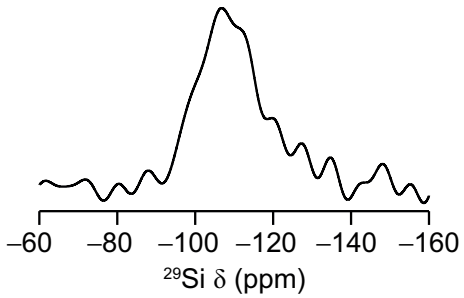

Figure A.1: (9.4 T, 14 kHz) ^{29}Si MAS NMR spectra of NaCl, recorded on a Bruker 4.0 mm low-γ wide bore probe at 9.4 T by averaging 680 transients with a recycle interval of 120 s.

Whilst this signal will be present in all ^{29}Si NMR presented in this thesis, the effect will be most pronounced in NMR spectra of samples with lower volume or lower levels of silicon. Practically this includes the low Si/Al **FAU** and PST-synthesised **CHA** materials discussed in Chapter 6 in this thesis and particularly their slurry and gas-enriched samples, for which small sample volumes are used.

Appendix B

^{17}O-enriched Sample Information

Some samples in this thesis possess high structural similarity. Small changes, *e.g.* hydration state and charge-balancing cation can have an effect on the observed characterisation, particularly for ^{17}O NMR spectra. The information detailed in this section describes the characteristics of the materials at the point at which their ^{17}O NMR spectra were recorded.

For all materials, hydration states have been assigned qualitatively, based on physical properties of the sample and prevalence of signals attributed to water in ^{17}O NMR spectra. Expected levels of hydration: wet > air-dried > incipient wetness > air dry > air hydrated > dehydrated.

B.1 ^{17}O-enriched Samples Chapter 4

Figure	Material	Framework Composition (Si, X)	Si/X	Extra-framework Cation	Enrichment Method	Hydration State
Figure 4.16	ADOR Intermediates	Si	n/a	n/a	hydrolysis	air-dried
Figure 4.17	ADOR Intermediates	Si	n/a	n/a	hydrolysis	air-dried
Figure 4.18	ADOR Intermediates	Si	n/a	n/a	hydrolysis	air-dried
Figure 4.19	ADOR Intermediates	Si	n/a	n/a	hydrolysis	air-dried
Figure 4.20	IPC-2P	Si	n/a	n/a	incipient wetness	air-dried
Figure 4.22b,d	IPC-2P	Si	n/a	n/a	slurry	air dry
Figure 4.22c,e	IPC-2P	Si	n/a	n/a	slurry	wet
Figure 4.24	IPC-2P	Si	n/a	n/a	slurry	air dry
Figure 4.26	Si-**UTL**	Si	n/a	n/a	slurry	air dry
Figure 4.28b,d	IPC-2P	Si, Al	≈ 10	n/a	slurry	wet
Figure 4.29	GeO_2	Ge	n/a	n/a	hydrolysis	air-dried
Figure 4.30	Ge-**UTL**	Si, Ge	4.5	n/a	gas	air-hydrated
Figure 4.31	Ge-**UTL**	Si, Ge	4.5	n/a	gas	air-hydrated
Figure 4.33	IPC-2P	Si, Ge	4.5	n/a	ball mill	air-dried
Figure 4.34	IPC-2P	Si, Ge	15	n/a	ball mill	air-dried

Table B.1: Structural and chemical characteristics of ^{17}O isotopically enriched materials presented in Chapter 4 of this thesis, ordered by thesis figure discussed.

B.2 ^{17}O-enriched Samples Chapter 5

Figure	Material	Framework Composition (Si, X)	Si/X	Extra-framework Cation	Enrichment Method	Hydration State
Figure 5.5	SSZ-13(H)	Si, Al	10	H	gas	air-hydrated
Figure 5.6	SSZ-13(H)	Si, Al	10	H	slurry	wet
Figure 5.8	SSZ-13(H)	Si, Al	10	H	slurry	wet
Figure 5.9	SSZ-13(H)	Si, Al	10	H	slurry	wet
Figure 5.14	SSZ-13(M)	Si, Al	10	Na, K, Cu, Zn	gas	air-hydrated
Figure 5.17	SSZ-13(M)	Si, Al	10	Na, K, Cu, Zn	slurry	wet
Figure 5.18	SSZ-13(M)	Si, Al	10	Na, K, Cu, Zn	slurry	wet
Figure 5.24	Si-**CHA**	Si	n/a	n/a	gas	air-hydrated
Figure 5.25	Si-**CHA**	Si	n/a	n/a	slurry	wet
Figure 5.27a,c	Ti-**CHA**(H)	Si, Ti	22	H	slurry	wet
Figure 5.27b,d	Zn-**CHA**(H)	Si, Zn	18	H	slurry	wet
Figure 5.28a,c	B-**CHA**(H)	Si, B	8	H	slurry	wet
Figure 5.28b,d	B-**CHA**(H)	Si, B	8	H	incipient wetness	air-dried
Figure 5.32	Al-**FAU**(Na)	Si, Al	1.7	Na	gas	air-hydrated
Figure 5.34	Al-**FAU**(Na)	Si, Al	1.7	Na	slurry	wet

Table B.2: Structural and chemical characteristics of ^{17}O isotopically enriched materials presented in Chapter 5 of this thesis, ordered by thesis figure discussed.

B.3 ^{17}O-enriched Samples Chapter 6

Figure	Material	Framework Composition (Si, X)	Si/X	Extra-framework Cation	Enrichment Method	Hydration State
Figure 6.1	Al-**CHA**(K)	Si, Al	1.6	K	PST	air-dried
Figure 6.9	Al-**FAU**(K)/ Al-**CHA**(K)	Si, Al	1.6	K	PST	air-dried
Figure 6.10a,d	Al-**FAU**(Na)	Si, Al	1.7	Na	slurry	wet
Figure 6.10b,e	Al-**FAU**(Na)	Si, Al	1.7	Na	gas	air-hydrated
Figure 6.10c,f	Al-**FAU**(K)	Si, Al	1.7	K	PST	air-dried
Figure 6.11a,d	Al-**CHA**(K)	Si, Al	5	K	slurry	wet
Figure 6.11b,e	SSZ-13(K)	Si, Al	10	K	slurry	wet
Figure 6.11c,f	Al-**CHA**(K)	Si, Al	1.7	K	PST	air-dried
Figure 6.12	Al-**FAU**(K)/ Al-**CHA**(K)	Si, Al	1.6	K	gas	air-hydrated
Figure 6.13	Al-**FAU**(K)/ Al-**CHA**(K)	Si, Al	1.6	K	gas	air-hydrated
Figure 6.14	Al-**FAU**(K)/ Al-**CHA**(K)	Si, Al	1.6	K	slurry	wet
Figure 6.15	Al-**FAU**(K)/ Al-**CHA**(K)	Si, Al	1.6	K	slurry	wet

Table B.3: Structural and chemical characteristics of ^{17}O isotopically enriched materials presented in Chapter 6 of this thesis, ordered by thesis figure discussed.

Appendix C

Diffraction Patterns of ADOR Intermediates

C.1 ADOR Intermediates Produced from Standard Hydrolysis Reactions

PXRD patterns of ADOR intermediates produced from standard hydrolysis reactions performed at 100 °C, with a solid : water of 1:200.

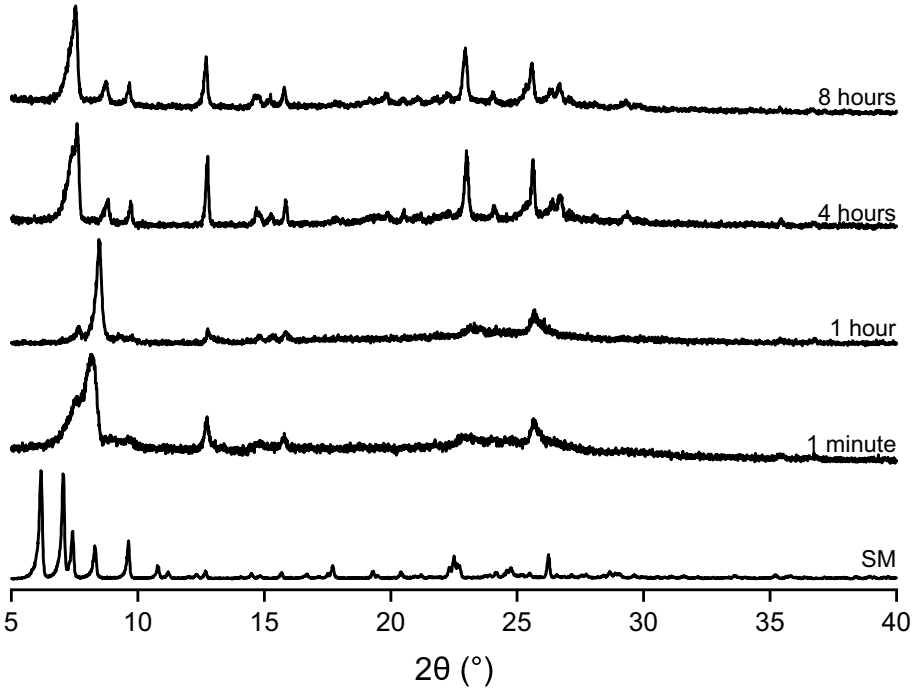

Figure C.1: PXRD patterns of ADOR intermediates produced from standard hydrolysis reactions of different length, performed at 100 °C, with a solid : water of 1:200.

Appendix D

NMR Spectra of Ball-milled Ge-UTL Materials

D.1 ^{29}Si MAS NMR Spectra of Ball-milled Ge-UTL Materials

^{29}Si MAS NMR spectra of intermediates formed through ball-milling of Ge-**UTL** with water. Solid : water of 5:1.

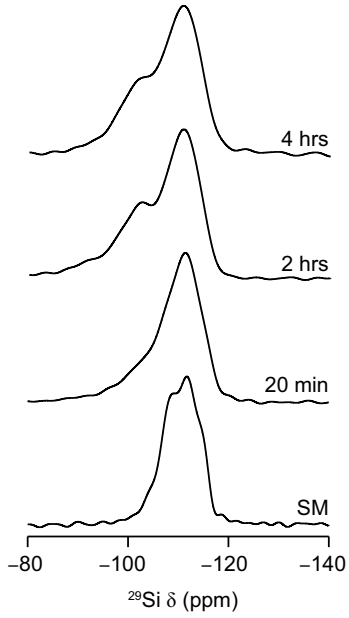

Figure D.1: (9.4 T, 14 kHz) ^{29}Si MAS NMR spectra of Ge-**UTL** ball-milled with water (solid : water = 5:1) for varying amounts of time.

Appendix E

$\{^1H\}^{27}Al$ MQMAS NMR Studies of SSZ-13 Materials

E.1 $\{^1H\}^{27}Al$ MQMAS NMR Spectra of $^{17}O_{2(g)}$-enriched Materials

Le Bail fits for PST materials are presented; **FAU**-**CHA** PST **FAU** starting material (Figure F.1), **FAU** 3 day PST steamed material (Figure F.2), **CHA** 5 day PST end product (Figure F.3).

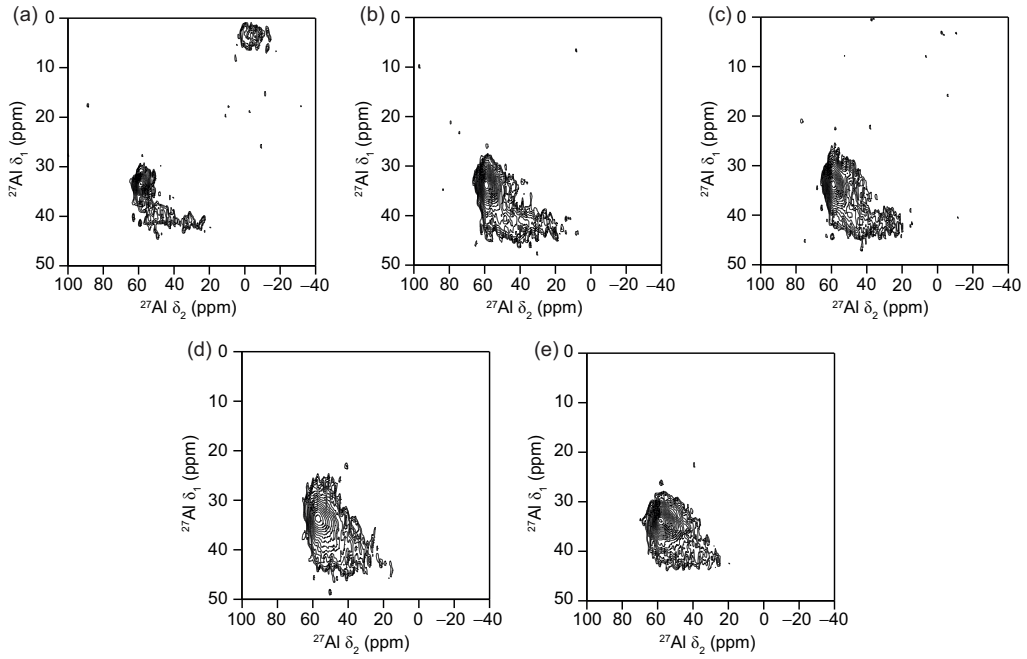

Figure E.1: (9.4 T, 14 kHz) $\{^1H\}^{27}Al$ MQMAS NMR spectra of $^{17}O_{2(g)}$-enriched SSZ-13(X) materials. X = (a) H, (b) Na, (c) K, (d) Cu, (e) Zn.

E.2 $\{^1H\}^{27}Al$ MQMAS NMR Spectra of $H_2^{17}O$ Slurry Materials

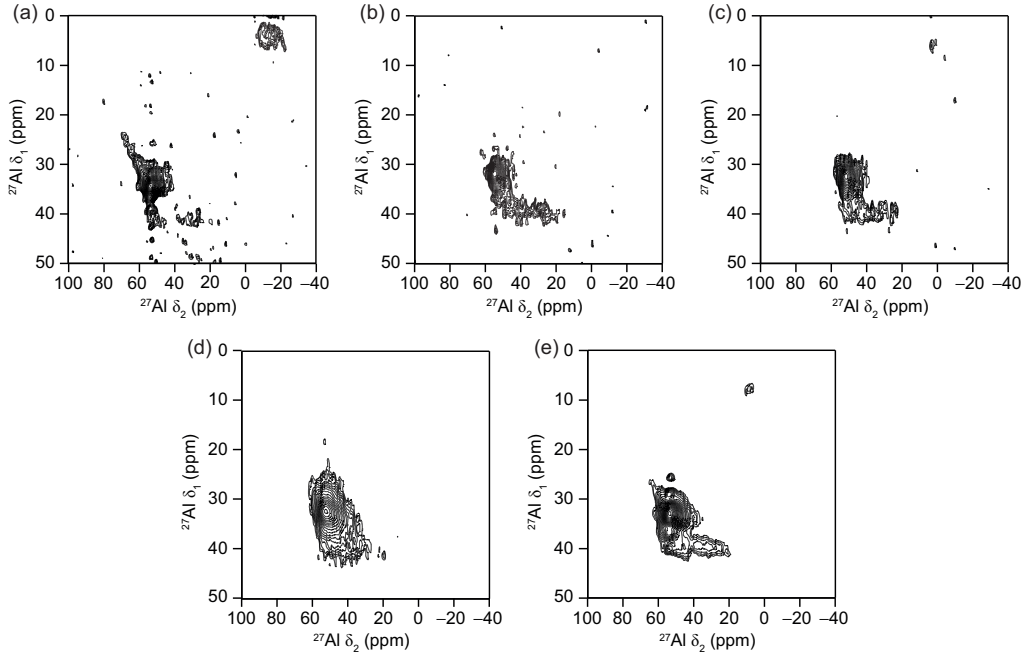

Figure E.2: (9.4 T, 14 kHz) $\{^1H\}^{27}Al$ MQMAS NMR spectra of $H_2{}^{17}O$ slurry materials SSZ-13(X) materials, slurried with small amounts of 40% $H_2{}^{17}O$ for 330 days. X = (a) H, (b) Na, (c) K, (d) Cu, (e) Zn.

Appendix F

Le Bail Fits for PST Materials

F.1 Le Bail Fits

Le Bail fits for PST materials are presented; **FAU**-**CHA** PST **FAU** starting material (Figure F.1), **FAU** 3 day PST steamed material (Figure F.2), **CHA** 5 day PST end product (Figure F.3).

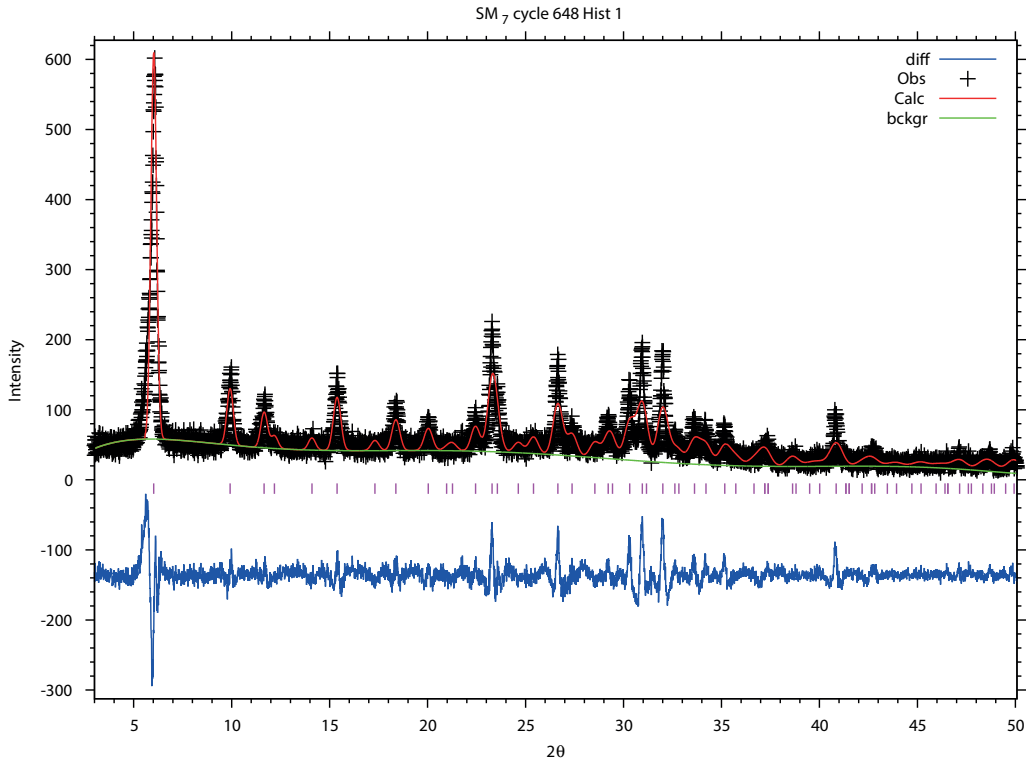

Figure F.1: Le Bail fit of **FAU**-**CHA** PST **FAU** starting material. Powder pattern (black), background (green), fit (red) and difference (blue).

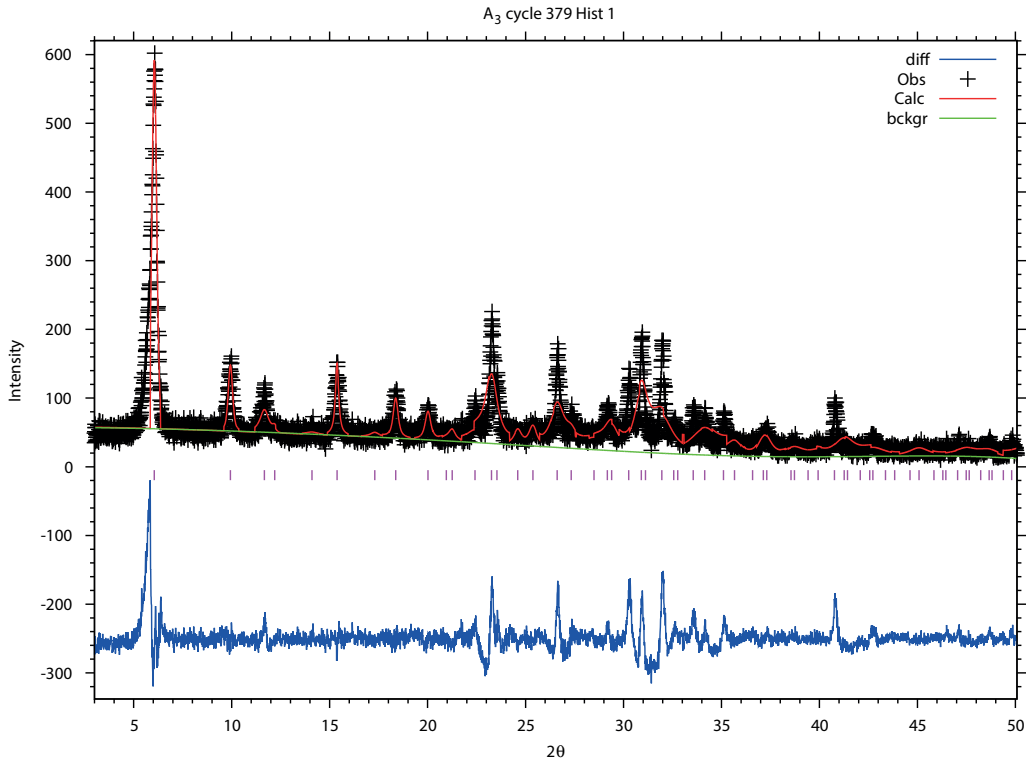

Figure F.2: Le Bail fit of **FAU** 3 day PST steamed material. Powder pattern (black), background (green), fit (red) and difference (blue).

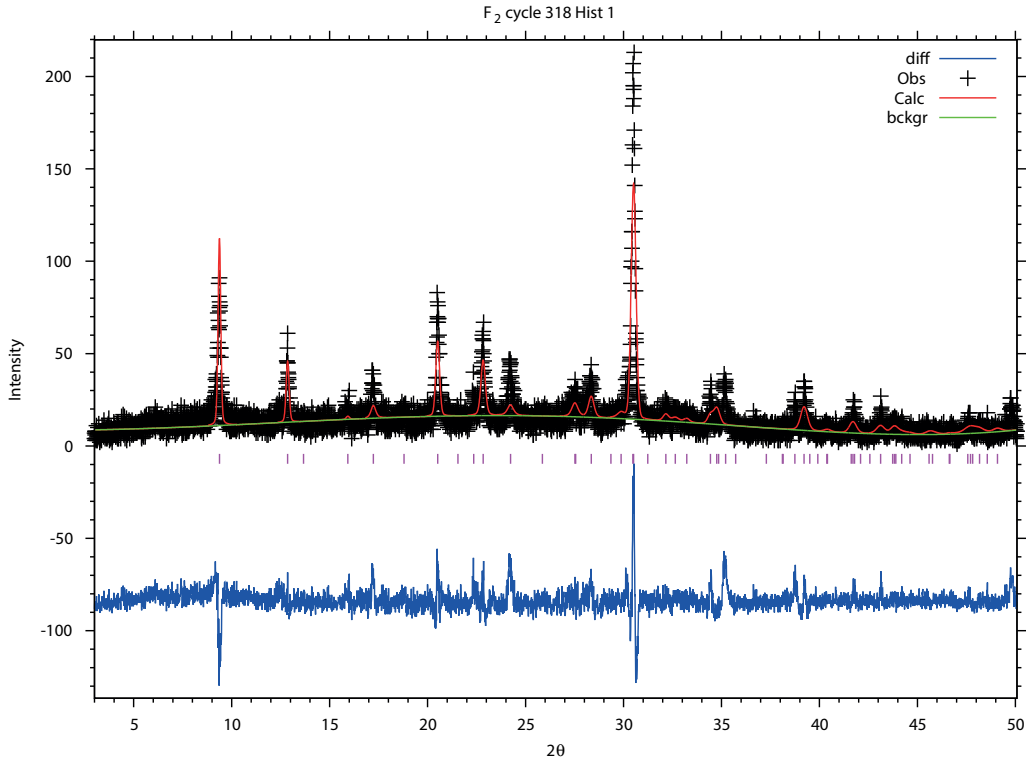

Figure F.3: Le Bail fit of **CHA** 5 day PST end product. Powder pattern (black), background (green), fit (red) and difference (blue).

Appendix G

Further ^{17}O-enriched PST Materials

G.1 $^{17}O_{2(g)}$-enriched PST materials

NMR spectra of natural abundance PST-synthesised materials are provided. ^{29}Si and ^{27}Al NMR spectra for three-day **FAU** starting material, 2 day mixed phase PST intermediate and 4 day PST **CHA** product are shown in Figure F.1 and Figure F.2, respectively.

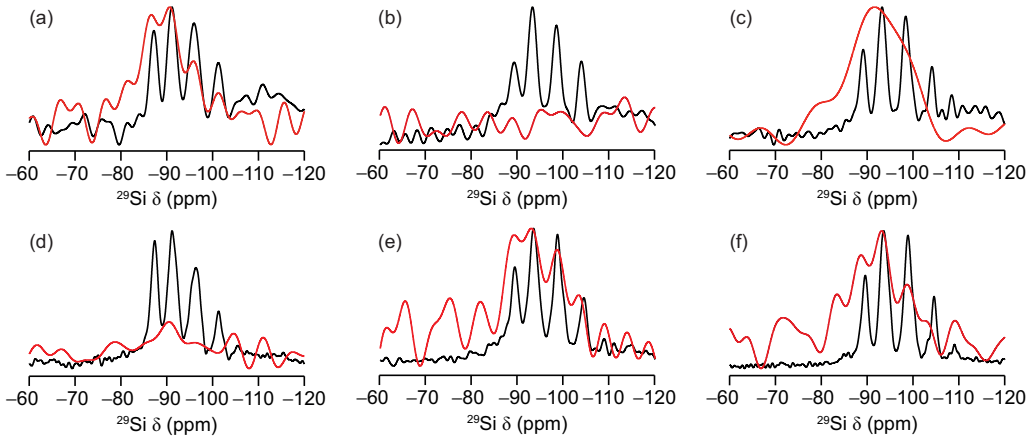

Figure G.1: (9.4 T, 14 kHz) ^{29}Si MAS NMR spectra of (a-c) starting and (d-f) $^{17}O_{2(g)}$-enriched materials for natural abundance (a,d) K^+-exchanged **FAU** SM, (b,e) 2 day PST intermediate phase and (c,f) 4 day PST **CHA** materials. Red overlay corresponds to ^{1}H^{29}Si CP NMR spectrum (5000 μs contact time).

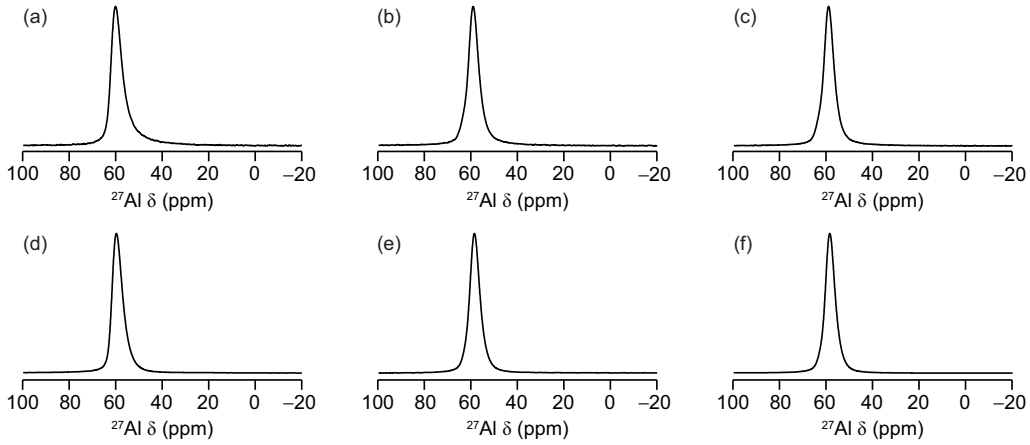

Figure G.2: (9.4 T, 14 kHz) ^{27}Al MAS NMR spectra of (a-c) starting and (d-f) $^{17}O_{2(g)}$-enriched materials for natural abundance (a,d) K^+-exchanged **FAU** SM, (b,e) 2 day PST intermediate phase and (c,f) 4 day PST **CHA** materials.

G.2 $H_2{}^{17}O$ slurry-enriched PST materials

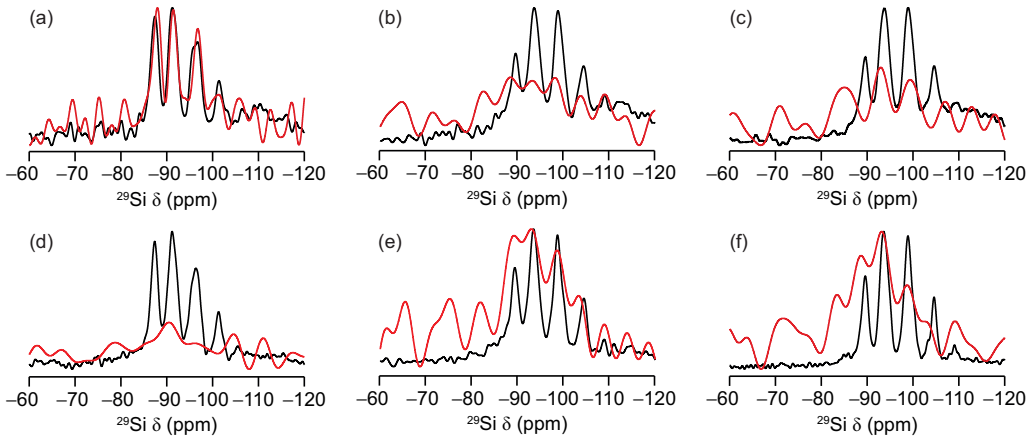

Figure G.3: (9.4 T, 14 kHz) ^{29}Si MAS NMR spectra of (a-c) starting and (d-f) $H_2{}^{17}O$ slurry-enriched materials for natural abundance (a,d) K^+-exchanged **FAU** SM, (b,e) 2 day PST intermediate phase and (c,f) 4 day PST **CHA** materials. Red overlay corresponds to $^1H^{29}$Si CP NMR spectrum (5000 μs contact time).

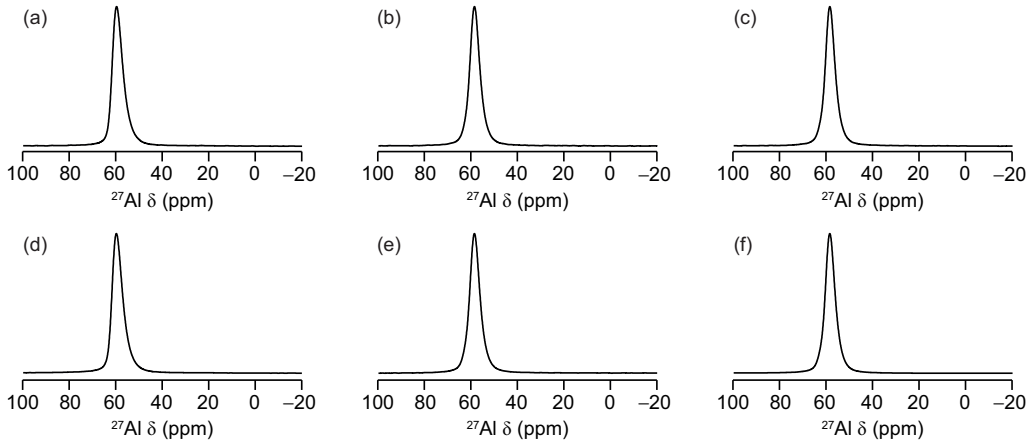

Figure G.4: (9.4 T, 14 kHz) ^{27}Al MAS NMR spectra of (a-c) starting and (b-d) $H_2{}^{17}O$ slurry-enriched materials for natural abundance (a,d) K^+-exchanged **FAU** SM, (b,e) 2 day PST intermediate phase and (c,f) 4 day PST **CHA** materials.